Technische Universität München
Max-Planck–Institut für Quantenoptik

Quantum Information Processing with Atoms and Photons

Christine A. Muschik

Vollständiger Abdruck der von der Fakultät für Physik
der Technischen Universität München
zur Erlangung des akademischen Grades eines

Doktors der Naturwissenschaften (Dr. rer. nat.)

genehmigten Dissertation.

Vorsitzender :	Univ.-Prof. Dr. Dr. h.c. A. Laubereau
Prüfer der Dissertation :	1. Hon.-Prof. J. I. Cirac, Ph.D.
	2. Univ.-Prof. Dr. H. Friedrich

Die Dissertation wurde am 30.08.2011 bei der
Technischen Universität München eingereicht und
durch die Fakultät für Physik am 15.09.2011 angenommen.

To Annemarie, Brigitte and Hans Muschik

Abstract

In this Thesis, we present new tools for the study of quantum systems and propose several novel schemes for practical applications in quantum information science. We explore two main topics, engineered dissipation and light-matter quantum interfaces, and investigate both with a focus on collective effects that arise if a large number of particles interact coherently with an optical quantum field. The majority of the considered physical systems are ensembles of neutral atoms. We study mainly atomic vapor at room temperature interacting with light. We use here a refined description of this interaction, which generalizes the model employed during the last decade and allows us to develop new protocols for this type of system. We also consider ultracold atoms in optical lattices for the implementation of the ideas and schemes put forward here. Besides these two main systems, we also investigate Bose-Einstein condensates and single atoms in optical cavities.

The central part of this Thesis focuses on harnessing dissipative processes for quantum information science, which represents a radically new approach. We explore this route and devise a scheme for the generation of long-lived entangled states which are obtained as the steady states of a dissipative evolution. This method leads to very robust entanglement, which does not require the initialization of the system in a specific state. We present here also the theoretical description of the corresponding experiment, where entanglement has been maintained up to one hour by combining the dissipative mechanism with continuous measurements. This exceeds the entanglement life-times observed so far by several orders of magnitude. In this context, we also propose a dissipative approach to the challenge of entanglement distribution over large distances. We show how many weakly entangled states can be dissipatively transformed into few highly entangled ones. Based on these results, we propose a continuous quantum repeater scheme, which produces long-range high-quality steady state entanglement.

Another large part of this Thesis is concerned with the application of light-matter interface techniques in different contexts. We analyze a scheme which enables the deterministic teleportation of quantum states between two macroscopic ensembles under realistic experimental conditions. Light acts here as an auxiliary system which connects the two material systems. We also propose a protocol for the realization of an entangling gate for photons, which is based on the opposite approach. Here, an atomic ensemble acts as auxiliary system to enable an effective interaction between photons. Apart from these quantum technology related projects, we investigate the use of light-matter quantum interface techniques for the study of quantum many-body systems and propose a novel spectroscopy scheme which uses quantum memories for probing spin systems.

Zusammenfassung

In dieser Doktorarbeit stellen wir neuartige Untersuchungsmethoden für quantenmechanische Systeme sowie verschiedene Protokolle für praktische Anwendungen in der Quanteninformationswissenschaft vor. Wir untersuchen hier hauptsächlich zwei Themengebiete - die gezielte Manipulation von Dissipation und Quantenschnittstellen zwischen Licht und Materie. Kollektive Effekte, die auftreten, wenn eine große Anzahl von Teilchen kohärent mit einem optischen Quantenfeld wechselwirkt, bilden hierbei einen besonderen Schwerpunkt. Bei den physikalischen Systemen handelt es sich haupsächlich um Ensembles neutraler Atome. Wir betrachten dabei insbesondere die Wechselwirkung von atomaren Wolken bei Raumtemperatur mit Licht. Wir verwenden hierbei eine verbesserte Beschreibung dieser Wechselwirkung, die das Modell, das während des letzten Jahrzehnts verwendet wurde, verallgemeinert und es uns so erlaubt, neue Protokolle für dieses System zu entwickeln. Eine weitere Möglichkeit für die Implementierung der Protokolle, die hier diskutiert werden, sind Ensembles ultrakalter Atome in optischen Gittern. Neben diesen beiden Systemen untersuchen wir auch Bose-Einstein Kondensate und einzelne Atome in optischen Kavitäten.

Der zentrale Teil dieser Arbeit widmet sich dem Einsatz dissipativer Prozesse in der Quanteninformationswissenschaft. Die gezielte Nutzung von Dissipation ist hierbei ein radikal neuer Ansatz. Mit Hilfe dieser Idee entwickeln wir eine Methode zur Erzeugung langlebiger verschränkter Zustände, die hierbei als stationäre Zustände einer dissipativen Entwicklung erzielt werden. Diese Methode führt zu sehr robuster Verschränkung und erfordert nicht die Initialisierung des Systems in einem speziellen Anfangszustand. Wir stellen hier weiterhin die theoretische Beschreibung eines Experiments vor, in dem Verschränkung bis zu einer Stunde lang aufrecht erhalten werden konnte. Dieses wurde durch die Kombination des dissipativen Mechanismus mit kontinuierlichen Messungen erreicht und übertrifft die Lebensdauern, die bisher erzielt wurden, um mehrere Größenordnungen. Wir entwickeln in diesem Zusammenhang auch einen dissipativen Lösungsansatz für eines der Grundprobleme der Quantentechnologie, nämlich Verschränkung über weite Distanzen hinweg zu erzeugen. Dazu zeigen wir, wie viele schwach verschränkte Zustände dissipativ in wenige stark verschränkte umgewandelt werden können. Basierend auf diesen Ergebnissen entwickeln wir ein Schema für einen kontinuierlichen Quantenrepeater, der die Erzeugung stark verschränkter Zustände über weite Distanzen hinweg erlaubt.

Ein weiterer wesentlicher Teil dieser Arbeit widmet sich der Anwendung von Quantenschnittstellen zwischen Licht und Materie. Wir analysieren ein Schema, das die

deterministische Teleportation von Quantenzuständen zwischen zwei makroskopischen Ensembles unter realistischen Bedingungen ermöglicht. Licht agiert hierbei als ein Hilfssystem, das die beiden Materiesysteme koppelt. Wir schlagen zudem ein Protokoll für die Realisierung eines verschränkenden Quantengatters vor, das auf dem umgekehrten Ansatz beruht. In diesem Fall agiert ein atomares Ensemble als Hilfssystem und ermöglicht so eine effektive Wechselwirkung zwischen Photonen. Neben diesen auf Quantentechnologie bezogenen Projekten erforschen wir auch die Anwendbarkeit von Quantenschnittstellen für neue Untersuchungsmethoden von Quanten-Vielteilchensystemen und entwickeln eine neuartige Spektroskopiemethode, die Quantenspeicher für die Untersuchung von Spinsystemen nutzt.

Publications

Articles

[I] *Quantum processing photonic states in optical lattices,*
Christine A. Muschik, Inés de Vega, Diego Porras, and J. Ignacio Cirac.
Phys. Rev. Lett. **100**, 063601 (2008).

[II] *Entanglement distillation by dissipation and continuous quantum repeaters,*
Karl Gerd H. Vollbrecht, Christine A. Muschik, and J. Ignacio Cirac.
arXiv:1011.4115 (2010), to be published in Phys. Rev. Lett.

[III] *Entanglement generated by dissipation and steady state entanglement of two macroscopic objects.*
Hanna Krauter*, Christine A. Muschik*, Kasper Jensen, Wojciech Wasilewski, Jonas M. Petersen, J. Ignacio Cirac, and Eugene S. Polzik.
Phys. Rev. Lett. **107**, 080503 (2011).

[IV] *Dissipatively driven entanglement of two macroscopic atomic ensembles.*
Christine A. Muschik, Eugene S. Polzik, and J. Ignacio Cirac.
Phys. Rev. A **83**, 052312 (2011).

[V] *Quantum Memory Assisted Probing of Dynamical Spin Correlations.*
Oriol Romero-Isart, Matteo Rizzi, Christine A. Muschik, Eugene S. Polzik, Maciej Lewenstein, and Anna Sanpera.
arXiv:1105.6308 (2011).

[VI] *Quantum state engineering, purification, and number resolved photon detection with high finesse optical cavities.*
Anne E. B. Nielsen, Christine A. Muschik, Géza Giedke and Karl Gerd H. Vollbrecht.
Phys. Rev. A **81**, 043832 (2010).

[VII] *Single mode quadrature entangled light from room temperature atomic vapor.*
Wojciech Wasilewski, Thomas Fernholz, Kasper Jensen, Lars S. Madsen, Hanna Krauter, Christine Muschik, and Eugene S. Polzik.
Opt. Express **17**, 14444 (2009).

*These authors contributed equally to this work.

[VIII] *Detecting entanglement in two mode squeezed states by particle counting.*
Christine A. Muschik, Eugene S. Polzik, and J. Ignacio Cirac.
arXiv:0806.3448 (2008).

[IX] *Quantum Information at the Interface of Light with Mesoscopic Objects.*
Christine A. Muschik, Hanna Krauter, Klemens Hammerer, and Eugene S. Polzik.
arXiv:1105.2947 (2011).

Book chapter

[X] *Quantum processing photonic states in optical lattices.*
Christine A. Muschik, Inés de Vega, Diego Porras, and J. Ignacio Cirac.
Advances in Information Optics and Photonics, ICO Book IV, 533, SPIE Press, (2008).

Proceedings

[XI] *Quantum memory, entanglement and sensing with room temperature atoms.*
Kasper Jensen, Wojciech Wasilewski, Hanna Krauter, Thomas Fernholz, Bo M. Nielsen, Jonas M. Petersen, Jelmer J. Renema, Michael V. Balabas, Masaki Owari, Martin B. Plenio, Alessio Serafini, Michael M. Wolf, Christine A. Muschik, J. Ignacio Cirac, Jörg H. Müller and Eugene S. Polzik.
J. Phys.: Conf. Ser. **264**, 012022 (2011).

In preparation

[XII] *Deterministic quantum teleportation between two macroscopic objects.*
Christine A. Muschik, Hanna Krauter, Eugene S. Polzik, and J. Ignacio Cirac.

[XIII] *Entanglement generated by dissipation.*
Christine A. Muschik, Hanna Krauter, Kasper Jensen, Wojciech Wasilewski, Jonas M. Petersen, J. Ignacio Cirac, and Eugene S. Polzik.

Contents

Chapter 1

Motivation and outline

The laws of quantum mechanics can be harnessed for information processing schemes, which yield a quantum advantage compared their classical counterparts. These applications include fast and powerful computers [1–3], unconditionally secure communication [4–6] and quantum simulations [7–9], which can provide new insights into otherwise intracable problems in physics. The implications of quantum mechanics for information processing are studied in the field of quantum information science (QIS), which aims at gaining a deeper understanding of quantum correlations and explores the potential of quantum technologies (the prospects and achievements in the main branches of QIS are briefly reviewed in App. A). Most applications in quantum communication and distributed quantum networks rely on the transmission of quantum states of light, since photons are natural travelling carriers of information. However, for the same reason, photonic systems are not well suited for storage. Atomic systems, in contrast, provide excellent platforms for quantum memories[1]. Light-matter interfaces, which allow for the transfer of quantum information between flying and stationary qubits are therefore an essential prerequisite for technological applications in QIS.

Efficient quantum interfaces require strong light-matter interactions. This can, be achieved by placing atoms in a high finesse cavity [11]. We consider this type of setup in Sec. 5.1, where we explore the potential applications of an array of linear optical elements and single atoms in optical cavities for quantum state engineering and show how it can be used for number resolved photon detection. An experimentally less demanding alternative to obtain strong coupling is provided by atomic ensembles consisting of a large number of atoms [12, 13]. In this case, the coupling is enhanced by means of collective effects which arise due to the coherent radiation of a large number of dipoles. We investigate this effect considering atomic vapor at room temperature. More specifically, we consider ensembles of alkali atoms confined in glass cells. This setup is very robust and practical from an experimental point of view. At first glance, it may appear surprising that quantum effects can be observed under these conditions. However,

[1] Using quantum memories, information can be stored coherently, such that the quantum nature of the state is preserved. Such a device cannot rely on a classical strategy, since any approach which involves the measurement of a quantum state and its subsequent reconstruction is fundamentally limited by the no-cloning theorem [10].

as explained in Sec. 2.1, quantum information can be encoded in collective atomic spin states which are unaffected by the thermal motion of the atoms. Due to special paraffin-based spin preserving coatings, the atoms can collide multiple times with the walls of the cell, before the collective quantum state is deteriorated. This way, the atoms in the ensemble can interact coherently with light. An important part of this Thesis is concerned with a refined description of this interaction. So far, experiments with atomic ensembles at room temperature have been described assuming a quantum-nondemolition (QND) interaction[2] [12]. Using a more general model, a new generation of developments and experiments has become possible [IX]. Since it includes effects which have not been taken into account before and have therefore been treated as noise, it enables a better performance of light-matter interface schemes[3]. Moreover, it allows for the design and implementation of protocols which go beyond the possibilities that can be realized using QND interactions, for instance the purely dissipative generation of entanglement as described in Sec. 3.1. This new description plays also a central role in Sec. 4.1, where we discuss a protocol for the teleportation of a macroscopic quantum state between two ensembles and show that this scheme is experimentally feasible.

Apart from vapor at room temperature, we also consider ultracold gases in optical lattices [19–21]. This system consists of neutral atoms at nanokelvin temperatures which are trapped in a periodic potential of standing waves created by counter-propagating laser fields. This system provides another excellent platform for the realization of light-matter interface schemes [22]. In Sec. 4.2, we show how this fact can be used to gain insights into phenomena in quantum many-body physics. More specifically, we propose a novel spectroscopy technique which uses quantum memories to probe important properties of spin systems which are realized or simulated by ultracold atoms in optical lattices. Ultracold atoms in deep optical lattices can form a Mott insulator [23, 24], i.e. a state of matter, where the atoms are strongly localized at individual lattice sites. These localized atoms are in the motional ground state and quantum information can be encoded in internal ground state levels. This system features strong short-range interactions, which can be induced in a highly controlled way (see Sec. 2.2). In Sec. 4.3, we use these interactions in order to realize an entangling gate for photons. We propose here a scheme, where a photonic state is mapped to an ensemble of atoms using light-matter interface techniques. The resulting atomic state is processed employing inter-atomic interactions and subsequently transferred back to a light field.

Apart from the systems described above, we also consider Bose-Einstein condensates (BECs) interacting with optical fields. We study the superradiant scattering of laser light from elongated BECs and propose schemes for the detection and application of the correlations that are created between atoms and photons in this process.

[2] This description has been successfully used for many different experiments including the demonstration of a quantum memory for light [14], quantum teleportation between light and matter [15] and the generation of entanglement between two distant atomic samples using measurements and feedback operations [16].

[3] Recent experiments using the refined description include improved entanglement assisted and backaction evading magnetometry approaching the quantum Cramér-Rao limit [17] and a quantum memory for squeezed states of light [18].

These ideas, tools and protocols are based on the control of *unitary* dynamics. However, a central part of this Thesis is devoted to the investigation and application of *dissipative* time evolutions. The coupling of a quantum system to its environment, generally referred to as dissipation, is traditionally considered to be the main problem impairing experiments involving quantum superposition states and the development of quantum technologies. Therefore, experiments are typically performed under strict isolation conditions. Harnessing dissipation[4] rather than avoiding it, is a radically new concept and represents a paradigm shift in QIS. In Sec. 3, we show that even limited control of the coupling between system and environment can enable one to turn a major problem into an asset. This change in perspective is not only of conceptual interest, but yields also significant practical advantages. The coupling of a system with a reservoir can be engineered such that the desired state is obtained as the steady state of the dissipative evolution. This way, the desired state is reached independently of the initial state. The initialization of the system in a well defined state, which is typically considered a critical issue [60], is therefore rendered unnecessary. Moreover, the resulting state is stabilized by the dissipative dynamics and can be maintained, in principle, for arbitrary long times. Using these ideas, it is therefore possible to overcome important restrictions set by the limited coherence times of quantum systems.

We conclude this introduction, by providing an overview to the following chapters and summarizing main results. **Chapter 2** introduces the physical systems and interactions investigated in this Thesis. The main system under consideration, atomic vapor at room temperature, is described in Sec. 2.1. The next section, Sec. 2.2, is devoted to ultracold atoms in optical lattices. Finally, we briefly review the physics of Bose-Einstein condensates and single atoms in optical cavities in Sec. 2.3 and Sec. 2.4.
Chapter 3 is concerned with new methods utilizing dissipation. In Sec. 3.1, we propose a scheme for the generation of long-lived atomic entanglement by dissipation [IV]. This protocol can be implemented in any system where a tunable quadratic interaction with an active and a passive part corresponding to two sideband modes can be realized, for instance in ions or using optomechanical resonators. Here, we analyze the scheme in detail for atomic ensembles at room temperature and present the theoretical description of the corresponding experiment [III], which has been performed at the Niels Bohr Institute in Copenhagen. This implementation does not only include the first purely dissipative generation of unconditional entanglement but also the generation of an inseparable steady state by means of a hybrid approach, which combines the dissipative mechanism with continuous measurements. This way, it has been possible to maintain entanglement for up to an hour, which exceeds the entanglement life times observed so far [61,62] by several orders of magnitude. Sec. 3.2 addresses the question how the quality of dissipatively produced entanglement can be improved in the presence of additional noise. Moreover, we investigate how steady state entanglement can be put to work in a continuous quantum repeater protocol which does not require the decoupling of the system from the environment, as would be the case for standard schemes. We devise and analyze a new type of repeater scheme, which allows for the distribution of high-quality,

[4] See for example [25–49, 49–59].

long-range entanglement in a steady state [II].

Chapter 4 regards the use of light-matter interface schemes for applications in QIS and for the study of quantum many-body systems. In Sec. 4.1, we analyze an experimentally feasible scheme for the teleportation of an atomic state between two ensembles at room temperature. The deterministic teleportation between two matter systems over a macroscopic distance is an essential prerequisite for quantum networks, but could not yet be implemented. In atomic vapors at room temperature, teleportation between light and matter has been realized [15, 63]. However, the teleportation of quantum states between two atomic ensembles could not be realized so far due to the lack of an experimentally realizable protocol. Here, we devise a scheme which is particularly designed for this specific system. We take typical sources of noise into account and show that the scheme is feasible under current experimental conditions. In Sec. 4.2, we develop a novel technique for probing dynamical spin correlations by merging the concept of QND spectroscopy [64, 65] with quantum memory technology [12, 66]. The latter is used to introduce a time delay in the measurement process, while storing information coherently such that dynamical correlations in spin degrees of freedom can be accessed directly and the dynamical spin structure factor can be measured [V]. The investigation of quantum memory techniques for spectroscopy is a promising starting point for using light-matter interfaces for the study of correlated systems. The range of applicability of this idea is very broad, since it can for example be used to study non-equilibrium dynamics. Moreover, it opens the door towards new possibilities for the manipulation of quantum many-body states. The fully coherent character of the probing scheme provides promising prospects for the investigation and engineering of quantum states and complex dynamics, since it allows one to monitor a system nondestructively and act back on it conditioned on the result of the measurement. In Sec. 4.3, we propose a scheme for quantum information processing of light states. This scheme [I] combines ideas from interface schemes in atomic ensembles [12, 66, 67] with tools available for ultracold atoms in optical lattices [68, 69]. The implementation of a two-qubit gate for light [70–76] is a very difficult task, as photons are non-interacting particles in principle. Photons can interact via optical nonlinearities, but up to now there are no materials available which allow for reasonably short gate times. Approaches involving linear optics and measurements [77] are intrinsically probabilistic and therefore not very efficient. The scheme put forward here is deterministic and uses atomic interactions to provide an effective nonlinearity. The required operations are within the state of the art and the protocol is robust against the main sources of errors in a realistic setup.

In **chapter 5**, entanglement is studied in terms of particle number correlations. Unlike in the other chapters, the physical systems under consideration are not vapors at room temperature or ultracold atoms in optical lattices, but single atoms high-finesse optical cavities and Bose-Einstein condensates. More specifically, in Sec. 5.1 a cavity-based filtering scheme is proposed and analyzed, which enables several quantum communication related tasks such as the creation and purification of photon number entangled states and non-destructive photon counting [VI]. In Sec. 5.1, superradiance in Bose-Einstein condensates is studied and protocols for the creation and purification of entanglement between two condensates in different momentum states are put forward [VIII].

Chapter 6 concludes this Thesis with a summary and an outlook.

Chapter 2

Physical systems

In this chapter, we introduce the four physical systems which are considered in this Thesis, atomic ensembles at room temperature (Sec. 2.1), ultracold atoms in optical lattices (Sec. 2.2), single atoms in high finesse optical cavities (Sec. 2.3) and Bose-Einstein condensates (Sec. 2.4). We describe these systems in the context of the results presented in the following chapters and highlight special features which make them particularly interesting candidates for the implementation of the ideas put forward here. Since large and important parts of this Thesis center on the study of atomic ensembles at room temperature (Sec. 2.1), this system is described in more detail. The other sections are specifically tailored to the aspects, which are relevant for the following chapters. In this and all following chapters we use the convention $\hbar = 1$.

2.1 Atomic ensembles at room temperature

Atomic ensembles provide an excellent platform for the realization of light-matter interface schemes and related applications. As outlined in chapter 1, strong motivation for using many particles comes from the quest for achieving high interaction strengths such that atoms and light induce changes to the mutual quantum states with high efficiency[1]. Due to collective enhancement, ensemble based quantum interfaces can be realized even in free space. This effect originates from the fact that the initial state of the light field excites a collective mode in the atomic ensemble, which is shared by all particles in the sample. This type of mapping between atoms and light can be achieved using different techniques involving Raman transitions [78], electromagnetically induced transparency [79, 80] or photon echo methods [81, 82]. We focus here on Faraday interaction based interface schemes [14, 83] and consider macroscopic gas samples at room temperature. More specifically, we describe in the following the interaction of an ensemble of alkali atoms, which are contained in glass cells with freely propagating light [12]. This setup features simplicity from an experimental point of view and long coherence times. Faraday interactions between light and macroscopic ensembles have been used extensively in many different experiments over the last decade and enabled the realization of several important tasks

[1] Comprehensive recent reviews on the various approaches based on atomic ensembles can be found in [12, 13].

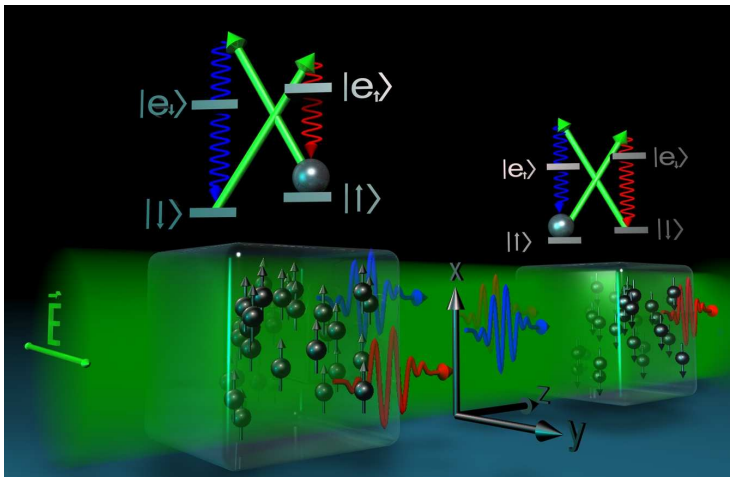

Figure 2.1: Light-matter interaction involving a strong $\hat{\mathbf{y}}$-polarized laser field (depicted in green) and two atomic ensembles, which are spin polarized parallel and antiparallel with respect to a homogeneous magnetic background field which is oriented along $\hat{\mathbf{x}}$ and defines the quantization axis. Atoms are assumed to possess two ground and two excited states $|\uparrow\rangle$, $|\downarrow\rangle$ and $|e_\uparrow\rangle$, $|e_\downarrow\rangle$. The strong off-resonant driving field induces diagonal transitions $|\uparrow\rangle \rightarrow |e_\downarrow\rangle$, $|\downarrow\rangle \rightarrow |e_\uparrow\rangle$ which lead to the emission of photons in $\hat{\mathbf{x}}$-polarization (corresponding to the transitions $|e_\uparrow\rangle \rightarrow |\uparrow\rangle$, $|e_\downarrow\rangle \rightarrow |\downarrow\rangle$). Due to the Zeeman splitting Ω of the atomic ground states, photons are scattered into the upper and lower sideband (shown in blue and red respectively) which are centered at $\omega_L \pm \Omega$, where ω_L is the frequency of the incident classical field.

in quantum information science, such as the demonstration of a quantum memory for coherent and squeezed states [14,18], the teleportation between light and matter [15], the creation of entanglement between two macroscopic objects [16] and sensing beyond the standard quantum limit [17].
In Sec. 2.1.1 and in Sec. 2.1.2, we introduce the specific setup considered here and explain how light and atoms interact. In Sec. 2.1.3, we present the corresponding input-output relations, which relate the photonic and atomic variables before and after the interaction.

2.1.1 The physical system - description of atoms and light

In the following, we explain how atoms and light can be described in terms of bosonic variables and introduce the setting which will be used (with minor modifications) in Sec. 3.1, Sec. 4.1 and Sec. 4.2.

Setup and light variables

We consider the setup shown in Fig. 2.1. A strong $\hat{\mathbf{y}}$-polarized laser pulse propagates along $\hat{\mathbf{z}}$ and passes two atomic ensembles in a homogeneous magnetic field, which defines the quantization axis and is oriented along $\hat{\mathbf{x}}$. Each atomic ensemble consists of a large number N of hydrogen-like atoms with an internal level structure as depicted in Fig. 2.1.

These atoms are confined in cubic glass cells which are separated by a distance of approximately 0.5m and have a spatial extent of several cm. Each cell contains on the order of 10^{12} alkali atoms and is equipped with a paraffin-based spin-preserving coating. The length of the laser pulse irradiating the ensembles is several orders of magnitude larger than the spatial extent of the cells[2]. The laser field covers a very narrow bandwidth b around the central frequency ω_L and is far off-resonant with respect to the atomic transitions such that absorption effects can be neglected.
We adopt here a one-dimensional model[3], i.e. we consider only light scattered in forward direction. The scattering of photons in other directions can be included in this description in the form of noise processes [84]. A three-dimensional analysis of the scattering interaction considered here can be found in [85, 86]. The strong coherent field in $\hat{\mathbf{y}}$-polarization is described by a $\mathbb{C}$-number, while the co-propagating $\hat{\mathbf{x}}$-polarized light field is described quantum mechanically[4]. The strong classical field induces diagonal transitions $|\uparrow\rangle \rightarrow |e_\downarrow\rangle$, $|\downarrow\rangle \rightarrow |e_\uparrow\rangle$ which result in the emission of $\hat{\mathbf{x}}$-polarized photons through decay processes $|e_\uparrow\rangle \rightarrow |\uparrow\rangle$, $|e_\downarrow\rangle \rightarrow |\downarrow\rangle$. This way, the classical field couples the atoms and the quantized radiation field. The strength of this effective interaction depends on the Rabi frequency of the driving field and its detuning from the relevant atomic transitions. In the following, the quantum field will be described in terms of spatially localized modes [12, 63, 87, 88]

$$\begin{aligned} x_L(z) &= \frac{1}{\sqrt{4\pi}} \int_b d\omega \left(a_\omega e^{-i(\omega-\omega_L)z/c} + H.C. \right), \\ p_L(z) &= \frac{-i}{\sqrt{4\pi}} \int_b d\omega \left(a_\omega e^{-i(\omega-\omega_L)z/c} - H.C. \right), \end{aligned} \tag{2.1}$$

where the annihilation and creation operators a_ω and $a_\omega^\dagger$ refer to a $\hat{\mathbf{x}}$-polarized photon with frequency ω and obey the commutation relations $[a_\omega, a_{\omega'}^\dagger] = \delta(\omega - \omega')$, $[a_\omega, a_{\omega'}] = 0$. The spatial argument z refers to the distance along the optical path and ω_L is the central frequency of the classical beam. Due to the finite bandwidth b of this field, the canonical commutation relation $[x_L(z), p_L(z')] = ic\delta_b(z - z')$ involves a Dirac delta function with a finite width on the order of c/b.

Atomic variables

We will describe the atomic state of an ensemble in terms of its collective spin $\mathbf{J} = \sum_{i=1}^N \mathbf{F}_i$, where $\mathbf{F}_i$ is the total angular momentum of the i^{th} atom. For a two-level system as considered here, $F = 1/2$. In the following, we consider strongly polarized samples. More specifically, we assume that the ensemble is initially prepared in a coherent spin state (CSS) where all atoms are in state $|\uparrow\rangle$, $|\Psi_{\text{CSS}}\rangle = |\uparrow_1 ... \uparrow_N\rangle$, such that the collective spin along the quantization axis $\hat{\mathbf{x}}$, $\langle J_x \rangle = N/2$, is a macroscopic quantity. If the light field

[2] Under the experimental conditions considered here, the pulse is several hundred kilometers long.
[3] Only the light field in forward direction is of interest for the protocols, which are described by means of this formalism in the following chapters. These schemes rely on measurements, to which only photons scattered along $\hat{\mathbf{z}}$ contribute. As shown in Sec. 3.1, these processes are weaker, since forward scattering is enhanced for samples of high optical depth.
[4] In the specific example considered here, this field is initially in the vacuum. In general, any other state containing only few photons can be considered along the lines explained here.

interacts with the ensemble via a Faraday interaction [12], the collective atomic spin is rotated depending on the Stokes vector of the applied light field. We assume that the deviations from perfect $\hat{\mathbf{x}}$-alignment which occur during the interaction are small such that the collective atomic state remains close to the CSS. In this case, the longitudinal component of the collective spin J_x can be considered to be a classical quantity and can accordingly be replaced by its mean value $\langle J_x \rangle \approx \langle J \rangle \approx N/2$. The transverse components of the collective spin J_y and J_z can be described in terms of canonical variables x_A and p_A (with $[x_A, p_A] = i$) using the Holstein-Primakoff approximation [89, 90], as will be explained in the following.
The Holstein-Primakoff transformation maps spin operators to bosonic creation and annihilation operators a_A and $a_A^\dagger$ with $[a_A, a_A^\dagger] = 1$. To this end, the collective ladder operators $J_\pm = J_y \pm iJ_z$ are expressed in terms of a_A and $a_A^\dagger$ by

$$J_+ \;=\; \sqrt{N}\sqrt{1 - \frac{a_A^\dagger a_A}{N}}\; a_A, \qquad J_- = \sqrt{N}\; a_A^\dagger \sqrt{1 - \frac{a_A^\dagger a_A}{N}}. \tag{2.2}$$

The transformation for J_x can be obtained using the identity

$$J_x^2 \;=\; J(J+1) - J_y^2 - J_z^2 = J(J+1) - \frac{1}{2}(J_+ J_- + J_- J_+) = (J - a_A^\dagger a_A)^2.$$

By identifying $J_x = J - a_A^\dagger a_A$, the fully polarized initial state $|\Psi_{\mathrm{CSS}}\rangle = |\uparrow_1 \ldots \uparrow_N\rangle = |J, J\rangle$ can be mapped to the ground state of an harmonic oscillator $|J, J\rangle \mapsto |0\rangle_A$, such that the expression $J_x|J, J\rangle = J|J, J\rangle$ corresponds to $(J - a_A^\dagger a_A)|0\rangle_A = J|0\rangle_A$. This transformation is exact. If the atomic state is close to the CSS, $\langle a_A^\dagger a_A \rangle / \langle J \rangle \ll 1$ can be assumed[5]. In this case, Eq. (2.2) can be expanded in a series to first order and approximated by

$$J_+ \;\approx\; \sqrt{N}\; a_A, \qquad J_- \approx \sqrt{N}\; a_A^\dagger.$$

Within this approximation, the transverse components of the collective spin are given by $J_y = (J_+ + J_-)/2 \approx \sqrt{\langle J \rangle}(a_A + a_A^\dagger)/\sqrt{2}$ and $J_z = -i(J_+ - J-)/2 \approx \sqrt{\langle J \rangle}(a_A - a_A^\dagger)/2$ and can be identified with the atomic quadratures

$$x_A \;\approx\; J_y/\sqrt{\langle J \rangle}, \qquad p_A \approx J_z/\sqrt{\langle J \rangle},$$

where $x_A = (a_A + a_A^\dagger)/\sqrt{2}$ and $p_A = -i(a_A - a_A^\dagger)/\sqrt{2}$ has been used. Within the approximation outlined above, these atomic operators obey the canonical commutation relations $[x_A, p_A] = [J_y, J_z]/\langle J \rangle \approx i$. In the following we will use either the atomic quadratures x_A and p_A or the corresponding creation and annihilation operators $a_A^\dagger$ and a_A, depending on which description is more convenient.

2.1.2 Interaction between an atomic ensemble and light

Light and atoms interact off-resonantly via the electric dipole interaction. In the parameter regime considered here, the corresponding dipole Hamiltonian (or level shift operator)

[5] This condition corresponds to the assumption that the number of collective excitations $\langle a_A^\dagger a_A \rangle$ is small compared to the number of atoms in the ensemble. In the experimental parameter regime considered here, this condition is very well fulfilled, since $\langle a_A^\dagger a_A \rangle$ is on the order of one, while $N \approx 10^{12}$.

describes processes where the population of the excited levels is negligible and the atomic polarization follows the ground state population adiabatically. More precisely, if the detuning $|\Delta|$ is large compared to the effective atomic rates for ground state transitions $|\uparrow\rangle \leftrightarrow |\downarrow\rangle$ and the Doppler width, the excited levels can be adiabatically eliminated (see Sec. 3.1). This way, an effective light-matter interaction which involves only photons and atomic ground states is obtained. For the type of level scheme considered here, the resulting effective interaction is referred to as Faraday interaction and can be interpreted as follows. The collective spin experiences a small (Faraday-) rotation due to the interaction with the light field. In return, the Stokes vector of the light field undergoes a (Stark-shift induced) rotation which depends on the collective spin state of the ensemble. This way, the interaction leads to a mutual exchange of quantum statistics between the two systems. Experiments involving this effect have been described assuming a quantum-nondemolition (QND) interaction during the past decade [12]. As explained below, the QND Hamiltonian, H_{QND}, corresponds to the limiting case of a more general model of the Faraday interaction. This generalized approach leads to a refined description of the corresponding experiments and enables a new generation of protocols that can be realized using Faraday rotations [IX]. In this subsection, the interaction of light with an atomic ensemble is introduced and discussed for two-level systems. We also consider its implementation in Cesium ensembles and explain how this interaction can be tuned by varying externally controllable parameters.

Light-matter interaction in a simple model including the ground states $|\uparrow\rangle$ and $|\downarrow\rangle$ and two excited states

To start with, we consider the simple model illustrated in Fig. 2.1. In this subsection, we focus on the interaction of the light field with the first ensemble. As explained in Sec. 2.1.1, atoms and light are described by means of the operators a_A, $a_A^\dagger$ and $a_L(z)$, $a_L^\dagger(z)$ respectively. The operator $a_A^\dagger = \frac{1}{\sqrt{N}} \sum_{i=1}^{N} |\downarrow\rangle_i\langle\uparrow|$, refers to a collective atomic excitation. The action of this collective operator on the product state $|0\rangle_A \equiv |\uparrow_1, \uparrow_2, \ldots, \uparrow_N\rangle$ results in the symmetric coherent superposition of all N possible terms which represents a state where one spin in the ensemble has been flipped $a_A^\dagger|0\rangle_A = \frac{1}{\sqrt{N}} \sum_{i=1}^{N} |\uparrow_1, \ldots, \downarrow_i, \ldots, \uparrow_N\rangle$.
The atomic ensemble and the light field can be shown to interact according to a Hamiltonian which is quadratic in the operators x_A, p_A, x_L and p_L within the approximations described above[6] [VII], [83]. By means of suitable local operations, any quadratic Hamiltonian describing the interaction of two one-mode continuous variable systems can be expressed as a sum of a passive and an active contribution [91] $H_{\mathrm{int}} = s_1 H_{\mathrm{pas}} + s_2 H_{\mathrm{act}}$. The passive contribution[7] $H_{\mathrm{pas}} = a_L(0)a_A^\dagger + H.C.$ is excitation number conserving. If a collective atomic excitation is created, a photon is annihilated. In contrast, the active interaction $H_{\mathrm{act}} = a_L^\dagger(0)a_A^\dagger + H.C.$ corresponds to the creation (or annihilation) of atomic

[6] In the following, Gaussian input states and Gaussian measurements (homodyne detection on the quadratures of the light field) are considered. The time evolution according to a quadratic Hamiltonian is a linear transformation which preserves the Gaussian character of the involved quantum states. Therefore, the setting under consideration can be conveniently described using the Gaussian formalism (see Sec. 3.1.5).

[7] We assume here a pointlike atomic ensemble located at $z = 0$.

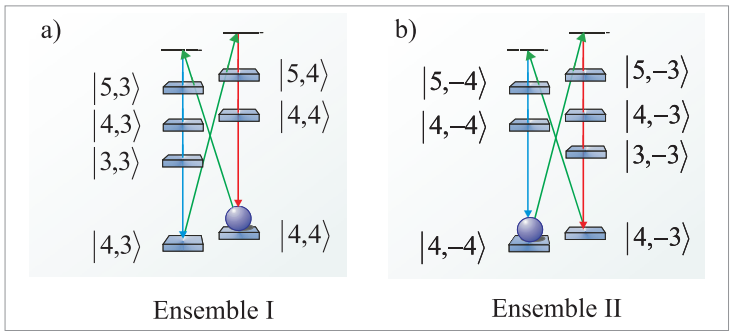

Figure 2.2: Off-resonant probing of the D_2 line in spin polarized ^{133}Cs ensembles as shown in Fig. 2.1. The strong coherent field in $\hat{\mathbf{y}}$-polarization is depicted in green while the quantum field in $\hat{\mathbf{x}}$-polarization is shown in blue and red. Only desired transitions are shown - the level splittings are not depicted true to scale.

and photonic excitations in pairs. The former interaction can be understood as the interspecies analog of a beamsplitter interaction while the latter creates entanglement and is referred to as "squeezing interaction". The light-matter interaction considered here involves both types and will be parametrized by the parameters $\kappa/\sqrt{T}$ (where T is the pulse duration) and Z

$$H_{\text{int}} = \frac{\kappa}{\sqrt{T}}(\mu - \nu)\left[\mu H_{\text{pas}} + \nu H_{\text{act}}\right], \tag{2.3}$$

where $\mu = (Z + \frac{1}{Z})/2$ and $\nu = (Z - \frac{1}{Z})/2$. The QND Hamiltonian corresponds to the special case $|\mu| = |\nu|$, where H_{pas} and H_{act} contribute exactly with equal strength. In the simple model considered here, an imbalance $|\mu| \neq |\nu|$ can arise due to the Larmor splitting of the ground state, which leads to different detunings $\Delta + \Omega$ and $\Delta - \Omega$ for the two-photon transitions associated with the active and the passive part of the interaction (see Sec. 3.1.3 and Fig. 3.2a). However, in the experimental settings considered here, the detuning Δ is much larger than the Larmor splitting such that this effect is negligible (in a magnetic field of 1 Gauss, the Zeeman shift of magnetic sublevels is about 10^5Hz while the detuning is on the order of 10^8 Hz). The non-QND character of the light-matter interaction in Cesium atoms is due to the fact that the levels $|\uparrow\rangle$ and $|\downarrow\rangle$ couple to several excited levels [92–95] as described below.

Light-matter interaction including the multi-level structure of the manifold of excited states in Cesium

In contrast to the simple model considered above, Cesium atoms have a multi-level structure. We consider here ^{133}Cs vapor as used in [III,VII], [14–16]. As illustrated in Fig. 2.2a, a two-level subsystem can be encoded in the $6S_{1/2}$ ground state[8] with total spin $F = 4$ by identifying the states $|\uparrow\rangle$ and $|\downarrow\rangle$ with the outermost levels corresponding to the magnetic

[8] Since ^{133}Cs atoms have a single electron outside a closed shell and nuclear spin $I = 3/2$, the $6S_{1/2}$ ground state consists of two manifolds with total spin $F = 4$ and $F = 3$.

quantum numbers (the projection of the spin along $\hat{\mathbf{x}}$) $m_F = 4$ and $m_F = 3$, such that $|\uparrow\rangle \equiv |F = 4, m_F = 4\rangle \equiv |4,4\rangle$ and $|\downarrow\rangle \equiv |F = 4, m_F = 3\rangle \equiv |4,3\rangle$. If all atoms have been initialized in state $|\uparrow\rangle$, it can be assumed that only a small fraction is transferred to state $|\downarrow\rangle$ during the interaction and that the population in all other levels can be neglected. The strong laser field in $\hat{\mathbf{y}}$-polarization probes the D_2 line and couples these levels off-resonantly to the excited states in $6P_{3/2}$. This way, the passive part of the interaction (corresponding to the transfer of atoms from $|\downarrow\rangle$ to $|\uparrow\rangle$ and the creation of a photon in the red sideband) involves the upper levels with $F = 4, 5$, while the active part of the light-matter interaction (corresponding to the transfer $|\uparrow\rangle \rightarrow |\downarrow\rangle$ and the creation of a photon in the blue sideband) involves the manifolds with $F = 3, 4, 5$. The corresponding Z-parameter can be easily determined if the detuning and the corresponding Clebsch-Gordan coefficients are known. In this specific case, one obtains $Z = (\mu + \nu) = 2.5$ for a blue detuning of $\Delta = 850$MHz with respect to the state with total spin $F = 5$ within $6P_{3/2}$. In general, Z can be calculated as follows. The effective rate for ground state transitions $|\uparrow\rangle \leftrightarrow |\downarrow\rangle$ involving the excited state $|l\rangle$ is given by $\Gamma_{|a\rangle\rightarrow|l\rangle\rightarrow|b\rangle} = \Omega^2_{\text{probe}} |\frac{c_{al}c_{lb}}{\Delta_l + i\gamma_{\text{LW}(l)}}|^2 \gamma_{\text{LW}(l)} \approx \Omega^2_{\text{probe}} \frac{|c_{al}c_{lb}|^2}{\Delta_l^2} \gamma_{\text{LW}(l)}$, where Ω^2_{probe} is the Rabi frequency of the applied laser field[9], c_{al} and c_{lb} are the Clebsch-Gordan coefficients for the transitions $|a\rangle \rightarrow |l\rangle$ and $|l\rangle \rightarrow |b\rangle$, $\gamma_{\text{LW}(l)}$ is the natural line width of the excited state and $\Delta_l \gg \gamma_{\text{LW}(l)}$ was assumed. If several excited states contribute, the different paths can interfere and the effective rate for the off-resonant transition $|a\rangle \rightarrow |b\rangle$ is therefore given by the sum $\gamma_{|a\rangle\rightarrow|b\rangle} = \Omega^2_{\text{probe}} |\sum_l \frac{c_{al}c_{lb}}{\Delta_l}|^2 \gamma_{\text{LW}}$, where the line widths of the involved excited levels have been assumed to be approximately equal. If the ratio $r^2 = \frac{\Gamma_{|\downarrow\rangle\rightarrow|\uparrow\rangle}}{\Gamma_{|\uparrow\rangle\rightarrow|\downarrow\rangle}} = \frac{\mu^2}{\nu^2}$ is calculated, $Z^2 = \frac{r+1}{r-1}$ can be determined.

The character of the interaction can be changed from the predominantly passive to the active type by altering the sign of the detuning (by using for example red instead of blue detuning). A change in the type of interaction can also be achieved by switching the polarization of the classical and the quantum field. As illustrated in Fig. 2.2a, using a $\hat{\mathbf{x}}$-polarized classical field (which drives vertical transitions, in this picture) and correspondingly a quantum field in $\hat{\mathbf{y}}$-polarization (which is associated with diagonal transitions) would involve the excited levels with $F = 3, 4, 5$ for the passive part of the interaction and the levels with $F = 4, 5$ for the active one (as opposed to the setting discussed above, where it is the other way round). The imbalance between the active and the passive part becomes less pronounced for large detunings. If Δ is much larger than the hyperfine splitting of the excited states, the interaction Hamiltonian can be well approximated by H^{QND} [12, 84, 95].

The light matter-interaction can be equivalently described in terms of the ground state polarizability $H_{\text{int}} \propto \sum_j \mathbf{E}^-(0)\alpha_j \ \mathbf{E}^+(0)$, where $\mathbf{E}^{\pm}(0)$ describes the electric field[10] interacting with the atomic ensemble at the position $z = 0$ and α_j is the ground state polarizability tensor operator of the j^{th} atom. It is proportional to the square of the

[9] We use here a notation, where the Rabi frequency is independent of the atomic transition and the corresponding Clebsch-Gordan coefficient are stated expicitely.

[10] $\mathbf{E}^-(z) = E^-(z)\hat{\mathbf{e}}_x + \mathcal{E}^-(z)\hat{\mathbf{e}}_y$, where $\hat{\mathbf{e}}_{x/y}$ is the unit vector in x/y-direction, $\mathcal{E}(z)$ is the electric field of the classical beam and $E^-(z) = \rho(\omega_L) \int_b d\omega a^\dagger_\omega e^{-i(\omega-\omega_L)z/c}$ (the mode density $\rho(\omega)$ is assumed to be approximately constant for the narrow-band laser light considered here).

relevant reduced dipole matrix element μ_d and can always be decomposed into its scalar, vector and tensor part $\alpha_j = \frac{\mu_\mathrm{d}^2}{\Delta}(\alpha_S \mathbb{1} + i\alpha_V \mathbf{F}_j\times + \alpha_T T_j)$, where $\mathbf{F}_j\times$ is the Cartesian vector product of the ground state spin of the j^{th} atom $\mathbf{F}_j$ and the vector applied to its right side. The scalar part depends neither on the quantum state of light nor on the atomic state. It adds therefore only a global phase to the input-wave function and represents the index of refraction. The physical meaning of the vector and the tensor part can be best understood by considering their action on the Stokes operators of the light field

$$S_1 = \frac{1}{2}\left(N_x - N_y\right), \qquad S_2 = \frac{1}{2}\left(N_{+45^\circ} - N_{+45^\circ}\right), \qquad S_3 = \frac{1}{2}\left(N_{\sigma_+} - N_{\sigma_-}\right),$$

where $N_{x/y}$, $N_{\pm 45^\circ}$ and $N_{\sigma_\pm}$ are the numbers of photons in x/y, $\pm 45^\circ$ and $\sigma_\pm$-polarization respectively. The vector part of the atomic polarizability leads to circular birefringence of the medium, i.e. different indices of refraction for σ_+ and σ_--polarized light $n_{\sigma_+} \neq n_{\sigma_-}$, while $n_x = n_y$ and $n_{+45^\circ} = n_{-45^\circ}$. This way, S_3 is conserved, but not S_1 and S_2. The tensor part leads to linear birefringence, (i.e. different indices of refraction for x and y-polarized light $n_x \neq n_y$) such that S_1 is conserved, but not S_2 and S_3. The tensor part vanishes asymptotically for large detunings. Due to symmetry reasons, it equals zero for spin-$\frac{1}{2}$ systems. H^{QND} corresponds to pure circular birefringence (which leaves S_3 unchanged). If a tensor term is added to the interaction, none of the Stokes operators of the light field is conserved and the interaction is not of QND-type any more.

2.1.3 Input-output relations and characteristic properties of the interaction

In the following, the canonical quadratures $x = (a+a^\dagger)/\sqrt{2}$ and $p = -i(a-a^\dagger)/\sqrt{2}$ will be used. As explained in Sec. 2.1.1, the atomic quadratures x_A and p_A can be identified with the transverse components of the collective spin. In terms of quadratures, the quadratic Hamiltonian introduced above (2.3) is given by

$$H_{\mathrm{int}} = \frac{\kappa}{\sqrt{T}}\left(p_A p_L(0) + \frac{1}{Z^2} x_A x_L(0)\right). \tag{2.4}$$

As will become apparent in Sec. 2.1.3 (see Eq. (2.8)), Z quantifies the squeezing[11] (and corresponding anti-squeezing) of the variances involved in the process [95]. In the balanced case ($|\mu| = |\nu|$), H_{int} reduces to the QND Hamiltoninan $H_{QND} = \frac{\kappa}{\sqrt{T}} p_A p_L(0)$. Below, we introduce the input-output relations which describe the light-matter interaction and highlight characteristic features of the imbalanced and the balanced (QND) type. A general derivation of the input-output relations can be found in App. D.1.1.

QND interaction

The balanced type of the interaction corresponds to the limit $Z \to \infty$ (where $\kappa/\sqrt{T}$ is constant). $H_{QND} = \kappa p_A p_L$ is referred to as quantum-nondemolition interaction since the

[11] $Z = \sqrt{\frac{a_V}{14 a_T}}$, where a_V and a_T are the atomic vector and tensor polarizabilities [95]. The calculation of these values can be found in [12].

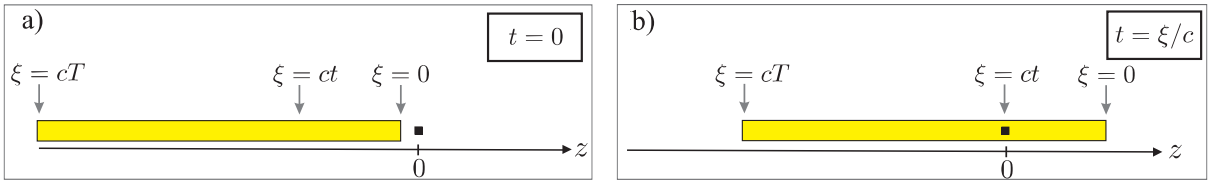

Figure 2.3: Illustration of the propagating light field in terms of spatially localized modes. a) At time $t = 0$, the front part of the light pulse enters the ensemble. b) At a later time $t = \xi/c$, the atoms interact with the localized light mode with quadratures $\bar{x}_L(\xi, t)$, $\bar{p}_L(\xi, t)$.

p-quadratures of atoms and light are conserved. We describe this case here explicitly, since we discuss an interesting application, which relies on a QND interaction and is not necessarily related to a specific implementation in an atomic multi-level structure in Sec. 4.2. The QND case will also be discussed in Sec. 4.1.3. The input-output relations for a single cell in the absence of a magnetic field [63] are given by

$$\begin{aligned} x_A^{out} &= x_A^{in} + \kappa p_L^{in}, \qquad p_A^{out} = p_A^{in}, \\ x_L^{out} &= x_L^{in} + \kappa p_A^{in}, \qquad p_L^{out} = p_L^{in}, \end{aligned} \tag{2.5}$$

where $x_L^{in} = \frac{1}{\sqrt{T}} \int_0^T dt \bar{x}_L(ct, 0)$ and $x_L^{out} = \frac{1}{\sqrt{T}} \int_0^T dt \bar{x}_L(ct, T)$ (analogous definitions hold for p_L^{in} and p_L^{in}). Here, the variable transformation $x_L(r, t) \to x_L(ct - \xi, t) = \bar{x}_L(\xi, t)$ has been made. The spatial variable $\xi = ct - z$ refers to a coordinate system which is fixed to the propagating light pulse as illustrated in Fig. 2.3. $\xi = 0$ refers to the front part of the pulse which enters the ensemble first, while the rear part which passes last corresponds to $\xi = cT$. Shot-noise limited measurements of the collective spin by homodyne detection of the light field require the application of magnetic fields. In the presence of magnetic fields, atomic ground states are Zeeman-shifted by the Larmor splitting Ω as shown in Fig. 2.2. The scattering of a narrow-band classical field with central frequency ω_L leads therefore to the emission of photons into sideband modes, which are centered around $\omega_c \pm \Omega$ in frequency space, as illustrated in Fig. 2.1 which allows for noise reduced measurements on the light field using lock-in methods (see [96]). In the time domain, atomic information is mapped to $\sin(\Omega t)$ and $\cos(\Omega t)$ modulated light modes

$$\begin{aligned} x_{h,cos}^{in} &= \sqrt{\frac{2}{T}} \int_0^T dt h(t) \cos(\Omega t) \bar{x}_L(ct, 0), \\ x_{h,cos}^{out} &= \sqrt{\frac{2}{T}} \int_0^T dt h(t) \cos(\Omega t) \bar{x}_L(ct, T). \end{aligned} \tag{2.6}$$

$x_{h,cos/sin}$ and $p_{h,cos/sin}$ refer to a light mode with an arbitrary envelope function $h(t)$, which varies slowly on the time scale set by the Larmor frequency Ω. The envelope function $h(t)$ is normalized such that $\frac{1}{T} \int_0^T dt h(t)^2 = 1$. In the limit $\Omega T \gg 1$, which is well fulfilled under the experimental conditions considered here, sine and cosine modulated modes are canonical and independent $[x_{h,sin/cos}, p_{h,sin/cos}] = i$, $[x_{h,sin/cos}, p_{h,cos/sin}] = 0$.

The input-output relations for a single ensemble in a magnetic field involve an infinite hierarchy of coupled backaction modes [63], whose envelope functions are given by Legendre polynomials. The input-output relations for the atomic quadratures

$$x_A^{out} = x_A^{in} + \frac{\kappa}{\sqrt{2}} p_{L_0,cos}^{in}, \qquad p_A^{out} = p_A^{in} + \frac{\kappa}{\sqrt{2}} p_{L_0,sin}^{in},$$

involve only light modes of 0$^{\text{th}}$ order with modulation function $L_0(t) = 1$. The input-output relations for these light modes

$$\begin{aligned} x_{L_0,cos}^{out} &= x_{L_0,cos}^{in} + \frac{\kappa}{\sqrt{2}} p_A^{in} + \frac{\kappa^2}{4} p_{L_0,sin}^{in} + \frac{\kappa^2}{4\sqrt{3}} p_{L_1,sin}^{in}, \\ p_{L_0,cos}^{out} &= p_{L_0,cos}^{out}, \\ x_{L_0,sin}^{out} &= x_{L_0,sin}^{in} - \frac{\kappa}{\sqrt{2}} x_A^{in} - \frac{\kappa^2}{4} p_{L_0,cos}^{in} - \frac{\kappa^2}{4\sqrt{3}} p_{L_1,cos}^{in}, \\ p_{L_0,sin}^{out} &= p_{L_0,sin}^{out}, \end{aligned} \tag{2.7}$$

involve light modes of the next (1$^{\text{st}}$) order and are described by the quadratures $x_{L_1,sin/cos}^{in}$ and $p_{L_1,sin/cos}^{in}$ with $L_1(t) = \frac{2\sqrt{3}}{T^{3/2}}\left(\frac{T}{2} - t\right)$. The general expression for the symplectic transformation $R^{out} = S(\Omega)R^{in}$, which relates the infinitely dimensional vectors $R^{in/out} = \left(x_A, p_A, x_{L_0,sin}^{in/out}, p_{L_0,sin}^{in/out}, x_{L_0,cos}^{in/out}, p_{L_0,cos}^{in/out}, x_{L_1,sin}^{in/out}, p_{L_1,sin}^{in/out} \dots\right)^T$ listing the atomic and photonic modes of all orders through the matrix $S(\Omega)$ can be found in [97]. If a setup as shown in Fig. 2.1 with antiparallel oriented spins, or equivalently, antiparallel oriented magnetic fields, is considered, the input-output relations $\tilde{R}^{out} = S_I(\Omega)S_{II}(-\Omega)\tilde{R}^{in}$, where $\tilde{R}^{in/out} = \left(x_{A,I}, p_{A,I}, x_{A,II}, p_{A,II}, x_{L_0,sin}^{in/out}, p_{L_0,sin}^{in/out}, \dots\right)^T$, simplify considerably since all photonic contributions except for the lowest order cancel such that

$$\begin{aligned} x_{A,cos}^{out} &= x_{A,cos}^{in} + \kappa p_{L_0,cos}^{in}, & x_{A,sin}^{out} &= x_{A,sin}^{in} + \kappa p_{L_0,sin}^{in}, \\ p_{A,cos}^{out} &= p_{A,cos}^{in}, & p_{A,sin}^{out} &= p_{A,sin}^{in}, \\ x_{L_0,cos}^{out} &= x_{L_0,cos}^{in} + \kappa p_{A,cos}^{in}, & x_{L_0,sin}^{out} &= x_{L_0,sin}^{in} + \kappa p_{A,sin}^{in}, \\ p_{L_0,cos}^{out} &= p_{L_0,cos}^{in}, & p_{L_0,sin}^{out} &= p_{L_0,sin}^{in}, \end{aligned} \tag{2.8}$$

where the EPR-operators $x_{A,cos} = (x_{A,I} + x_{A,II})/\sqrt{2}$, $p_{A,cos} = (p_{A,I} + p_{A,II})/\sqrt{2}$ and $x_{A,sin} = -(p_{A,I} - p_{A,II})/\sqrt{2}$, $p_{A,sin} = (x_{A,I} - x_{A,II})/\sqrt{2}$ have been used. A comparison of Eq. (2.5) with Eq. (2.8) shows that the the input-output relations for two atomic ensembles which are Larmor precessing in opposite directions are formally equivalent to two independent sets of input-output relations describing the simple case of a single ensemble in the absence of a magnetic field.

This antiparallel setup has for instance been used for the implementation of a quantum memory for light [14] and entanglement generation between two ensembles [16]. Since only the p-quadrature of each set of variables is mapped by the interaction, the realization of a quantum memory required the measurement of the p-quadrature of the light field and a subsequent feedback operation on the atoms in order to transfer both quadratures $x_{L_0,sin/cos}$ and $p_{L_0,sin/cos}$. Also the creation of entanglement based on a QND interaction

requires measurements on the light field. The light-matter interaction itself does not create entanglement, but it allows for a projection onto an Einstein-Podolski-Rosen (EPR) entangled state with squeezed non-local variances $\mathrm{var}(x_{A,sin})$ and $\mathrm{var}(x_{A,cos})$ if $x_{L_0,sin}$ and $x_{L_0,cos}$ are measured.
However, an ideal beamsplitter or squeezing interaction which would allow for perfect mapping or for the creation of infinitely entangled states in the limit $\kappa \to \infty$, can be realized based on a QND interaction by means of a double-pass scheme [98–100], in which one of the two contributions, H_P or H_A is cancelled by interference.

Non-QND interaction

In the following, we consider the general interaction described by Eq. (2.4). The input-output relations for a single cell in a magnetic field are given by

$$\begin{aligned}
\begin{pmatrix} x_A^{out} \\ p_A^{out} \end{pmatrix} &= e^{-\frac{\kappa^2}{2Z^2}} \begin{pmatrix} x_A^{in} \\ p_A^{in} \end{pmatrix} + \sqrt{1-e^{-\frac{\kappa^2}{Z^2}}} \begin{pmatrix} x_{+,\mathrm{r}}^{in} \\ p_{+,\mathrm{r}}^{in} \end{pmatrix}, \\
\begin{pmatrix} x_{-,\mathrm{r}}^{out} \\ p_{-,\mathrm{r}}^{out} \end{pmatrix} &= e^{-\frac{\kappa^2}{2Z^2}} \begin{pmatrix} x_{+,\mathrm{r}}^{in} \\ p_{+,\mathrm{r}}^{in} \end{pmatrix} - \sqrt{1-e^{-\frac{\kappa^2}{Z^2}}} \begin{pmatrix} x_A^{in} \\ p_A^{in} \end{pmatrix},
\end{aligned}$$

where the exponentially rising/falling reading modes with quadratures $x_{\mathrm{r},\pm}$, $p_{\mathrm{r},\pm}$ are given by

$$\begin{pmatrix} x_{\pm,\mathrm{r}}^{in} \\ p_{\pm,\mathrm{r}}^{in} \end{pmatrix} = \frac{1}{2}\left(\left(Z+\frac{1}{Z}\right)\begin{pmatrix} x_{\pm,us}^{in} \\ p_{\pm,us}^{in} \end{pmatrix} + \left(Z-\frac{1}{Z}\right)\begin{pmatrix} p_{\pm,ls}^{in} \\ x_{\pm,ls}^{in} \end{pmatrix}\right).$$

$x_{\pm,us}$, $p_{\pm,us}$ and $x_{\pm,ls}$, $p_{\pm,ls}$ refer to exponentially modulated modes

$$\begin{aligned}
\begin{pmatrix} x_{\pm,us}^{in} \\ p_{\pm,us}^{in} \end{pmatrix} &= \frac{\kappa}{\sqrt{T}ZN_\pm}\int_0^T d\tau e^{\pm\frac{\kappa^2\tau}{2Z^2T}} R(\tau) \begin{pmatrix} \bar{p}_L(c\tau,0) \\ -\bar{x}_L(c\tau,0) \end{pmatrix}, \\
\begin{pmatrix} p_{\pm,ls}^{in} \\ x_{\pm,ls}^{in} \end{pmatrix} &= \frac{\kappa}{\sqrt{T}ZN_\pm}\int_0^T d\tau e^{\pm\frac{\kappa^2\tau}{2Z^2T}} R(\tau) \begin{pmatrix} \bar{p}_L(c\tau,0) \\ \bar{x}_L(c\tau,0) \end{pmatrix},
\end{aligned}$$

which are located at $\omega_L \pm \Omega$ in frequency space respectively (compare Fig. 2.1). The subscripts us and ls refer accordingly to the upper and lower sideband. The normalization constants N_+, N_- and the rotation matrix $R(\tau)$ are given by

$$\begin{aligned}
N_+ &= \sqrt{e^{\frac{\kappa^2}{Z^2}}-1}, \quad N_- = \sqrt{1-e^{-\frac{\kappa^2}{Z^2}}}, \\
R(\tau) &= \begin{pmatrix} \cos(\Omega\tau) & -\sin(\Omega\tau) \\ \sin(\Omega\tau) & \cos(\Omega\tau) \end{pmatrix}.
\end{aligned}$$

As outlined above, the setup involving two antiparallel oriented ensembles in magnetic fields can be conveniently described in terms of EPR modes such that two independent sets of equations are obtained

$$\begin{pmatrix} x_{A,sin/cos}^{out} \\ p_{A,sin/cos}^{out} \end{pmatrix} = e^{-\frac{\kappa^2}{2Z^2}} \begin{pmatrix} x_{A,sin/cos}^{in} \\ p_{A,sin/cos}^{in} \end{pmatrix} + \sqrt{1-e^{-\frac{\kappa^2}{Z^2}}} \begin{pmatrix} Z & 0 \\ 0 & -\frac{1}{Z} \end{pmatrix} \begin{pmatrix} p_{+,sin/cos}^{in} \\ x_{+,sin/cos}^{in} \end{pmatrix}, \tag{2.9}$$

$$\begin{pmatrix} x_{-,sin/cos}^{out} \\ p_{-,sin/cos}^{out} \end{pmatrix} = e^{-\frac{\kappa^2}{2Z^2}} \begin{pmatrix} x_{+,sin/cos}^{in} \\ p_{+,sin/cos}^{in} \end{pmatrix} + \sqrt{1-e^{-\frac{\kappa^2}{Z^2}}} \begin{pmatrix} Z & 0 \\ 0 & -\frac{1}{Z} \end{pmatrix} \begin{pmatrix} p_{A,sin/cos}^{in} \\ x_{A,sin/cos}^{in} \end{pmatrix}. \tag{2.10}$$

The quadratures $x_{\pm,sin}$, $p_{\pm,sin}$ and $x_{\pm,cos}$, $p_{\pm,cos}$ refer to light modes with an exponentially rising/falling envelope function. They are defined according to Eq. (2.6) with $h(t) = \frac{\kappa\sqrt{2}}{ZN_{\pm}} e^{\pm\frac{\kappa^2 t}{2Z^2 T}}$. Due to the inherent backaction of the interaction, these input-output relations display an exponential scaling in the coupling strength, as opposed to Eq. (2.8). This is due to the fact that the light field is continuously mapped to both atomic quadratures x_A and p_A which in turn are mapped to the passing photonic field. This way, the light field passing the ensembles at time $t = t_1$ is subject to an interaction which involves the photonic contributions which have been mapped to the atomic state during the time $t < t_1$ and experiences therefore an effective backaction mediated by the atoms. An imbalanced quadratic interaction ($|\mu| \neq |\nu|$) allows for the realization of protocols which are not possible employing an interaction of QND-type, for instance the creation of entanglement by dissipation (see Sec. 3.1).

2.2 Ultracold atoms in optical lattices

Neutral atoms at nanokelvin temperatures which are trapped in optical lattices constitute are a very clean and controllable system [101]. As explained below, they can be designed such that atoms in different internal states experience different trapping potentials resulting in so-called spin dependent lattices [68, 69]. Optical lattices are also very versatile since they allow for the realization of different trapping geometries in one, two and three dimensions as well as superlattice structures [102–106]. Most importantly, many relevant parameters such as the interaction strength between the particles and the tunneling rate between lattice sites can be controlled with high precision and tuned over a wide range. Due to these features, ultracold atoms in optical lattices are an ideal testbed for simulating condensed matter systems and also a promising system for quantum information processing [19–21] (see App. A.3). The success story of ultracold atoms in optical lattices includes the realization of the Bose-Hubbard model, the observation of the quantum phase transition from a superfluid to a Mott insulator [23, 24] and the creation of highly entangled cluster states [68, 69]. Optical lattices are an interesting platform for the realization of the ideas presented in this Thesis, since atoms in a Mott insulating state are promising candidates for quantum registers[12] and provide an optically thick sample, which is very well suited for the implementation of light-matter interface schemes [22].
Ultracold atoms play a central role in Sec. 4.2 and Sec. 4.3. In the following, we focus on introducing the concepts and phyiscal mechanisms which are used in Sec. 4.3 for the realization of an entangling gate for photons[13]. To this end, we briefly review the physics of cold atoms in optical lattices (Sec. 2.2.1) and explain the two types of operations involved in the processing of atomic states in Sec. 4.3, i.e. state dependent transport (Sec. 2.2.2) and controlled collisions between neighboring atoms (Sec.2.2.3).

[12] Very recently, novel techniques have been developed which allow for the imaging and manipulation of single atoms at individual lattice sites [107–109]. This unpreceded level of control opens up many possibilities to be explored in future.

[13] This protocol is based on the transfer of the photonic input state to a sample of cold atoms in an optical lattice using a light-matter interface scheme. Subsequently, the resulting atomic quantum state is processed by means of the methods explained here and afterwards converted back to a photonic state.

2.2.1 Mott insulating states in optical lattices

An artificial one-dimensional atom lattice can be created by loading a cold gas of neutral atoms into the standing wave which is produced by interfering retro-reflected laser beams. By adding standing waves along other spatial directions, higher dimensional atom lattices can be obtained. The interaction of the atoms with the light field constituting the standing wave can be dissipative (arising due to the absorption of photons by the atoms and subsequent spontaneous emission), or conservative (produced by the interaction of the light field with the induced dipole moment of the atom). The dissipative part of the interaction can be used for cooling, while the conservative part can be employed for trapping. If the detuning of the lasers constituting the standing wave with respect to the relevant atomic transitions Δ is chosen large enough, the conservative interaction dominates and gives rise to an energy level shift of the atoms [19–21]. This Stark shift depends on the amplitude of the standing wave field at each point of space. The spatial dependency of the shift in the potential energy gives rise to a dipolar force, which leads to trapping of the atoms in the minima of the standing wave for positive detuning $\Delta > 0$ [110]. For negative detuning $\Delta < 0$, the interaction between the standing waves and the atoms leads to an optical potential, where the atoms tend to stay at the maxima of the light field. For a three-dimensional optical lattice created by laser fields with wave vector $k = 2\pi/\lambda$, this potential takes the form

$$V(x, y, z) = V_{0x} \sin^2(kx) + V_{0y} \sin^2(ky) + V_{0z} \sin^2(kz),$$

where V_0 is proportional to the dynamic polarizability of the trapped atoms and the intensity of the applied laser fields. For many experimental settings, atoms in optical lattices can be described by the standard Bose-Hubbard Hamiltonian [23, 24].

$$H_{\mathrm{BH}} = -J \sum_{\langle i,j \rangle} \left(b_i^\dagger b_j + b_i b_j^\dagger \right) + \frac{U}{2} \sum_i n_i \left(n_i - 1 \right),$$

where $\sum_{\langle i,j \rangle}$ is a sum over neighboring lattice sites i, j. $b_i^\dagger$ is the creation operator for a particle at site i (with $[b_i, b_i^\dagger] = i$) and $n_i = b_i^\dagger b_i$ is the number of particles at this site. J and U denote the tunneling matrix element and the on-site interaction energy respectively. More specifically, the second term of the Hamiltonian (which is proportional to U) describes the repulsion between two atoms occupying the same lattice site due to contact collisions, while the kinetic term (which is proportional to J) describes atoms moving from one lattice site to the next one by tunneling through the intermediate optical potential barrier. An important advantage of ultracold atoms in optical lattices lies in the fact that the parameters J and U can be externally manipulated. The ratio J/U can be increased by decreasing the lattice depth V_0. Similarly, the scattering length a_s characterizing collisions between two atoms can be increased using an external magnetic field which is tuned to a Feshbach resonance. Since $U \propto a_s$, the ratio J/U can be rendered arbitrarily small close to this resonance. An adiabatic transition between the regimes $J/U \gg 1$ and $J/U \ll 1$ gives rise to a quantum phase transition between a superfluid and a Mott insulating state. In the superfluid phase, atoms are delocalized over the whole lattice and strong long range correlations and large fluctuations in the

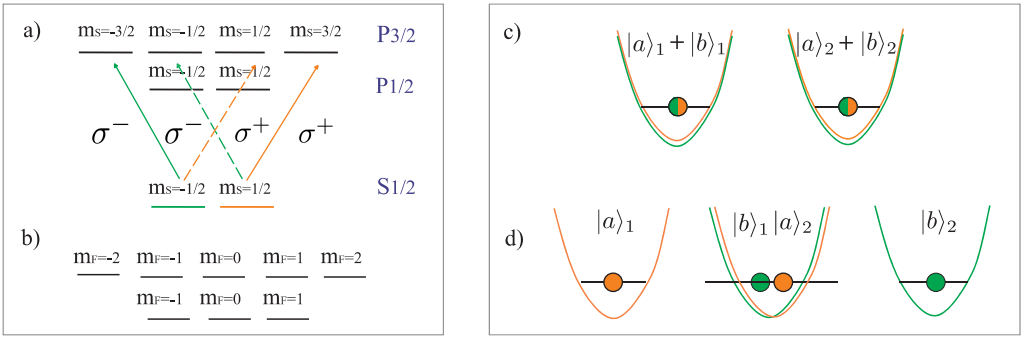

Figure 2.4: State dependent transport and controlled collisions in optical lattices. Panels a) and b) show the fine structure and hyperfine splitting of the $S_{1/2}$ ground state of the most commonly used alkali atoms ^{23}Na and ^{87}Rb (which have nuclear spin $I = 3/2$). $\sigma^{\pm}$-polarized light fields give rise to state dependent optical potentials as described in the text. Panels c) and d) illustrate how state dependent lattice shifts can be used to implement a controlled phase gate. Panel c) depicts the situation at times $t = \pm\tau$, while panel d) illustrates the situation at $-\tau < t < \tau$, corresponding to the explanation given in the text. Orange (green) lines represent σ^+ (σ^-) -polarized optical potentials affecting the atomic levels $|a\rangle$ ($|b\rangle$).

particle number can be observed. In the Mott insulating state, the atoms are strongly localized. For the realization of the quantum gate as described in Sec. 4.3, the atomic system is assumed to be prepared in the ground state of the Bose-Hubbard Hamiltonian in the Mott insulating regime. For lattices with filling factor one, this state can be written as $|\Psi_{\mathrm{MI}}\rangle \propto \prod_i b_i^\dagger |\mathrm{vac}\rangle$ [19]. In the following, it is explained how a Mott insulator with one atom per site can be used for quantum information processing by inducing collisions between atoms in a coherent and controlled way [68, 69].

2.2.2 State dependent transport

Controlled collisions in optical lattices rely on state dependent transport, which can be implemented using two counter-propagating linearly polarized laser beams, whose rotation axes are rotated by an angle 2θ with respect to each other. We assume here propagation in $\pm\hat{\mathbf{x}}$-direction. The resulting light field can be decomposed into two standing waves with positive and negative circular polarization, σ^+ and σ^-, with corresponding potentials $V_\pm \cos^2(kx \pm \theta)$. As mentioned above, the strength of the optical potential depends on the dynamic polarizability, which is proportional to the atomic dipole moment. Hence, selection rules for the optical transitions induced by $\sigma^{\pm}$-polarized standing waves can be used to create different trap potentials for different atomic levels. For example, for the most commonly used alkali atoms ^{23}Na and ^{87}Rb [19], the σ^+-polarized light field couples the $S_{1/2}$ ground state levels with $m_s = -1/2$ (where m_s is the magnetic quantum number associated with the spin) to two excited levels, $P_{1/2}$ and $P_{3/2}$, with $m_s = 1/2$, as shown in Fig. 2.4a). The detunings of the light field with respect to these two atomic transitions have opposite signs and the frequency is chosen such that their resulting contributions to

the Stark shift of ground state levels with $m_s = -1/2$ cancel. This way, ground state levels with $m_s = -1/2$ are not trapped by the σ^+-polarized light field and these levels are only affected by the optical potential in σ^--polarization, V_-. Analogously, $S_{1/2}$ ground state levels with $m_s = 1/2$ are only affected by V_+. By shifting the potentials $V_\pm$ with respect to each other (which can be done by changing their relative phase θ), atoms occupying different internal states corresponding to $m_s = -1/2$ and $m_s = 1/2$ can be displaced in the lattice in opposite directions.
For the alkali atoms ^{23}Na and ^{87}Rb considered here, the hyperfine structure of the $S_{1/2}$ ground state consists of two manifolds with total spin $F = 2$ and $F = 1$, respectively. Each of these manifolds consists of $2F + 1$ levels with magnetic quantum numbers $m_F = -F, \cdots, F$, as shown in Fig. 2.4b. A two-level system $|a\rangle$, $|b\rangle$ can be encoded, for instance, by identifying $|a\rangle = |F = 2, m_F = 2\rangle$ and $|b\rangle = |F = 1, m_F = -1\rangle$ [19]. By representing $|a\rangle$ and $|b\rangle$ as combinations of ground state fine levels with $m_s = -1/2$ and $m_s = 1/2$, their corresponding level shifts can be expressed in terms of $V^\pm$ as $V_a = V_+$, $V_b = V_+/4 + 3V_-/4$, where the factors $1/4$ and $3/4$ follow from the corresponding Clebsch-Gordan coefficients. Hence, the hyperfine levels $|a\rangle$ and $|b\rangle$ are affected differently by the optical potentials in σ^+ and $\sigma-$-polarization and can be displaced with respect to each other.

2.2.3 Collisional phases

In the following, we explain how state dependent transport can be used to induce controlled collisions and therefore entanglement between atoms in the lattice [68, 69]. We consider two adjacent atoms placed at positions $\mathbf{r}_1$, and $\mathbf{r}_2$. The atoms are assumed to be prepared in the states

$$\psi_j(\mathbf{r}_j, t) = \frac{1}{\sqrt{2}} \left(\psi_j^a(\mathbf{r}_j, t) + \psi_j^b(\mathbf{r}_j, t) \right)$$

at time $t = -\tau$. $\psi_j^\beta(\mathbf{r}_j, t)$ denotes the wave function of atom j in state $\beta = a, b$. After the preparation of the two atoms, a state dependent shift of the optical potentials is performed, as shown schematically in Fig. 2.4c and d. For illustration, we assume here that the potential V_b moves to the right while V_a moves to the left, such that the wave functions $|b\rangle_1$ and $|a\rangle_2$ start to overlap. The interatomic interaction is described by a contact potential $V^{ba}(\mathbf{r}_1 - \mathbf{r}_2) = (4\pi a_s^{ba}/m)\delta^3(\mathbf{r}_1 - \mathbf{r}_2)$, where m is the atomic mass and a_s^{ba} is the scattering length corresponding to the collision. Subsequently the lattices are shifted back such that the atoms reach their original positions at $t = \tau$. The phase accumulated in the time interval $[-\tau, \tau]$ is given by

$$\phi^{ba} = \int_{-\tau}^{\tau} dt \Delta E^{ba}(t),$$

where $\Delta E^{ba}(t)$ is the energy shift due to the collision, which can be calculated perturbatively. This energy is proportional to the scattering length a_s^{ba} and the overlap of the wave functions at each time [19]. In addition to the collisional phase, the lattice movement leading to a displacement of the atomic wave functions ψ_i^β during the time interval $[-\tau, \tau]$ gives rise to a kinetic phase ϕ^β. Within the adiabatic limit, in which both atoms

remain in the motional ground state during the shift, the kinetic phase can be expressed as

$$\phi^\beta = \frac{m}{2}\int_{-\tau}^{\tau} dt(\dot{\mathbf{r}}^\beta)^2,$$

where $\dot{\mathbf{r}}^\beta$ denotes the spatial trajectory followed by the wave function ψ^β of the atom. Adiabaticity requires the condition $|\ddot{\mathbf{r}}^\beta| \ll v_{\text{osc}}/\tau$, where v_{osc} is the mean velocity of atoms in the vibrational ground state. Considering both collisional and kinetic phases, the internal states of the atoms after the controlled interaction are given by

$$\begin{aligned}
|a\rangle_1|a\rangle_2 &\to e^{-2i\phi^a}|a\rangle_1|a\rangle_2,\\
|a\rangle_1|b\rangle_2 &\to e^{-i(\phi^a+\phi^b)}|a\rangle_1|b\rangle_2,\\
|b\rangle_1|a\rangle_2 &\to e^{-i(\phi^a+\phi^b+\phi^{ba})}|b\rangle_1|a\rangle_2,\\
|b\rangle_1|b\rangle_2 &\to e^{-2i\phi^b}|b\rangle_1|b\rangle_2.
\end{aligned}$$

In Sec. 4.3, this scheme is used to realize a fundamental two-qubit gate by choosing the interaction time τ such that $\phi_{\text{col}} = \phi^{ba} = \pi$.

2.3 High-finesse optical cavities

Cavities allow for the realization of strong light-matter couplings via the Purcell effect. We are particularly interested in the strong coupling regime, where the interaction between single atoms and photons can be studied at the quantum level [11, 111]. The realm of strong coupling has already been reached in several experiments [112–115] and cavities have been used for many proof of principle realizations, which include for example the observation of quantum jumps by quantum non-demolition measurements [116, 117], the realization of a non-classical light source [118], the implementation of a two-photon gateway [119] and the demonstration of electromagnetically induced transparency with a single atom [120].
The protocols put forward in Sec. 5.1 rely on the ability to use the internal state of a single atom in a high finesse optical cavity to apply a controlled phase to a light field [121]. In the following we will explain how this can be done. In Sec. 2.3.1, we briefly introduce the basics of cavity quantum electrodynamics. The quantum gate which allows for the control of phases is described in Sec. 2.3.2.

2.3.1 Basic properties of optical cavities and light-atom coupling in the strong coupling regime

In this subsection, we briefly introduce some basic properties of optical cavities and explain how light and matter interact in the strong coupling regime [122]. For simplicity, we consider here planar cavities, - the concepts reviewed here can easily be generalized to other types of cavities. The quality of a cavity can be characterized in terms of its finesse

$$\mathcal{F} = \frac{\pi\,(R_1R_2)^{1/4}}{1-\sqrt{R_1R_2}},$$

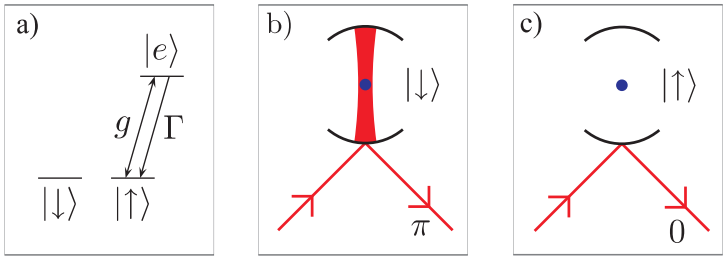

Figure 2.5: Realization of a controlled phase-flip gate between a single atom and light. An atom with a level structure as shown in a) is placed in a cavity in the strong coupling regime. The light field is on resonance with the cavity and couples the ground state $|\uparrow\rangle$ resonantly to the excited state $|e\rangle$. $|e\rangle$ decays to $|\uparrow\rangle$ through spontaneous emission at a rate Γ. b) If the atom is in state $|\downarrow\rangle$, the incident field is not affected by the presence of the atom, and for a sufficiently slowly varying input pulse, the interaction with the resonant cavity changes the phase of the light field by π. c) If the atom is initially in state $|\uparrow\rangle$, it couples to the cavity mode. Due to the resulting normal mode splitting, the incoming light field is detuned from the atom-cavity system and is reflected from the input mirror without acquiring a phase shift. This transformation is insensitive to the precise values of g, Γ, and the cavity decay rate as long as the system is in the strong coupling and weak driving regime.

where R_1 and R_2 are the reflectivities of the mirrors as indicated in Fig. 2.5a. A high finesse corresponds to very low cavity leakage, such that light travels back and forth many times between the mirrors, before it leaves the cavity. If there is no incident light field entering the cavity from outside, a fraction of $p_{\text{loss}} = 2\pi/\mathcal{F}$ of the power circulating inside is lost after one round trip. In the following, we will be interested in a related quantity, the photon decay rate κ. The photon decay rate is defined by $\kappa = 1/\tau_{\text{cav}}$, where τ_{cav} is the photon life time in the cavity. For cavities with highly reflecting mirrors, the decay rate can be shown to be inversely proportional to the finesse, $\kappa = \pi c/(\mathcal{F} L_{\text{cav}})$.
The finesse can also be directly related to the transmissivity $\mathcal{T}$. For a symmetric cavity($R_1 = R_2$) of length L_{cav}, the transmissivity for light with wavelength λ is given by

$$\mathcal{T} = \frac{1}{1 + (4\mathcal{F}^2/\pi^2)\sin^2(\phi(\lambda)/2)},$$

where $\phi(\lambda) = 4\pi L_{\text{cav}}/\lambda$ is the phase shift acquired in one round trip. If $\phi(\lambda) = 2\pi m$, where m is an integer, the light field and the cavity are on resonance. In this case, the light field travelling forth and back in the cavity is in phase after each reflection leading to constructive interference. For high values of $\mathcal{F}$, this resonance condition corresponds to sharp peaks in the transmissivity at $\phi(\lambda) = 2\pi m \pm \pi/\mathcal{F}$, which have a full width at half maximum (FWHM) $\Delta\Phi_{FWHM} = 2\pi/\mathcal{F}$. Accordingly, high finesse cavities have sharp resonant modes.
In the following we will model the cavity field by a single mode and consider its coupling to an atom. We consider here a two-level atom with ground state $|g\rangle$ and excited state $|e\rangle$ which interacts with the light field via the electric dipole interaction. The atom can decay from $|e\rangle$ to $|g\rangle$ through spontaneous emission at a rate Γ, as shown in Fig. 2.5a. The

cavity is assumed to be tuned to the atomic transition, such that the resonant exchange of excitations between the atom the cavity is possible. We consider here the strong coupling limit, $g \gg \kappa, \Gamma$, where g is the atom-photon coupling parameter, which characterizes the strength of the coherent light-matter interaction. In this regime, the unitary interaction between the atom and the light field is faster than the dissipative dynamics which leads to the loss of photons (which can either happen through cavity leakage at a rate κ, or through spontaneous emission at the non-resonant atomic rate Γ. The atom-photon coupling parameter is given by $g = \sqrt{\mu_{ge}^2 \omega / 2\epsilon_0 V_0}$, where μ_{ge} is the electric dipole matrix element of the transition, V_0 is the modal volume of the cavity and ϵ_0 is the vacuum permittivity. The resonant interaction between a two-level atom and a cavity mode in the strong coupling regime can be described by the Jaynes-Cummings model [123]. If the cavity mode and the two-level atom are not coupled, the composite system can be described by the (bare) states $|\phi_A, n\rangle$, where $n \in \mathbb{N}$ is the number of excitations in the system and ϕ_A refers to the internal state of the atom. Apart from the ground state, these states are doubly degenerate. The ground state $|g, 0\rangle$, where the atom is in state $|g\rangle$ and no photons are in the cavity, corresponds to the energy $E_0 = \omega/2$. The excited states $|e, n-1\rangle$ and $|g, n\rangle$ (for $n \geq 1$) correspond to the energy $E_n = (n + \frac{1}{2})\omega$. If the two systems are coupled, the degeneracy is lifted and the new eigenstates of the system in the presence of a strong light-matter interaction are given by the dressed states

$$|\Phi\rangle_n^{\pm} = \frac{1}{\sqrt{2}} \left(|g, n\rangle \pm |e, n-1\rangle \right).$$

The eigenstates of the coupled system form doublets with energies

$$E_n^{\pm} = \left(n + \frac{1}{2} \right) \omega \pm \sqrt{n} g.$$

The emergence of doublets with an energy difference of $\Delta E_n = 2\sqrt{n} g$ is referred to as normal mode splitting. This frequency shift between the eigenstates of the uncoupled systems (bare states) and the strongly coupled atom-cavity system (dressed states) lies at the heart of the controlled phase flip gate described in the next subsection.

2.3.2 Realization of a controlled phase-flip gate

In the following, we explain how a phase-flip can be applied to a light field depending on the internal state of a single atom in a high finesse optical cavity [121]. The phase flip gate used in Sec. 5.1 is illustrated in Fig. 2.6 and has many possible applications in quantum information science, including the preparation of superpositions of coherent states [124], continuous two-qubit parity measurements in a cavity quantum electrodynamics network [125], and low energy switches [126]. The basic mechanism can be understood by considering a light field, which is reflected from a cavity. In the completely off-resonant case, the light field acquires a phase shift π, when it is reflected from the cavity, while a resonant field is reflected without changing its phase. This effect is due to interference between the field which is reflected from the first mirror and the field which travels through the cavity and is reflected back by the second mirror. To show this, we

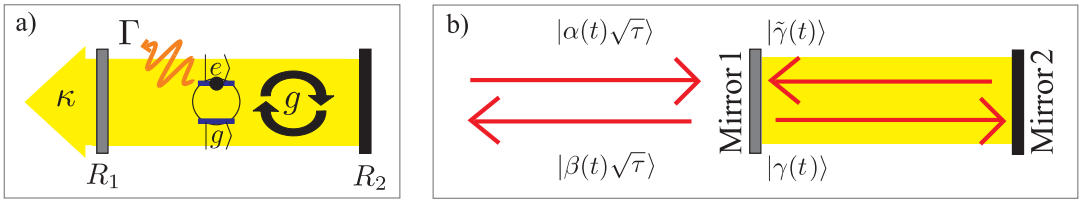

Figure 2.6: Illustration of a cavity consisting of two mirrors with reflectivities R_1 and R_2 (the depicted setting corresponds to the asymmetric case $R_1 < R_2 = 1$). a) Photon-atom coupling in a cavity. An atom with levels $|g\rangle$ and $|e\rangle$ interacts coherently with a single photon at a rate g. The photon can be lost through cavity leakage (with rate κ) or through spontaneous emission (at the non-resonant atomic decay rate Γ). b) Phase shift at a cavity. As explained in the text, an incoming coherent field is divided into infinitesimally short segments of length $c\tau$, where τ is the round trip time of the the light in the cavity. $|\alpha(t)\sqrt{\tau}\rangle$ denotes the state entering at time t, $|\tilde{\gamma}(t)\rangle$ and $|\gamma(t)\rangle$ refer to the field inside the cavity and $|\beta(t)\sqrt{\tau}\rangle$ denotes the state leaving it.

consider a coherent input state [127]. Since any quantum state can be expressed in terms of coherent states (which form an overcomplete basis), the result holds for arbitrary input states. The incoming light pulse is divided into infinitesimally small segments of length $c\tau$, where $\tau = 2L_{\rm cav}/c$ is the round trip time of the light in the cavity. We assume that the length of the incoming light pulse $L_{\rm in}$ is large compared to the cavity length $L_{\rm in} \gg L_{\rm cavity}$ and that the round trip time is short on the time scale set by the cavity decay, $\tau \ll 1/\kappa$. The considered setting is illustrated in Fig. 2.5b. Mirror 2 is assumed to be perfectly reflecting while mirror 1 is modelled as a beamsplitter with transmissivity $t_{\rm BS} = \sqrt{\kappa\tau}$ and reflectivity $r_{\rm BS} = \sqrt{1 - t_{\rm BS}^2} = 1 - \frac{1}{2}\kappa\tau + \mathcal{O}(\tau^2)$. We denote the state corresponding to the input light segment at time t by $|\alpha(t)\sqrt{\tau}\rangle$ (note that the expectation value of the number of photons in this segment, $n_\alpha = |\alpha^2|\tau$, is proportional to τ). This input field can either be reflected at mirror 1 and contribute to the field leaving the cavity or be transmitted and add to the field inside the cavity. Analogously, the field inside the cavity can either be reflected from this mirror or be transmitted and leave the cavity such that[14]

$$\begin{aligned} \beta(t)\sqrt{\tau} &= -\sqrt{\kappa\tau}\tilde{\gamma}(t) + \left(1 - \frac{1}{2}\kappa\tau + \mathcal{O}(\tau^2)\right)\alpha(t)\sqrt{\tau} \\ &= -\tilde{\gamma}(t)\sqrt{\kappa\tau} + \alpha(t)\sqrt{\tau} + \mathcal{O}(\tau^{\frac{3}{2}}), \qquad (2.11) \\ \gamma(t) &= \alpha(t)\sqrt{\kappa}\,\tau + \left(1 - \frac{1}{2}\kappa\tau + \mathcal{O}(\tau^2)\right)\tilde{\gamma}(t) \\ &= \alpha(t)\sqrt{\kappa}\,\tau + \tilde{\gamma}(t) - \frac{\kappa}{2}\tilde{\gamma}(t)\tau + O(\tau^2). \qquad (2.12) \end{aligned}$$

We consider only terms up to first order in τ. If the wavelength of the incoming light field $\lambda_{\rm in}$ is resonant with the cavity, i.e. $\lambda_{\rm in} = 2L_{\rm cav}/m$, where m is an integer, an overall

[14] We use the beamsplitter transformation $b_1 = -ta_1 + ra_2$ and $b_2 = ta_2 + ra_1$ (with input modes a_1, a_2 and output modes b_1, b_2). The input fields $|\tilde{\gamma}(t)\rangle$ and $|\alpha(t)\rangle$, transform here into the output fields $|\beta(t)\rangle$ and $|\gamma(t)\rangle$.

phase of $m2\pi$ is acquired during one round trip. In this case, $\tilde{\gamma}(t) = \gamma(t-\tau)$. This leads to the differential equation

$$\frac{d\gamma(t)}{dt} = -\frac{\kappa}{2}\gamma(t) + \alpha\sqrt{\kappa}$$

and to the steady state (ss) solution, $\gamma_{\mathrm{ss}} = \frac{\alpha_{\mathrm{ss}}}{\sqrt{\kappa}}$. By inserting this result in Eq. (2.11), $\beta_{\mathrm{ss}} = -\alpha_{\mathrm{ss}}$ is obtained. This sign change of the coherent state amplitude corresponds to a phase shift of π per photon. If the cavity field is off-resonant and an overall phase shift of $(2m+1)\pi$ is acquired, $\tilde{\gamma}(t) = -\gamma(t-\tau)$. The off-resonant case results therefore for in $\beta_{\mathrm{ss}} = \alpha_{\mathrm{ss}}$.
If an atom with an internal level structure as shown in in Fig. 2.6a is placed in the cavity, the internal state of the atom determines whether the incoming light field is resonant or off-resonant. We assume here that the incoming light field is resonant with the bare cavity mode. If the atom is in state $|\downarrow\rangle$, it does not influence the reflection of the light field from the cavity and a phase π is acquired (see Fig. 2.6b). However, if the atom is in state $|\uparrow\rangle$, it can interact resonantly with the light field in the cavity. Due to the resulting normal mode splitting, the incoming light field is detuned from the dressed cavity mode. In contrast to the resonant case, no light field is built up in the cavity. The cavity acts here like a normal mirror and the incoming light field is reflected without a phase change. The basic ingredients of the scheme such as the trapping of a single atom in a strongly coupled cavity and the preparation of the initial atomic state have been demonstrated experimentally in [128], where the decrease in the cavity field intensity for an atom in state $|\uparrow\rangle$ compared to the case of an atom in state $|\downarrow\rangle$ is used to measure the state of the atom. State preparation and readout for a single atom in a cavity have also been demonstrated in [129]. Apart from these systems, circuit quantum electrodynamics provides another promising platform for an experimental realization (see, for instance, [130] for a review).

2.4 Bose-Einstein condensates

A dilute gas of weakly interacting bosons trapped in an external potential can form a Bose-Einstein condensate (BEC) when cooled to nanokelvin temperatures. In this peculiar state of matter, a large number of bosons occupy a single quantum state and quantum effects appear on a macroscopic scale. Since the development of the Bose-Einstein statistics of noninteracting particles [131, 132] in 1924 and 1925 and the first realization of Bose-Einstein condensation in 1995 [133–135], BECs have become a very interesting and well-developed platform for implementations in quantum information science. Due to their high optical density and unique coherence properties, BECs are attractive candidates for the study and applications of quantum effects in light-matter interactions.
We consider this system in Sec. 5.2, where we study the creation of entanglement in superradiant Raman scattering from an elongated BEC. Due to strong collective effects of coherently decaying atoms, the scattering of laser light from a BEC can be enhanced and highly directional. Superradiance has been first proposed by Dicke in 1954 [136, 137] and been studied in many different systems. BEC superradiance has been observed for Rayleigh scattering involving two atomic levels [138–140] as well as for Raman scattering

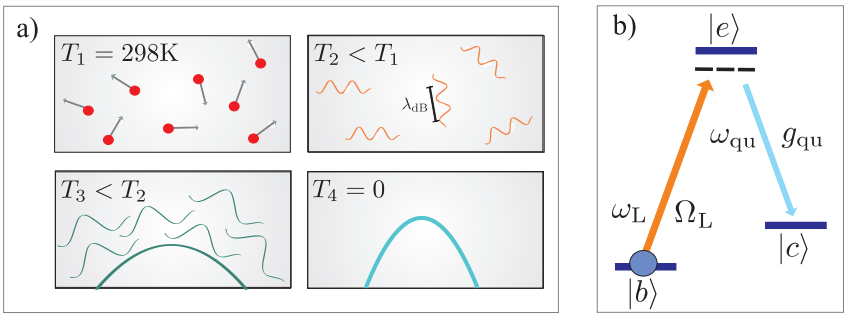

Figure 2.7: Atoms at low temperatures. a) Dilute gas of noninteracting bosons at different temperatures $298\mathrm{K} = T_1 > T_2 > T_3 > T_4 = 0$. At temperatures close to the absolute zero point, a macroscopic fraction of the sample occupies the ground state of the external potential if the phase space density is larger than unity, i.e. if the interatomic distance is comparable to the de Broglie wavelength λ_{dB} of the atoms. b) Raman scattering in a Λ configuration. The atoms are assumed to possess two long-lived ground states $|b\rangle$ and $|c\rangle$ an an excited state $|e\rangle$. A strong classical driving field with frequency ω_L (and Rabi frequency Ω_L) couples the levels $|b\rangle$ and $|e\rangle$. The levels $|e\rangle$ and $|c\rangle$ are coupled via a quantized radiation field with frequency ω_{qu} with coupling strength g_{qu}.

processes [141,142], which involve an atomic level structure of the type shown in Fig. 2.7. Below, we briefly introduce the basic properties of Bose-Einstein condensates (Sec. 2.4.1) and explain how collective Raman scattering from BECs leads to entanglement between atoms and light (Sec. 2.4.2).

2.4.1 Basic properties of Bose-Einstein condensates

We consider a gas of N non-interacting identical bosonic particles with mass m at temperature T [143]. The atomic sample is assumed to be trapped in a harmonic external potential

$$U(x,y,z) = \frac{m}{2}\left(\omega_x^2 x^2 + \omega_y^2 y^2 + \omega_z^2 z^2\right). \tag{2.13}$$

The Bose-Einstein distribution function, which determines the number of bosons which occupy a quantum level with energy E is given by

$$f(E) = \frac{1}{e^{\frac{E-\mu}{k_{\mathrm{B}}T}} - 1}, \tag{2.14}$$

where k_{B} is the Boltzmann constant. The energy scale is here defined such that $E_0 = 0$. The chemical potential μ is defined by the condition that the total number of particles equals the total occupancy of all single particle energy levels. It is bounded from above by the energy of the lowest lying energy eigenstate of the external potential $\mu \leq E_0 = 0$. The number of particles in the system $N = N_0 + N_e$, can be expressed as a sum of particles occupying the ground state N_0 and the number of particles in excited states N_e. The

latter can be calculated by means of the Bose-Einstein distribution function $f(E)$ and the density of states $g(E)$. For the harmonic potential defined by Eq. (2.13), $g(E)$ is given by $g(E) = E^2/(2\omega_x\omega_y\omega_z)$ and accordingly

$$N = N_0 + \int_0^\infty dE f(E)g(E) = N_0 + \frac{1}{2\omega_x\omega_y\omega_z}\int_0^\infty dE \frac{E^2}{e^{\frac{E-\mu}{k_BT}} - 1}. \quad (2.15)$$

Using this expression, we consider now the dependence of the chemical potential μ at constant particle number density for decreasing temperature T. For high temperatures, the chemical potential takes large negative values. If the gas is cooled to lower temperatures, while keeping N constant, μ increases. At a critical temperature $T = T_c$, a quantum phase transition occurs. The chemical potential approaches the energy of the lowest lying energy eigenstate $\mu = E_0$, such that the energy required to add a particle (at constant entropy) is given by the ground state energy $E_0 = 0$. At this point, a macroscopic fraction of the sample occupies the lowest energy state, i.e. the state with zero velocity[15]. In the thermodynamic limit, the condensate fraction is given by

$$\frac{N_0}{N} = 1 - \left(\frac{T}{T_c}\right)^3$$

With decreasing temperature, an increasing percentage of particles occupies the ground state. The rest of the particles occupies the states with $E > 0$ according to a thermal distribution. In the ideal case, the fraction of atoms in the ground state with zero velocity approaches unity as $T \to 0$.

2.4.2 Superradiance in Bose-Einstein condenstaes

In this subsection, we consider superradiant Raman scattering of laser light from a BEC. We derive the Hamiltonian used in Sec. 5.2 and show how entanglement between atoms and light is generated by means of this interaction. This short overview follows the discussion of collective atomic recoil lasing from a three-level atomic BEC in [144].

Superradiant scattering of light from a BEC involves the highly directional emission of photons. The selection of particular superradiant modes can be due to several factors [145]. If an elongated (cigar-shaped) BEC is used, geometrical effects favor certain directions. Alternatively, this can be achieved by placing the BEC in a low finesse ring cavity or by creating a seed matter wave using a Bragg pulse [146, 147]. If a cigar shaped BEC with length L and diameter D is used, the number of modes in the axial direction is approximately given by the Fresnel number $F = D^2/(L\lambda)$, where λ is the wavelength of the superradiant transition. In typical experiments, this number is equal or larger than one, such that the so-called endfire modes along the main axis of the condensate can successfully compete with all other modes [148]. This is due

[15] T_c is defined as the temperature at which a significant fraction of particles contributes to N_0. At the transition point, $N = N_e(T_c, \mu = 0)$. Using Eq. (2.15), $N = T_c^3\zeta(3)/(\omega_x\omega_y\omega_z)$ is obtained, where $\zeta(x)$ is the Riemann zeta function ($\zeta(3) \approx 1.2$). The transition temperature is accordingly given by $T_c \approx 0.94(N\omega_x\omega_y\omega_z)^{\frac{1}{3}}/k_B$.

to the fact that collective effects along the main axis of the condensate correspond to processes which profit from the high optical depth of the sample in this direction, while coherent processes in the other directions are weak. If the Fresnel number of the sample equals approximately one, the dynamics of the system can be well described by a one dimensional theory. We consider here a Bose-Einstein condensate at zero temperature, which is assumed to be very dilute, such that atom-atom interactions can be neglected. The atoms are assumed to possess two ground states, $|b\rangle$ and $|c\rangle$, and an excited level $|e\rangle$ with energies ω_a, ω_b and ω_e in a Λ-configuration, as shown in Fig. 2.7b. The two ground states are assumed to be long-lived and can for example correspond to hyperfine levels. Atoms in state $|\alpha\rangle$ at position $\mathbf{x}$ are described by bosonic annihilation and creation operators in the interaction picture with respect to the internal atomic energies $a_{A,\alpha}(\mathbf{x},t)$, $a^\dagger_{A,\alpha}(\mathbf{x},t)$ with $[a_{A,\alpha}(\mathbf{x},t), a^\dagger_{A,\alpha'}(\mathbf{x}',t)] = \delta_{\alpha,\alpha'}\delta(\mathbf{x}-\mathbf{x}')$ and $[a_{A,\alpha}(\mathbf{x},t), a_{A,\alpha'}(\mathbf{x}',t)] = [a^\dagger_{A,\alpha}(\mathbf{x},t), a^\dagger_{A,\alpha'}(\mathbf{x}',t)] = 0$. The free Hamiltonian of the atomic system is given by

$$H_{\rm A} = -\frac{1}{2m}\sum_{\alpha=a,b,e}\int d^3x\; a^\dagger_{A,\alpha}(\mathbf{x},t)\nabla^2 a_{A,\alpha}(\mathbf{x},t),$$

where m is the atomic mass. The atomic sample is irradiated by a strong narrow-band laser field with central frequency ω_L, which induces transitions between the atomic ground state $|b\rangle$ and the excited state $|e\rangle$. As shown in Fig. 2.7, atoms in state $|e\rangle$ can decay to state $|b\rangle$ by emitting a photon at frequency $\omega_{\rm qu}$. This quantized radiation field is described by the annihilation and creation operators $a_{\rm qu}$ and $a^\dagger_{\rm qu}$ (with $[a^\dagger_{\rm qu}, a_{\rm qu}] = 1$), while the strong coherent driving field is treated classically. For simplicity, we consider here a one-dimensional single-mode model. This description corresponds to a setting, where the BEC is placed in a cavity which selects the mode with annihilation operator $a_{\rm qu}$. The light-matter interaction is assumed to be far off-resonant and is governed by the Hamiltonian

$$\begin{aligned} H_{\rm int} &= -\frac{\Omega_L}{2}\int d^3x\; a^\dagger_{A,b}(\mathbf{x},t)a_{A,e}(\mathbf{x},t)e^{-i(\mathbf{k}_L\mathbf{x}-\Delta_L t)} + H.C. \\ &+ g_{\rm qu}\int d^3x\; a_{A,e}(\mathbf{x},t)a^\dagger_{A,c}(\mathbf{x},t)a^\dagger_{qu}(t)e^{-i(\mathbf{k}_{\rm qu}\mathbf{x}-\Delta_{qu}t)} + H.C.\,, \end{aligned}$$

where the dipole approximation has been made. $\mathbf{k}_L$ and $\mathbf{k}_{\rm qu}$ denote the wave vectors of the classical and the quantum field. The detunings Δ_L and $\Delta_{\rm qu}$ are given by $\Delta_L = \omega_L - \omega_e + \omega_b$ and $\Delta_{\rm qu} = \omega_{\rm qu} - \omega_e + \omega_c$. $\Omega_L = \mu_{be}E_L$, where $\mu_{\alpha\alpha'}$ is the dipole matrix element of the transition $|\alpha\rangle \to |\alpha'\rangle$ and E_L is the electric field amplitude of the driving beam. The coupling strength $g_{\rm qu}$ is given by $g_{\rm qu} = \mu_{ce}\sqrt{\omega_{\rm qu}/2\epsilon_0 V}$, where ϵ_0 is the vacuum permittivity and V the modal volume. The excited level $|e\rangle$ can be adiabatically eliminated if the detuning Δ_L is much larger than the natural linewidth $\gamma_{\rm LW,ec}$ corresponding to the transition $|e\rangle \to |c\rangle$. This way, an effective Hamiltonian involving only atomic ground state levels is obtained[16]

$$H_{\rm eff} = -\frac{1}{2m}\sum_{\alpha=a,b}\int d^3x\, a^\dagger_{A,\alpha}(\mathbf{x},t)\nabla^2 a_{A,\alpha}(\mathbf{x},t) - \delta\tilde{a}^\dagger_{\rm qu}\tilde{a}_{\rm qu}$$

[16] Stark-shifts due to Rayleigh scattering are absorbed into the level energies. Dipole forces due to inhomogeneous mode profiles are neglected in this one-dimensional treatment.

$$+ \quad i\, g_{\text{eff}} \int d^3x \left(\tilde{a}^\dagger_{\text{qu}} a^\dagger_{A,c}(\mathbf{x},t) a_{A,b}(\mathbf{x},t) e^{i\Delta\mathbf{k}\mathbf{x}} - H.C. \right),$$

where $g_{\text{eff}} = \frac{g_{\text{qu}}\Omega_L}{2\Delta_L}$ is the effective coupling strength. $\delta = \omega_L - \omega_{\text{qu}} - \Delta_{cb}$, where $\Delta_{cb} = \omega_c - \omega_b$, is the detuning of the Raman transition from two-photon resonance, $\tilde{a}_{\text{qu}} = i a_{\text{qu}} e^{i\delta t}$ and $\Delta\mathbf{k} = \mathbf{k}_L - \mathbf{k}_{\text{qu}}$ is the momentum difference transferred to an atom if a photon is scattered. As next step, the Hamiltonian is expressed in terms of momentum eigenstates using the transformation

$$a_{A,b}(\mathbf{x}) \propto \sum_{-\infty}^{\infty} b_n e^{in\Delta\mathbf{k}\mathbf{x}}, \qquad a_{A,c}(\mathbf{x}) \propto \sum_{-\infty}^{\infty} c_n e^{in\Delta\mathbf{k}\mathbf{x}},$$

where we omitted the explicit time dependence in the notation. The creation and annihilation operators b_n, $b_n^\dagger$ (c_n, $c_n^\dagger$) refer to modes corresponding to an atom in state $|b\rangle$ ($|c\rangle$) with momentum $\mathbf{p} = n\Delta\mathbf{k}$, $|b,n\rangle$ ($|c,n\rangle$). These operators fulfill the commutation relations $[b_n, b_m^\dagger] = \delta_{n,m}$, $[c_n, c_m^\dagger] = \delta_{n,m}$ and $[b_n, c_m] = [b_n, c_m^\dagger] = 0$. Using these modes, the effective Hamiltonian can be reexpressed in the form[17]

$$H_{\text{eff}} \quad = \quad \omega_r \sum_{-\infty}^{\infty} n^2 \left(b_n^\dagger b_n + c_n^\dagger c_n \right) - \delta \tilde{a}^\dagger_{\text{qu}} \tilde{a}_{\text{qu}} + i g_{\text{eff}} \sum_{-\infty}^{\infty} \left(\tilde{a}^\dagger_{\text{qu}} b_n^\dagger c_{n-1} - H.C. \right),$$

where the recoil frequency ω_r is given by $\omega_r = \Delta k^2/2m$. This Hamiltonian describes a two-photon Raman process, where atoms in state $|b,n\rangle$ are transferred to the state $|c,n+1\rangle$ by scattering a pump photon into the quantized radiation field. In the following, we assume that the atoms are initially prepared in the state $|b,0\rangle$. In the linear regime, where the number of atoms in the recoiling state is small compared to the number of atoms in the initial state, N_0 (such that there is no depletion of atoms in the resting condensate), the Holstein-Primakoff approximation can be made (see Sec. 2.1.1). In this case, it can be assumed that $b_0 \approx \sqrt{N_0}$, such that

$$H_{\text{eff}} \quad = \quad \omega_1 c_1^\dagger c_1 - \delta \tilde{a}^\dagger_{\text{qu}} \tilde{a}_{\text{qu}} + i g_{\text{eff}} \sqrt{N_0} \left(\tilde{a}^\dagger_{\text{qu}} c_1^\dagger - H.C. \right).$$

The interaction part of this Hamiltonian is of the active (two-mode squeezing) type discussed in Sec. 2.1.2 (compare Eq. 2.3). It leads to the creation of correlated atom-photon pairs and represents the inter-species analogue of an optical parametric amplifier, which produces entangled photon pairs and is a key element in many applications in quantum information science. The resulting two-mode squeezed state (TMSS) is of the form

$$|TMSS\rangle = \left(1 - \lambda^2\right) \sum_{n=0}^{\infty} \lambda^n |n,n\rangle,$$

with $\lambda = \tanh(r)$, where $r \in \mathbb{C}$ is the so-called squeezing parameter. This state is expressed in the Fock basis. The ket $|n,n\rangle$ on the right side refers to a state with n scattered photons in the quantized radiation field and n atoms, which have been coherently transferred from level $|b\rangle$ to level $|c\rangle$.

[17] Finite size effects of the condensate are neglected.

Chapter 3

Engineered Dissipation

Any quantum technology is challenged by dissipation. The interaction of the system with its environment is typically regarded to be a major obstacle, and in particular the degradation of entangled states due to dissipation is traditionally considered to be a key problem. Contrary to this belief, new approaches aim at utilizing dissipation for quantum information processes [31, 33, 50, 58, 149–151], including quantum state engineering [25, 40, 42], quantum computing [42], quantum simulations [49, 59], quantum memories [152] and error correction [153, 154]. In this chapter, new ideas and tools harnessing dissipation for generating robust entangled states are put forward. More specifically, in Sec. 3.1, a method for the creation of steady state entanglement is described, which allows for the continuous production of event-ready entanglement which can in principle be maintained for arbitrary long times. This section is complemented by App. B. Sec. 3.2 (which is supplemented by App. C) is concerned with the dissipative distillation of steady state entanglement and its distribution over large distances by means of a continuous quantum repeater scheme. The results presented in Sec. 3.1 and Sec. 3.2 have been published in [IX, IV, III, XI][1] and [II] respectively.

3.1 Entanglement generated by dissipation

In this section, a robust method for generating steady state entanglement between two distant atomic ensembles is presented. The proposed scheme relies on the interaction of the two atomic systems with the common vacuum modes of the electromagnetic field which act as an engineered environment. In the following, the theoretical framework for two-level systems including dipole-dipole interactions is described in detail and complemented by a general discussion of the implementation in multi-level ground states. Based on these results, the first realization of purely dissipative entanglement generation has been demonstrated experimentally in [III], as described below.
This section is organized as follows. In Sec. 3.1.1, the proposed scheme is introduced and the current status of related work is briefly reviewed. The main idea of the proposal is explained in Sec. 3.1.2, which also contains a summary of the central results. In Sec. 3.1.3 the full master equation is derived for two-level atoms and the evolution of the amount of

[1] Related results have been published in [VII].

entanglement which is created in the atomic system is calculated. In Sec. 3.1.4, the generation of steady state entanglement in multi-level systems is discussed and in Sec. 3.1.5 the experimental realization of the scheme is described. Sec. 3.1.6 summarizes and concludes this section.

3.1.1 State of the art and related work

The pursuit of the generation of persistent entanglement is not only of fundamental interest in view of the investigation of entangled quantum states at long time scales but also vital for many applications, such as quantum repeaters [12,66,67,155–162]. On account of this problem, quantum systems are usually strictly isolated in the endeavor to avoid their interaction with the environment. In contrast, an ostensibly counter-intuitive approach using dissipation [25–49, 49–59] is adopted in the following. Here, the interaction of the system with the environment is employed such that dissipation drives the system into the desired state. More specifically, a scheme for the generation of long-lived entanglement between two distant, mesoscopic ensembles is proposed and analyzed (see also [163]). Both atomic samples are placed in magnetic fields and interact with an environment consisting of the vacuum modes of the electromagnetic field. A laser field mediates the coupling of the atomic system to the environment. The interaction of the system and the bath can be controlled via laser- and magnetic fields, which allow one to engineer the coupling in such a way that the unique steady state of the dissipative evolution is an entangled state. This dissipative approach has several remarkable advantages. For example, the scheme performs well starting from an arbitrary initial state. This feature renders the initialization of the system in a pure state unnecessary. Most importantly, the evolution is robust against moderate external noise. Entanglement is obtained in a steady state. This auspicious property is very promising in view of the quest for viable, extremely long-lived entanglement. Protocols, where entanglement is needed at instants of time which are not specified in advance (e.g. protocols including probabilistic subroutines) benefit from this type of entanglement[2]. Moreover, the production of endurable entanglement is crucial in applications which require the continuous presence of entanglement, as for example dissipative quantum repeater schemes [II], which provide a novel way of overcoming typical T_2 times in the creation of long-distance entanglement (see Sec. 3.2).
Below, it is shown for two-level systems that steady state entanglement can be generated even in the presence of undesired transitions and fluctuating magnetic fields. Moreover, external pump fields are included and it is demonstrated that, surprisingly, incoherent pumping can be beneficial in a certain parameter range. In atoms with multi-level ground states, additional dynamics leads to particle losses, which result in the production of a quasi-steady state. Remarkably, incoherent pumping can enable the creation of entanglement in a true steady state. Finally, the first demonstration of purely dissipative entanglement generation [III] is reported on. This experiment includes also the creation of atomic steady state entanglement by combining the dissipative mechanism outlined above with continuous measurements. This hybrid method allowed for the observation of

[2] If dissipatively generated entanglement is used in standard schemes, the driving fields which stabilize the state are switched off and the entangled atomic state can either be used directly (for example for teleportation) or can be read out on demand [98].

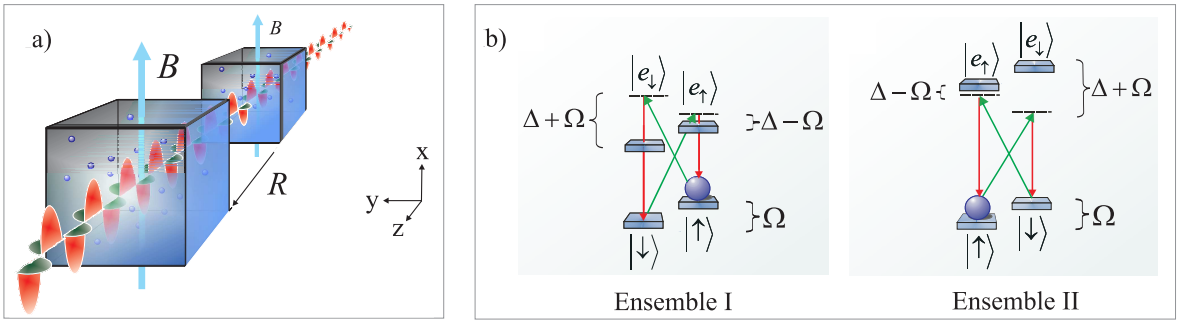

Figure 3.1: Setup for creating steady state entanglement between two atomic ensembles. a) The ensembles are separated by a distance R and placed in magnetic fields $\mathbf{B}$, which are oriented along $\hat{\mathbf{x}}$ (see Sec. 2.1). A strong $\hat{\mathbf{y}}$-polarized laser beam (shown in green) couples the atomic system to the environment which consists of the vacuum modes of the copropagating electromagnetic field in $\hat{\mathbf{x}}$ polarization (depicted in red). Panels b) and c) show the atomic level schemes. The magnetic field causes a Zeeman splitting Ω of the atomic ground-states levels $|\uparrow\rangle$ and $|\downarrow\rangle$ and defines the quantization axis. Atoms and light interact as explained in Sec. 2.1. A static electric field is applied to the second ensemble, such that the energy difference between ground and excited states is enhanced by 2Δ.

continuously produced event-ready entanglement for up to an hour.

3.1.2 Main idea and central results

In the following, the basic idea for generating purely dissipatively driven entanglement in atomic ensembles is explained and a realistic description including noise effects is introduced. First, the underlying concept is explained for two bosonic modes with annihilation operators a and b. The entangled target state under consideration is a two mode squeezed (TMS) state $|\Psi_{\mathrm{TMS}}\rangle$, which is characterized in terms of

$$\tilde{A}|\Psi_{\mathrm{TMS}}\rangle = \tilde{B}|\Psi_{\mathrm{TMS}}\rangle = 0,$$

where the nonlocal annihilation operators $\tilde{A}$ and $\tilde{B}$ are given by[3]

$$\tilde{A} = \mu\, a + \nu\, b^\dagger, \quad \tilde{B} = \mu\, b + \nu\, a^\dagger. \tag{3.1}$$

These equations uniquely characterize the pure squeezed state with squeezing parameter r where $\mu = \cosh(r)$ and $\nu = \sinh(r)$. This state can be prepared by means of a dissipative evolution governed by the master equation

$$\begin{aligned} d_t\rho(t) &= \kappa_{\tilde{A}}\left(\tilde{A}\rho(t)\tilde{A}^\dagger - \tilde{A}^\dagger\tilde{A}\rho(t)/2 - \rho(t)\tilde{A}^\dagger\tilde{A}/2\right) \\ &+ \kappa_{\tilde{B}}\left(\tilde{B}\rho(t)\tilde{B}^\dagger - \tilde{B}^\dagger\tilde{B}\rho(t)/2 - \rho(t)\tilde{B}^\dagger\tilde{B}/2\right), \end{aligned} \tag{3.2}$$

[3] Here, the operators $\tilde{A}$, $\tilde{B}$ (labelled with a tilde) refer to bosonic modes. Later in the text, operators A, B (without a tilde) are used to denote linear combinations of spins.

where the coefficients $\kappa_{\tilde{A}}$ and $\kappa_{\tilde{B}}$ are positive. This time evolution drives the system into the unique steady state $\rho_\infty = |\Psi_{\mathrm{TMS}}\rangle\langle\Psi_{\mathrm{TMS}}|$, for $t \to \infty$ (see App. B.2). Starting from this result, it is now explained how this concept can be applied for creating entanglement between two macroscopic atomic ensembles and how a dissipative evolution of type (3.2) can be realized. More specifically, two ensembles which are placed in magnetic fields as shown in Fig. 3.1a are considered. Atoms are assumed to possess a two-level ground state with internal states $|\uparrow\rangle$ and $|\downarrow\rangle$ (see Fig. 3.1b). The target state is an entangled state where the collective spins of the two samples are correlated in $\hat{\mathbf{y}}$ and in $\hat{\mathbf{z}}$ direction. The amount of entanglement generated can be measured by the quantity [16, 164]

$$\xi = \frac{\mathrm{var}(\mathrm{J_{y,I}} + \mathrm{J_{y,II}}) + \mathrm{var}(\mathrm{J_{z,I}} - \mathrm{J_{z,II}})}{|\langle J_{x,I}\rangle| + |\langle J_{x,II}\rangle|}. \tag{3.3}$$

For separable states $\xi \geq 1$. $J_{x,I} = \sum_{i=1}^{N_I} j_{x,I}^i$ is the collective spin in $\hat{\mathbf{x}}$ direction in the first ensemble, where N_I is the number of atoms and $j_{x,I}^i$ is the $\hat{\mathbf{x}}$-spin component of the ith atom[4]. Analogous definitions hold for for spins in $\hat{\mathbf{y}}$ and $\hat{\mathbf{z}}$ direction and for the collective spin of the second ensemble. In order to prepare this target state, a dissipative evolution governed by a master equation of type (3.2) is used, where the nonlocal operators $\tilde{A}$ and $\tilde{B}$ are replaced by

$$A = \frac{1}{\sqrt{N}}\left(\mu J_I^- + \nu J_{II}^+\right), \quad B = \frac{1}{\sqrt{N}}\left(\mu J_{II}^- + \nu J_I^+\right). \tag{3.4}$$

$\mu, \nu \in \mathbb{R}$ with $\mu^2 - \nu^2 = 1$ and $J_{\mathrm{I/II}}^{\pm}$ are collective spin operators[5], with $J^- = \sum_{i=1}^N |\uparrow\rangle_i\langle\downarrow|$ and $J^+ = \sum_{i=1}^N |\downarrow\rangle_i\langle\uparrow|$ such that $J_y = \frac{1}{2}(J^+ + J^-)$ and $J_z = \frac{i}{2}(J^+ - J^-)$. The light-matter interaction shown in Fig. 3.1b gives rise to the desired master equation. More specifically, after adiabatic elimination of excited states, the effective ground state Hamiltonian is of the form $H \propto \int_{\Delta\omega_{ls}} d\mathbf{k}\left(Aa_{\mathbf{k}}^\dagger + A^\dagger a_{\mathbf{k}}\right) + \int_{\Delta\omega_{us}} d\mathbf{k}\left(Ba_{\mathbf{k}}^\dagger + B^\dagger a_{\mathbf{k}}\right)$, where $a_{\mathbf{k}}^\dagger$ is the creation operator for a photon with wave vector $\mathbf{k}$. The first and second integral cover narrow bandwiths $\Delta\omega_{ls}$ and $\Delta\omega_{us}$ centered around the lower and upper sideband respectively (see Sec. 3.1.3). The modes of the light field are treated as bath and are therefore traced out. Using the Born-Markov approximation, one obtains a master equation of standard Lindblad form (compare Eq. (3.2)). Collective Lamb shifts can be shown to be negligible in the setting considered here (see App. B.3.2). In the limit $t \to \infty$, this evolution drives the system into an entangled steady state. In the absence of noise and for $N \gg 1$,

$$\xi_\infty^{\mathrm{ideal}} = \left(|\mu| - |\nu|\right)^2.$$

Next, additional processes such as thermal motion, undesired atomic transitions and fluctuating magnetic fields as well as resonant pump fields are included. Details can be found

[4] The quantization axis is defined by the direction of the magnetic field, which is oriented along $\hat{\mathbf{x}}$, hence $j_x = \frac{1}{2}\left(|\uparrow\rangle\langle\uparrow| - |\downarrow\rangle\langle\downarrow|\right)$.

[5] For large, strongly polarized atomic ensembles, collective spins can be described by bosonic modes $J_I^- \propto a$, $J_{II}^- \propto b$ using the Holstein-Primakoff approximation. The results derived here are based on related approximations and are valid for $N \gg 1$ (compare App. B.4).

in Sec. 3.1.3. For large particle numbers $N_I = N_{II} = N \gg 1$ and $t \to \infty$,

$$\xi_\infty = \frac{1}{P_{2,\infty}} \frac{\tilde{\Gamma} + d\Gamma P_{2,\infty}^2 \left(|\mu| - |\nu|\right)^2}{\tilde{\Gamma} + d\Gamma P_{2,\infty}}, \tag{3.5}$$

where $P_{2,\infty}$ is the steady state value of the atomic polarization $P_2 = \frac{1}{N}\sum_{i=1}^{N}\left(|\uparrow\rangle_i\langle\uparrow| - |\downarrow\rangle_i\langle\downarrow|\right)$, Γ is the single particle decay rate and $\tilde{\Gamma}$ is the dephasing rate associated with noise effects and d is the optical depth of one atomic ensemble. As shown in Sec. 3.1.3, the application of resonant pump fields can be beneficial even though noise is added by doing so. Note that for $d \to \infty$ we get $\xi_\infty \to \xi_\infty^{\text{ideal}}$. For a large optical depth, the entangling dynamics is significantly enhanced by collective effects. In contrast, noise processes are single particle effects and therefore not amplified by a factor d. Eq. (3.5) shows that for strong coupling between atoms and light, entanglement can be generated in a steady state. This is the main theoretical result of this section.

Intuitively, entanglement is created by virtue of interference of different processes in the first and second ensemble. As illustrated in Fig. 3.1b, the interaction of light and atoms in the first ensemble is chosen such that the emission of a photon in the upper sideband corresponds to a spin flip $|\uparrow\rangle \to |\downarrow\rangle$. Similarly, in the second ensemble the emission of a photon in the upper sideband involves a spin flip $|\downarrow\rangle \to |\uparrow\rangle$. Due to collective effects [12], light is emitted in forward direction with high probability, for samples with large optical depth. As spin flips in either ensemble lead to emission of light into the same spatial mode, both processes are indistinguishable if a photon is detected. An analogous argument holds for photons in the lower sideband. In this respect, the setup resembles quantum repeater schemes [66, 67, 156–162], where collective excitations in two atomic ensembles are converted to photons, which subsequently interfere at a 50/50 beamsplitter such that entanglement can be created conditioned on the detection of a photon in one of the two output ports of the beamsplitter[6]. Here, no beamsplitter is needed, since both ensembles emit into the same spatial mode. The most important difference, however, lies in the fact that the scheme presented here is not conditioned on a specific measurement outcome. It works deterministically and does not require a detection of the emitted photon.

The ideas put forward here are devised and elaborated for two-levels systems, but the proposed scheme can also be realized using atoms with multi-level ground states. In a multi-level setting, the population in the two-level subsystem is continually reduced due to undesired transitions to other ground state levels. Below, this and other features of the multi-level structure are taken into account and it is found that the continuous reduction of the collective spin leads to the formation of a quasi steady state: the steady state with respect to the relevant two-level subsystem is superposed by slow additional dynamics due to the multi-level structure. This can be counteracted by the application of external

[6] The basic working principle of this approach can be illustrated by considering two single atoms with ground state $|g\rangle$ and excited state $|e\rangle$, which are placed in two different cavities. Both atoms are initially prepared in the excited state $|\Psi^{\text{in}}\rangle = |e\rangle_1|e\rangle_2$. Atoms can spontaneously decay to their ground state $|e\rangle \to |g\rangle$ while emitting a photon. The light emitted from both cavities is combined at a beamsplitter and photon detectors are placed at each output port. The atoms are projected into a maximally entangled state $|\Psi^{\text{out}}\rangle = \left(|e\rangle_1|g\rangle_2 + |g\rangle_1|e\rangle_2\right)/\sqrt{2}$ if a photon is detected at one of the two output ports.

pump fields. These fields add noise to the system and limit therefore the amount of entanglement that can be generated. However, for samples with large optical depth, incoherent pumping can render the creation of true steady state entanglement in atoms with multilevel ground states possible. This is illustrated in Sec. 3.1.4 by considering ^{133}Cs vapors at room temperature and typical experimental parameters. There, the most fundamental limitations imposed by undesired radiative processes are taken into account and it is estimated that steady state entanglement with $\xi_\infty = 0.9$ should be attainable for a moderate optical depth $d = 30$ in the absence of other (implementation-dependent) sources of noise. The described scheme has been realized recently [III] using Cs atoms. In this experiment, purely dissipatively driven entanglement between two macroscopic atomic ensembles at room temperature has been demonstrated yielding an order of magnitude improvement in the entanglement life time compared to previous experiments, where entanglement has been generated in this system using standard methods. By combining the dissipative mechanism with continuous measurements on the light field scattered in forward direction, steady state entanglement can be continuously generated and has been observed for up to an hour. These results represent a new step in the quantum control of entanglement. Dissipatively generated entanglement provides not only event-ready entangled links for standard protocols but is also an elementary resource for future applications in continuous quantum information processing schemes, such as dissipative distillation and repeater protocols, which allow for the distribution of long-range high-quality steady state entanglement as described in the next section (Sec. 3.2).

3.1.3 Creation of steady state entanglement in a two-level system

As outlined above, light modes act as environment and the interaction between the system and the bath is controlled by means of laser- and magnetic fields. In the following, the interaction between atoms and light is explained in more detail. The master equation governing the dissipative evolution of the reduced density matrix of the atomic system ρ is given by

$$d_t\rho = \mathcal{L}_{\text{ent}}\rho + \mathcal{L}_{\text{noise}}\rho,$$

where $\mathcal{L}_{\text{ent}}$ and $\mathcal{L}_{\text{noise}}$ are Lindblad operators. Desired interactions give rise to the entangling dynamics represented by $\mathcal{L}_{\text{ent}}\rho$. The second term $\mathcal{L}_{\text{noise}}\rho$ summarizes all undesired effects. Below, $\mathcal{L}_{\text{ent}}\rho$ and $\mathcal{L}_{\text{noise}}\rho$ are determined. To this end, the master equation corresponding to the light-matter interaction in Fig. 3.1 is derived, including undesired radiative processes. Then, excited states are adiabatically eliminated such that an effective master equation for atomic ground states $|\uparrow\rangle$ and $|\downarrow\rangle$ is obtained. Finally, thermal motion of atoms is taken into account and additional effects due to pump fields and noise processes are included. Based on these results, the amount of entanglement that can be produced is calculated.

Light–matter interaction

In this subsection, the setup for the creation of entanglement between two atomic ensembles is described and the interaction between light and matter is explained. The considered setup is shown in Fig. 3.1 and explained in Sec. 2.1.1. The laser field is assumed to be far off-resonant such that the interaction is well within the dispersive regime. The detuning $|\Delta|$ is considered to be large compared to the Doppler width δ_{Doppler} and atomic decay rates Γ_{atomic}. Here and in the following, Γ_{atomic} denotes the largest effective atomic rate for transitions between ground state levels, including single particle as well as collective rates (see below). The strong $\hat{\mathbf{y}}$-polarized coherent beam is treated as classical field. With respect to quantization along $\hat{\mathbf{x}}$, it drives diagonal transitions $|\uparrow\rangle \rightarrow |e_\downarrow\rangle$, $|\downarrow\rangle \rightarrow |e_\uparrow\rangle$. Fig. 3.1 depicts only desired transitions, where photons are scattered into the copropagating $\hat{\mathbf{x}}$-polarized quantum field in two independent frequency bands, the upper and the lower sideband, centered around $\omega_L \pm \Omega$.
For the realization of the proposed scheme, several setups are possible. In a simple two-level model, where the Larmor splitting of excited states equals the Larmor splitting of ground states, a homogeneous static electric field can be applied to the second ensemble such that the resulting Stark shift enhances the energy difference between ground and excited states by 2Δ as shown in Fig. 3.1b. This yields the following effective ground state Hamiltonian $H = H_A + H_L + H_{\text{int}}$, where excited states have been eliminated under the condition $|\Delta| \gg \Gamma_{\text{atomic}},\ \delta_{\text{Doppler}}$. $H_A = \Omega\,(J_{x,I} - J_{x,II})$ accounts for the Zeeman splitting of atoms in the external magnetic field and $H_L = \int dk\,(\omega_k - \omega_L)\,a_k^\dagger a_k$ is the free Hamiltonian of the light field. In a rotating frame, the interaction Hamiltonian is given by

$$\begin{aligned} H_{\text{int}} =& \int_{\Delta\omega_{ls}} d\mathbf{k} \sum_{\lambda_\mathbf{k}} \bar{g}(\mathbf{k}) \left(\mu \sum_{i=1}^{N} \sigma_{I,i} e^{i\Delta\mathbf{k}\mathbf{r}_i} + \nu \sum_{j=1}^{N} \sigma_{II,j}^\dagger e^{i\Delta\mathbf{k}\mathbf{r}_j} \right) a_\mathbf{k}^\dagger \\ &+ \int_{\Delta\omega_{us}} d\mathbf{k} \sum_{\lambda_\mathbf{k}} \bar{g}(\mathbf{k}) \left(\mu \sum_{i=1}^{N} \sigma_{II,i} e^{i\Delta\mathbf{k}\mathbf{r}_i} + \nu \sum_{j=1}^{N} \sigma_{I,j}^\dagger e^{i\Delta\mathbf{k}\mathbf{r}_j} \right) a_\mathbf{k}^\dagger + H.C.\ , \end{aligned} \tag{3.6}$$

where the first and second integral cover narrow bandwidths $\Delta\omega_{\text{ls}}$ and $\Delta\omega_{\text{us}}$ centered around the lower and upper sideband respectively (a complete treatment based on the full Hamiltonian including all light modes can be found in App. B.3.1). $\lambda_\mathbf{k}$ specifies the two orthogonal polarizations of the light mode with wave vector $\mathbf{k}$. The atomic operator $\sigma_{I/II,i} = |\uparrow\rangle_{I/II,i}\langle\downarrow|$ refers to a particle in ensemble I/II at position $\mathbf{r}_i$, $\Delta\mathbf{k} = \mathbf{k}_L - \mathbf{k}$, and $\mathbf{k}_L$ is the wave vector of the applied classical field. AC Stark shifts have been absorbed in the detuning. $\bar{g}(\mathbf{k})\mu$ and $\bar{g}(\mathbf{k})\nu$ are the effective coupling strengths for the passive (beamsplitter-like) part of the interaction and the active (squeezing) component of the Hamiltonian respectively. More specifically, $\bar{g}(\mathbf{k})\mu = \frac{\Omega_{\text{probe}}}{\Delta-\Omega} g_\mathbf{k}$ and $\bar{g}(\mathbf{k})\nu = \frac{\Omega_{\text{probe}}}{\Delta+\Omega} g_\mathbf{k}$, where Ω_{probe} is the Rabi frequency of the applied classical field. Here and in the following, the off-resonant (entangling) light field is referred to as probe field. Later in the text, resonant fields are introduced which will be referred to as pump fields. The definition of the coupling constant for transitions between ground and excited states $g_\mathbf{k}$ can be found in App. B.3.1. The parameters $\mu = \frac{\Delta+\Omega}{2\sqrt{\Delta\Omega}}$ and $\nu = \frac{\Delta-\Omega}{2\sqrt{\Delta\Omega}}$ are normalized such that $\mu^2 - \nu^2 = 1$.

A Hamiltonian of type (3.6) can be realized in many different ways. In general, the scheme presented here can be implemented in any system where a tunable quadratic interaction with an active and a passive part corresponding to two sideband modes can be realized, for example in ions or using optomechanical resonators. Here, the focus is on the creation of dissipatively driven entanglement in atomic ensembles and in the following the level structure depicted in Fig. 3.1b is therefore considered. If the Larmor splitting of excited states is considerably larger than the splitting of ground states, a $\lambda/2$ plate can be introduced between the two ensembles instead of applying an external electric field[7]. As discussed in Sec. 3.1.4, alkali atoms provide another possibility to realize the desired light-matter interaction. Due to their multi-level structure is is not even necessary to introduce electric fields or passive optical elements. It is remarked for clarity, that the possibility illustrated in Fig. 3.1b implies that the effective coupling constants (after adiabatic elimination) $\bar{g}(\mathbf{k})\mu$ and $\bar{g}(\mathbf{k})\nu$ describing the interaction of light with the first and the second ensemble have different signs, as the light is blue detuned in the former and red detuned in the latter, such that $\mu_I = -\mu_{II}$ and $\nu_I = -\nu_{II}$. This is not the case in the implementation considered in Sec. 3.1.4. Due to the complex levels structure, both effective coupling constants have the same sign and therefore $\mu_I = \mu_{II}$ and $\nu_I = \nu_{II}$. In order to describe both alternatives in a compact way, a unified notation is used and the sign is absorbed in the definition of the atomic operators referring to the second ensembles $\sigma_{II,i} \rightarrow \mathrm{sgn}(\mu_I\mu_{II})\sigma_{II,i}$ as explained in App. B.3.2.

It is instructive to consider Hamiltonian (3.6), where excited levels have been adiabatically eliminated, because it shows clearly that the light matter interaction depicted in Fig. 3.1b corresponds to a beamsplitting interaction of the type $H \propto \int_{\Delta\omega_{ls}} d\mathbf{k} \left(A a_{\mathbf{k}}^\dagger + A^\dagger a_{\mathbf{k}}\right) + \int_{\Delta\omega_{us}} d\mathbf{k} \left(B a_{\mathbf{k}}^\dagger + B^\dagger a_{\mathbf{k}}\right)$ between photons in the upper and lower sideband with the nonlocal operators A and B (with additional phase factors $e^{\pm i\Delta\mathbf{k}\mathbf{r}_i}$). By deriving the corresponding master equation and including thermal motion as explained below, it can be shown that this Hamiltonian yields a master equation which consists of a desired part of type (3.2) with jump operators A and B and an additional contribution representing noise terms. However, in the following, the master equation is derived starting from the full Hamiltonian including excited levels since this approach is better suited to take dipole-dipole interactions into account.

Effective master equation for ground states

In the following, the derivation of the master equation for atomic ground states $|\Uparrow\rangle$ and $|\Downarrow\rangle$ is outlined and the approximations used to obtain the shown result are commented on. The full calculation can be found in App. B.3.1. For brevity, a short hand notation is used and master equations of Lindblad form $d_t\rho(t) = \kappa/2\left(A\rho(t)A^\dagger - A^\dagger A\rho(t)\right) + H.C.$ with complex decay rate κ and jump operator A are abbreviated by the expression

[7] A $\lambda/2$ plate interchanges the fields in $\hat{\mathbf{x}}$ and $\hat{\mathbf{y}}$ polarization. If such a passive optical element is placed between the first and the second atomic ensemble, the roles of classical and quantum fields are therefore interchanged. Accordingly, the classical field drives π-transitions $|\uparrow\rangle \rightarrow |e_\uparrow\rangle$, $|\downarrow\rangle \rightarrow |e_\downarrow\rangle$ in the second ensemble, while the quantum field is associated with transitions which change the magnetic quantum number $\Delta_m = \pm 1$.

$d_t\rho(t) = \kappa/2A\rho(t)A^\dagger + \ldots$.
Here, the full Hamiltonian including excited levels and undesired transitions[8] is considered without applying the rotating wave approximation for quantum fields (see Eq. B.2). As explained in App. B.3.1, counter-rotating terms play an important role in the calculation of the imaginary parts of the master equation, but do not affect the real parts. Starting from the full Hamiltonian, a master equation of Lindblad form for the reduced atomic density matrix is obtained (see Eqs. (B.3)-(B.5)). To this end, the approximation of independent rates of variation is applied [165] following the standard procedure assuming Born-Markov dynamics. The approximation of independent rates of variations is valid if the Rabi frequency of the applied laser field Ω_{probe} is very small compared with the frequencies of atomic transitions. Since we consider here transitions in the optical domain, this assumption is clearly legitimate. More generally, here and in the following sections situations exhibiting two very different time scales for variations in the system and in the bath of light modes are considered $\Gamma_{\text{atomic}}\tau_c \ll 1$, where τ_c is the correlation time in the reservoir. For optical frequencies this is very well justified and Born-Markov dynamics can be assumed. Moreover, the discussion is restricted to settings, where the level splitting Ω between the states $|\uparrow\rangle$ and $|\downarrow\rangle$ is sufficiently large, such that the upper and lower sideband can be treated as independent baths[9] (compare App. B.3.1). Finally, it is assumed that the condition $k_L \gg R/L^2$ is fulfilled. k_L is the wave vector of the applied laser field. Since frequencies in the optical domain are considered, k_L is on the order of 10^7m^{-1}. L is the spatial extent of the atomic ensembles, which is assumed to be on the order of cm, while the distance between the two ensembles R is about one meter.

As next step, excited states are adiabatically eliminated under the condition $|\Delta| \gg \Gamma_{\text{atomic}},\ \delta_{\text{Doppler}}$. This leads to an effective master equation for atomic ground states. Using the abbreviated notation introduced in the beginning of this subsection,

$$\begin{aligned} d_t\rho(t) = & \frac{1}{2}\sum_{i,j=1}^{N} e^{-i\mathbf{k}_L(\mathbf{r}_j-\mathbf{r}_i)} J_{ij}\left(A_i\rho(t)A_j^\dagger + B_i\rho(t)B_j^\dagger\right) \\ & + \frac{1}{2}\sum_{i,j=1}^{N} e^{-i\mathbf{k}_L(\mathbf{r}_j-\mathbf{r}_i)} \check{J}_{ij}\left(C_i\rho(t)C_j^\dagger + D_i\rho(t)D_j^\dagger\right) \\ & + \ldots , \end{aligned} \tag{3.7}$$

where J_{ij} and $\check{J}_{ij}$ are complex decay rates which are discussed below and $A = \frac{1}{\sqrt{N}}\sum_{i=1}^{N} A_i$. The operators B, C and D are defined analogously. A_i, B_i, C_i and D_i are given by

$$\begin{aligned} A_i &= \mu\ \sigma_{I,i} + \nu\ \sigma_{II,i}^\dagger, \qquad & C_i &= \mu\ \sigma_{\downarrow\downarrow,I,i} + \nu\ \sigma_{\uparrow\uparrow,II,i}, \\ B_i &= \mu\ \sigma_{II,i} + \nu\ \sigma_{I,i}^\dagger, \qquad & D_i &= \mu\ \sigma_{\downarrow\downarrow,II,i} + \nu\ \sigma_{\uparrow\uparrow,I,i}, \end{aligned}$$

where the abbreviations $\sigma_{\uparrow\uparrow,I/II,i} = |\uparrow\rangle_{I/II,i}\langle\uparrow|$ and $\sigma_{\downarrow\downarrow,I/II,i} = |\downarrow\rangle_{I/II,i}\langle\downarrow|$ are used. Terms involving the operators A and B represent desired transitions involving a spin

[8] Undesired radiative transitions $|\uparrow\rangle \to |\uparrow\rangle$ and $|\downarrow\rangle \to |\downarrow\rangle$ involve the emission of a photon but no change of the internal atomic state. These processes are not explicitely shown in Fig. 3.1b.

[9] If the upper and lower sideband are not treated as independent baths, cross terms appear, which rotate fast (with frequency $\pm 2\Omega$) compared to the single-bath terms, (which do not rotate in this picture). These cross terms can be neglected in a rotating wave approximation if $\Omega \gg \Gamma_{\text{atomic}}$.

flip $|\uparrow\rangle \rightarrow |\downarrow\rangle$ or $|\downarrow\rangle \rightarrow |\uparrow\rangle$ as shown in Fig. 3.1b. Terms involving the operators C or D represent undesired transitions which lead to dephasing. Desired and undesired transitions are associated with different decay rates J_{ij} and $\check{J}_{ij}$ respectively. In the four level model considered here, $\check{J}_{ij} = 2J_{ij}$, due to the ratio of Clebsch-Gordan coefficients $|\langle\frac{1}{2},\pm\frac{1}{2};1,\mp1|\frac{1}{2},\mp\frac{1}{2}\rangle|^2/|\langle\frac{1}{2},\pm\frac{1}{2};1,0|\frac{1}{2},\pm\frac{1}{2}\rangle|^2 = 2$. As introduced above, $J_{ij} = \gamma(\mathbf{r}_{ij}) + ig(\mathbf{r}_{ij})$ is a complex decay rate with real part $\gamma(\mathbf{r}_{ij}) = \gamma(\mathbf{r}_{ji})$ and imaginary part $g(\mathbf{r}_{ij}) = g(\mathbf{r}_{ji})$. Imaginary single particle terms represent energy shifts (single atom Lamb shift) and are absorbed in the definition of detunings. Therefore, only imaginary terms $g(\mathbf{r}_{ij})$ with $i \neq j$ are considered in the following and renormalized atomic energies and the resulting effective detunings are used. The real and imaginary part of J_{ij} are given by [166]

$$\gamma(\mathbf{r}_{ij}) = \frac{3}{2}\Gamma\big(1-(\hat{\mathbf{p}}\cdot\hat{\mathbf{r}}_{ij})^2\big)\frac{\sin(k_\mathrm{L}r_{ij})}{k_\mathrm{L}r_{ij}} + \frac{3}{2}\Gamma\big(1-3\,(\hat{\mathbf{p}}\cdot\hat{\mathbf{r}}_{ij})^2\big)\left(\frac{\cos(k_\mathrm{L}r_{ij})}{(k_\mathrm{L}r_{ij})^2} - \frac{\sin(k_\mathrm{L}r_{ij})}{(k_\mathrm{L}r_{ij})^3}\right), \quad (3.8)$$

$$g(\mathbf{r}_{ij}) = -\frac{3}{2}\Gamma\big(1-(\hat{\mathbf{p}}\cdot\hat{\mathbf{r}}_{ij})^2\big)\,\frac{\cos(k_\mathrm{L}r_{ij})}{k_\mathrm{L}r_{ij}} + \frac{3}{2}\Gamma\big(1-3\,(\hat{\mathbf{p}}\cdot\hat{\mathbf{r}}_{ij})^2\big)\left(\frac{\sin(k_\mathrm{L}r_{ij})}{(k_\mathrm{L}r_{ij})^2} + \frac{\cos(k_\mathrm{L}r_{ij})}{(k_\mathrm{L}r_{ij})^3}\right),$$

where $\hat{\mathbf{p}}$ is the unit vector of the dipole matrix element $\mathbf{p} = \langle e_\uparrow|e\,\hat{\mathbf{x}}|\uparrow\rangle$, which is assumed to be real. $\hat{\mathbf{r}}_{ij}$ is the unit vector of the interatomic distance $\mathbf{r}_{ij} = \mathbf{r}_i - \mathbf{r}_j$ and $r_{ij} = r_{ji}$ is the length of the vector $\mathbf{r}_{ij}$. Γ is the effective decay rate of a single isolated atom.

Master equation including thermal motion and noise processes

In this subsection, atomic motion is taken into account [85, 167, 168]. As shown below, thermal motion gives rise to noise terms which are small compared to the desired contributions for samples with large optical depth. Atoms are statistically distributed. The dynamics of the whole system is governed by two different time scales, the characteristic time of radiative emission $1/\Gamma_\mathrm{atomic}$ and the characteristic time of atomic redistribution $\frac{L}{v}$, where L is the length of a cubic ensemble and v is the average velocity. In the limit, where the time scale of atomic motion is fast compared to the time scale of radiative decay $\Gamma_\mathrm{atomic}\frac{L}{v} \ll 1$, the emission can be described independently of the evolution of atomic positions which enters the master equation in the form of averaged coefficients, where the average in time corresponds to an average in space[10]. The atomic positions can be treated as independent random variables. For simplicity, a Gaussian probability distribution of width L is chosen, $P(r) = \frac{1}{\pi^{3/2}L^3}e^{-\frac{r^2}{L^2}}$ [85]. As shown in App. B.3, the imaginary parts of the averaged decay rates can be neglected. The averaged master equation is given by

$$d_t\rho(t) = \frac{1}{2}\sum_{i,j=1}^{N}\Gamma_{ij}\Big(A_i\rho(t)A_j^\dagger + B_i\rho(t)B_j^\dagger\Big) + \frac{1}{2}\sum_{i,j=1}^{N}\check{\Gamma}_{ij}\Big(C_i\rho(t)C_j^\dagger + D_i\rho(t)D_j^\dagger\Big) + \ldots\,. \quad (3.9)$$

with $\check{\Gamma}_{ij} = 2\Gamma_{ij}$ for the basic model discussed here. For $k_L L \gg 1$ and $i \neq j$, $\Gamma_{ij} = \Gamma\frac{3}{4(k_L L)^2}$. The resonant optical depth of one atomic ensemble is $d = N\frac{\Gamma_{ij}}{\Gamma} = \frac{3N}{4(k_L L)^2}$. Using this

[10] An analysis of the generation of entanglement between two atomic ensembles in the opposite limit of fixed atomic positions can be found in [93].

definition and $1/(k_L L)^2 \ll 1$, one obtains

$$\begin{aligned} d_t\rho(t) &= d\frac{\Gamma}{2}A\rho(t)A^\dagger + d\frac{\Gamma}{2}B\rho(t)B^\dagger \\ &+ \mu^2\frac{\Gamma}{2}\sum_{i=1}^{N}\left(\sigma_{I,i}\rho(t)\sigma_{I,i}^\dagger + \sigma_{II,i}\rho(t)\sigma_{II,i}^\dagger\right) \\ &+ \nu^2\frac{\Gamma}{2}\sum_{i=1}^{N}\left(\sigma_{I,i}^\dagger\rho(t)\sigma_{I,i} + \sigma_{II,i}^\dagger\rho(t)\sigma_{II,i}\right) \\ &+ d\frac{\check{\Gamma}}{2}C\rho(t)C^\dagger + d\frac{\check{\Gamma}}{2}D\rho(t)D^\dagger + \frac{\check{\Gamma}}{2}\left(\mu^2+\nu^2\right) \\ &\quad \sum_{i=1}^{N}(\sigma_{\downarrow\downarrow,I,i}\rho(t)\sigma_{\downarrow\downarrow,I,i} + \sigma_{\downarrow\downarrow,II,i}\rho(t)\sigma_{\downarrow\downarrow,II,i}) \\ &+ \ \ldots\ . \end{aligned} \tag{3.10}$$

The first three lines correspond to the first sum in Eq. (3.9). The entangling terms in the first line are enhanced by a factor d. For sufficiently optically thick samples, additional noise terms in the second and third line, which reflect thermal motion, are small compared to the desired contributions. The last two lines correspond to the second sum in Eq. (3.9), where $|\uparrow\rangle\langle\uparrow| + |\downarrow\rangle\langle\downarrow| = \mathbb{1}$ was used. The first two terms $d(\check{\Gamma}/2)C\rho(t)C^\dagger + d(\check{\Gamma}/2)D\rho(t)D^\dagger$ are collective dephasing terms. They do not have an effect on the entanglement generated (see App. B.4.2) and can therefore be omitted.
In the following sections, the effect of pump fields is considered. Resonant pump fields cause incoherent cooling (and heating) processes, which can be taken into account by adding cooling (and heating) terms which correspond to a transfer of atoms from level $|\downarrow\rangle$ to level $|\uparrow\rangle$ (and back). Finally, additional processes, which do not lead to spin flips but cause dephasing, such as fluctuating magnetic fields are included. The full master equation is given by

$$\begin{aligned} d_t\rho(t) &= d\frac{\Gamma}{2}A\rho(t)A^\dagger + d\frac{\Gamma}{2}B\rho(t)B^\dagger \\ &+ \frac{\Gamma_{\text{cool}}}{2}\sum_{i=1}^{N}\left(\sigma_{I,i}\rho(t)\sigma_{I,i}^\dagger + \sigma_{II,i}\rho(t)\sigma_{II,i}^\dagger\right) \\ &+ \frac{\Gamma_{\text{heat}}}{2}\sum_{i=1}^{N}\left(\sigma_{I,i}^\dagger\rho(t)\sigma_{I,i} + \sigma_{II,i}^\dagger\rho(t)\sigma_{II,i}\right) \\ &+ \frac{\Gamma_{\text{d}}}{2}\sum_{i=1}^{N}(\sigma_{\downarrow\downarrow,I,i}\rho(t)\sigma_{\downarrow\downarrow,I,i} + \sigma_{\downarrow\downarrow,II,i}\rho(t)\sigma_{\downarrow\downarrow,II,i}) \\ &+ \ \ldots\ . \end{aligned} \tag{3.11}$$

Note that the last three lines represent single particle processes. They do not feature a collective enhancement factor d as the entangling terms in the first line. The noise terms proportional to $\Gamma\mu^2$ and $\Gamma\nu^2$ in the second and third line in expression (3.10) have been absorbed in lines two and three of Eq. (3.11). Hence, Γ_{cool} (Γ_{heat}) is the total single-particle

cooling (heating) rate. Noise terms proportional to $\Gamma(\mu^2+\nu^2)$ in expression (3.10) have been absorbed in the last line, such that Γ_d is the total dephasing rate. More details concerning the derivation of the full master equation (3.11) can be found in App. B.4.2.

Creation of entanglement

In this subsection, the amount of entanglement which can be generated in the presence of noise processes is determined for a given optical depth d and given parameters μ and ν. Details of the calculation can be found in App. B.4. For simplicity, identical conditions for both ensembles are assumed. The amount of entanglement produced is measured by means of the quantity ξ defined in Eq. (3.3). Hence, the time evolution of $\Sigma_J = \mathrm{var}(\mathrm{J_{y,I}}+\mathrm{J_{y,II}}) + \mathrm{var}(\mathrm{J_{z,I}}-\mathrm{J_{z,II}})$ as well as the evolution of the mean value of the longitudinal spin $|\langle J_{x,I}\rangle| = |\langle J_{x,II}\rangle|$ need to be calculated. Here and in the following, the limit $N \gg 1$ is considered. Σ_J decays according to

$$d_t\Sigma_J \;=\; -\left(\tilde{\Gamma}+d\Gamma P_2(t)\right)\Sigma_J + Nd\Gamma P_2(t)^2\left(|\mu|-|\nu|\right)^2,$$

where $\tilde{\Gamma}=\Gamma_\mathrm{cool}+\Gamma_\mathrm{heat}+\Gamma_\mathrm{d}$ and $P_2(t)=\frac{2}{N}\langle J_x\rangle$. The evolution of the mean value of the longitudinal spin is given by

$$d_t\langle J_x\rangle = -\frac{1}{2}\left(\Gamma_\mathrm{heat}+\Gamma_\mathrm{cool}\right)\langle J_x\rangle_t + \frac{N}{2}\left(\Gamma_\mathrm{cool}-\Gamma_\mathrm{heat}\right).$$

There are two distinct time scales. For atomic ensembles with large optical depth, the evolution of the transverse spin components is collectively enhanced and therefore fast compared to the decay of $\langle J_x\rangle$ which is due to single particle processes. In the limit where the entangled quantum state follows the changing atomic polarization adiabatically, the time evolution of $\xi(t)$ is given by

$$\xi(t) \;=\; \frac{1}{P_2(t)}e^{-\left(\tilde{\Gamma}+d\Gamma P_2(t)\right)t}+\frac{1}{P_2(t)}\frac{\tilde{\Gamma}+d\Gamma P_2(t)^2(|\mu|-|\nu|)^2}{\tilde{\Gamma}+d\Gamma P_2(t)}\left(1-e^{-\left(\tilde{\Gamma}+d\Gamma P_2(t)\right)t}\right).$$

In the steady state

$$\xi_\infty = \frac{1}{P_{2,\infty}}\frac{\tilde{\Gamma}+d\Gamma P_{2,\infty}^2\left(|\mu|-|\nu|\right)^2}{\tilde{\Gamma}+d\Gamma P_{2,\infty}}, \quad P_{2,\infty}=\frac{\Gamma_\mathrm{cool}-\Gamma_\mathrm{heat}}{\Gamma_\mathrm{cool}+\Gamma_\mathrm{heat}}.$$

This result shows that for high optical depth, the system reaches an entangled steady state. Under the dissipative dynamics considered here, entanglement persists for arbitrarily long times. In the absence of noise, $\tilde{\Gamma}=0$ and Eq. (3.12) reduces to $\xi_\infty=\left(|\mu|-|\nu|\right)^2$.

Fig. 3.2a shows the attainable amount of entanglement in the steady state ξ_∞ for moderate optical depth $d=30$ versus $Z=\left(|\mu|-|\nu|\right)^{-1}$ if only probe fields are applied. In this case $\Gamma_\mathrm{cool}^\mathrm{probe}=\mu^2\Gamma$ and $\Gamma_\mathrm{heat}^\mathrm{probe}=\nu^2\Gamma$. The dephasing rate $\Gamma_\mathrm{d}=\Gamma_\mathrm{d}^\mathrm{rad}+\Gamma_d^\mathrm{add}$ consists of a radiative part[11] $\Gamma_\mathrm{d}^\mathrm{rad,probe}=2\left(\mu^2+\nu^2\right)\Gamma$, which is due to light-induced transitions

[11] In the two-level model shown in Fig. 3.1b, $\Gamma_\mathrm{d}^\mathrm{rad,probe}=2\left(\Gamma_\mathrm{cool}^\mathrm{probe}+\Gamma_\mathrm{heat}^\mathrm{probe}\right)$, due to the ratio of Clebsch-Gordan coefficients $|\langle\frac{1}{2},\pm\frac{1}{2};1,\mp1|\frac{1}{2},\mp\frac{1}{2}\rangle|^2/|\langle\frac{1}{2},\pm\frac{1}{2};1,0|\frac{1}{2},\pm\frac{1}{2}\rangle|^2=2$.

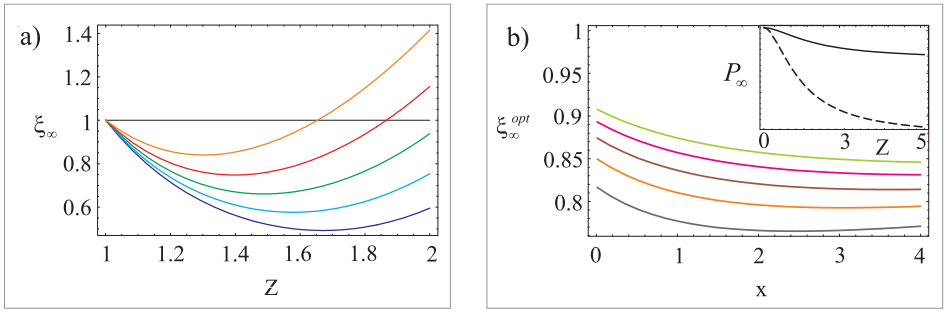

Figure 3.2: Steady state entanglement ξ_∞ in a two-level system for an optical depth $d = 30$ per ensemble. a) ξ_∞ versus $Z = (|\mu| - |\nu|)^{-1}$. The horizontal black line indicates the separable limit (for separable states $\xi \geq 1$, the smaller ξ, the higher the amount of entanglement). The lowest line (violet) depicts ξ_∞ for purely radiative dephasing $\Gamma_{\rm d}^{\rm add} = 0$. The next curves show in ascending order $\Gamma_d^{\rm add} = 2\Gamma$ (blue), $\Gamma_{\rm d}^{\rm add} = 5\Gamma$ (green), $\Gamma_{\rm d}^{\rm add} = 10\Gamma$ (red) and $\Gamma_{\rm d}^{\rm add} = 20\Gamma$ (orange), where Γ is the single particle decay rate. b) Steady state entanglement $\xi_\infty^{\rm opt}$ for optimal squeezing parameter Z versus pump parameter x. The curves correspond in ascending order to $\Gamma_{\rm d}^{\rm add} = 15$(grey), $\Gamma_{\rm d}^{\rm add} = 20\Gamma$ (orange), $\Gamma_{\rm d}^{\rm add} = 25\Gamma$ (brown), $\Gamma_{\rm d}^{\rm add} = 30\Gamma$ (pink) and $\Gamma_{\rm d}^{\rm add} = 35\Gamma$ (green). The inset shows the steady state polarization $P_{2,\infty}$ versus Z in the absence of pump fields $x = 0$ (dashed line) and for $x = 5$ (solid line).

$|\uparrow\rangle \rightarrow |\uparrow\rangle$ and $|\downarrow\rangle \rightarrow |\downarrow\rangle$, and an additional term $\Gamma_{\rm d}^{\rm add}$ which summarizes all non-radiative sources of dephasing such as fluctuating magnetic fields. This additional component can take values up to $\Gamma_{\rm d}^{\rm add} = 20\Gamma$ while still allowing for a reduction of ξ_∞ by 15%. For large values of $\Gamma_d^{\rm add}$, the limiting mechanism is the decrease in polarization for high squeezing parameters and can be counteracted by applying resonant σ_+ and σ_- polarized pump fields to the first and second ensemble respectively, which drive the transition $|\downarrow\rangle \rightarrow |e_\uparrow\rangle$. In this case, the cooling rate can be roughly estimated[12] as $\Gamma_{\rm cool} = (1+x)\,\Gamma\mu^2$. The pump parameter x is given by $x = \frac{\Omega_{\rm pump}^2}{\gamma_{\rm LW}^2}\frac{(\Delta-\Omega)^2}{\Omega_{\rm probe}^2}k$, where $\Omega_{\rm pump}$ is the Rabi frequency of the pump field and $\gamma_{\rm LW}$ is the natural line width of excited levels. The correction factor k takes Doppler broadening due to thermal motion into account[13]. In the presence of pump fields, radiative dephasing is enhanced $\Gamma_{\rm d}^{\rm rad} = 2\left((1+x)\,\mu^2 + \nu^2\right)\Gamma$. The heating

[12] Rates Γ_{ab} are calculated using the formula $\Gamma_{ab} = \Omega_{ab}^2 \frac{c_{ab}^2}{|\Delta_{ab}+i\gamma_{\rm LW}|^2}\gamma_{\rm LW}$, where Ω_{ab} is the Rabi frequency, Δ_{ab} the detuning, $\gamma_{\rm LW}$ the natural line width of excited levels and $c_l^{\rm ab} = \langle j_b, m_b; j_{L_2}, m_{L_2}|j_e, m_e\rangle\langle j_e, m_e|j_a, m_a; j_{L_1}, m_{L_1}\rangle$ is the product of the Clebsch-Gordan coefficients for the transition under consideration ($j_{L_{1/2}}$ and $j_{L_{1/2}}$ refer to the absorbed and emitted photons involved in the process). The cooling rate $\Gamma_{\rm cool} = \Gamma_{\rm cool}^{\rm probe} + \Gamma_{\rm cool}^{\rm pump}$ consists of a probe- and a pump induced part. As probe fields are considered to be far off-resonant, the corresponding cooling rate is calculated using the approximation $\Gamma_{\rm cool}^{\rm probe} = \Omega_{\rm probe}^2 \frac{1}{(\Delta-\Omega)^2}\gamma_{\rm LW}$. Contributions due to resonant pump fields are given by $\Gamma_{\rm cool}^{\rm pump} = \Omega_{\rm pump}^2 \frac{1}{\gamma_{\rm LW}^2}\gamma_{\rm LW}$.

[13] The correction factor k takes into account that due to the Doppler broadening of atoms moving at room temperature only a fraction $k = \frac{\gamma_{\rm LW}}{\delta_{\rm Doppler}}$ of all atoms in the cell is on resonance with the applied field. The Doppler width is given by $\delta_{\rm Doppler} = \frac{\nu}{c}\left(\frac{2k_BT}{m\ln 2}\right)^{1/2}$, where $c/\nu = \lambda$ is the wavelength of the applied light field, k_B is the Boltzmann constant, T is the temperature and m is the atomic mass.

rate is unaffected. Fig. 3.2b shows the maximal attainable amount of entanglement $\xi_\infty^{\rm opt}$ (entanglement for optimal squeezing parameter Z), for $d = 30$ versus pump parameter x. For $x = 5$, additional dephasing up to $\Gamma_{\rm d}^{\rm add} = 37\Gamma$ can be tolerated while still allowing for a reduction of $\xi_\infty^{\rm opt}$ by 15%. Remarkably, the application of external pump fields, which amounts to adding extra noise to the system, is advantageous in this case.

3.1.4 Implementation in multi-level systems

In Sec. 3.1.3, the theoretical framework for creating steady state entanglement between two atomic ensembles at room temperature is presented in detail for two-level systems. This section complements the main results derived in Sec. 3.1.3 by considering the implementation in multi-level systems. In the following, the possibility of transferring the concepts developed for two-level systems to atoms with multi-level ground states is investigated by means of a general simplified model and the conditions for obtaining entanglement in a steady state are analyzed qualitatively.
As specific example, the implementation of the proposed scheme in ensembles of alkali atoms is studied, where the two-level system is encoded in a multi-level ground state manifold. Due to the richer internal structure, no external electric fields or optical elements need to be employed in contrast to the setup discussed in the previous section. As explained below, suitable values $\mu_I = \mu_{II}$ and $\nu_I = \nu_{II}$ are realized naturally. In principle, it is possible to include all magnetic sublevels and all possible transitions of a particular alkali atom in the following consideration. However, rather than aiming for a complete description which takes the entire level structure of a specific atom into account, the general model used here is primarily intended to describe the underlaying physics. In Sec. 3.1.4, it is shown how additional dynamics in a multi-level system can be taken into account by means of this simplified model which allows one to describe the physical effects with a small set of parameters while capturing all relevant features. Below, the attainable degree of entanglement is estimated.

Including multi-level dynamics

In the following, encoding of a two-level subsystem in a multi-level ground state is considered. For example, the ground state of alkali atoms with nuclear spin I is split in two manifolds with total angular momentum $F = I + 1/2$ and $F' = I - 1/2$ respectively. The relevant two-level subsystem can be encoded in the two outermost states of the $F = I + 1/2$ ground state manifold such that $|\uparrow\rangle \equiv |F, \pm F\rangle$ and $|\downarrow\rangle \equiv |F, \pm(F-1)\rangle$ in the first/second ensemble.
In general, the maximum attainable amount of entanglement $\xi^{\rm ideal} = (|\mu| - |\nu|)^2$ is determined by the different rates $\mu^2\Gamma$ and $\nu^2\Gamma$ at which probe-field induced transitions $|\downarrow\rangle \rightarrow |\uparrow\rangle$ and $|\uparrow\rangle \rightarrow |\downarrow\rangle$ occur. The values of the parameters μ and ν depend on the multi-level structure of the excited states as well as on polarization and detuning of the applied laser field. This can be illustrated by considering the off-resonant probing of ^{133}Cs atoms on the D_2 line using the setup shown in Fig. 3.1a. $\hat{\mathbf{y}}$-polarized probe light which propagates along $\hat{\mathbf{z}}$, interacts successively with two Cs ensembles in $\hat{\mathbf{x}}$-oriented magnetic fields. It is assumed that the applied magnetic fields are weak ($B \approx 1$Gauss), such that the Lar-

mor splitting $\Omega \approx 300$kHz is much smaller than the fine structure splitting of excited states. The first ensemble is strongly spin polarized along the orientation of the magnetic field, while the second ensemble is polarized antiparallel. As explained in Sec. 2.1.2 and shown in Fig. 2.2, the passive and the active part of the interaction involve different the upper levels. Taking the different Clebsch-Gordan coefficients into account, one obtains $Z = (\mu - \nu)^{-1} = 2.3$ for blue detuning $\Delta = 700$MHz with respect to the $F = 5$ manifold of $6P_{3/2}$. (Both parameters, μ and ν, are positive). Alternatively, $\hat{\mathbf{x}}$-polarized probe light can be used in combination with red detuning. Both variants are possible; for the reminder of this subsection, $\hat{\mathbf{x}}$-polarized probe fields will be considered.
More generally, the multi-level structure of excited states affects only the value of ξ^{ideal}. The multi-level character of the ground state leads to additional dynamics that needs to be taken into account. Firstly, atoms can leave the relevant two-level subsystem. While matter and light interact, atoms redistribute or are lost to other groundstate manifolds. Therefore, the atomic population in the two-level subsystem is continually reduced. This is accounted for by introducing a time- dependent population $N_2(t)$ and including the effect accordingly in the corresponding polarization $P_2(t)$. The subscript "2" emphasizes that these quantities are defined with respect to the two-level subsystem $\{|\uparrow\rangle, |\downarrow\rangle\}$. In order to calculate $N_2(t)$ and $P_2(t)$, a general model is introduced which allows one to analyze the realization of the proposed scheme in atoms with multi-level ground states. A high degree of population and polarization with respect to the two-level subsystem is required in the process of generating long-lived entanglement. Therefore $\sigma_\pm$ polarized pump and repump fields have to be applied. These additional fields induce transitions with $\Delta m_F = +1$ in the first ensemble and transitions with $\Delta m_F = -1$ in the second one. For alkali ensembles, pump fields drive transitions within the manifold $F = I + 1/2$ while repump fields transfer atoms in $F' = I - 1/2$ back to $F = I + 1/2$. In the desired case of high polarization with respect to the two outermost states, the atomic population in sublevels with $F = I + \frac{1}{2}$, $m_F < F - 1$ ($m_F > -F + 1$) in the first (second) ensemble can be neglected. In this regime, it is sufficient to restrict the description to three states, $|\uparrow\rangle$, $|\downarrow\rangle$ and $|h\rangle$, where $|h\rangle \equiv |F', F'\rangle$ for the first and $|h\rangle \equiv |F', -F'\rangle$ for the second ensemble. Finally, one has to distinguish between spin operators which refer to the relevant two-level subsystem and experimentally measurable quantities which are defined with respect to $F = I + 1/2$. For clarity, operators referring to the full multi-level structure are labelled with the subscript "exp". The longitudinal spin of each ensemble is given by

$$J_{x,\text{exp}} = \sum_{i=1}^{N} \sum_{m=-F}^{F} m |m\rangle_i\langle m| \approx \sum_{i=1}^{N} (F|\uparrow\rangle_i\langle\uparrow| + (F-1)|\downarrow\rangle_i\langle\downarrow|) = J_{x,2} + \frac{2F-1}{2} N_2(t), \quad (3.12)$$

where $N_2 = \sum_{i=1}^{N} (|\uparrow\rangle_i\langle\uparrow| + |\downarrow\rangle_i\langle\downarrow|)$. For transverse spin components,

$$J_{y,\text{exp}} = \frac{1}{2} \sum_{i=1}^{N} \sum_{m=-F}^{F} \sqrt{F(F+1) - m(m+1)} (|m+1\rangle_i\langle m| + |m\rangle_i\langle m+1|) \approx \sqrt{2F} J_{y,2}, \quad (3.13)$$

such that

$$\Sigma_{J,\text{exp}} = 2F\Sigma_{J,2} + 2(2F-1)N_\downarrow, \quad (3.14)$$

with $N_\downarrow = \sum_{i=1}^{N} |\downarrow\rangle_i\langle\downarrow|$.

Dissipatively driven entanglement between two alkali ensembles

In the following, the calculation of the entanglement which can be produced in the described setting is outlined and the time evolution of $\xi_{\mathrm{exp}}(t)$ is computed. The master equation governing the evolution of the atomic system according to the general model outlined in Sec. 3.1.4, as well as details of the calculation summed up below, can be found in App. B.5. Atomic populations $N_\uparrow = \sum_{i=1}^{N} |\uparrow\rangle_i\langle\uparrow|$, $N_\downarrow = \sum_{i=1}^{N} |\downarrow\rangle_i\langle\downarrow|$ and $N_h = \sum_{i=1}^{N} |h\rangle_i\langle h|$ can be calculated using the rate equations

$$d_t \begin{pmatrix} N_\uparrow(t) \\ N_\downarrow(t) \\ N_h(t) \end{pmatrix} = M \begin{pmatrix} N_\uparrow(t) \\ N_\downarrow(t) \\ N_h(t) \end{pmatrix}, \tag{3.15}$$

where

$$M = \begin{pmatrix} -(\Gamma_{\uparrow\downarrow} + \Gamma_{\uparrow h}) & \Gamma_{\downarrow\uparrow} & \Gamma_{h\uparrow} \\ \Gamma_{\uparrow\downarrow} & -(\Gamma_{\downarrow\uparrow} + \Gamma_{\downarrow h}) & \Gamma_{h\downarrow} \\ \Gamma_{\uparrow h} & \Gamma_{\downarrow h} & -2\left(\Gamma_{h\uparrow + \Gamma_{h\downarrow}}\right) \end{pmatrix}.$$

Γ_{ab} is the single-particle rate for the transition $|a\rangle \rightarrow |b\rangle$. If the transition rates are known, the number of atoms in the relevant two-level subsystem $N_2(t) = N_\uparrow + N_\downarrow$ and the polarization $P_2(t) = (N_\uparrow - N_\downarrow)/N_2(t)$ can be directly computed. Based on this result, the time evolution of $\Sigma_{J,2} = \mathrm{var}\,(J_{y,I} + J_{y,II})_2 + \mathrm{var}\,(J_{z,I} - J_{z,II})_2$ can be calculated. Again, the situation exhibits two different time scales. The decay collective of $\Sigma_{J,2}$ is fast compared to the evolution of $N_2(t)$ and $P_2(t)$. A calculation analogous to the one described in App. B.4 leads to

$$\Sigma_{J,2} = N_2(0) e^{-\left(\bar{\Gamma} + d(t)\Gamma P_2(t)\right)t} + N_2(t) \frac{\bar{\Gamma} + d(t)\Gamma P_2(t)^2\,(\mu-\nu)^2}{\bar{\Gamma} + d(t)\Gamma P_2(t)} \left(1 - e^{-\left(\bar{\Gamma} + d(t)\Gamma P_2(t)\right)t}\right), \tag{3.16}$$

with $d(t) = dN_2(t)/N$ and $\bar{\Gamma} = \Gamma_{\uparrow\downarrow} + \Gamma_{\downarrow\uparrow} + \Gamma_{\uparrow h} + \Gamma_{\downarrow h} + \Gamma_{\uparrow\uparrow} + \Gamma_{\downarrow\downarrow} + \Gamma_{\mathrm{d}}^{\mathrm{add}}$, where $\Gamma_{\mathrm{d}}^{\mathrm{add}}$ accounts for non-radiative dephasing. On time scales which are long compared to the fast desired dynamics (but short enough to avoid profuse depletion of the relevant two-level subsystem, such that $N_2(t) \gg 1$ is guaranteed), $\Sigma_{J,2}$ is given by the long-time (lt) solution

$$\Sigma_{J,2}^{\mathrm{lt}} = N_2(t) \frac{\bar{\Gamma} + d(t)\Gamma P_2(t)^2\,(\mu-\nu)^2}{\bar{\Gamma} + d(t)\Gamma P_2(t)}. \tag{3.17}$$

Now, this result is related to experimentally measurable quantities. Inserting Eqs. (3.12), (3.13), (3.14) and (3.17) into the definition $\xi_{\mathrm{exp}} = \Sigma_{J,\mathrm{exp}}/\left(2\,|\langle J_x\rangle_{\mathrm{exp}}|\right)$ yields

$$\xi_{\mathrm{exp}}^{\mathrm{lt}} = \frac{\bar{\Gamma} + d(t)\Gamma P_2(t)^2\,(\mu-\nu)^2}{\bar{\Gamma} + d(t)\Gamma P_2(t)} \frac{2F}{P_2(t) + 2F - 1} + \frac{N_\downarrow(t)}{N_2(t)} \frac{2(2F-1)}{P_2(t) + 2F - 1}. \tag{3.18}$$

This long-time solution is a generalization of Eq. (3.5) which takes multi-level dynamics into account. Particle losses result in a decrease in $d(t)$ and $P_2(t)$. If transitions out of the two-level subsystem can be counteracted efficiently by pump- and repump-fields, a true entangled steady state can be reached. Otherwise, a quasi steady state is produced. These

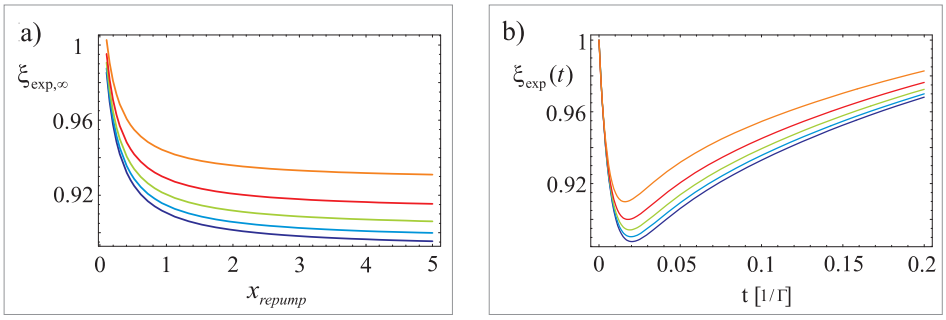

Figure 3.3: Entanglement between ^{133}Cs ensembles with optical depth $d = 30$ for blue detuned probe light ($\Delta = 700$MHz). a) Steady state entanglement $\xi_{\mathrm{exp},\infty}$ versus strength of the repump fields x_{repump} (see Sec. 3.1.4 and App. B.6) for different values for the non-radiative dephasing rate Γ_d^{add}. The curves correspond in ascending order to $\Gamma_d^{\mathrm{add}} = 0$ (violet), $\Gamma_d^{\mathrm{add}} = 2$ (blue), $\Gamma_d^{\mathrm{add}} = 5$ (green), $\Gamma_d^{\mathrm{add}} = 10$ (red) and $\Gamma_d^{\mathrm{add}} = 20$ (orange). b) Entanglement versus time in units $1/\Gamma$ in the absence of repump fields ($x_{\mathrm{repump}} = 0$; all other parameters take values as in a). The fast entangling dynamics results in a drop in $\xi_{\mathrm{exp}}(t)$ (indicating the creation of an inseparable state), but since particle losses are not counteracted by repump-fields, this additional slow dynamics eventually causes $\xi_{\mathrm{exp}}(t)$ to rise. Hence, a quasi steady state is produced. The behavior on long time scales is determined by the stationary state given by Eq. (3.12) superposed by slow multi-level dynamics.

two cases are illustrated in Figs. 3.3a and 3.3b respectively using the concrete example of ^{133}Cs ensembles (F=4) at room temperature. Fig. 3.3a shows the amount of steady state entanglement generated in case of sufficient repump power. More specifically, the depicted curves represent solutions for different values of $\Gamma_{\mathrm{d}}^{\mathrm{add}}$ versus the repump parameter x_{repump}, starting from $x_{\mathrm{repump}} = 0.01$. The repump parameter x_{repump} quantifies the strength of the applied repump fields and is given by the ratio $x_{\mathrm{repump}} = \Omega^2_{\mathrm{repump}}/\Omega^2_{\mathrm{pump,opt}}$, where $\Omega^2_{\mathrm{pump,opt}}$ is the optimal Rabi frequency that can be chosen for the pump field within the validity of the model considered here ($\Omega^2_{\mathrm{pump,opt}}$ is the minimal Rabi frequency of the pump field leading to $N_{\uparrow,\infty}/N_{2,\infty} \geq 0.95$ in the steady state). Details of the calculations leading to the plots can be found in App. B.6. Fig. 3.3b illustrates the case, where particle losses dominate the evolution of $\xi_{\mathrm{exp}}(t)$. The curves in this figure show the amount of entanglement generated in the absence of repump fields as a function of time in ms. For short times the time evolution is governed by the desired dynamics within the relevant two-level subsystem and reaches quickly an entangled steady state. For longer times this stable state with respect to the entangling dynamics is superposed by the slow additional evolution imposed by the multi-level structure of the ground state. The fast desired dynamics entangles the collective spins of both ensembles, while particle losses cause a slow but continuing shortening of the spins. In this sense, Fig. 3.3b shows the creation of a quasi-steady state. For $t > 0.05/\Gamma$, the time evolution is given by Eq. (3.19), that is, the time evolution is solely determined by particle loss-related dynamics.
In this section, emphasis is put on the general, implementation independent limitations of the proposed scheme imposed by radiative transitions. These undesired processes

are characteristic for a given level scheme and intimately linked to the tradeoff between enhanced entangling dynamics due to increased probe, - or pump power and added noise. Depending on the concrete experimental realization, other undesired processes impairing the performance of the proposed scheme can occur like for example spin flips due to collisions. Atomic transitions and additional dephasing due to collisions with the walls can be taken into account by including terms of the type

$$\begin{aligned} d_t\rho(t) &= \frac{\Gamma_{\text{col}}}{2}\sum_{i=1}^{N}\Big(\sigma_{I,i}\rho(t)\sigma_{I,i}^{\dagger}+\sigma_{II,i}\rho(t)\sigma_{II,i}^{\dagger}\Big) \\ &+ \frac{\Gamma_{\text{col}}}{2}\sum_{i=1}^{N}\Big(\sigma_{I,i}^{\dagger}\rho(t)\sigma_{I,i}+\sigma_{II,i}^{\dagger}\rho(t)\sigma_{II,i}\Big) \\ &+ \frac{\Gamma_{\text{col}}}{2}\sum_{i=1}^{N}\left(\sigma_{\downarrow\downarrow,I,i}\rho(t)\sigma_{\downarrow\downarrow,I,i}+\sigma_{\downarrow\downarrow,II,i}\rho(t)\sigma_{\downarrow\downarrow,II,i}\right) \\ &+ \ldots \end{aligned}$$

to the master equation. Since the thermal energy of atoms is typically much larger than the atomic level splittings, the same collisional rate Γ_{col} can be assumed for all atomic transitions. The value of Γ_{col} has to be determined phenomenologically for the specific experimental setup under consideration (compare [III]).

3.1.5 Experimental realization

In this section, we describe the experimental realization of the proposed scheme. In the experiment [III], entanglement has been generated purely dissipatively between two Cesium ensembles and has been maintained for 0.04s at room temperature. Moreover, a hybrid approach has been implemented, which combines the dissipative entangling mechanism with continuous measurements of the light field, which allowed for the realization of an entangled steady state. Below, we briefly describe the experimental setting, summarize the results and explain the theoretical fits to the measured data. In the last part of this section, we show how measurements on the light field can improve the dissipative generation of entanglement in the presence of noise sources.

Experimental setting

The experiment is performed using two dilute ^{133}Cs gas samples in 2.2cm cubic cells containing about 10^{12} atoms each, separated by 0.5m as described in [12]. The two-level system $|\uparrow\rangle_{I/II}$ and $|\downarrow\rangle_{I/II}$ is encoded in the $6S_{1/2}$ ground state sublevels $|F=4,m_F=\pm4\rangle$ and $|F=4,m_F=\pm3\rangle$ in the first and second ensemble respectively. A bias magnetic field of 0.9G leads to a Zeeman splitting of $\Omega = 322$kHz. The anti-relaxation coating of the cell walls and careful magnetic shielding [17] provide a non-radiative decoherence time for populations and coherences of $T_1 \approx 130$ms and $T_2 \approx 40$ms. The two ensembles are initialized in the states $|4,\pm4\rangle$ with orientation up to $P = 0.998(3)$ by applying a pump laser polarizing the $F = 4$ manifold and a laser repumping atoms from $F = 3$ to $F = 4$ for 10 to 50ms as shown in Fig. 3.4a. The driving laser is $\hat{\mathbf{y}}$ polarized and blue

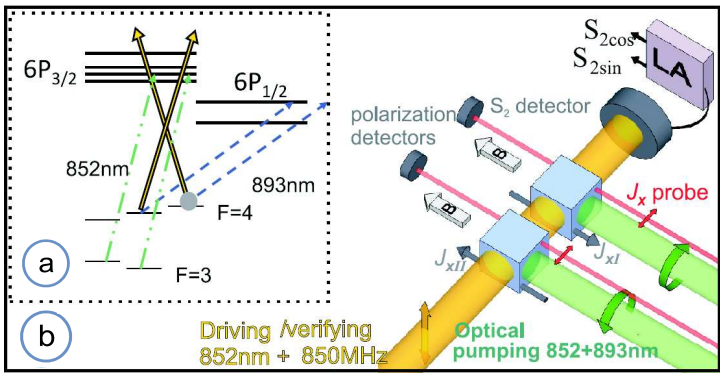

Figure 3.4: Optical pumping scheme and experimental setup. a) Atomic spin states and applied laser fields. The entangling driving field is represented by yellow arrows. Grey dashed and green dash-dotted lines represent pump and repump fields respectively. b) Geometry of the experiment. The (dc) polarization detectors on the left measure the Faraday rotation angle, which is proportional to the macroscopic spin J_x. The (ac) S_2 detector signal processed by the lock-in amplifier (LA) is used to determine the transverse atomic quantum spin components $J_{y,z}$ as described in the text.

detuned by 850MHz from the $F = 4 \leftrightarrow F = 5$ transition of the D_2 line corresponding to $(\mu - \nu)^2 = 0.16$.

The nonlocal atomic state variance $\xi = \Sigma_{J_{\rm exp}} / \left(2|\langle J_{x,\rm exp}\rangle|\right)$ is inferred, and the entanglement condition $\xi < 1$ is verified by a polarization measurement on the light transmitted through the two ensembles (see Fig. 3.4b). In this setup, the same laser is used to create and to verify the entanglement which significantly simplifies the experiment. In the period $t < T$, up to a variable time T (see pulse sequence in Fig. 3.5b) the laser serves only as driving field for the entangling dissipative process. The results of the measurements on the transmitted light are not used, which is equivalent to tracing out the light field. Beginning at $t = T$, the corresponding mode of the transmitted light field is used for the determination of the atomic state at time T [12, 169–171]. The particular mapping employed in the experiment is described by the input-output relations for atomic and light operators before and after the interaction as explained in Sec. 2.1.3 (a detailed derivation of the input-output relations can be found in App. D.1) and has also been utilized in several other contexts [VII], [17, 18]. As indicated in Fig. 3.4b and Fig. 3.5e, the Stokes operator $S_2 = \frac{1}{2}\left(n_{+45} - n_{-45}\right)$ is measured, where n_{+45} is the number of photons in ± 45 polarization. More specifically, the $\sin(\Omega t)$ and $\cos(\Omega t)$ modulated components of S_2 are determined, where Ω is the Larmor frequency. This fast oscillating signal is evaluated according to a slowly varying (exponential) envelope function $h(t)$, which corresponds to measuring the quantity $x_{h,sin/cos}$ introduced in Sec. 4.1.4 (see Eq. (2.6)). This way, Eq. (2.10) allows one to infer the atomic variance from the measured signal in the ideal case. Atomic decay can be included as described in App. D.1.2. The measurement of the atomic EPR variance $\Sigma_{J_{\rm exp}}(T)$ at time T as well as the specific atomic noise reconstruction method is explained in detail in [III]. The calibration and verification of the reconstruction of the atomic state (compare [III]) shows that the measurement of ξ is

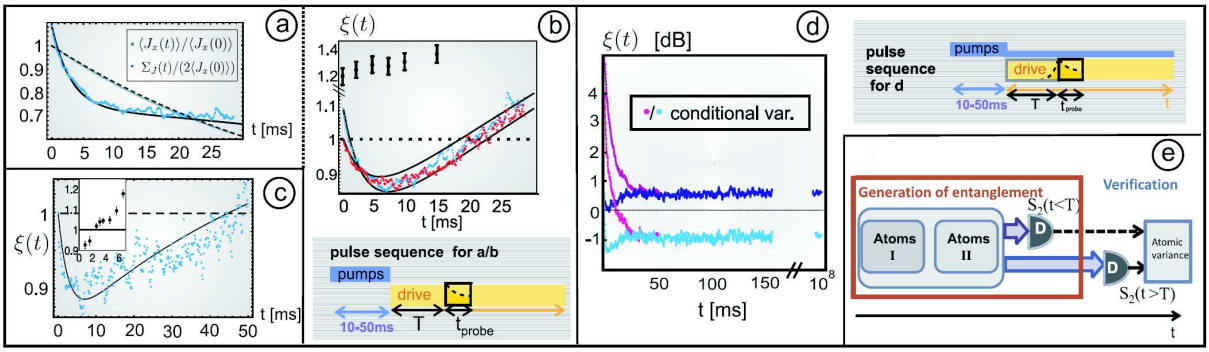

Figure 3.5: Experimental results a) Time evolution of $\Sigma_J(t)/\left(2|\langle J_x(0)\rangle|\right)$ (blue) and $\langle J_x(t)\rangle/\langle J_x(0)\rangle$ (grey). The theoretical fits (full and dashed black line) are based on the parameters $d = 55$, $\Gamma_{\rm col} = 0.002{\rm ms}^{-1}$, $\tilde{\Gamma} = 0.193{\rm ms}^{-1}$ and $\Gamma = 0.002{\rm ms}^{-1}$ (see main text). b) Entanglement $\xi(t)$ versus time in ms. Blue data points correspond to the results shown in a). Orange data points are obtained for a lower optical depth ($d = 35$). The other parameters in the fits take the same values as in a). The pulse sequence is shown below. The data taken in the absence of the driving field (black points) show no entanglement. c) Dissipative entanglement generation in the presence of a pump field with pump rate $\Gamma_{\rm pump} = 0.168{\rm ms}^{-1}$. $d = 37$, the fitting parameters $\Gamma_{\rm col}$ and Γ take the same values as in a) and $\tilde{\Gamma} = 0.233{\rm ms}^{-1}$. The inset shows the evolution of $\xi(t)$ after the driving field is switched off. d) Entanglement $\xi(t)$ for different initial conditions. The upper curves show a purely dissipative evolution. The lower curves show the measurement assisted entanglement. Points on the right represent an average over measurements of one hour where atoms were kept in a steady state. e) Entanglement generation and verification. The signal from the detector D for times $t > T$ is used for verification of entanglement in (a-c). In d) the signal taken at $t < T$ is sent to the verifier as additional information (see main text).

reliable within the uncertainty of $\pm 4\%$ arising from uncertainty in the measurements of the coupling strength, the detection efficiency and the shot noise of light.

Experimental results

In the first set of experiments, entanglement is generated purely dissipatively. In the first series of this set, the pump- and repump fields are turned off at time $t = 0$ (Fig. 3.5a,b) and the driving (entangling) laser is turned on. The single atom spontaneous emission reduces T_2 to 6ms and T_1 to 34ms. This decoherence has been considered the fundamental limitation for the entanglement generated by measurements [12]. Here, the collective entangling dissipative mechanism due to forward scattering[14] dominates over the single atom decoherence and leads to a rapid reduction of $\Sigma_{J_{\rm exp}}(t)$. Fig. 3.5a shows the time evolution of $\Sigma_{J_{\rm exp}}(t)$ normalized to $2|\langle J_{x,{\rm exp}}(0)\rangle|$. For a coherent spin state (CSS) $\xi = 1$. $\Sigma_{\rm CSS} = 2|\langle J_{x,{\rm exp}}\rangle|$ defines the projection noise (PN) level, below which lies the noise level

[14] Note that the generation of entanglement cannot be explained by the interaction of photons emitted by the first ensemble with the second one, which is negligible in the accessible parameter regime.

of entangled states. The dynamics of $2|\langle J_{x,\mathrm{exp}}(t)\rangle|$ due to single atom spontaneous emission and collisions on the slow time scale of T_1 is also shown in Fig. 3.5a. Fig. 3.5b displays the time evolution of entanglement for two different values of the optical depth $d = 35$ and $d = 55$. Note that for $d = 55$, the entanglement generated by dissipation can be created and maintained even though the initial atomic noise $\Sigma_{J_{\mathrm{exp}}}(0)$ is significantly above the PN level. The life time of entanglement of 0.015s is several times longer than the best previous results obtained for measurement induced entanglement [12,66] and much longer than T_2. For comparison, if the driving (entangling) laser is off during $0 < t < T$ and is turned on only at $t = T$ to measure the atomic state, $\xi(T)$ predictably stays above the PN level (black points in Fig. 3.5b). In this series of experiments, entanglement is created in a quasi-steady state rather than in a steady state, as would be the case for a true two-level atomic ground state. On the time scale of T_1, atoms are lost to other magnetic sublevels of $F = 4$ and to the level $F = 3$, which leads to a decreasing population and modified polarization in the relevant two-level subsystem as explained in Sec. 3.1.4. This causes the eventual extinction of entanglement as described well by the theoretical fits shown in Fig. 3.5a,b where a simplified model is used, which is described below.
In the next series of experiments, a resonant pumping field (see Fig. 3.4a) of optimal strength is applied continuously during the entangling period $t > 0$ (Fig. 3.5c). Remarkably, this incoherent process does not suppress the generation of entanglement, but leads to an improvement. The increase in entanglement lifetime to 0.04s is due to the pumping of atoms which have decayed to sublevels with $|m_F| < 3$ and thus lead to an increase in the atomic noise contribution, back to $|m_F| = 4$ which is a dark state for the pump beam. The eventual loss of entanglement is in part due to atoms which are lost to the $F = 3$ ground state, which effectively reduces d. If the entangling mechanism is turned off, the entangled state decays in 2ms (inset in Fig. 3.5c), as expected [12].
Finally, the generation of steady state entanglement is demonstrated. To this end, a repumping field which induces transitions $F = 3 \rightarrow F = 4$ (see Fig. 3.4a) is added during the generation of entanglement. The atoms reach a steady state which is not entangled since the collective processes are not sufficiently strong to overcome the noise added by the incoherent repumping field. A calculation using the current experimental parameters shows that steady state entanglement can be achieved for $d = 100$, but this is experimentally not feasible. Therefore, we developed an alternative approach, which enables the creation of steady state entanglement using a hybrid method which combines the dissipative entangling mechanism with measurements on the light field. The measurement results are used in order to purify and therefore enhance entanglement (this is possible because the photons scattered in forward direction are not completely uncorrelated with the atoms due to single atom decoherence). In the series of experiments described above, measurements of light variables have only been used to verify the presence of entanglement. More specifically, the verification of entanglement in the atomic system at time T involves the evaluation of photonic variables corresponding to times $t > T$. Using the results of the continuous measurement on the open atomic quantum system during the interval $t < T$, the generated entanglement can be enhanced and maintained in a steady state, as is explained in more detail below. These central results are displayed in Fig. 3.5d, which shows the evolution of the variances of the purely dissipatively generated atomic state (upper curves) and the entanglement produced using the hybrid method including

dissipation and continuous measurements (lower curves). Each pair of curves corresponds to two different initial conditions. These results demonstrate that the generated steady state is independent of the initial state, and that entanglement is maintained for up to an hour, if dissipative processes are combined with measurements.

Comparison of experimental data and theoretical predictions

In the following, details regarding the theoretical fits presented in Fig. 3.5 are provided. The generated amount of entanglement $\xi(t)$ can be calculated as described in detail in Sec. 3.1.4. As explained there, the produced entanglement is given by

$$\xi_{\mathrm{exp}}(t) = \frac{8\Sigma_{J_2} + 14N_{\downarrow}(t)}{N_2(t)\,(P_2(t)+7)}. \tag{3.19}$$

The time evolution of the EPR variance Σ_{J_2} can be calculated using Eq. (3.16) if the collective decay rate ($d\Gamma$) and the effective dephasing rate ($\tilde{\Gamma}$) as well as $N_2(t)$ and $P_2(t)$ are known. In the following, we outline how these quantities can be inferred and explain the theoretical fits to the measured data shown in Fig. 3.5.
The essential features of the experiment can be described by means of the simplified model introduced in Sec. 3.1.4, which involves only the three atomic states[15] $|4,\pm4\rangle$, $|4,\pm3\rangle$ and $|h\rangle_{I/II} \equiv |3,\pm3\rangle$. Since the model is primarily intended to predict the physical effects observed in the experiment qualitatively with very few parameters, $\Gamma_{|\uparrow\rangle\rightarrow|h\rangle} \approx \Gamma_{|\downarrow\rangle\rightarrow|h\rangle} = \Gamma_{\mathrm{out}}$ and $\Gamma_{|h\rangle\rightarrow|\uparrow\rangle} \approx \Gamma_{|h\rangle\rightarrow|\downarrow\rangle} = \Gamma_{\mathrm{in}}$ is used, such that

$$\begin{aligned}
\frac{d}{dt}N_2(t) &= -\left(\Gamma_{\mathrm{out}} + 2\Gamma_{\mathrm{in}}\right)N_2(t) + 2N\Gamma_{\mathrm{in}},\\
\frac{d}{dt}\tilde{P}_2(t) &= -\left(\Gamma_{\downarrow\uparrow} + \Gamma_{\uparrow\downarrow} + \Gamma_{\mathrm{out}}\right)\tilde{P}_2(t) + \left(\Gamma_{\downarrow\uparrow} - \Gamma_{\uparrow\downarrow}\right)N_2(t)/N,
\end{aligned}$$

where $\tilde{P}_2(t) = P_2(t)N_2(t)/N$ and the abbreviations $\Gamma_{\uparrow\downarrow} = \Gamma_{|\uparrow\rangle\rightarrow|\downarrow\rangle}$ and $\Gamma_{\downarrow\uparrow} = \Gamma_{|\downarrow\rightarrow|\uparrow\rangle}$ have been used. Atomic transitions can be either induced by the driving field or be due to collisions. Since the thermal energy of atoms is much larger than the atomic level splittings, the same collisional rate Γ_{col} is assumed for all atomic transitions. Accordingly,

$$\begin{aligned}
\Gamma_{\downarrow\uparrow} &= \mu^2\,\Gamma + \Gamma_{\mathrm{col}}, \qquad \Gamma_{\mathrm{out}} = \Gamma_{\mathrm{L}}^{\mathrm{out}} + \Gamma_{\mathrm{col}},\\
\Gamma_{\uparrow\downarrow} &= \nu^2\,\Gamma + \Gamma_{\mathrm{col}}, \qquad \Gamma_{\mathrm{in}} = \Gamma_{\mathrm{col}},
\end{aligned}$$

where $\mu^2\Gamma$ and $\nu^2\Gamma$ are the driving field induced cooling and heating rate respectively. $\Gamma_{\mathrm{L}}^{\mathrm{out}}$ is the rate at which atoms leave the two-level subsystem due to radiative transitions caused by the driving field. The number of free parameters in these equations can be reduced to two, using the experimentally determined time derivative of the atomic polarization $P_{\mathrm{exp}} = \langle J_{x,\mathrm{exp}}(t)\rangle / \langle J_{x,\mathrm{exp}}(0)\rangle$ at time $t = 0$

$$\left.\frac{d}{dt}P_{\mathrm{exp}}(t)\right|_{t=0} = \frac{-\left(\Gamma_{\uparrow\downarrow} + 4\Gamma_{\mathrm{out}}\right)N_{\uparrow}(0) + \left(\Gamma_{\downarrow\uparrow} - 3\Gamma_{\mathrm{out}}\right)N_{\downarrow}(0)}{\langle J_{x,\mathrm{exp}}(0)\rangle},$$

[15] For the time scales considered here, the atomic population in other sublevels can be neglected.

where it is taken into account that the initial spin state is not perfectly polarized, but contains a small fraction of atoms in state $|4,\pm 3\rangle$. The initial populations $N_{\uparrow}(0)=0.99$, $N_{\downarrow}(0)=0.01$ and $N_{\mathrm{h}}(0)=0$ are estimated based on measurements of the orientation of the initial spin state after optical pumping. Using this constraint, $P_{\mathrm{exp}}(t)$ can be fitted using two free parameters. This way, fixed expressions for $P_2(t)$ and $N_2(t)$ are obtained. As mentioned above, the values of the collective decay rate $d\Gamma$ and the dephasing rate due to noise effects, $\tilde{\Gamma}$, have to be known in order to calculate the generated amount of entanglement as described in Sec. 3.1.4. These parameters are determined based on the measured slope of the variance $\Sigma_{J,\mathrm{exp}}(t)/\left(2|\langle J_{x,\mathrm{exp}}\rangle|\right)$ at time $t=0$ and the decay of the transverse spin. These two quantities are given by

$$\frac{d}{dt}\frac{\Sigma_{J_{\mathrm{exp}}}(t)}{2|\langle J_{x,\mathrm{exp}}(0)\rangle|}\bigg|_{t=0}=-4Nd\Gamma P_2(0)\big(1-P_2(0)/(\mu-\nu)^2\big)+7\Gamma_{\mathrm{in}}P_2(0)-7\left(\Gamma_{\mathrm{out}}+\Gamma_{\downarrow\uparrow}-\Gamma_{\uparrow\downarrow}\right)N_{\downarrow}(0),$$

and $\langle J_{y,\mathrm{exp}}(t)\rangle = e^{-\frac{1}{2}\left(\tilde{\Gamma}+d\Gamma\tilde{P}_2(t)\right)t}\langle J_{y,\mathrm{exp}}(0)\rangle$, where Eq. (3.16) and the identities relating quantities defined with respect to a two-level system to quantities defined with respect to a multi-level structure stated in Sec. 3.1.4 have been used.

Dissipative entanglement assisted by measurements

In the following, we show by means of a simple model how measurements on the light field can improve the generation of entanglement under the dissipative dynamics described above in the presence of noise sources. In order illustrate the relevant effects, we describe the atomic system in terms of the quadratures

$$x_{A,I/II} \;=\; J_{y,I/II}/\sqrt{|\langle J_{x,I/II}\rangle|}, \qquad p_{A,I/II}=J_{z,I/II}/\sqrt{|\langle J_{x,I/II}\rangle|},$$

within the Holstein-Primakoff approximation [89], as explained in Sec. 2.1.1. We include noise in the form of decay of the transverse spin components J_y and J_z at a rate γ_{extra}. We explain here the dissipative generation of entanglement assisted by measurements in terms of input-output relations, since this approach is more illustrative than the master equation formalism employed above. Both descriptions are equivalent and yield the same results. As described in Sec. 2.1.1, the light field is characterized in terms of spatially localized modes [87,88], $x_L(z)$, $p_L(z)$ with $[x_L(z),p_L(z')]=ic\delta_b(z-z')$. The spatial argument refers to the distance along the propagation direction of the light field $\hat{z}$. The spatial resolution is determined by the width of the delta function, which is on the order of c/b, where b is the frequency bandwidth of the applied classical laser field. Light and matter interact via a Faraday interaction (see Sec. 2.1.2). The corresponding input-output relations for atoms and light are given by[16]

$$\begin{pmatrix} x^{out}_{\mathrm{A,cos/sin}} \\ p^{out}_{\mathrm{A,cos/sin}} \end{pmatrix} \;=\; e^{-\frac{\kappa^2}{2Z^2}}\begin{pmatrix} x^{in}_{\mathrm{A,cos/sin}} \\ p^{in}_{\mathrm{A,cos/sin}} \end{pmatrix}+\sqrt{1-e^{-\frac{\kappa^2}{Z^2}}}\begin{pmatrix} 0 & Z \\ -1/Z & 0 \end{pmatrix}\begin{pmatrix} x^{in}_{\mathrm{cos/sin,+}} \\ p^{in}_{\mathrm{cos/sin,+}} \end{pmatrix},$$

$$\begin{pmatrix} x^{out}_{\mathrm{cos/sin,-}} \\ p^{out}_{\mathrm{cos/sin,-}} \end{pmatrix} \;=\; e^{-\frac{\kappa^2}{2Z^2}}\begin{pmatrix} x^{in}_{\mathrm{cos/sin,-}} \\ p^{in}_{\mathrm{cos/sin,-}} \end{pmatrix}+\sqrt{1-e^{-\frac{\kappa^2}{Z^2}}}\begin{pmatrix} 0 & Z \\ -1/Z & 0 \end{pmatrix}\begin{pmatrix} x^{in}_{\mathrm{A,cos/sin}} \\ p^{in}_{\mathrm{A,cos/sin}} \end{pmatrix},$$

[16] We use here the notation employed in the experiment. This notation differs from the one used in the previous part of this section by local rotations (according to the notation used in the in Sec. 3.1.1-Sec. 3.1.4, $H\propto p_Ap_L+\frac{1}{Z^2}x_Ax_L$, while here $H\propto x_Ax_L+\frac{1}{Z^2}p_Ap_L$).

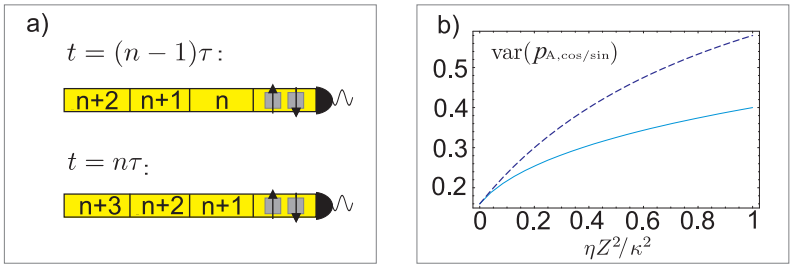

Figure 3.6: Steady state entanglement assisted by measurements. a) Illustration of the interaction of atoms and light in terms of spatially localized modes. b) Squeezed atomic variance var $(p_{\mathrm{A,cos/sin}})$ in the steady state versus the ratio $\eta Z^2/\kappa^2$ if the x-quadrature of the scattered light field is measured (full line) and in the absence of measurements (dashed line). The parameters κ^2/Z^2 and η quantify the relative strength of the rates of the desired entangling processes and the atomic decay respectively.

where the notation and definitions introduced in Sec. 2.1.3 have been used. As next step, continuous measurements on the light field are included and the corresponding time evolution of the atomic state is considered in the Schrödinger picture. The continuous interaction and measurement process shown in Fig. 3.5e (see also Fig. 3.4b) is illustrated schematically in Fig. 3.6a in a discretized way, where spatially localized light modes correspond to infinitesimally short pulses of duration $\tau \sim 1/b$, which interact successively with the atomic system. Each of these spatially localized light modes is initially in the vacuum state, such that the quantum state at time $t = n\tau$ is given by $|\Psi(t)\rangle_A|0\rangle_{L,n+1}$, where $|\Psi(t)\rangle_A$ denotes the atomic state at time t. Then, atoms and light are subject to an entangling interaction resulting in the quantum state $e^{-iH\tau}|\Psi(t)\rangle_A|0\rangle_{L,n+1}$. Finally, the x-quadrature of the light field is measured yielding the measurement outcome x_n, such that $|\Psi(t+\tau)\rangle_A = \frac{1}{\sqrt{P(x_n)}}{}_{\mathrm{L,n+1}}\langle x_n|e^{-iH\tau}|0\rangle_{L,n+1}|\Psi(t)\rangle_A$, where $P(x_n)$ is the probability to obtain the result x_n. The resulting expression can be expanded up to first order in the parameter τ yielding a differential equation for the time evolution of the atomic system. The atomic state obtained after a measurement depends on the measurement outcome x_n. However, since the states, interactions and measurements considered here are Gaussian, the entanglement of the resulting state is completely determined by the atomic variance var $(p_{\mathrm{A,cos/sin}})$, which does not depend on x_n [172]. Therefore, the resulting entanglement is independent of the measurement outcome. If the measurement results are traced out $(\rho(t+\tau) = \sum_{x_n} M_n\rho(t)M_n^\dagger$, where $M_n = {}_{L,n+1}\langle x_n|e^{-iH\tau}|0\rangle_{L,n+1})$, and the resulting expression is evaluated to first order in τ, the master equation used in the previous sections is recovered.

The whole process can be conveniently described by means of the Gaussian formalism, where atomic states are expressed in terms of their covariance matrix Γ_c, and displacement vector $\mathbf{D}$, which display the second moments (variances and covariances) and first moments (mean values) of the system respectively, $|\Psi(t)\rangle_{\mathrm{A}} = |\Gamma_c(t), \mathbf{D}(t)\rangle$. In particular, this formalism allows one to calculate easily the variances of atomic quadratures after the Gaussian measurement of the x-quadrature of the light field, var $(p_{\mathrm{A,cos/sin}})_{\mathrm{cond}}$ at the end

of each time step depending on the variance prior to the measurement

$$\mathrm{var}\left(p_{\mathrm{A,cos/sin}}\right)_{\mathrm{cond}} = \mathrm{var}(p_{\mathrm{A,cos/sin}}) - \frac{\langle p_{\mathrm{A,cos/sin}} x_{\mathrm{L,cos/sin}} + x_{\mathrm{L,cos/sin}} p_{\mathrm{A,cos/sin}}\rangle^2}{4\mathrm{var}(x_{\mathrm{L,cos/sin}})}, \tag{3.20}$$

where $x_{\mathrm{L,cos/sin}}$ and $p_{\mathrm{L,cos/sin}}$ refer to the localized light mode interacting with the ensemble in the n^{th} time step and $\kappa^2\tau/(Z^2T) \ll 1$ is assumed. This way, a differential equation for the squeezed atomic variances is derived. In the ideal case,

$$\mathrm{var}\left(p_{\mathrm{A,cos/sin}}\right)_{\mathrm{cond}}(t+\tau) = \mathrm{var}\left(p_{\mathrm{A,cos/sin}}\right)_{\mathrm{cond}}(t) + \mathrm{var}\left(p_{\mathrm{A,cos/sin}}\right)_{\mathrm{cond}}(t)\left(1 - \mathrm{var}\left(p_{\mathrm{A,cos/sin}}\right)(t) Z^2\right)\frac{\kappa^2\tau}{2Z^2T},$$

which yields

$$\mathrm{var}\left(p_{\mathrm{A,cos/sin}}\right)_{\mathrm{cond}}(t) = \frac{1}{e^{-\frac{\kappa^2 t}{2Z^2T}}\ \left(\mathrm{var}\left(p_{\mathrm{A,cos/sin}}\right)(0)\right)^{-1} + Z^2\left(1 - e^{-\frac{\kappa^2 t}{2Z^2T}}\right)},$$

whereas in the absence of measurements,

$$\mathrm{var}\left(p_{\mathrm{A,cos/sin}}\right)(t) = e^{-\frac{\kappa^2 t}{2Z^2T}}\ \mathrm{var}\left(p_{\mathrm{A,cos/sin}}\right)(0) + \frac{1}{Z^2}\left(1 - e^{-\frac{\kappa^2 t}{2Z^2T}}\right).$$

Both time evolutions result in a steady state with $\mathrm{var}\left(p_{c/s}\right)_\infty = 1/Z^2 = (\mu-\nu)^2$, since atoms and light decouple for $t \to \infty$. Accordingly, the steady state entanglement can not be improved by means of measurements on the light field in the ideal case. The situation is different in the presence of noise sources, which prevent the decoupling of atoms and light. In this case, residual correlations between atoms and light persist in the steady state and measurements on the light field can be used to improve the entanglement. Here, this effect is illustrated by including atomic transverse decay[17] at a rate η/T. If the x-quadrature of the scattered light field is measured, one obtains

$$\xi_{\mathrm{cond},\infty} = \frac{1}{2Z^2}\left(1 - \frac{\eta Z^2}{\kappa^2} + \sqrt{\left(1 - \frac{\eta Z^2}{\kappa^2}\right)^2 + 4Z^2\,\frac{\eta Z^2}{\kappa^2}}\right).$$

Fig. 3.6b shows that for $\eta > 0$, the steady state entanglement described by this equation is higher than the steady state if no measurements are performed, which is given by

$$\xi_\infty = \frac{\frac{\kappa^2}{Z^4} + \eta}{\frac{\kappa^2}{Z^2} + \eta}.$$

Note that in principle, all measurement results $x(t)$ obtained during the continuous measurement procedure could be used to perform feedback operations which stabilize the

[17] In this case, the Hamiltonian is given by $H = H_{\cos} + H_{\sin}$, where $H_{\cos/\sin} = H^{\mathrm{ent}}_{\cos/\sin} + H^{\mathrm{noise}}_{\cos/\sin}$. $H^{\mathrm{ent}}_{\cos/\sin} = \frac{\kappa}{\sqrt{T}}\left(\frac{1}{Z^2}x_{\mathrm{A,cos/sin}}x_{\mathrm{L,cos/sin}} + p_{\mathrm{A,cos/sin}}p_{\mathrm{L,cos/sin}}\right)$ corresponds to the desired entangling interaction, while $H^{\mathrm{noise}}_{\cos/\sin} = \sqrt{\frac{\eta}{T}}\left(x_{\mathrm{A,cos/sin}}x_{\mathrm{N,cos/sin}} + p_{\mathrm{A,cos/sin}}p_{\mathrm{N,cos/sin}}\right)$ describes transverse dephasing at a rate η/T. $x_{\mathrm{N,cos/sin}}$ and $p_{\mathrm{N,cos/sin}}$ refer to noise modes with $\langle x_{\mathrm{N,cos/sin}}(t)\rangle = \langle p_{\mathrm{N,cos/sin}}(t)\rangle = 0$, $\langle x_{\mathrm{N,cos/sin}}(t)x_{\mathrm{N,cos/sin}}(t')\rangle = \langle p_{\mathrm{N,cos/sin}}(t)p_{\mathrm{N,cos/sin}}(t')\rangle = \delta(t-t')$ and $[x_{\mathrm{N,cos/sin}}, p_{\mathrm{N,sin/cos}}] = 0$.

atomic state at a certain position in phase space. However, this is not necessary here, since the atomic quantum state at time t depends only on the recent history of the measurements, i.e. on $x(t')$ for $t_{ss} \leq t' \leq t$, where t_{ss} is the time it takes to reach the steady state. For the dissipative processes considered here, the atomic state $\rho(t)$ is memoryless regarding events which occurred in a time interval longer than t_{ss}. Thus, only measurement results obtained during a fixed time interval t_{ss}, which is independent of t are needed to localize the atomic state in phase space.
Experimentally, the conditional variance $\mathrm{var}\left(p_{\mathrm{A,cos/sin}}\right)_{\mathrm{cond}}$ at time $t = T$ is inferred by measuring continuously the x-quadrature of the light field for $t < T$ (see Fig. 3.5e). The measured value of the photonic x-quadrature, $x_{L,\mathrm{cos/sin}}(t < T)$ is fed back[18] to the atomic variable $p_{A,\mathrm{cos/sin}}$ with feedback gain α yielding $\mathrm{var}\left(p_{\mathrm{A,cos/sin}}\right)_{\mathrm{cond}} = \mathrm{var}\left(p_{\mathrm{A,cos/sin}} - \alpha x_{\mathrm{L,cos/sin}}\right)$. The feedback gain and the exponential envelope function of the read-out mode are optimized to yield the maximal noise reduction (see [III] for details). Using the formalism introduced above, it can be shown that for optimal feedback parameter α, $\mathrm{var}\left(p_{\mathrm{A,cos/sin}} - \alpha x_{\mathrm{L,cos/sin}}\right)$ is identical to Eq. (3.20).

3.1.6 Concluding remarks

In summary, a technique for entangling two mesoscopic atomic ensembles at room temperature which are separated by a macroscopic distance is proposed. The core idea is to engineer the coupling of the atomic system to its environment in such a way that the steady state of the dissipative time evolution is the desired inseparable state. As entanglement is produced in the steady state of the system, it is long-lived and immune to noise.
The reservoir consists of the common modes of the electromagnetic field and the coupling of the bath to the system can be controlled by means of laser- and magnetic fields. A detailed theoretical description including dipole-dipole interactions for two-level systems is provided and it is shown that the imaginary parts of the master equation (collective Lamb shifts) are negligible. Hence, light-induced collisions do not play an important role in the setup considered here. The proposed scheme for generation of entanglement by dissipation is analyzed for two-level systems and complemented by considering the implementation in multi-level ground states. The scheme has been experimentally implemented leading to an order of magnitude improvement in the entanglement life-time compared to standard methods. Aside from the purely dissipative creation of entanglement, the generation of an inseparable steady state could be observed for up to an hour by supplementing the dissipative mechanism with measurements on the light field. Moreover, the independence of the produced entangled state from the initial state has been experimentally demonstrated.
Future directions include the transfer of the ideas presented here to other systems, where a quadratic interaction involving two sideband modes can be realized. The system may either be described by bosonic modes (compare Sec. 3.1.2 and App. B.2) or spin degrees of freedom. If the Hamiltonian corresponding to the interaction between this system and light can be decomposed into an active and a passive part such that each part involves

[18] In principle, it is not necessary to carry out the feedback operation as long as the measurement result is known.

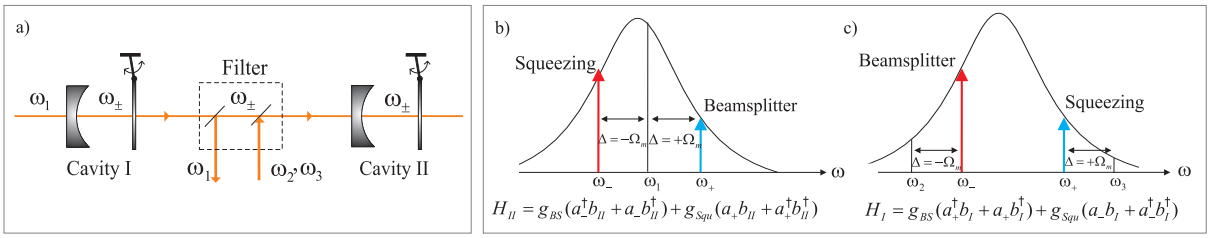

Figure 3.7: Creation of entanglement between two optomechanical resonators. a) A driving field with frequency ω_1 interacts with the first oscillator and causes scattering into the upper/lower sideband centered around the frequency $\omega_\pm = \omega_1 \pm \Omega_\mathrm{m}$ as shown in b). Transmitted light passes through a filter which exchanges the driving fields, such that the laser field at frequency ω_1 is replaced by driving fields with frequencies ω_2 and ω_3, while the quantum fields which are centered at $\omega_\pm$, remain unchanged. Panels b) and c) illustrate the interaction of light with the first and second nanomechanical mirrors as explained in the text. Here, mechanical modes are described by bosonic annihilation operators b_I and b_{II} . Photonic modes corresponding to narrow sidebands centered around the frequencies $\omega_\pm = \omega_1 \pm \Omega_\mathrm{m}$ are described by operators a_+ and a_-.

one sideband, as in Hamiltonian (3.6), dissipatively driven entanglement can be generated using the method described here. Optomechanical resonators [173–175] interacting with light are promising candidates. A possible implementation of the proposed scheme is illustrated in Fig. 3.7. In this setup, two movable nanomechanical mirros which each constitute one end of an optical cavity are driven into an entangled state[19]. Both mechanical resonators are assumed to have the same resonance frequency Ω_m and cavities with a broad linewidth $\delta_\mathrm{c} > \Omega_\mathrm{m}$, and very narrow sideband modes are considered (see Fig. 3.7b,c). If such an optomechanical system is driven by a strong pump laser, the linearized radiation-pressure Hamiltonian gives rise to a passive (beam-splitter) interaction for positive detuning between cavity and pump-frequency H_pas [176, 177]. The resulting effective interaction is active, corresponding to a squeezing Hamiltonian H_act for negative detuning $\Delta < 0$. The corresponding effective optomechanical coupling rates g_BS, g_squ can be adjusted by tuning the intensities of the driving fields [178]. Hence, the quadratic interaction in this system provides naturally the basic prerequisites for the implementation of the proposed scheme.

3.2 Entanglement distillation by dissipation and continuous quantum repeaters

As shown in the previous section, entanglement can be created by purely dissipative processes. Yet, the attainable degree of entanglement is profoundly limited in the presence of noise sources. In this section, it is shown that distillation can also be realized dissipatively, leading to a highly entangled steady state. Moreover, it is shown how dissipative

[19] Equivalently, membranes coupled to Fabri-Perot cavity modes could be used.

distillation can be employed in a continuous quantum repeater architecture, in which the resources scale polynomially with the distance.
This section is organized as follows. The main results are summarized in Sec. 3.2.1. In Sec. 3.2.2 and Sec. 3.2.3, two types of dissipative distillation protocols are introduced and described. Their application in a quantum repeater scheme is explained in Sec. 3.2.4.

3.2.1 Overview and main results

As explained in the previous section, a major advantage of dissipative entanglement generation lies in the fact that entanglement is created in a steady state. This implies that in contrast to standard methods, the desired state is reached independently of the initial one. Moreover, by coupling two quantum systems to a common environment (e.g. the electromagnetic field, as described in Sec. 3.1) a robust entangled steady state can be quickly generated and maintained for an arbitrary long time without the need for error correction such that entanglement is available any time. However, as any other scheme, dissipative protocols are exposed to noise sources, which degrade the quality of the produced state and render it inapplicable for many important applications in quantum information, like quantum communication where noise effects increase dramatically with the distance. By means of distillation [179], entanglement can be improved at the expense of using several copies. In combination with teleportation, this method allows for the construction of quantum repeaters [155, 180], which enable the distribution of high-quality entanglement for long distance quantum communication with a favorable scaling of resources. Unfortunately, existing schemes for distillation and teleportation are incompatible with protocols generating entanglement in a steady state, since they require the decoupling of the system from the environment, such that the advantages are lost. Hence, new procedures which are suitable to accommodate dissipative methods such that all advantages can be retained and used for quantum repeaters are highly desirable.
Here, dissipatively driven distillation protocols are introduced and analyzed, which allow for the production of highly entangled steady states independently of the initial one and a novel quantum repeater scheme featuring the same properties is presented. More specifically, this protocol continuously produces high-quality long-range entanglement. The required resources scale only polynomially in the distance. Once the system is operating in steady state, the resulting entangled link can be used for applications. Remarkably, the time required to drive a new pair into a highly entangled steady state is independent of the length of the link[20] such that this setup provides a continuous supply of long distance entanglement [155, 180]. Apart from that, the proposed distillation protocols exhibit several intriguing features. For example, a method is presented which allows for distillation in steady state where none of the individual source pairs is entangled, and another one is described whose performance can be improved by deliberately adding noise to the system.

[20] Retardation effects due to classical communication over very long distances are not taken into account.

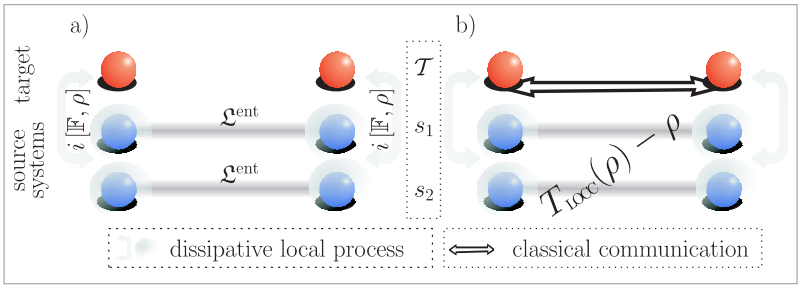

Figure 3.8: Entanglement distillation by dissipation a) Distillation setup without communication. b) Distillation setup including classical communication.

3.2.2 Scheme I: Dissipative entanglement distillation for source states close to pure states

In the following, two types of dissipative distillation protocols suitable for different situations are introduced. In this subsection, scheme I which is physically motivated is explained and the situation shown in Fig. 3.8 is considered. Two parties, Alice and Bob, share two source qubit pairs s_1 and s_2, which are each dissipatively driven into an entangled steady state and used as resource for creating a single highly entangled pair in target system $\mathcal{T}$. Assuming Markov dynamics, the time evolution of the density matrix ρ can be described by a master equation of Lindblad form $\dot{\rho} = \gamma\left(A\rho A^\dagger - \frac{1}{2}\left(\rho A^\dagger A + A^\dagger A\rho\right)\right)$ with rate γ and will be abbreviated by the short hand notation $\dot{\rho} = \gamma\mathfrak{L}^A(\rho)$ in the following. The entangling dissipative process acting on the source qubits considered here, is the single-particle version of the collective dynamics realized discussed in Sec. 3.1 and corresponds to the master equation $\dot{\rho} = \mathfrak{L}^{\text{ent}}(\rho) = \gamma\left(\mathfrak{L}^A(\rho) + \mathfrak{L}^B(\rho)\right)$ with $A = \cosh(r)\sigma^-_{\text{Alice}} + \sinh(r)\sigma^+_{\text{Bob}}$ and $B = \cosh(r)\sigma^-_{\text{Bob}} + \sinh(r)\sigma^+_{\text{Alice}}$, where $\sigma^- = |0\rangle\langle 1|$ and $\sigma^+ = |1\rangle\langle 0|$. The unique steady state of this evolution is the pure entangled state $|\psi\rangle = \left(|00\rangle - \lambda|11\rangle\right)/\sqrt{1+\lambda^2}$, where $\lambda = \tanh(r)$. It is subject to local cooling, heating and dephasing noise described by $\mathfrak{L}^{\text{noise}}(\rho) = \varepsilon_{\text{c}}\left(\mathfrak{L}^{\sigma^-_{\text{Alice}}}(\rho) + \mathfrak{L}^{\sigma^-_{\text{Bob}}}(\rho)\right) + \varepsilon_{\text{h}}\left(\mathfrak{L}^{\sigma^+_{\text{Alice}}}(\rho) + \mathfrak{L}^{\sigma^+_{\text{Bob}}}(\rho)\right) + \varepsilon_{\text{d}}\left(\mathfrak{L}^{|1\rangle\langle 1|_{\text{Alice}}}(\rho) + \mathfrak{L}^{|1\rangle\langle 1|_{\text{Bob}}}(\rho)\right)$.

Dissipative entanglement distillation without communication

It is assumed that the entangling dynamics acting on s_1 and s_2 is noisy, while the target system is protected (this assumption will be lifted below). The source qubits are locally coupled to $\mathcal{T}$ such that

$$\dot{\rho} = \mathfrak{L}^{\text{ent}}_{s_1}(\rho) + \mathfrak{L}^{\text{ent}}_{s_2}(\rho) + \mathfrak{L}^{\text{noise}}_{s_1}(\rho) + \mathfrak{L}^{\text{noise}}_{s_2}(\rho) + \mathfrak{L}_{\text{Alice}}(\rho) + \mathfrak{L}_{\text{Bob}}(\rho),$$

where $\mathfrak{L}_{\text{Alice}}(\mathfrak{L}_{\text{Bob}})$ acts only on Alice's (Bob's) side. Here, $\mathfrak{L}_{\text{Alice}}(\rho) = -\mathfrak{L}_{\text{Bob}}(\rho) = i\delta_{\mathbb{F}}\,[\mathbb{F},\rho]$, corresponding to the unitary evolution with respect to the Hamiltonian $\mathbb{F} = \sum_{i,j}|j_{\text{t}}\hat{i}_{\text{s}}\rangle\langle i_{\text{t}}\hat{j}_{\text{s}}|$, where $|\hat{0}_{\text{s}}\rangle = |0_{\text{s}_1}1_{\text{s}_2}\rangle$ and $|\hat{1}_{\text{s}}\rangle = |1_{\text{s}_1}0_{\text{s}_2}\rangle$ is chosen. Note that this distillation protocol does not require any classical communication or pre-defined correlations. As can be seen in Fig. 3.9a, the efficiency is mainly determined by the mixedness of the

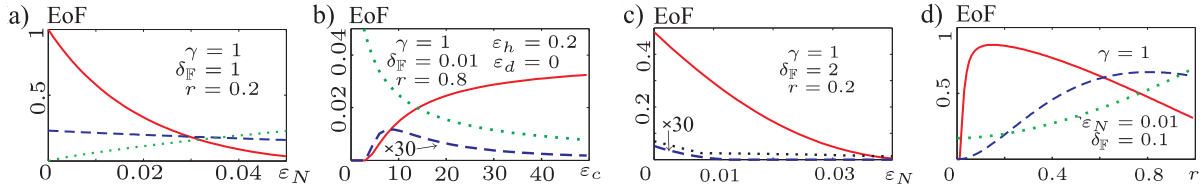

Figure 3.9: Dissipative distillation according to scheme I without communication (panel a) and including classical communication (panels b-d). The full red lines show the steady state entanglement of formation (EoF) of system $\mathcal{T}$. The dashed blue lines depict the steady state EoF of the source state s_1 if no distillation is performed (a,c,d) and during the protocol (b). For better visibility the blue dashed curve is multiplied by a factor 30 in panels b and c. The dotted green lines show the entropy of s_1 which is a measure of its mixedness. a) EoF attainable without communication versus error rate $\varepsilon_N \equiv \varepsilon_h = \varepsilon_c = \varepsilon_d$. b) EoF versus the noise parameter ε_c. c) EoF versus error rate ε_N. The black dotted curve represents the entanglement of the total source system measured in log negativity. d) EoF versus the parameter r.

source states rather than their entanglement. In the absence of errors, the target system reaches a maximally entangled state.

Classical communication in the master equation formalism

In order to allow also for noise acting on $\mathcal{T}$, classical communication is included. The continuous exchange of classical communication is added in the framework of dissipative quantum information processing, by assuming that Alice and Bob have access to a system, which is used for communication only and described by the master equation

$$\dot{\rho} = \Gamma \left(\sum_i \langle i_{c_A} | \rho_{\text{Alice}} | i_{c_A} \rangle | 0_{c_A} i_{c_B} \rangle \langle 0_{c_A} i_{c_B} | - \rho \right) \equiv \mathfrak{C}_{A \to B}(\rho).$$

States referring to the communication system at Alice's and Bob's side are labelled by subscripts c_A and c_B. Alice's communication system is continuously measured in the computational basis yielding the quantum state $|i_{c_A}\rangle$ with probability $\langle i_{c_A} | \rho_{\text{Alice}} | i_{c_A} \rangle$ and reset to the state $|0_{c_A}\rangle$, while the communication system on Bob's side is set to the measurement outcome. This way, classical information can be sent at a rate Γ, but no entanglement can be created (see App. C.2.1). As proven in App. C.2, any operation that can be realized by means of local operations and classical communication (LOCC) can be constructed in a continuous fashion using communication processes $\mathfrak{C}_{A \to B}$ and $\mathfrak{C}_{B \to A}$, if the rate Γ is fast compared to all other relevant processes including the retardation due to back and forth communication. Therefore, any Lindblad operator of the form $\mathfrak{L}^{T_{\text{LOCC}}}(\rho) = (T_{\text{LOCC}}(\rho) - \rho)$, where T_{LOCC} is an arbitrary LOCC channel[21], can be realized using local dissipative processes in combination with classical communication[22].

[21] LOCC channels are completely positive trace preserving maps that can be realized by means of Local Operations and Classical Communication.

Distillation using scheme I including classical communication

The continuous implementation of LOCC operations allows for the stabilization of the distillation schemes discussed below against errors acting on the target system by running them using m blocks of source pairs, which are all coupled to the same target state (see App C.3) as illustrated in Fig. 3.10a. If sufficiently many source-blocks, m, are used, the dynamics is dominated by the desired processes. For clarity, the following distillation schemes are discussed in the absence of target errors, which corresponds exactly to the limit $m \to \infty$. Thus, the master equation

$$\dot{\rho} = \mathfrak{L}_{s_1}^{\text{ent}}(\rho) + \mathfrak{L}_{s_2}^{\text{ent}}(\rho) + \mathfrak{L}_{s_1}^{\text{noise}}(\rho) + \mathfrak{L}_{s_2}^{\text{noise}}(\rho) + \delta_{\mathbb{F}}\left(T_{\mathbb{F}}(\rho) - \rho\right)$$

is considered. The LOOC map $T_{\mathbb{F}}(\rho)$ is defined by the four Kraus operators $\mathbb{F}_A \otimes \mathbb{F}_B$, $P_A^{\perp} \otimes P_B$, $P_A \otimes P_B^{\perp}$, $P_A^{\perp} \otimes P_B^{\perp}$, where $P, P^{\perp}$ are the projection onto the one excitation subspace and its orthogonal complement. Alice and Bob measure the number of excitations on their side. After successful projection onto the subspace with one excitation $P_A \otimes P_B$, a flip operation $\mathbb{F}$ is performed, in the unsuccessful case no operation is carried out.
As shown in Fig. 3.9b, the scheme is robust against local noise of cooling-type ($\mathfrak{L}^{\sigma^-}(\rho)$). This kind of noise can even be used to enhance the performance of the distillation protocol in the steady state at the cost of a lower convergence rate. Thus, counterintuitively it can be beneficial to add noise in order to increase the distilled entanglement. Moreover, the steady state entanglement of the source pairs is zero in the absence of cooling noise for the parameters considered in Fig. 3.9b, if no distillation scheme is performed. For increasing ϵ_c, the entanglement in s_1 and s_2 increases, reaches an optimal point an decreases again. Yet, the entanglement that can be distilled from these pairs is monotonously increasing and displays a boost effect. Panel c also hints at another counterintuitive effect,- entanglement can be distilled even though none of the source pairs is (individually) entangled in the steady state. This can be explained by noticing that the two-copy entanglement can be maintained for high noise rates when the single-copy entanglement is already vanishing. Fig. 3.9d shows that the distilled entanglement increases considerably for small values of the parameter r despite the decrease in the entanglement of the source pairs. This is due to the fact that the protocol is most efficient for source states close to pure states, where it allows one to distill quickly highly entangled state.

3.2.3 Scheme II: dissipative entanglement distillation for Werner states

In settings where the source states can be highly mixed, another distillation scheme (scheme II hereafter) is a method of choice and will be explained in this subsection. Here, a generic model, which can be solved exactly and allows one to reduce the discussion to the essential features of dissipative entanglement distillation is analyzed. As in standard distillation schemes, the general problem is studied in terms of Werner states [181, 182], since many situations can be described this way and a wide range of

[22] It is assumed, that the time scales for classical communication Γ^{-1} (see App. C.2) are sufficiently long such that retardation effects can be ignored.

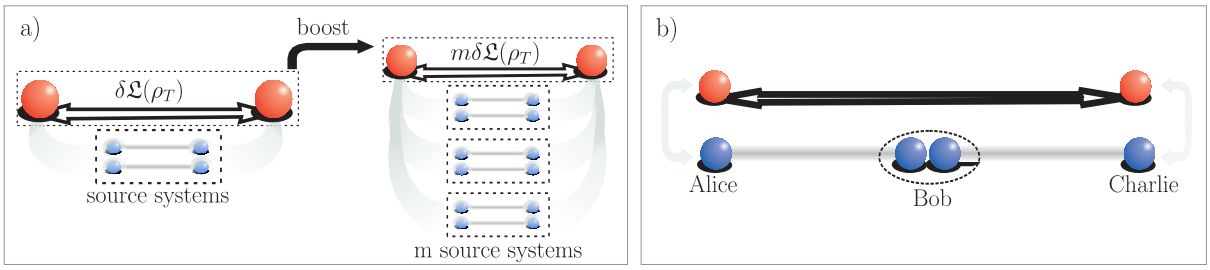

Figure 3.10: Building blocks of a dissipative quantum repeater. a) Noise resistent distillation setup. The process acting on the target system is boosted using several copies of the source system. b) Continuous entanglement swapping procedure.

processes can be cast in this form by twirling [181, 182]. Werner states are of the simple form $\rho_{\mathrm{W}}(f) = f\Omega + (1-f)(\mathbb{I}-\Omega)/3$, where Ω is a projector onto the maximally entangled state $|00\rangle + |11\rangle$, and $\mathbb{I}$ the identity operator. A process which drives each source pair into the state Ω, $\dot{\rho} = \gamma\left(\mathrm{tr}(\rho)\Omega - \rho\right) \equiv \gamma E(\rho)$ is assumed. Local depolarizing noise is added in the form of the Lindblad term $N(\rho) \equiv (\rho_{\mathrm{Alice}} \otimes \mathbb{1} - \rho) + (\mathbb{1} \otimes \rho_{\mathrm{Bob}} - \rho)$, where ρ_{Alice} (ρ_{Bob}) denotes the reduced density matrix of Alice's (Bob's) system and $\mathbb{1}$ the normalized identity. This term describes the continuous replacement of the initial state by the completely mixed one. The source system reaches the steady state $\rho_s \propto \gamma\Omega + \varepsilon\mathbb{1}$ of the total master equation $\dot{\rho} = \gamma E(\rho) + \frac{\varepsilon}{2}N(\rho)$ at least exponentially fast in γ (see App. C.4.1.). A continuous distillation process based on a standard protocol [183] can be constructed considering n source pairs which are independently driven into the steady state ρ_s and a target system $\mathcal{T}$. $\mathcal{T}$ is coupled to the source pairs by a dissipative dynamics of the form $\dot{\rho} = \delta_{\mathrm{D}}\left(\mathrm{tr}(\rho)T_D(\rho) - \rho\right)$, where the completely positive map $T_D(\rho)$ corresponds to a process which acts on the n source pairs and distills a single potentially higher entangled copy. The output state is written on $\mathcal{T}$, while the n source pairs are re-initialized in the state $\mathbb{1}$. The total master equation is given by

$$\dot{\rho} = \sum_{i=1}^{n}\left(\gamma E_i(\rho) + \frac{\varepsilon}{2}N_i(\rho)\right) + \delta_D(T_D(\rho) - \rho),$$

where E_i, N_i denote entangling and noise processes on the ith source qubit pair. The steady state has a fidelity of $f = \int_0^1 dx f_D(f_s - (f_s - 0.25)x^{\frac{\gamma+\varepsilon}{\delta_{\mathrm{D}}}})$, where f_s and $f_D(f) = \mathrm{tr}(\Omega T_D(\rho_{\mathrm{W}}(f)^{\otimes n}))$ are the fidelity of ρ_s and the output of the distillation protocol with n input states of fidelity f. High fidelities require low values of δ_{D}. However, the solution $\rho(t)$ (see App. C.4) shows that fast convergence requires high values of this parameter. A low convergence speed on the target system is extremely disadvantageous if noise is acting on $\mathcal{T}$. Therefore, a boost of the process as illustrated in Fig. 3.10a is required. This way, the new convergence rate is given by $m\delta_{\mathrm{D}}$ while the back action on each source system remains unchanged (see App. C.3).

3.2.4 Continuous quantum repeaters

The distribution of entanglement over large distances is one of the big challenges in quantum information science. In quantum repeater schemes, entanglement is generated over short distances with high accuracy and neighboring links are connected by entanglement swapping. This procedure allows one to double the length of the links, but comes at the cost of a decrease in entanglement for non-maximally entangled states. Therefore a distillation scheme has to be applied before proceeding to the next stage, which consists again of entanglement swapping and subsequent distillation. The basic setup for a continuous entanglement swapping procedure is sketched in Fig. 3.10b. It consists of three nodes operated by Alice, Bob and Charlie, where Alice and Bob as well as Bob and Charlie share an entangled steady state. By performing a teleportation procedure, an entangled link is established between Alice and Charlie and written onto the target system, while the source systems are re-initialized in the state $\mathbb{1}$. This corresponds to LOCC operation $T_{\mathrm{sw}}(\rho)$. The whole dynamics is described by the master equation

$$\dot{\rho} = \sum_{i=1}^{2} \left(\gamma E_i(\rho) + \frac{\varepsilon}{2} N_i(\rho) \right) + \delta_{\mathrm{sw}}(T_{\mathrm{sw}}(\rho) - \rho).$$

The steady state has a target fidelity of $f = \frac{2\gamma^2}{(2\gamma+\delta_{sw})(\gamma+\delta_{\mathrm{sw}})}(f_{sw}(f_s) - \frac{1}{4}) + \frac{1}{4}$, where $f_{sw}(f_s)$ is the output fidelity of the entanglement swapping protocol for two input states with fidelity f_s (see App. C.5.1). The basic idea of a nested steady state quantum repeater is illustrated in Fig. 3.11. At the lowest level, entangled steady states are generated over a distance L_0. At each new level, two neighboring states are connected via a continuous entanglement swapping procedure and subsequently written onto a target pair separated by twice the distance. The distillation and boost processes, that are required in each level to keep the fidelity constant are not shown in this picture. The resources required for this repeater scheme can be estimated as follows. Entanglement swapping processes acting on source pairs of length l with fidelity f_l result in entangled target pairs of length $2l$, with degraded fidelity $f_{2l} < f_l$. This reduction is due to the swapping procedure, noise acting on the target system and the back-action from entanglement distillation. Stabilization against noise acting on the target systems is achieved by coupling each of them to m copies of the source system and requires therefore $2m$ source pairs of length l. In order to obtain a fidelity $f_{2l} \geq f_l$, n copies of these error stabilized links are used as input for a n to 1 distillation process. The distilled state is mapped to another target pair of length $2l$, which also needs to be stabilized against errors using m copies of the blocks described. Hence, in total $2m^2n$ pairs of length l are required for a repeater stage which doubles the distance over which entanglement is distributed. For creating a link of length $L = L_0 2^k$, $(2m^2n)^k$ source pairs are needed, where k is the number of required iterations of the repeater protocol. Therefore, the required resources scale polynomial with $(L/L_0)^{Log_2(2m^2n)}$. In App. C.5.2, a specific example scaling with $(L/L_0)^{16.4}$ is discussed. The convergence time of the total system scales only logarithmically with the distance L. Once the steady state is reached, the entanglement of the last target system can be used e.g. for quantum communication or cryptography. The underlying source systems are not effected by this process and remain in the steady state. Therefore, the target state is restored in constant time.

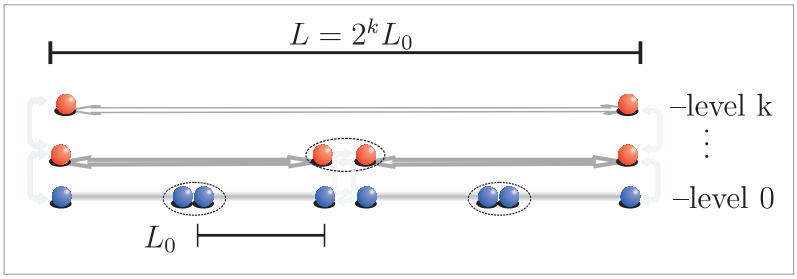

Figure 3.11: Nested steady state quantum repeater scheme. In contrast to common repeater schemes, the levels of the nested protocol are physically present all the time and connected via dissipative processes.

In conclusion, it has been shown how entanglement can be distilled in a steady state and distributed over long distances by means of a dissipative quantum repeater scheme serving as stepping stone for future work aiming at the optimization in view of efficiency and experimental implementations. The development of concrete schemes for realistic physical realizations will be an important topic for future work. Possible implementations could for example be based on atoms in cavities by extending ideas put forward in [184].

Chapter 4

Applications of light-matter interface schemes

In this chapter, we study light-matter interface techniques in view of applications in several different contexts including quantum information science and the study of condensed matter systems. More specifically, we present three protocols which are based on the interaction of light with ensembles of neutral atoms. In Sec. 4.1, we analyze a teleportation scheme, which aims at the transfer of a quantum state between two macroscopic matter systems. This section is complemented by App. D. In Sec. 4.2, we propose a scheme for the study of correlated many-body systems using an atomic quantum memory as auxiliary system. This new method has been published in [V] and allows for the measurement of dynamical correlations by probing a quantum many-body system at different times while storing information coherently. In Sec. 4.3, we devise a protocol for the implementation of an entangling gate for photons, which relies on the mapping of photonic states to matter systems (and vice versa) and renders efficient quantum information processing of photonic states possible. The results have been published in [I, X]. We consider ultracold atoms in optical lattices for the implementation of the proposals in Sec. 4.2 and 4.3, and analyze the teleportation scheme in Sec. 4.1 for atomic ensembles at room temperature.

4.1 Deterministic quantum teleportation between two macroscopic objects

The ability to teleport quantum states between matter systems over macroscopic distances is required for many applications of quantum information science and plays an important role in the realization of distributed quantum networks and long-distance communication. Recent experimental progress towards this challenging goal includes the deterministic implementation between ions in the same trap [185–187] and the probabilistic teleportation between two single particles over a large distance [188]. Here, we study a protocol which allows for the deterministic teleportation of a quantum state between two macroscopic atomic ensembles at room temperature interacting with freely propagating coherent light. We analyze the scheme assuming a quantum-nondemolition interaction between atoms and light and show that very high fidelities can be obtained by means of pulse shaping.

Moreover, we study the performance of the teleportation scheme for a general quadratic interaction and in the presence of atomic decoherence and show that the protocol is feasible under current experimental conditions.
This section is organized as follows. In Sec. 4.1.1, we briefly review related work and experimental progress on the teleportation of atomic states. In Sec. 4.1.2, we summarize the main results. In Sec. 4.1.3, we discuss the teleportation of atomic quantum states between two ensembles using a QND interaction between light and matter. This subsection is supplemented by App. D.2. In Sec. 4.1.4, we analyze the proposed scheme in view of a possible experimental implementation. To this end, we study a general quadratic interaction, which allows us to take deviations from the ideal QND dynamics into account (see also Sec. 2.1 and App. D.1).

4.1.1 Teleportation of atomic states

Teleportation [189] is an essential element in quantum information science [3] and is intimately linked to and enabled by the distribution of entanglement between two parties. Once an entangled link is established, a quantum state can, in principle, be transferred exactly across the link independent of the distance using only classical communication in the process of transmission. This procedure provides a possibility to circumvent the problems posed by the difficulty to transmit quantum states directly (physically) with high fidelity and the limitations of strategies based on the measurement, sending and re-preparation, imposed by the no-cloning theorem. Therefore, teleportation is a key ingredient in distributed quantum networks and lies at the heart of the practical realization of long-distance quantum communication [5,155]. Moreover, it plays an important role in quantum information science. Supplemented with local operations and suitable entangled resource states, teleportation allows for universal quantum computing [190]. The teleportation of quantum states between atomic systems is particularly relevant, since long-lived degrees of freedom are required for the storage of quantum information and matter systems are needed for the efficient processing of quantum states and the extension to large quantum networks which include multiple remote nodes. However, the reliable deterministic teleportation of quantum states between distant matter qubits is a challenging goal. In photonic systems [191–207], the teleportation of quantum states has been realized covering macroscopic distances up to 16km [204]. The teleportation between matter systems has been implemented deterministically using ions in close vicinity held in the same trap [185–187] and over a macroscopic distance [188] by means of a probabilistic protocol.
In the following, we present a scheme for the teleportation between two atomic samples which allows for both, the deterministic transfer of a quantum state and the transmission over a macroscopic distance. The protocol involves freely propagating coherent light interacting with two atomic ensembles consisting of a large number N of alkali atoms at room temperature [12, 14–16, 83] as described in Sec. 2.1.1. Since the quantum state to be teleported is shared by about $N = 10^{12}$ particles in an ensemble with a spatial extent of about 2cm, the scheme discussed here allows for quantum teleportation between two macroscopic objects. Atomic ensembles have been successfully used for interspecies teleportation, where the quantum state of light has been transferred to the collective spin

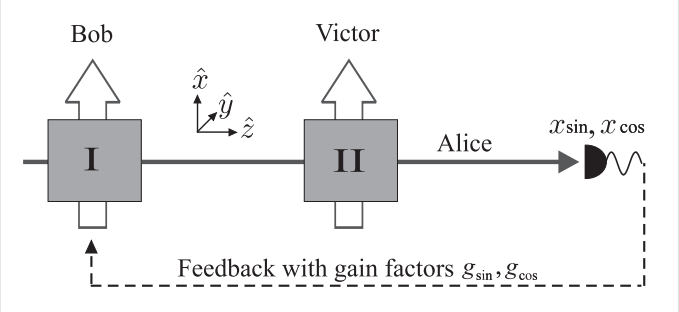

Figure 4.1: Deterministic quantum teleportation between two macroscopic objects. The collective spin state of ensemble II is teleported to ensemble I by virtue of an off-resonant scattering interaction between the atoms and coherent light, homodyne detection of the scattered field and a conditional feedback operation as described in the text.

state of an atomic sample [15,63,97,162]. However, the teleportation between two ensembles [208–210] has not been possible so far, due to the low achievable fidelities of the quantum state transfer for the limited coupling strength that can be realized experimentally. Here, we analyze a protocol for continuous variable teleportation [211–213] involving two atomic ensembles as well as a light field acting as auxiliary system. We consider two different types of interaction. First, we study the scheme assuming a quantum-nondemolition (QND) interaction between atoms and light as used in [14–16] and optimize the teleportation fidelity by tailoring the pulse shape of the light field. Then, we analyze the scheme in general, assuming an arbitrary quadratic interaction, as explained in Sec. 2.1.2. This allows for a more detailed description of the interaction encountered in experiments involving ensembles of Cesium atoms [III, IV, VII, IX], [17,18]. Finally, we investigate the performance in the presence of noise. More specifically, we consider atomic decay which represents the dominant source of noise in a realistic setting and show that the scheme is well feasible under current experimental conditions.

4.1.2 Overview and main results

We consider the setup shown in Fig. 4.1. It resembles the setup introduced in Sec. 2.1.1 apart from the fact that the ensembles are not oriented antiparallel[1] (as used for memory schemes [14, 18] or entanglement generation [III], [16]), but in parallel. As shown in [63], the interaction of light with atomic ensembles in a magnetic field involves a infinite hierarchy of backaction modes which simplifies considerably if two antiparallel oriented ensembles are used (as explained in Sec. 2.1.3, two counter-oriented ensembles in a magnetic field B correspond formally to a single cell with $B = 0$). For high-fidelity teleportation between two ensembles, the richer multi-mode structure encountered in the parallel configuration is required.

A standard teleportation scheme involving the three parties Alice, Bob and Victor consists of the following three steps, which allow Alice to teleport a quantum state provided by

[1] This setting is formally equivalent to using parallel polarized ensembles in oppositely oriented magnetic fields.

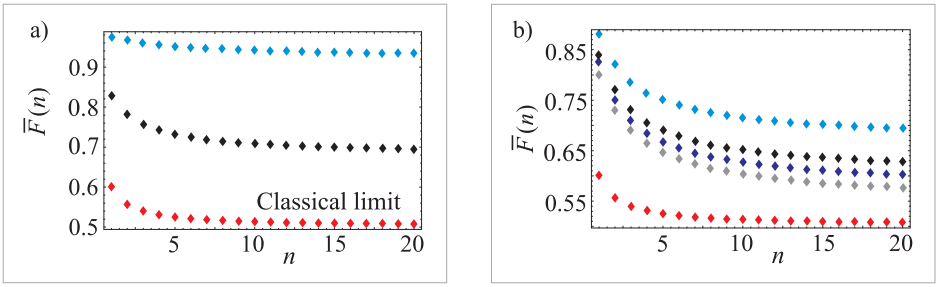

Figure 4.2: Average teleportation fidelity $\bar{F}(n)$ versus width of the distribution of input states n. The lowest curve in each panel (shown in red) represents the classical limit. a) QND teleportation. The upmost (blue) and middle (black) curve depict the optimized average fidelity with and without pulse shaping respectively (see Sec. 4.1.3). b) Non-QND teleportation fidelity for realistic experimental parameters as reported in [III]. Light and atoms interact as shown in Fig. 4.1 according to $H_{\rm int} = \frac{\kappa}{\sqrt{T}}\left(p_A p_L - \frac{1}{Z^2} x_A x_L\right)$ with Z=2.5 (which corresponds to a predominantly active interaction, as explained in Sec. 2.1.2). The upmost curve (blue) shows the maximal fidelity for arbitrary exponential readout modes in the absence of decoherence. The next three curves show in descending order the attainable fidelity if transverse atomic decay at a rate η/T is included for $\eta = 0.5\kappa$ (black), $\eta = 0.75\kappa$ (violet) and $\eta = 1.01\kappa$ (grey).

Victor to Bob. (i) Alice and Bob establish an entangled link, which is shared between the two remote parties. (ii) Alice performs a Bell measurement on her part of the entangled state shared with Bob and an unknown quantum state prepared by Victor. (iii) Alice uses a classical channel to communicate the measurement outcome to Bob, who performs a local operation on his quantum state conditioned on Alice's result.

In the setup shown in Fig. 4.1, the quantum state prepared by Victor is stored in ensemble II on the right side. This state is teleported to ensemble I, on the left, which represents Bob, while the light field in $\hat{\mathbf{x}}$-polarization plays the role of Alice. Step (i) in the standard protocol outlined above corresponds to the interaction between the light field and the first atomic ensemble which results in an entangled state. The distribution of entanglement between the two remote sites is realized by means of the free propagation of the photonic state. Step (ii) corresponds to the interaction of the light field with the second ensemble and the subsequent measurement of the x-quadrature of the transmitted light by means of homodyne detection. Step (iii) is implemented in the form of a feedback operation realizing a conditional displacement on ensemble I using radio-frequency magnetic fields. In principle, it is not necessary to perform the displacement as long as the outcome of the measurement in step (ii) is known. We start out by considering a QND interaction between atoms and light (compare Sec. 2.1.2). The performance of the scheme is fundamentally limited (see Fig. 4.2a, middle curve) since this type of the interaction does for example not allow for a perfect Bell measurement. The fidelity is also restricted by the experimental limitations of the coupling strength[2]. Therefore, we investigate different

[2] In the following, the value $\kappa \approx 1$ reported in [15] is used for comparison.

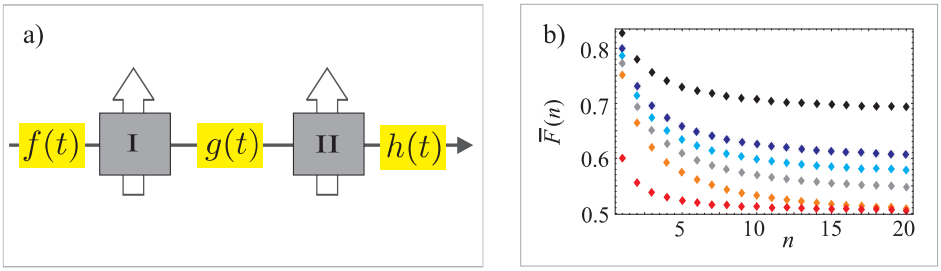

Figure 4.3: QND teleportation. a) Setup including different functions for the time dependent coupling strengths $\kappa_1(t) = \kappa f(t)$ and $\kappa_2(t) = \kappa g(t)$ characterizing the first and second interaction and arbitrary readout modes $h(t)$ ($\frac{1}{T}\int_0^T f(t)^2dt = \frac{1}{T}\int_0^T g(t)^2dt = \frac{1}{T}\int_0^T h(t)^2dt = 1$, see Sec. 4.1.3). b) QND teleportation fidelity $\bar{F}(n)$ versus the width n of the distribution of input states for $f(t)=g(t)=h(t)=1$. The fidelity is optimized with respect to the feedback parameters g_{sin}, g_{cos} and coupling strengths κ_1, κ_2. The topmost (black) and lowermost (red) curves represent the maximum attainable fidelity for arbitrary couplings and the classical limit. The intermediate curves show in descending order the achievable fidelity if κ is limited to $\kappa_{max} = 1.3$ (violet), $\kappa_{max} = 1.2$ (blue), $\kappa_{max} = 1.1$ (grey) and $\kappa_{max} = 1.0$ (orange).

means to increase the performance of the scheme and shown that a judicious choice of slowly varying functions used for the modulation of the intensity of the classical beam and the temporal mode used for the readout (see Fig. 4.3a) allows for high-fidelity teleportation. To this end, the $\hat{\mathbf{y}}$-polarized classical laser field, which copropagates with the quantum field in $\hat{\mathbf{x}}$-direction has to be replaced between the first and the second interaction, which can for example be done using a polarizing beamsplitter[3]. The average fidelities which can be attained using exponential functions $f(t)$ and $g(t)$ for the pulse shape of the classical light in the first and second interaction and $h(t)$ as readout mode are shown in Fig. 4.2a (upmost curve).

In Sec. 4.1.4, we consider a general quadratic interaction between matter and light according to the Hamiltonian given by Eq. (2.4). We derive the input-output relations describing the teleportation in this general case and study the fidelity for different settings and readout modes. More specifically, we asses the experimental feasibility of this scheme in ^{133}Cs vapor [III, VII], [14–18] by evaluating the performance for realistic parameters in this system, - to this end, the consideration is restricted to basic settings which involve only techniques which have already been used in previous experiments and include atomic decay assuming decay rates as measured in [III]. Fig. 4.2b shows the achievable fidelity including noise and in the ideal case. These results render the scheme analyzed here a promising candidate for the teleportation of a collective spin state between two atomic ensembles.

[3] The coupling strength is proportional to the number of photons in the laser pulse (in $\hat{\mathbf{y}}$-polarization) and can be modulated by means of a time varying intensity of the classical field. $\kappa_1(t) \neq \kappa_2(t)$ can for example be realized by means of a polarizing beamsplitter with high reflectivity for $\hat{\mathbf{y}}$ -polarized photons and high transmissivity for the quantum field in $\hat{\mathbf{x}}$-polarization, which is placed between the ensembles and allows for the exchange of the classical field between the two interactions.

4.1.3 QND teleportation

In this section, we study the teleportation scheme shown in Fig. 4.1 assuming a QND interaction between atoms and light. In the following two subsections, we explain the basic protocol and evaluate its performance for general slowly varying functions modulating the interaction strengths and the readout mode.

Basic QND protocol

Atoms and light interact according to the Hamiltonian $H = H_A + H_L + H_{\rm int}^{\rm QND}$, where $H_A = \frac{\Omega}{2}(x_B^2 + p_B^2) + \frac{\Omega}{2}(x_V^2 + p_V^2)$ describes the Zeeman splitting of the atomic levels in the homogeneous magnetic field. Ω denotes the Larmor frequency at which the atoms precess in the magnetic field, x_B, p_B and x_V, p_V refer to Bob's and Victor's ensemble respectively and H_L accounts for the free propagation of the light field. The interaction Hamiltonian is given by $H_{\rm int}^{\rm QND} = \frac{\kappa}{\sqrt{T}}(p_B p_L(0) + p_V p_L(R))$, where pointlike atomic ensembles which are separated by a distance R are assumed[4](compare Sec. 2.1 and App. D.1.1).

Input-output relations for the basic protocol

Step (i), the entangling interaction of the light field with ensemble I (Bob) with constant coupling strength κ_1, is described by the input-output relations

$$\begin{aligned}
\begin{pmatrix} x_B^{out} \\ p_B^{out} \end{pmatrix} &= \begin{pmatrix} x_B^{in} \\ p_B^{in} \end{pmatrix} + \frac{\kappa_1}{\sqrt{2}} \begin{pmatrix} p_{cos}^{in} \\ p_{sin}^{in} \end{pmatrix}, \\
\begin{pmatrix} x_{cos}^{out} \\ x_{sin}^{out} \end{pmatrix} &= \begin{pmatrix} x_{cos}^{in} \\ x_{sin}^{in} \end{pmatrix} + \frac{\kappa_1}{\sqrt{2}} \begin{pmatrix} p_B^{in} \\ -x_B^{in} \end{pmatrix} + \frac{\kappa_1^2}{4} \begin{pmatrix} p_{sin}^{in} \\ -p_{cos}^{in} \end{pmatrix} + \frac{\kappa_1^2}{4\sqrt{3}} \begin{pmatrix} p_{sin,1}^{in} \\ -p_{cos,1}^{in} \end{pmatrix},
\end{aligned}$$

as explained[5] in Sec. 2.1.3 (note that the flat-top mode and the first order backaction mode are independent $[x_{sin/cos}, p_{sin/cos,1}] = 0$). The p-quadratures of the light field are conserved. Step (ii) includes the interaction of the light field emitted from ensemble I with ensemble II (Victor) with constant coupling strength κ_2, which results in

$$\begin{aligned}
\begin{pmatrix} x_V^{out} \\ p_V^{out} \end{pmatrix} &= \begin{pmatrix} x_V^{in} \\ p_V^{in} \end{pmatrix} + \frac{\kappa_2}{\sqrt{2}} \begin{pmatrix} p_{cos}^{in} \\ p_{sin}^{in} \end{pmatrix}, \\
\begin{pmatrix} \tilde{x}_{cos}^{out} \\ \tilde{x}_{sin}^{out} \end{pmatrix} &= \begin{pmatrix} x_{cos}^{in} \\ x_{sin}^{in} \end{pmatrix} + \frac{\kappa_1}{\sqrt{2}} \begin{pmatrix} p_B^{in} \\ -x_B^{in} \end{pmatrix} + \frac{\kappa_2}{\sqrt{2}} \begin{pmatrix} p_V^{in} \\ -x_V^{in} \end{pmatrix} + \frac{\kappa_1^2 + \kappa_2^2}{4} \begin{pmatrix} p_{sin}^{in} \\ -p_{cos}^{in} \end{pmatrix} + \frac{\kappa_1^2 + \kappa_2^2}{4\sqrt{3}} \begin{pmatrix} p_{sin,1}^{in} \\ -p_{cos,1}^{in} \end{pmatrix}.
\end{aligned}$$

The operators referring to the light field after the second scattering interaction are labelled by a tilde. Subsequently, a measurement of the sine and cosine modulated components of the x-quadrature is performed. In step (iii), the obtained measurement results are fed

[4] In the setting considered here, the atomic ensembles are separated by about half a meter such that the distance $R \ll cT$ can be neglected in the derivation of the input-output relations.

[5] Unlike in Sec. 2.1.3, we use here a simplified notation where the $0^{\rm th}$ and $1^{\rm st}$ order modes are denoted by $x_{sin/cos}$, $p_{sin/cos}$ and $x_{sin/cos,1}$, $p_{sin/cos,1}$.

back onto Bob's ensemble with gain factors g_{sin} and g_{cos} such that

$$\begin{aligned}\begin{pmatrix} x_B^{fin} \\ p_B^{fin} \end{pmatrix} &= \begin{pmatrix} x_B^{out} \\ p_B^{out} \end{pmatrix} + \begin{pmatrix} g_{sin}\ \tilde{x}_{sin}^{out} \\ g_{cos}\ \tilde{x}_{cos}^{out} \end{pmatrix} \\ &= \begin{pmatrix} -\frac{\kappa_2 g_{sin}}{\sqrt{2}}\ x_V^{in} \\ \frac{\kappa_2 g_{cos}}{\sqrt{2}}\ p_V^{in} \end{pmatrix} + \begin{pmatrix} (1-\frac{\kappa_1 g_{sin}}{\sqrt{2}})\ x_B^{in} \\ (1+\frac{\kappa_1 g_{cos}}{\sqrt{2}})\ p_B^{in} \end{pmatrix} + \begin{pmatrix} g_{sin}\ x_{sin}^{in} \\ g_{cos}\ x_{cos}^{in} \end{pmatrix} \\ &+ \begin{pmatrix} (\frac{\kappa_1}{\sqrt{2}} - g_{sin}\frac{\kappa_1^2+\kappa_2^2}{4})\ p_{cos}^{in} \\ (\frac{\kappa_1}{\sqrt{2}} + g_{cos}\frac{\kappa_1^2+\kappa_2^2}{4})\ p_{sin}^{in} \end{pmatrix} + \frac{\kappa_1^2+\kappa_2^2}{4\sqrt{3}} \begin{pmatrix} -g_{sin}\ p_{cos,1}^{in} \\ g_{cos}\ p_{sin,1}^{in} \end{pmatrix}. \end{aligned} \tag{4.1}$$

The first term on the right side represents the desired contribution. By choosing the gainfactors $g_{sin} = -\sqrt{2}/\kappa_2$ and $g_{cos} = \sqrt{2}/\kappa_2$, the mean values can be transmitted perfectly[6] $\langle x_B^{fin}\rangle = \langle x_V^{in}\rangle$, $\langle p_B^{fin}\rangle = \langle p_V^{in}\rangle$. However due to the presence of the last four terms on the right, the variance exceeds the variance of the input state $\mathrm{var}(x_B^{fin}) > \mathrm{var}(x_V^{in})$, $\mathrm{var}(p_B^{fin}) > \mathrm{var}(p_V^{in})$.

Performance of the basic protocol

The performance of the protocol is assessed using the average fidelity with respect to a Gaussian distribution of coherent input states as figure of merit. The fidelity $F = |\langle \Psi_B^{fin} | \Psi_B^{opt}\rangle|^2$ is given by the overlap of Bob's final state $|\Psi_B^{fin}\rangle$, which is described by x_B^{fin} and p_B^{fin} and the optimal final state which is defined by Victor's initial state x_V^{in}, p_V^{in}. For a given coherent input state with mean values $\langle x_V\rangle$ and $\langle p_V\rangle$ (and variances $\mathrm{var}(x_V) = \mathrm{var}(p_V) = 1/2$), the single-shot fidelity is given by

$$F(\langle x_V\rangle, \langle p_V\rangle) = 2\, \frac{e^{\frac{-\left(|\langle x_V\rangle| - |\langle x_B^{fin}\rangle|\right)^2}{1+2\mathrm{var}(x_B^{fin})}}\, e^{\frac{-\left(|\langle p_V\rangle| - |\langle p_B^{fin}\rangle|\right)^2}{1+2\mathrm{var}(p_B^{fin})}}}{\sqrt{\left(1+2\mathrm{var}(x_B^{fin})\right)\left(1+2\mathrm{var}(p_B^{fin})\right)}},$$

such that the average fidelity $\bar{F}(n)$ with respect to a Gaussian distribution with width n,

$$\bar{F}(n) = \frac{1}{2\pi n}\int_{-\infty}^{\infty} d\langle x_V\rangle d\langle p_V\rangle F(\langle x_V\rangle, \langle p_V\rangle) e^{-\frac{\langle x_V\rangle^2 + \langle p_V\rangle^2}{2n}} \tag{4.2}$$

can be directly evaluated. Using expressions (4.1) one obtains

$$\bar{F}_{\mathrm{basic}}(n) = \frac{\sqrt{2}}{\sqrt{\left(1+2\mathrm{var}\left(x_B^{fin}\right)+2n\left(1-\frac{\kappa_2|g_{sin}|}{\sqrt{2}}\right)\right)}} \frac{\sqrt{2}}{\sqrt{\left(1+2\mathrm{var}\left(p_B^{fin}\right)+2n\left(1-\frac{\kappa_2|g_{cos}|}{\sqrt{2}}\right)\right)}}.$$

This result has to be compared to the classical limit $F_{\mathrm{clas}} = (2n+1)/(4n+1)$, which cannot be surpassed by classical means [199, 214, 215]. The topmost curve in Fig. 4.3b

[6] Here, we used the fact that Bob's ensemble as well as the light fields are initially prepared in the vacuum state with $\langle x_B^{in}\rangle = \langle x_{\mathrm{sin/cos}}^{in}\rangle = \langle p_{\mathrm{sin/cos}}^{in}\rangle = \langle p_{\mathrm{sin/cos},1}^{in}\rangle = 0$.

shows the average fidelity for optimized coupling strengths κ_1, κ_2 and gainfactors g_{sin}, g_{cos} (due to the symmetry of the protocol, $g_{sin}^{\rm opt} = -g_{cos}^{\rm opt}$). The coupling strength required to achieve this maximal average fidelity is higher than the values which have been realized experimentally in this system so far. In the following, the value $\kappa^2 \approx 1$ reported in [15] is used for comparison. Fig. 4.3b depicts also the achievable fidelity for restricted coupling strengths and shows that for $\kappa_{max} = 1$, the achievable fidelity decreases quickly with the width of the distribution of input states such that the classical limit can not be surpassed for large n. The fidelity can for example be improved by measuring the first-order backaction modes, using squeezed light or employing a double-pass scheme as discussed in App. D.2. However, these strategies are experimentally challenging. In contrast, the strategy studied in the next section is not only easier to realize experimentally, but also very efficient, since it is specifically tailored to resolve the incompatibility problem associated with the generation of a high degree of entanglement with a low amount of added noise for the specific interaction under consideration.

Improved QND teleportation using suitable modulation functions

The performance of the scheme can be substantially improved by modulating the coupling strengths $\kappa_1(t)$ and $\kappa_2(t)$ appropriately in time and choosing the corresponding mode function for the readout. Below, we derive the input-output relations including time dependent couplings and arbitrary readout modes. We optimize the fidelity using exponential test functions and evaluate the performance of the protocol in the presence of atomic decay.

Teleportation with time dependent couplings in the ideal case

In the following, we consider a time dependent coupling strength $\kappa(t) = \kappa f(t)$, where the function $f(t)$ describing the temporal profile is assumed to vary slowly compared to the atomic Larmor precession and to be normalized such that $\frac{1}{T}\int_0^T f(t)^2 dt = 1$. The derivation of the input-output relations for a single cell in a homogeneous magnetic field using the time dependent interaction Hamiltonian

$$H_{\rm int}^{\rm QND} = \frac{\kappa(t)}{\sqrt{T}} p_A p_L$$

and arbitrary readout modes can be found in App. D.2.2. If the interaction between the photonic mode and a single ensemble is considered in the ideal case, shaping the incoming light field, i.e. modulation of the intensity of the beam, is equivalent to choosing a nontrivial readout mode. Since κ^2 is proportional to the number of photons, doubling the intensity in a light pulse has the same effect as doubling its length. For example, considering a linearly modulated pulse corresponds to redefining the time windows during the readout process, which amounts to choosing a linear readout mode. However, this equivalence is not valid in the presence of atomic decoherence, which will be included below. According to Fig. 4.3a, step (i) of the teleportation protocol is described by the

input-output relations

$$\begin{aligned}
\begin{pmatrix} x_B^{out} \\ p_B^{out} \end{pmatrix} &= \begin{pmatrix} x_B^{in} \\ p_B^{in} \end{pmatrix} + \frac{\kappa_1}{\sqrt{2}} \begin{pmatrix} p_{f,cos}^{out} \\ p_{f,sin}^{out} \end{pmatrix}, \\
\begin{pmatrix} x_{h,sin}^{out} \\ x_{h,cos}^{out} \end{pmatrix} &= \begin{pmatrix} x_{h,sin}^{in} \\ x_{h,cos}^{in} \end{pmatrix} + \frac{\kappa_1}{\sqrt{2}T} \int_0^T dt f(t)h(t) \begin{pmatrix} -x_B^{in} \\ p_B^{in} \end{pmatrix} \\
&+ \frac{\kappa_1}{\sqrt{2}T^{\frac{3}{2}}} \int_0^T dt f(t)h(t) \int_t^T d\tau f(\tau) \begin{pmatrix} -\cos(\Omega\tau)\bar{p}_L(c\tau,0) \\ \sin(\Omega\tau)\bar{p}_L(c\tau,0) \end{pmatrix},
\end{aligned}$$

and step (ii) results in

$$\begin{aligned}
\begin{pmatrix} \tilde{x}_{h,sin}^{out} \\ \tilde{x}_{h,cos}^{out} \end{pmatrix} &= \begin{pmatrix} x_{h,sin}^{in} \\ x_{h,cos}^{in} \end{pmatrix} + \frac{\kappa_1}{\sqrt{2}T} \int_0^T dt f(t)h(t) \begin{pmatrix} -x_B^{in} \\ p_B^{in} \end{pmatrix} + \frac{\kappa_2}{\sqrt{2}T} \int_0^T dt g(t)h(t) \begin{pmatrix} -x_V^{in} \\ p_V^{in} \end{pmatrix} \\
&+ \frac{1}{\sqrt{2}T^{\frac{3}{2}}} \int_0^T d\tau \int_\tau^T dt\, h(t) \left(\kappa_1^2 f(t)f(\tau) + \kappa_2^2 g(t)g(\tau)\right) \begin{pmatrix} -\cos(\Omega\tau)\bar{p}_L(c\tau,0) \\ \sin(\Omega\tau)\bar{p}_L(c\tau,0) \end{pmatrix}.
\end{aligned}$$

After step (iii)

$$\begin{aligned}
\begin{pmatrix} x_B^{fin} \\ p_B^{fin} \end{pmatrix} &= \frac{\kappa_2}{\sqrt{2}T} \int_0^T dt g(t)h(t) \begin{pmatrix} -g_{sin} x_V^{in} \\ g_{cos} p_V^{in} \end{pmatrix} + \begin{pmatrix} g_{sin} x_{h,sin}^{in} \\ g_{cos} x_{h,cos}^{in} \end{pmatrix} + \left[\mathbb{1} + G_- \frac{\kappa_1}{\sqrt{2}T} \int_0^T dt h(t) f(t)\right] \begin{pmatrix} x_B^{in} \\ p_B^{in} \end{pmatrix} \\
&+ \int_0^T d\tau \bar{p}_L(c\tau,0) \left[\mathbb{1} \frac{\kappa_1 f(\tau)}{\sqrt{T}} + G_- \frac{1}{\sqrt{2}T^{\frac{3}{2}}} \int_\tau^T dt\, h(t) \left(\kappa_1^2 f(t)f(\tau) + \kappa_2^2 g(t)g(\tau)\right)\right] \\
&\quad \begin{pmatrix} \cos(\Omega\tau)\bar{p}_L(c\tau,0) \\ \sin(\Omega\tau)\bar{p}_L(c\tau,0) \end{pmatrix}
\end{aligned}$$

is obtained, where is $\mathbb{1}$ is the 2×2 unit matrix and

$$G_\pm = \begin{pmatrix} \pm g_{sin} & 0 \\ 0 & g_{cos} \end{pmatrix}. \tag{4.3}$$

As shown in Fig. 4.2a, the teleportation fidelity can be improved considerably by choosing appropriate modulation functions. Here, the mode functions $f(t) \propto e^{f_1 t}$, $g(t) \propto e^{g_1 t}$ and $h(t) \propto e^{h_1 t}$ are used since the eigenmodes of the generalized problem are exponential. The result shown in Fig. 4.2a is obtained by optimizing the average fidelity with respect to the parameters κ_1, κ_2, g_{sin}, g_{cos}, f_1, g_1 and h_1. In the ideal case, it is sufficient to optimize over two out of the three parameters f_1, g_1 and h_1. If, for example, a flat-top readout mode is chosen ($h(t) = 1$), the optimal solution involves an exponentially falling mode for $\kappa_1(t)$ ($f_1 < 0$) and a rising function for $\kappa_2(t)$ ($g_1 > 0$).

Teleportation with time dependent couplings including atomic decoherence

In the following, atomic decay at a constant rate η/T is considered. As explained in App. D.1, atomic decoherence is modelled by including a beamsplitter operation which attenuates the signal x_A, p_A and introduces vacuum noise to the atomic spin state. The generalized input-output relations describing the final state of Bob's ensemble for time

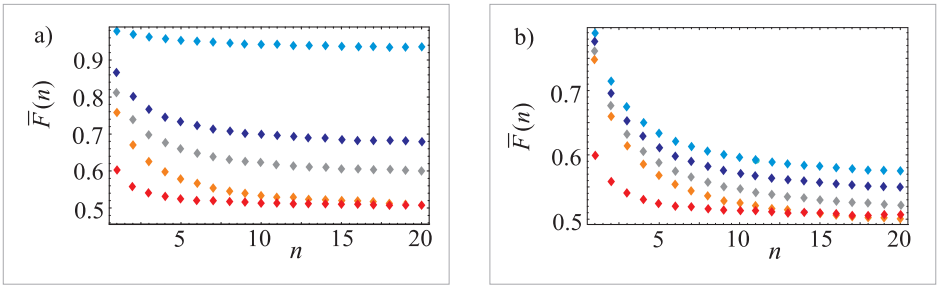

Figure 4.4: QND teleportation fidelities for three variable exponential functions and constant atomic decay at a rate η/T as explained in the main text. Panels a) and b) depict the optimized average fidelity $\bar{F}(n)$ versus width of the input distribution n for arbitrary coupling strength and $\kappa = 1.2$ respectively. The four upper curves correspond (in descending order) to $\eta = 0$ (blue), $\eta = 0.1\kappa^2$ (violet), $\eta = 0.2\kappa^2$ (grey) and $\eta = 0.3\kappa^2$ (orange). The bottom red line shows the classical limit.

dependent coupling strength and an arbitrary readout mode in the presence of noise are given by

$$\begin{aligned}
\begin{pmatrix} x_B^{fin} \\ p_B^{fin} \end{pmatrix} = & \frac{\kappa}{\sqrt{2}T}\int_0^T dt\, h(t)g(t)e^{\frac{-\eta t}{2T}}\begin{pmatrix} -g_{sin}x_V^{in} \\ g_{cos}p_V^{in} \end{pmatrix} + \begin{pmatrix} g_{sin}x_{h,sin}^{in} \\ g_{cos}p_{h,cos}^{in} \end{pmatrix} + \left(e^{\frac{-\eta}{2}}\mathbb{1} + \frac{\kappa}{\sqrt{2}T}\int_0^T dt\, h(t)f(t)e^{\frac{-\eta t}{2T}}G_-\right) \\
& \begin{pmatrix} x_B^{in} \\ p_B^{in} \end{pmatrix} + \frac{\kappa}{\sqrt{T}}\int_0^T d\tau \int_\tau^T dt e^{\frac{\eta\tau}{2T}}\left[e^{\frac{-\eta}{2}}f(\tau)\mathbb{1} + \frac{\kappa}{\sqrt{2}T}e^{\frac{-\eta t}{2T}}h(t)\left(f(t)f(\tau)+g(t)g(\tau)\right)G_-\right] \\
& \begin{pmatrix} -\cos(\Omega\tau)\bar{p}_L(c\tau,0) \\ \sin(\Omega\tau)\bar{p}_L(c\tau,0) \end{pmatrix} + \frac{\kappa\sqrt{\eta}}{\sqrt{2}T^{\frac{3}{2}}}\int_0^T d\tau\int_\tau^T dt e^{\frac{-\eta(t-\tau)}{2T}}h(t)g(t)\,G_-\begin{pmatrix} f_{x,V}(\tau) \\ f_{p,V}(\tau) \end{pmatrix} \\
& + \frac{\sqrt{\eta}}{\sqrt{T}}\int_0^T d\tau e^{\frac{\eta\tau}{2T}}\left[e^{\frac{-\eta}{2}}\mathbb{1} + \frac{\kappa}{\sqrt{2}T}\int_\tau^T dt\, h(t)f(t)e^{\frac{-\eta t}{2T}}\,G_-\begin{pmatrix} f_{x,B}(\tau) \\ f_{p,B}(\tau) \end{pmatrix}\right],
\end{aligned}$$

for $\kappa_1 = \kappa_2 = \kappa$. $f_{x,B/V}(\tau)$, $f_{p,B/V}(\tau)$ denote independent atomic noise modes for Bob's/Victor's ensemble (see App. D.1.2) with $[f_{x,B/V}(\tau), f_{p,B/V}(\tau')] = i\delta(\tau - \tau')$. Using these expressions, the attainable fidelity can be evaluated for different levels of noise (see Fig. 4.3b and Fig. 4.4). The results show that QND teleportation may be feasible for narrow distributions (using $n = 1$, $\bar{F}(n) = 0.76$ for $\kappa = 1.2$ and $\eta = 0.3\kappa^2$, while $F_{\text{clas}} = 0.6$).

4.1.4 Non-QND Teleportation

In this section, we consider the teleportation scheme depicted in Fig. 4.1 for a general quadratic interaction between atoms and light. In the following, we derive the atomic input-output relations describing this general scheme in the ideal case as well as including noise. We compare different variants of the setup for realistic values characterizing the interaction and atomic decoherence.

General input-output relations for the interaction of light with an ensemble in a magnetic field

Any quadratic Hamiltonian describing the interaction between two single mode continuous variable systems which are described by the operators x_A, p_A and x_L, p_L can be characterized in terms of two parameters s_1 and s_2 and expressed in the diagonal form $H = s_1 p_A p_L + s_2 x_A x_L$ [91] by means of suitable local operations. As in Sec. 2.1.2, the interaction between an atomic ensemble and light is here parametrized in the form

$$H_{\rm int} = \frac{\kappa}{\sqrt{T}}\left(p_A p_L \pm \frac{1}{Z^2} x_A x_L\right) = \frac{\kappa}{\sqrt{T}}\left(\frac{1}{2}\left[1 \pm \frac{1}{Z^2}\right] H_{\rm pas} - \frac{1}{2}\left[1 \mp \frac{1}{Z^2}\right] H_{\rm act}\right). \quad (4.4)$$

The interaction is either predominantly active or passive depending on the sign of the non-QND contribution. Recent experiments using ^{133}Cs ensembles at room temperature were based on a predominantly passive interaction with $Z = 2.5$ [III]. As explained in Sec. 2.1.2, the active variant can be realized by interchanging the polarization of the classical and quantum field [IV, VII, IX].

Interaction of a single ensemble with light in the ideal case

We consider here the Hamiltonian $H = H_{\rm A} + H_{\rm L} + H_{\rm int}$, where $H_{\rm A} = -\frac{\Omega}{2}(x_A^2 + p_A^2)$ and $H_{\rm int}$ is given by Eq. (4.4). In a rotating frame, this leads to the differential equations[7]

$$\begin{aligned}
\begin{pmatrix} \dot{x}_A(t) \\ \dot{p}_A(t) \end{pmatrix} &= \frac{\kappa}{\sqrt{T}} A_{\rm P/A}(\Omega, t) \begin{pmatrix} \bar{x}_L(ct, t) \\ \bar{p}_L(ct, t) \end{pmatrix}, \\
\begin{pmatrix} \dot{\bar{x}}_L(\xi, t) \\ \dot{\bar{p}}_L(\xi, t) \end{pmatrix} &= \frac{\kappa}{\sqrt{T}} L_{\rm P/A}(\Omega, t) \begin{pmatrix} x_A(t) \\ p_A(t) \end{pmatrix} \delta(\xi - ct),
\end{aligned}$$

where the definitions

$$\begin{aligned}
A_{\rm P/A}(\Omega, t) &= \begin{pmatrix} \mp\frac{1}{Z^2}\sin(\Omega t) & \cos(\Omega t) \\ \mp\frac{1}{Z^2}\cos(\Omega t) & -\sin(\Omega t) \end{pmatrix}, \\
L_{\rm P/A}(\Omega, t) &= \begin{pmatrix} \sin(\Omega t) & \cos(\Omega t) \\ \mp\frac{1}{Z^2}\cos(\Omega t) & \pm\frac{1}{Z^2}\sin(\Omega t) \end{pmatrix},
\end{aligned}$$

have been used. The input-output relations for the atomic quadratures are given by

$$\begin{pmatrix} x_A^{out} \\ p_A^{out} \end{pmatrix} = e^{\mp\frac{\kappa^2}{2Z^2}} \begin{pmatrix} x_A^{in} \\ p_A^{in} \end{pmatrix} + N_{\mp} \begin{pmatrix} x^{in}_{\rm r(P/A),\pm} \\ p^{in}_{\rm r(P/A),\pm} \end{pmatrix}, \quad (4.5)$$

with $N_+ = \sqrt{e^{\frac{\kappa^2}{Z^2}} - 1}$ and $N_- = \sqrt{1 - e^{-\frac{\kappa^2}{Z^2}}}$. The passive (active) reading modes $x_{\rm r(P),\pm}$, $p_{\rm r(P),\pm}$ ($x_{\rm r(A),\pm}$, $p_{\rm r(A),\pm}$) are defined according to

$$\begin{pmatrix} x^{in}_{\rm r(P/A),\pm} \\ p^{in}_{\rm r(P/A),\pm} \end{pmatrix} = \frac{\kappa}{\sqrt{T} N_{\pm}} \int_0^T dt\, e^{\frac{\pm\kappa^2 t}{2Z^2 T}} A_{\rm P/A}(\Omega, t) \begin{pmatrix} \bar{x}_L(ct, 0) \\ \bar{p}_L(ct, 0) \end{pmatrix}.$$

[7] The derivation of the input-output relation is shown in detail in App. D.1.

Regarding the light field, we are interested in the easily experimentally accessible $\sin(\omega t)$ and $\cos(\Omega t)$ modulated modes. The input-output relations for sine and cosine modulated light modes with arbitrary slowly varying envelope functions $h(t)$ (see Eq. (2.6)) are given by

$$\begin{aligned}
\begin{pmatrix} x^{out}_{h,sin} \\ x^{out}_{h,cos} \end{pmatrix} &= \begin{pmatrix} x^{in}_{h,sin} \\ x^{in}_{h,cos} \end{pmatrix} + \frac{\kappa}{\sqrt{2}T} \int_0^T dt\, h(t) e^{\mp \frac{\kappa^2 t}{2Z^2 T}} \begin{pmatrix} x^{in}_A \\ p^{in}_A \end{pmatrix} \\
&+ \frac{\kappa^2}{\sqrt{2}T^{\frac{3}{2}}} \int_0^T dt \int_0^t d\tau h(t) e^{\mp \frac{\kappa^2 (t-\tau)}{2Z^2 T}} A_{\mathrm{P/A}}(\Omega,\tau) \begin{pmatrix} \bar{x}_L(c\tau,0) \\ \bar{p}_L(c\tau,0) \end{pmatrix}, \\
\begin{pmatrix} p^{out}_{h,sin} \\ p^{out}_{h,cos} \end{pmatrix} &= \begin{pmatrix} p^{in}_{h,sin} \\ p^{in}_{h,cos} \end{pmatrix} + \frac{\kappa}{\sqrt{2}TZ^2} \int_0^T dt\, h(t) e^{\mp \frac{\kappa^2 t}{2Z^2 T}} \begin{pmatrix} p^{in}_A \\ -x^{in}_A \end{pmatrix} \\
&+ \frac{\kappa^2}{\sqrt{2}T^{\frac{3}{2}}Z^2} \int_0^T dt \int_0^t d\tau h(t) e^{\mp \frac{\kappa^2 (t-\tau)}{2Z^2 T}} A'_{\mathrm{P/A}}(\Omega,\tau) \begin{pmatrix} \bar{x}_L(c\tau,0) \\ \bar{p}_L(c\tau,0) \end{pmatrix},
\end{aligned} \tag{4.6}$$

with

$$A'_{\mathrm{P/A}}(\Omega,\tau) = \frac{1}{\Omega}\frac{d}{d\tau} A_{\mathrm{P/A}}(\Omega,\tau) = \begin{pmatrix} \mp\frac{1}{Z^2}\cos(\Omega\tau) & -\sin(\Omega\tau) \\ \pm\frac{1}{Z^2}\sin(\Omega\tau) & -\cos(\Omega\tau) \end{pmatrix}.$$

Due to the imbalanced squeezing ($Z^2 > 1$), it is advantageous to measure the x-quadrature of the light field (rather than the photonic p-quadrature) in order to obtain information on the atomic variables.

Interaction of a single ensemble with light including atomic decoherence

In the following, we include atomic decay at a constant rate η/T (the derivation can be found in App. D.1). Using $\gamma_{\mathrm{P}} = \frac{\kappa^2}{Z^2} + \eta$ we obtain

$$\begin{pmatrix} x^{out}_A \\ p^{out}_A \end{pmatrix} = e^{-\frac{\gamma_{\mathrm{P}}}{2}} \begin{pmatrix} x^{in}_A \\ p^{in}_A \end{pmatrix} + \frac{\kappa}{Z\sqrt{\gamma_{\mathrm{P}}}} \sqrt{1-e^{-\gamma_{\mathrm{P}}}} \begin{pmatrix} x^{in}_{r(\mathrm{P}),+,\eta} \\ p^{in}_{r(\mathrm{P}),+,\eta} \end{pmatrix} + \sqrt{\frac{\eta}{\gamma_P}} \sqrt{1-e^{-\gamma_{\mathrm{P}}}} \begin{pmatrix} F^{in}_{x_A,+,\eta} \\ F^{in}_{p_A,+,\eta} \end{pmatrix},$$

for the predominantly passive interaction, where

$$\begin{pmatrix} x^{in}_{r(\mathrm{P}),\pm,\eta} \\ p^{in}_{r(\mathrm{P}),\pm,\eta} \end{pmatrix} = \sqrt{\frac{\gamma_{\mathrm{P}}}{T}} \frac{Z}{N_{\pm,\eta}} \int_0^T dt e^{\frac{\pm\gamma_{\mathrm{P}} t}{2T}} A_{\mathrm{P}}(\Omega,t) \begin{pmatrix} \bar{p}_L(ct,0) \\ \bar{x}_L(ct,0) \end{pmatrix},$$

with $N_{+,\eta} = \sqrt{e^{\gamma_P} - 1}$, $N_{-,\eta} = \sqrt{1-e^{-\gamma_P}}$, and

$$\begin{pmatrix} F^{in}_{x_A,\pm,\eta} \\ F^{in}_{p_A,\pm,\eta} \end{pmatrix} = \sqrt{\frac{\gamma_{\mathrm{P}}}{T}} \frac{1}{N_{\pm,\eta}} \int_0^T dt e^{\frac{\pm\gamma_{\mathrm{P}} t}{2T}} \begin{pmatrix} f_{x_A}(t) \\ f_{p_A}(t) \end{pmatrix},$$

with $[f_{x_A}(t), f_{p_A}(t')] = \delta(t-t')$, $\langle f_{x_A}(t)\rangle = \langle f_{p_A}(t)\rangle = 0$ and $\langle f^2_{x_A}(t)\rangle = \langle f^2_{p_A}(t)\rangle = 1/2$ as above. The input-output relation for $\sin(\Omega t)$ and $\cos(\Omega t)$ modulated modes with arbitrary slowly varying envelope including atomic decoherence are given by

$$\begin{aligned}
\begin{pmatrix} x^{out}_{h,sin} \\ x^{out}_{h,cos} \end{pmatrix} &= \begin{pmatrix} x^{in}_{h,sin} \\ x^{in}_{h,cos} \end{pmatrix} + \frac{\kappa}{\sqrt{2}T} \int_0^T dt\, h(t) e^{-\frac{\gamma_{\mathrm{P}} t}{2T}} \begin{pmatrix} x^{in}_A \\ p^{in}_A \end{pmatrix} + \frac{\sqrt{\eta}\kappa}{\sqrt{2}T^{\frac{3}{2}}} \int_0^T dt \int_0^t d\tau h(t) e^{\frac{-\gamma_{\mathrm{P}}(t-\tau)}{2T}} \begin{pmatrix} f_{x_A}(\tau) \\ f_{p_A}(\tau) \end{pmatrix} \\
&+ \frac{\kappa^2}{\sqrt{2}T^{\frac{3}{2}}} \int_0^T dt \int_0^t d\tau h(t) e^{\frac{-\gamma_{\mathrm{P}}(t-\tau)}{2T}} A_{\mathrm{P}}(\Omega,\tau) \begin{pmatrix} \bar{x}_L(c\tau,0) \\ \bar{p}_L(c\tau,0) \end{pmatrix}.
\end{aligned} \tag{4.7}$$

Analogous equations hold for the predominantly active type of the interaction with $\gamma_A = -\frac{\kappa^2}{Z^2} + \eta$.

Non-QND teleportation protocol

In this section, we study the experimental feasibility of the teleportation scheme by considering its implementation in ^{133}Cs vapor [III, VII], [14, 15] as concrete example. In order to check whether atomic state teleportation between two ensembles at room temperature can be realized directly using the current setup, we assume $Z = 2.5$, as reported in [III]. To this end, we take only techniques that are already routinely used into account. This includes the detection of sine and cosine modulated light modes with arbitrary slowly varying readout modes. In the following, we show that using exponential mode functions, high fidelities can be reached even in the presence of noise.

Non-QND teleportation in the ideal case

The setup shown in Fig. 4.1 can be run in different variants, involving parallel or antiparallel magnetic fields and different types of interactions (predominantly active or mainly passive) in the first and second interaction. We compare all possible configurations. As expected, we find that the parallel setting yields the best fidelities irrespective of the type of interaction. In the following, we discuss the teleportation scheme therefore in detail for parallel oriented magnetic fields (the derivations for the antiparallel configuration can be found in App. D.3). To start with, it is assumed that the interaction between light and the first and second ensemble is the same. If a predominantly passive/active interaction is used, the corresponding Hamiltonian is given by

$$H_{1/2} = \frac{\kappa}{\sqrt{T}}\left(p_{B/V}\; p_L(0) \pm \frac{1}{Z^2} x_{B/V}\; x_L(0)\right) - \frac{\Omega}{2}\left(x_{B/V}^2 + p_{B/V}^2\right) + H_L,$$

where H_L denotes the free Hamiltonian of the light field as above. Step (i) of the teleportation scheme is described by the input-output relations Eq. (4.5) and Eq. (4.6) introduced above. Step (ii) results in

$$\begin{aligned}\begin{pmatrix}\tilde{x}_{h,sin}^{out}\\ \tilde{x}_{h,cos}^{out}\end{pmatrix} &= \frac{\kappa}{\sqrt{2}T}\int_0^T dt\, h(t) e^{\mp\frac{\kappa^2 t}{2Z^2T}}\begin{pmatrix} x_V^{in}\\ p_V^{in}\end{pmatrix} + \frac{\kappa}{\sqrt{2}T}\int_0^T dt\, h(t) e^{\mp\frac{\kappa^2 t}{2Z^2T}}\left(1 \mp \frac{\kappa^2 t}{Z^2T}\right)\begin{pmatrix} x_B^{in}\\ p_B^{in}\end{pmatrix}\\ &+ \begin{pmatrix}x_{h,sin}^{in}\\ x_{h,cos}^{in}\end{pmatrix} + \frac{\kappa^2}{\sqrt{2}T^{\frac{3}{2}}}\int_0^T d\tau \int_\tau^T dt\, h(t) e^{\mp\frac{\kappa^2(t-\tau)}{2Z^2T}}\left(2 \mp \frac{\kappa^2(t-\tau)}{Z^2T}\right) A_{\mathrm{P/A}}(\Omega,\tau)\begin{pmatrix}\bar{x}_L(c\tau,0)\\ \bar{p}_L(c\tau,0)\end{pmatrix},\end{aligned}$$

where

$$\begin{aligned}\begin{pmatrix}x_V(t)\\ p_V(t)\end{pmatrix} &= e^{\mp\frac{\kappa^2 t}{2Z^2T}}\begin{pmatrix} x_V^{in}\\ p_V^{in}\end{pmatrix} \mp \frac{\kappa^2 t}{Z^2T} e^{\mp\frac{\kappa^2 t}{2Z^2T}}\begin{pmatrix} x_B^{in}\\ p_B^{in}\end{pmatrix}\\ &+ \frac{\kappa}{\sqrt{T}}\int_0^t d\tau\, e^{\mp\frac{\kappa^2(t-\tau)}{2Z^2T}}\left(1 \mp \frac{\kappa^2(t-\tau)}{Z^2T}\right) A_{\mathrm{P/A}}(\Omega,\tau)\begin{pmatrix}\bar{x}_L(c\tau,0)\\ \bar{p}_L(c\tau,0)\end{pmatrix}\end{aligned}$$

has been used. After step (iii) the final state of Bob's ensemble is given by

$$\begin{aligned}\begin{pmatrix} x_B^{fin} \\ p_B^{fin} \end{pmatrix} &= \frac{\kappa}{\sqrt{2}T}\int_0^T dt\, h(t) e^{\frac{\mp\kappa^2(t)}{2Z^2T}} G_+ \begin{pmatrix} x_V^{in} \\ p_V^{in} \end{pmatrix} + G_+ \begin{pmatrix} x_{g,sin}^{in} \\ x_{g,cos}^{in} \end{pmatrix} \\ &+ \left(e^{\frac{\mp\kappa^2}{2Z^2}} \mathbb{1} + \frac{\kappa}{\sqrt{2}T}\int_0^T dt\, h(t) e^{\frac{\mp\kappa^2 t}{2Z^2T}} (1 \mp \frac{\kappa^2 t}{Z^2T}) G_+ \right) \begin{pmatrix} x_B^{in} \\ p_B^{in} \end{pmatrix} + \frac{\kappa}{\sqrt{T}}\int_0^T d\tau e^{\frac{\pm\kappa^2\tau}{2Z^2T}} \\ &\left(e^{\frac{\mp\kappa^2}{2Z^2}} \mathbb{1} + \frac{\kappa}{\sqrt{2}T}\int_\tau^T dt\, h(t) e^{\frac{\mp\kappa^2 t}{2Z^2T}} \left(2 \mp \frac{\kappa^2(t-\tau)}{Z^2T}\right) G_+ \right) A_{\mathrm{P/A}}(\Omega,\tau) \begin{pmatrix} \bar{x}_L(c\tau,0) \\ \bar{p}_L(c\tau,0) \end{pmatrix},\end{aligned}$$

where G_+ is given by Eq. (4.3). The resulting average teleportation fidelities can be calculated using Eq. (4.2) and are shown in Fig. 4.5. Rather than using the same interaction in step (i) and step (ii), the protocol can also be run employing the predominantly active/passive type for the interaction between the light field and Bob's ensemble followed by by a predominantly passive/active light-matter interaction involving Victor's atomic state. This setting corresponds to

$$\begin{aligned} H_1 &= \frac{\kappa}{\sqrt{T}}\left(p_B\; p_L(0) \mp \frac{1}{Z^2} x_B\; x_L(0) \right) - \frac{\Omega}{2}\left(x_B^2 + p_B^2\right) + H_L, \\ H_2 &= \frac{\kappa}{\sqrt{T}}\left(p_V\; p_L(0) \pm \frac{1}{Z^2} x_V\; x_L(0) \right) - \frac{\Omega}{2}\left(x_V^2 + p_V^2\right) + H_L. \end{aligned}$$

Step (i) can be described by the input-output relations used before, Eq. (4.5) and Eq. (4.6) (with $Z^2 \to -Z^2$ for the active case). In the second step, the backaction modes cancel such that

$$\begin{pmatrix} x_V(t) \\ p_V(t) \end{pmatrix} = e^{\frac{\mp\kappa^2 t}{2Z^2T}} \begin{pmatrix} x_V^{in} \\ p_V^{in} \end{pmatrix} + \frac{\kappa}{\sqrt{T}}\int_0^t d\tau e^{\frac{\mp\kappa^2(t-\tau)}{2Z^2T}} A_{\mathrm{P/A}}(\Omega,\tau) \begin{pmatrix} \bar{x}_L(c\tau,0) \\ \bar{p}_L(c\tau,0) \end{pmatrix},$$

and step (ii) results accordingly in

$$\begin{aligned}\begin{pmatrix} \tilde{x}_{h,sin}^{out} \\ \tilde{p}_{h,cos}^{out} \end{pmatrix} &= \begin{pmatrix} x_{h,sin}^{in} \\ p_{h,cos}^{in} \end{pmatrix} + \frac{\kappa}{\sqrt{2}T}\int_0^T dt\, h(t) \left(e^{\frac{\pm\kappa^2 t}{2Z^2T}} \begin{pmatrix} x_B^{in} \\ p_B^{in} \end{pmatrix} + e^{\frac{\mp\kappa^2 t}{2Z^2T}} \begin{pmatrix} x_V^{in} \\ p_V^{in} \end{pmatrix} \right) \\ &+ \frac{\kappa^2}{\sqrt{2}T^{\frac{3}{2}}}\int_0^T dt \int_0^t d\tau h(t) \left(e^{\frac{\pm\kappa^2(t-\tau)}{2Z^2T}} A_{A/P}(\Omega,\tau) + e^{\frac{\mp\kappa^2(t-\tau)}{2Z^2T}} A_{P/A}(\Omega,\tau) \right) \begin{pmatrix} \bar{x}_L(c\tau,0) \\ \bar{p}_L(c\tau,0) \end{pmatrix}.\end{aligned}$$

The feedback operation in step (iii) leads to

$$\begin{aligned}\begin{pmatrix} x_B^{fin} \\ p_B^{fin} \end{pmatrix} &= \frac{\kappa}{\sqrt{2}T}\int_0^T dt\, h(t) e^{\frac{\mp\kappa^2 t}{2Z^2T}} G_+ \begin{pmatrix} x_V^{in} \\ p_V^{in} \end{pmatrix} + \left(e^{\frac{\pm\kappa^2}{2Z^2}} \mathbb{1} + \frac{\kappa}{\sqrt{2}T}\int_0^T dt\, h(t) e^{\frac{\pm\kappa^2 t}{2Z^2T}} G_+ \right) \begin{pmatrix} x_B^{in} \\ p_B^{in} \end{pmatrix} \\ &+ \frac{\kappa}{\sqrt{T}}\int_0^T d\tau \left(e^{\frac{\pm\kappa^2(T-\tau)}{2Z^2T}} + \frac{\kappa}{\sqrt{2}T}\int_\tau^T dt\; h(t) \left(e^{\frac{\pm\kappa^2(t-\tau)}{2Z^2T}} + e^{\frac{\mp\kappa^2(t-\tau)}{2Z^2T}} \right) G_+ \right) \begin{pmatrix} \sin(\Omega\tau)\bar{p}_L(c\tau,0) \\ \cos(\Omega\tau)\bar{p}_L(c\tau,0) \end{pmatrix} \\ &+ \int_0^T d\tau \left(\frac{\pm\kappa}{\sqrt{T}Z^2} e^{\frac{\pm\kappa^2(T-\tau)}{2Z^2T}} + \left(\sqrt{\frac{2}{T}} h(\tau) \pm \frac{\kappa^2}{\sqrt{2}T^{\frac{3}{2}}Z^2}\int_\tau^T dt\, h(t) (e^{\frac{\pm\kappa^2(t-\tau)}{2Z^2T}} - e^{\frac{\mp\kappa^2(t-\tau)}{2Z^2T}}) G_+ \right) \right) \\ &\begin{pmatrix} \sin(\Omega\tau)\bar{x}_L(c\tau,0) \\ \cos(\Omega\tau)\bar{x}_L(c\tau,0) \end{pmatrix}.\end{aligned}$$

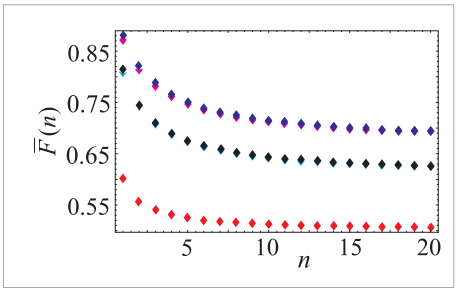

Figure 4.5: Average Non-QND teleportation fidelity $\bar{F}(n)$ versus width of the distribution of input states n for $Z = 2.5$, constant couplings and optimized exponential readout modes. The four topmost lines correspond (in descending order) to a active-active (violet), active-passive (pink), passive-active (black) and passive-passive (blue) configuration (see main text). The lowest line shown in red represents the classical limit.

Fig. 4.5 displays the attainable average teleportation fidelity $\bar{F}(n)$ for the four cases described in this section and shows that the active-active variant yields the best performance.

Non-QND teleportation including noise

As next step the teleportation scheme is analyzed in the presence of noise. The dominant source of noise impairing ensemble experiments of this type is the decay of the transverse spin components. Therefore, transverse decay is taken into account for realistic experimental parameters. In the following, the final expressions describing the quantum state of Bob's ensemble are presented and the corresponding average fidelity is evaluated. The derivation of the input-output relations can be found in App. D.3. If a setup involving the same type of light-matter interaction for both ensembles is considered and atomic decay at a constant rate η/T is assumed as in Sec. 4.1.4, Bob's final state is given by

$$
\begin{aligned}
\begin{pmatrix} x_B^{fin} \\ p_B^{fin} \end{pmatrix} &= \frac{\kappa}{\sqrt{2}T}\int_0^T dt\, h(t) e^{\frac{-\gamma_{\mathrm{A/P}} t}{2T}} G_+ \begin{pmatrix} x_V^{in} \\ p_V^{in} \end{pmatrix} + \frac{\kappa\sqrt{\eta}}{\sqrt{2}T^{\frac{3}{2}}}\int_0^T dt \int_0^t d\tau h(t) e^{-\frac{\gamma_{\mathrm{A/P}}(t-\tau)}{2T}} G_+ \begin{pmatrix} f_{x_V}(\tau) \\ f_{p_V}(\tau) \end{pmatrix} \\
&+ \left(e^{\frac{-\gamma_{\mathrm{A/P}}}{2}} \mathbb{1} + \frac{\kappa}{\sqrt{2}T}\int_0^T dt\, h(t) e^{\frac{-\gamma_{\mathrm{A/P}} t}{2T}} (1 \pm \frac{\kappa^2 t}{Z^2 T}) G_+ \right) \begin{pmatrix} x_B^{in} \\ p_B^{in} \end{pmatrix} \\
&+ \sqrt{\frac{\eta}{T}}\int_0^T d\tau e^{\frac{\gamma_{\mathrm{A/P}}\tau}{2T}} \left(e^{\frac{-\gamma_{\mathrm{A/P}}}{2}} \mathbb{1} + \frac{\kappa}{\sqrt{2}T}\int_\tau^T dt\, h(t) e^{\frac{-\gamma_{\mathrm{A/P}} t}{2T}} \left(1 \pm \frac{\kappa^2 (t-\tau)}{Z^2 T} \right) G_+ \right) \begin{pmatrix} f_{x_B}(\tau) \\ f_{p_B}(\tau) \end{pmatrix} \\
&+ \frac{\kappa}{\sqrt{T}}\int_0^T d\tau e^{\frac{\gamma_{\mathrm{A/P}}\tau}{2T}} \left(e^{\frac{-\gamma_{\mathrm{A/P}}}{2}} \mathbb{1} + \frac{\kappa}{\sqrt{2}T}\int_\tau^T dt\, h(t) e^{\frac{-\gamma_{\mathrm{A/P}} t}{2T}} \left(2 \pm \frac{\kappa^2 (t-\tau)}{Z^2 T} \right) G_+ \right) \\
&\begin{pmatrix} \cos(\Omega\tau)\bar{p}_L(c\tau, 0) \\ -\sin(\Omega\tau)\bar{p}_L(c\tau, 0) \end{pmatrix} + \int_0^T d\tau \frac{\kappa}{\sqrt{T}Z^2} e^{\frac{-\gamma_{\mathrm{A/P}}(T-\tau)}{2}} + \left(\sqrt{\frac{2}{T}} h(\tau) + \frac{\kappa^2}{\sqrt{2}T^{\frac{3}{2}}Z^2}\int_\tau^T dt \right. \\
&\left. h(t) e^{\frac{-\gamma_{\mathrm{A/P}}(t-\tau)}{2T}} (2 \pm \frac{\kappa^2 (t-\tau)}{Z^2 T}) G_+ \right) \right) \begin{pmatrix} \sin(\Omega\tau)\bar{x}_L(c\tau, 0) \\ -\cos(\Omega\tau)\bar{x}_L(c\tau, 0) \end{pmatrix}, \qquad (4.8)
\end{aligned}
$$

where the upper (lower) sign corresponds to a setting involving the active (passive) variant of the interaction. Using different types of interactions in step (i) and step (ii) as discussed above results in

$$\begin{aligned}
\begin{pmatrix} x_B^{fin} \\ p_B^{fin} \end{pmatrix} = & \frac{\kappa}{\sqrt{2}T}\int_0^T dt\, h(t) e^{\frac{-\gamma_{\mathrm{P/A}}\, t}{2T}} G_+ \begin{pmatrix} x_V^{in} \\ p_V^{in} \end{pmatrix} + \frac{\kappa\sqrt{\eta}}{\sqrt{2}T^{\frac{3}{2}}}\int_0^T dt \int_0^t d\tau h(t) e^{\frac{-\gamma_{\mathrm{P/A}}(t-\tau)}{2T}} G_+ \begin{pmatrix} f_{x_V}(\tau) \\ f_{p_V}(\tau) \end{pmatrix} \\
& + \left(e^{\frac{-\gamma_{\mathrm{A/P}}}{2}} \mathbb{1} + \frac{\kappa}{\sqrt{2}T}\int_0^T dt\, h(t) e^{\frac{-\gamma_{\mathrm{A/P}}\, t}{2T}} G_+ \right) \begin{pmatrix} x_B^{in} \\ p_B^{in} \end{pmatrix} \\
& + \sqrt{\frac{\eta}{T}}\int_0^T d\tau e^{\frac{\gamma_{\mathrm{A/P}}\,\tau}{2T}} \left(e^{-\frac{\gamma_{\mathrm{A/P}}}{2}} + \frac{\kappa}{\sqrt{2}T}\int_\tau^T dt\, h(t) e^{\frac{-\gamma_{\mathrm{A/P}}\, t}{2T}} G_+ \right) \begin{pmatrix} f_{x_B}(\tau) \\ f_{p_B}(\tau) \end{pmatrix} \\
& + \frac{\kappa}{\sqrt{T}}\int_0^T d\tau \left(e^{\frac{-\gamma_{\mathrm{A/P}}(T-\tau)}{2T}} \mathbb{1} + \frac{\kappa^2}{\sqrt{2}T}\int_\tau^T dt\, h(t) (e^{\frac{-\gamma_{\mathrm{A/P}}(t-\tau)}{2T}} + e^{\frac{-\gamma_{\mathrm{P/A}}(t-\tau)}{2T}}) G_+ \right) \begin{pmatrix} \cos(\Omega\tau)\bar{p}_L(c\tau,0) \\ -\sin(\Omega\tau)\bar{p}_L(c\tau,0) \end{pmatrix} \\
& + \int_0^T d\tau \left(\frac{\kappa}{Z^2\sqrt{T}} e^{\frac{-\gamma_A(T-\tau)}{2T}} + \sqrt{\frac{2}{T}} h(\tau) + \frac{\kappa^2}{\sqrt{2}T^{\frac{3}{2}}Z^2}\int_\tau^T dt\, h(t) (e^{\frac{-\gamma_{\mathrm{A/P}}(t-\tau)}{2T}} - e^{\frac{-\gamma_{\mathrm{P/A}}(t-\tau)}{2T}}) G_+ \right) \\
& \begin{pmatrix} \sin(\Omega\tau)\bar{x}_L(c\tau,0) \\ \cos(\Omega\tau)\bar{x}_L(c\tau,0) \end{pmatrix}, \qquad (4.9)
\end{aligned}$$

where the upper (lower) sign corresponds to an active-passive (passive-active) setting. The resulting teleportation fidelities are displayed in Fig. 4.2b. The obtained results show that the protocol studied here yields fidelities which well surpass the classical limit even if large decay rates are taken into account. This renders the protocol a very promising candidate for the immediate realization of atomic state teleportation between two ensembles at room temperature.

4.2 Quantum memory assisted probing of dynamical spin correlations

The high degree of controllability and versatility available in ultracold atoms in optical lattices renders this system a promising platform for the simulation and investigation of quantum many-body states and make it very attractive for studying new physics such as non-equilibrium phenomena. However, the realization of important prerequisites such as tools for the detection and manipulation of quantum many-body states is still challenging. In this section, a method for probing dynamical spin correlations of strongly interacting systems in optical lattices is proposed. As explained below, the scheme uses a light-matter quantum nondemolition interaction to map a nontrivial magnetic observable of a strongly correlated system to light. This probing procedure is performed at different instances of time and a quantum memory is used to coherently store the information between two subsequent applications of the mapping scheme for a time comparable to the many-body dynamics. A final readout of the memory yields direct access to dynamical correlations. This method introduces the use of quantum memories to the field of quantum simulation of many-body systems.

Below, the state of the art and related work are briefly reviewed in Sec. 4.2.1 and

the setup under consideration is introduced in Sec. 4.2.2. The new method proposed here is compared to an alternative approach based on the evaluation of data obtained from independent measurements, which is analyzed in Sec. 4.2.3. In Sec. 4.2.4, the protocol for accessing dynamical correlation in strongly correlated systems using a quantum memory is described and in Sec. 4.2.5, the application of the proposed scheme for probing the dynamics of coupled double-well superlattices is considered as specific example.

4.2.1 State of the art and related work

The quantum simulation of condensed matter physics with ultracold atoms in optical lattices requires the ability to prepare, manipulate, and probe many-body states [19–21]. Seminal experiments in this field range from the realization of a Bose-Einstein condensate with alkali atoms in the weak-coupling regime [133,134], to the Mott insulator to superfluid transition in the strongly interacting regime [23, 24]. The simulation of quantum magnetism with ultracold atoms has become one of the main goals in the field [106, 216–218]. Bosons or fermions in a Mott insulating state are particularly promising candidate systems. Through strongly suppressed on-site number fluctuations, spins can be simulated by considering the internal degrees of freedom of the atoms. Such spin states can be encoded in the hyperfine structure in alkali atoms [19–21] or using the nuclear spins of alkaline-earth fermions [219–221]. At sufficiently low temperatures and entropies, the spin-spin interactions arising perturbatively from super-exchange processes are predicted to give rise to important phenomena as Neél ordering, SU(N) magnetism, spin Hall effects, and Stoner magnetism (see for example [222]). Quantum simulation with cold gases does not only aim at mimicking the phenomena encountered in condensed matter physics, but also at exploring new frontiers in physics. In particular, ultracold atoms allow for the investigation of non-equilibrium phenomena of closed many-body systems, which is a very active research area [223, 224]. Especially interesting aspects include for example the study how certain observables reach equilibrium after changing abruptly ("quenching") some of the parameters of the system, the influence of metastable states during the dynamics, the effect of the initial conditions if they are close to a critical point, and the relation of steady states with statistical mechanics. To address these questions experimentally, methods to probe and manipulate quantum many-body dynamics are of utmost interest. Among the experimental methods to probe ultracold gases, Bragg spectroscopy [225–229] can be used to extract static and dynamical structure factors. In this section, a method to probe dynamical correlations in strongly interacting systems using a light-matter quantum non-demolition (QND) interaction and a quantum memory is proposed. The QND interface is used to coherently map a relevant magnetic operator $\mathcal{J}$ at different times $(t, t+\tau, \dots)$ to the light *without* performing a measurement. The quantum memory allows for the storage of $\mathcal{J}$ between two consecutive matter-light interactions for a time τ, which is comparable to the time scale of the internal many-body dynamics. A final readout of the memory yields information on the dynamical spin correlations $\langle\psi|\mathcal{J}(t)\mathcal{J}(t+\tau)\mathcal{J}(t+2\tau)\dots|\psi\rangle$ for a given state $|\psi\rangle$. This quantum memory-assisted probing (QMAP) scheme is minimally destructive, does not depend on the linear response of the system to an external perturbation [230], and is also suitable for systems out of equilibrium, *i.e.* if $|\psi\rangle$ is not an eigenstate of the many-body Hamiltonian. Moreover, it is shown that the correlations

obtained using QMAP are fundamentally different from those obtained by repeating a QND measurement of $\mathcal{J}(t)$ at different instances of time and performing a correlation analysis. As explained in more detail below, the QMAP scheme stores the observable of interest at different times without performing consecutive measurements. A final single measurement retrieves quantum correlations of the system with itself at different instances of time.

4.2.2 Setup

QND measurements have been employed to generate spin squeezed states in cold atomic ensembles [169, 170], and have also been proposed to be used in probing schemes [64, 65, 231,232]. In the following, the focus will be on QND probing schemes, which are based on a Faraday interaction. As shown theoretically in [233,234], this type of protocol can be used to detect nontrivial magnetic ordering. A Faraday rotation [12] occurs if strongly polarized light interacts off-resonantly with the internal spin degrees of freedom of an atomic system, as described in Sec. 4.1.3. Here, strongly $\hat{\mathbf{x}}$-polarized light propagating along the $\hat{\mathbf{z}}$-axis is considered and described by time-integrated canonical operators $x_L = S_2/\sqrt{N_{\rm ph}}$ and $p_L = S_3/\sqrt{N_{\rm ph}}$, where S_2 (S_3) is the Stokes operator corresponding to the difference in the number of photons in ± 45 (in the two circular) polarizations, and $N_{\rm ph}$ is the total number of photons in the beam[8]. After the Faraday interaction,

$$x_L^{\rm out} = x_L^{\rm in} - \kappa \mathcal{J}(0), \tag{4.10}$$

where $x_L^{\rm in}$ ($x_L^{\rm out}$) is the light quadrature before (after) the interaction [12, 65]. This mapping, Eq. (4.10), is called **F** for later convenience. The coupling strength can be expressed as $\kappa = \sqrt{d\eta_A}$, where d is the optical depth of the atomic sample, and η_A is the single atom spontaneous emission probability induced by the probing. For cold samples, d can be larger than 100 [22] and hence $\kappa^2 \approx 10$ should be within reach. The observable

$$\mathcal{J} = \frac{1}{\sqrt{N}} \sum_n c_n j_n^z, \tag{4.11}$$

corresponds to the total modulated magnetization of the atoms illuminated by the light beam. N denotes the total number of atoms confined in an optical lattice, and j_n^z the z-component of the atomic spin at site n. The modulation given by the coefficients c_n reflects the spatial dependence of the light beam; in a standing wave configuration [65], $c_n = 2\cos(kna - \alpha)^2$, where k is the wave number of the probing laser, a is the lattice spacing, and α describes the shift between the probing standing wave and the optical lattice (note that both c_n and $\mathcal{J}$ depend on the tunable physical parameters k and α). The many-body operator $\mathcal{J}$ is a QND observable [235] since it commutes with the Faraday Hamiltonian used for the measurement. As required to measure nontrivial dynamical correlations, $\mathcal{J}$ does not commute with the many-body Hamiltonian. The light-matter interaction time can be chosen in the μsec range [169, 170], *i.e.*, much shorter than the relevant timescale of the many-body system and be considered instantaneous, such that

[8] The variables x_L and p_L correspond to the flat-top mode ($h(t) = 1$) defined in Eq. (2.6) in the absence of a magnetic field, i.e. without a $\sin(\Omega t)$ or $\cos(\Omega t)$ modulation (see Se. 2.1.3).

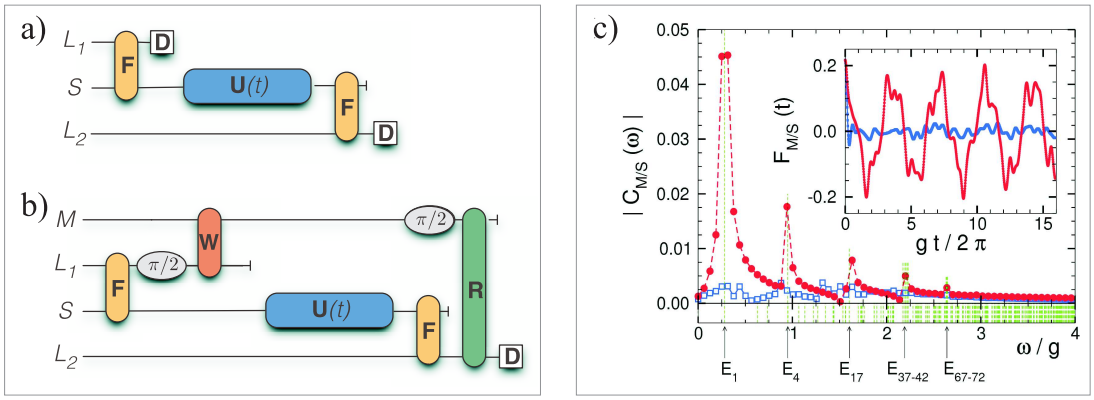

Figure 4.6: Quantum memory-assisted probing (QMAP). Panels a) and b) illustrate the probing of dynamical correlations, where S (M) denotes the many-body system (quantum memory), and L_i is the i-th light beam used in the respective protocols as described in the text. a) Scheme for measuring $\mathcal{J}$ at two different instances of time, yielding $F_S(t)$ after sufficiently many repetitions. b) Scheme for measuring $F_M(t)$ using a quantum memory. c) Signal obtained by probing the dynamics of coupled double-well superlattices. The results are obtained by exact diagonalization for a chain of 12 spins, considering a standing wave configuration with $k = \pi/(2a)$ and $\alpha = 0$. C_M (filled red circles and dashed line) and C_S (empty blue squares and solid line) are plotted as a function of ω. Vertical dashed green lines show the spectrum of the Hamiltonian Eq. (4.16). The inset shows $F_M(t)$ (see Eq. (4.15)) and $F_S(t)$ (see Eq. (4.12)) as a function of time t in red and blue color respectively.

the QND character of the interaction is preserved. As shown in [234], $\mathcal{J}$ corresponds to a nontrivial observable of magnetic systems. The proposal put forward here aims at using the QND probing scheme to access to correlations functions such as $\langle\psi|\mathcal{J}(t)\mathcal{J}(0)|\psi\rangle$ for any initial state ψ. Here, the measurement of two-time correlations is explained, extensions of this method to n-time correlations are straightforward.

4.2.3 Statistics based on independent measurements

In the following, the role of the quantum memory is explained by comparing the QMAP protocol to a scheme which relies on statistics based on independent measurements. More specifically, the information gained by a statistical analysis of independently performed QND measurements of $\mathcal{J}$ at different times, as schematically illustrated in Fig. 4.6a is analyzed. The many-body system (S) is initially prepared in state $|\psi\rangle$. At $t = 0$, a measurement of $\mathcal{J} = \sum_i a_i p_i$ is performed, where p_i projects onto the eigenspace with eigenvalue a_i. The measurement is realized by a QND Faraday interaction (F) between the system (S) and the light field (L), followed by a measurement of the relevant light quadrature. Depending on the outcome a_i, the state collapses to $p_i|\psi\rangle$. After the measurement, the state evolves ($U(t)$) under the many-body Hamiltonian during a time window of length t until a consecutive measurement of $\mathcal{J}$ is performed which yields the outcome

a_j. Accordingly, the statistical mean of the product of the two outcomes is given by

$$F_S(t,k,\alpha) = \sum_i a_i \langle\psi|p_i \mathcal{J}(t) p_i|\psi\rangle, \tag{4.12}$$

and depends on the standing wave configuration parameters k and α. Note that $F_S(t,k,\alpha)$ is related but not identical to $\langle\psi|\mathcal{J}(t)\mathcal{J}(0)|\psi\rangle$. If the system is initially prepared in the ground state, *i.e.* $|\psi\rangle = |E_0\rangle$, the Fourier transform of F_S is given by $C_S(\omega,k,\alpha) = \int dt e^{\mathrm{i}\omega t} F_S(t,k,\alpha) = \sum_{i,j} \xi_{ij}\delta(\omega-(E_i-E_j))$, where $\{E_i\}$ is the energy spectrum and ξ_{ij} can be trivially obtained. This quantity is peaked at frequencies corresponding to energy differences between the eigenenergies, which provides partial information regarding the energy spectrum. In Fig. 4.6c, $F_S(t,k,\alpha)$ and $C_S(\omega,k,\alpha)$ are plotted for a specific example which is discussed below. In the following, this result is compared to the information which can be obtained using quantum memory assisted probing.

4.2.4 Protocol for quantum memory assisted probing

In the following, the quantum memory assisted probing of spin dynamics is discussed with a focus on ensemble based memories [236]. As particular example, quantum memories which rely on an off-resonant Faraday interaction are considered, as described in [12] (see also Sec. 4.1.3). Faraday rotations have been experimentally realized using atomic samples at room temperature in [14], where a storage time of the order of 4 ms was reported. Longer storage times - up to 240 ms - have been achieved by means of electromagnetically induced transparency based memories using ultracold atoms in optical lattices [22]. The atomic ensembles are assumed to be strongly polarized along one direction, such that the transverse components of the collective spin, x_M and p_M, commute canonically within the Holstein-Primakoff approximation (compare Sec. 4.1). The Faraday interaction between the light field and the atomic ensemble (the quantum memory) yields the input-output relation[9]

$$x_M^{\mathrm{out}} = x_M^{\mathrm{in}} + \kappa_W p_L^{\mathrm{in}}, \tag{4.13}$$

with $x_M^{\mathrm{in}} = x_M(t=0)$ and $x_M^{\mathrm{out}} = x_M(t=\tau)$, where τ is the total (short) interaction time. This mapping will be referred to as writing operation **W**. The p - quadrature of the light field is conserved $p_L^{\mathrm{out}} = p_L^{\mathrm{in}}$. Both, light and matter quadratures, can be rotated according to $x \to \cos(\phi)x + \sin(\phi)p$ and $p \to \cos(\phi)p - \sin(\phi)x$ using linear optical elements. The quadrature stored in the quantum memory can be retrieved using a second light beam. The corresponding input-output relations for the light field are given by $x_L^{\mathrm{out}} = x_L^{\mathrm{in}} + \kappa_R p_M^{\mathrm{in}}$, $p_L^{\mathrm{out}} = p_L^{\mathrm{in}}$ and will be referred to as reading operation **R**. The QMAP protocol for measuring dynamical spin correlations using Faraday probing and a quantum memory is sketched in Fig. 4.6b and involves the following sequence of operations. **(F)**: At $t=0$, a Faraday interaction between the many-body system S and the first light pulse L_1 maps $\mathcal{J}$ to the light field, $x_{L_1}^{\mathrm{out}} = x_{L_1}^{\mathrm{in}} - \kappa_1 \mathcal{J}(0)$, $p_{L_1}^{\mathrm{out}} = p_{L_1}^{\mathrm{in}}$. A rotation of $\phi = \pi/2$ is applied to the output light quadrature. The rotated quadratures are labelled $\tilde{x}_{L_1}^{\mathrm{out}} = p_{L_1}^{\mathrm{out}}$ and $\tilde{p}_{L_1}^{\mathrm{out}} =$

[9] The QND input-output relations considered here differ from the ones used in Sec. 4.1, since the latter correspond to a setting involving a magnetic field, while the former do not.

$-x_{L_1}^{\text{out}}$. **(W)**: The p quadrature of the first light beam is mapped to the quantum memory M, which results in $x_M^{\text{out}} = x_M^{\text{in}} + \kappa_W \tilde{p}_{L_1}^{\text{out}} = x_M^{\text{in}} - \kappa_W(x_{L_1}^{\text{in}} - \kappa_1 \mathcal{J}(0))$. **(U)**: The many-body system evolves freely during a time interval t such that $\mathcal{J}(t) = U^\dagger(t)\mathcal{J}U(t)$. Due to the QND character of the Faraday interaction, $\mathcal{J}(t)$ is unaffected by the first interaction used to map its value to the memory. **(F+R)**: After rotating the quadratures of the atomic memory, $\tilde{x}_M^{\text{out}} = p_M^{\text{out}}$ and $\tilde{p}_M^{\text{out}} = -x_M^{\text{out}}$, the second light beam L_2 is sent through both the system and the memory such that $x_{L_2}^{\text{out}} = x_{L_2}^{\text{in}} - \kappa_2 \mathcal{J}(t) + \kappa_R \tilde{p}_M^{\text{out}}$. **(D)**: Finally, a balanced homodyne detection of $x_{L_2}^{\text{out}}$ is performed. The quantity of interest is the variance of this observable since $\text{var}(x_{L_2}^{\text{out}})$ yields the desired information on the dynamical correlations under investigation. More specifically, the variance of the x-quadrature of the light field is given by

$$\text{var}(x_{L_2}^{\text{out}}) = \eta(t) + \kappa_T F_M(t, k, \alpha), \tag{4.14}$$

where $\eta(t) = \mathcal{N} + \kappa_2^2 \,\text{var}\,(\mathcal{J}(t)) + \kappa_T^2/\kappa_2^2 \,\text{var}\,(\mathcal{J}(0))$ is the noise impairing the signal and $\kappa_T = \kappa_1\kappa_2\kappa_R\kappa_W$, with $\mathcal{N} = (1 + \kappa_R^2 + \kappa_R^2\kappa_W^2)/2$. Here, coherent input light fields and a coherent spin state for the memory with $\langle x^{\text{in}}\rangle = \langle p^{\text{in}}\rangle = 0$ and $\text{var}\left(x^{\text{in}}\right) = \text{var}\left(p^{\text{in}}\right) = 1/2$ are assumed. The noise contribution $\mathcal{N}$ can be neglected for $\kappa_1, \kappa_2 \gg \kappa_R, \kappa_W > 1$. By performing the two parts of the protocol independently, $\kappa_2^2 \text{var}\,(\mathcal{J}(t))$ and $\kappa_T^2/\kappa_2^2 \text{var}\,(\mathcal{J}(0))$ can be determined and thus subtracted. The remaining signal provides direct access to the symmetrized two-time dynamical correlation function of $\mathcal{J}$, that is,

$$F_M(t, k, \alpha) = \langle [\mathcal{J}(t), \mathcal{J}(0)]_+ \rangle - 2\langle \mathcal{J}(t)\rangle\langle \mathcal{J}(0)\rangle. \tag{4.15}$$

By inserting Eq. (4.11) into Eq. (4.15), $F_M(t, k, \alpha) = \sum_{n,m} c_n c_m \left[G_{mn}(t, 0) + G_{nm}(0, t)\right]/N$ is obtained, where the two point spin time correlation function $G_{mn}(t, t')$ is given by $G_{mn}(t, t') = \langle j_m^z(t) j_n^z(t')\rangle - \langle j_m^z(t)\rangle\langle j_n^z(t')\rangle$. If S is prepared in an eigenstate of the many-body Hamiltonian, the Fourier transform of F_M yields $C_M(\omega, k, \alpha) \propto \sum_n \xi_n[\delta(\omega - (E_n - E_0)) + \delta(\omega + (E_n - E_0))]$, which provides direct information on the energy spectrum. $C_M(\omega, \kappa, \alpha)$ can be related to the symmetric spin dynamical structure factor [237], which is well known to give access to the energy spectrum and the dispersion relation of the system. In this case, $\eta(t)$ is constant and the noise corresponds to a peak at zero frequency and can be thus easily distinguished from the signal with features at finite frequencies.

4.2.5 Probing of the dynamics of coupled double-well superlattices

As specific example, the dynamics of coupled double-well superlattices is considered and F_M (see Eq. (4.15)) is compared to the signal obtained by a statistical analysis F_S (see Eq. (4.12)) for this particular case. This system has been addressed both theoretically and experimentally in [106,238]. In the following, the one dimensional many-body Hamiltonian of $2N$ spins

$$H = \sum_{n=0}^{N-1} \left[g_1 \mathbf{j}_{2n} \cdot \mathbf{j}_{2n+1} + g_2 \mathbf{j}_{2n+1} \cdot \mathbf{j}_{2n+2}\right] \tag{4.16}$$

is considered, where $\mathbf{j} = (j^x, j^y, j^z)$, $j^{x,y,z}$ denote spin-1/2 operators, and $g_{1(2)}$ is the coupling between even-odd (odd-even) spins. This Hamiltonian can be implemented employing optical superlattices (see [106] and references therein) in the super-exchange regime obtained in deep lattices. In this case $g_{1(2)} = 4t_{1(2)}^2/U$, where $t_{1(2)}$ is the inter (intra) double well hopping rate, and U the on-site interaction energy. In this regime $g^{-1} \sim 10$ ms, which is of the same order of reported storing times (T) in quantum memories, cited before. The condition $gT \gg 1$ is required to resolve the dynamics of the many-body system, which demands either longer storage times or faster dynamics. Remarkably, a recent experiment [218] simulating antiferromagnetism using tilted optical lattices provides a faster dynamical timescale given by the tunneling rate, which relaxes the requirements on the quantum memory. Here, the equilibrium case with $g_1 = g_2 = g$ is addressed assuming that the system is initialized in the many-body ground state $|E_0\rangle$. In Fig. 4.6c, the discrete Fourier transforms of F_S and F_M (which are obtained using exact diagonalization) are plotted for the parameters stated in the figure caption (the inset shows F_S and F_M). The signal obtained by means of a statistical analysis F_S, is very weak and contains many frequencies. Therefore, the Fourier transform C_S is almost flat. If a quantum memory is used as explained above, much less frequencies are present in the signal and C_M shows large peaks at some of the energy levels, including the energy gap to the first excited state. It is also possible to study the non-equilibrium case by assuming that the system is initially prepared in the ground state of the Hamiltonian Eq. (4.16) with $g_1 = g$ and $g_2 = 0$, that is, a product of singlets between spins at even and odd lattice sites. At $t = 0$, the Hamiltonian is quenched to $g_1 = g_2 = g$, and the state evolves accordingly. The method put forward here allows one to explore thermalization effects characterized by dynamical correlations [239,240], which is an interesting study which is beyond the scope of this section.

In conclusion, it has been shown that a signal which exploits and benefits from quantum interference can be obtained by combining a QND light-matter interaction with a quantum memory. This method provides direct access to dynamical spin-spin correlations. It is remarkable that in the presence of a many-body Hamiltonian, which does not commute with the QND interaction, even the storage of a single quadrature in the quantum memory yields results, which are different from those obtained using a classical memory. The integration of quantum memories in coherent spectroscopy techniques offers many new possibilities. Particularly appealing are prospects for detection of multi-time correlations or the manipulation of many-body dynamics by performing conditional feedback operations on the quantum memory [12,171]. This could lead to novel studies of non-equilibrium physics and provide new tools for the engineering of quantum dynamics.

4.3 Quantum processing photonic states in optical lattices

In this section, a proposal for the realization of an entangling gate for photons is put forward. This scheme relies on light-matter interface techniques, which enable the map-

ping of the photonic input state to an ensemble of ultracold atoms in a Mott insulating state. The proposed protocol is deterministic and experimentally feasible under realistic conditions. In Sec. 4.3.1, the prospects and problems related to quantum information processing with photons are outlined and the current status in this field is briefly reviewed. The proposed scheme and its main features are outlined in Sec. 4.3.2. In Sec. 4.3.3, the key procedures are explained and in Sec. 4.3.4, the protocol is described in detail. Its performance in the presence of imperfections is discussed in Sec. 4.3.5.

4.3.1 Quantum information processing with light

Photons play a key role in applications of quantum information science since they are ideally suited to transmit quantum states between distant sites. This feature makes them indispensable for the realization of quantum communication protocols and the construction of quantum networks. While being a good flying carrier of information, photons are naturally less adequate for storage than atomic degrees of freedom. For this reason, long-lived matter systems are employed as quantum memories. In order to combine both elements in a quantum network (i.e. photons as flying qubits and atoms as memory devices), light-matter interface schemes have been developed to transfer quantum states of light to an atomic system. Some of these schemes are based on quantum-nondemolition interactions [14,241], electromagnetically induced transparency [157,159] and Raman processes [158]. Moreover, Raman processes have been used to entangle two distant atomic ensembles [158], which represents an important step towards the realization of quantum repeaters [67,180] and thus towards the solution of the problem of losses and decoherence existing in photonic channels. Apart from storing and transmitting information, the processing of quantum states is another important task in quantum networks. However, the manipulation of quantum states of light is still challenging, since this requires the ability to create entanglement between photons. This task is difficult because photons are noninteracting particles, in principle. One possibility to entangle photons is to employ materials possessing optical nonlinearities, but so far, there are no materials available whose nonlinearities are strong enough to allow for short gate times. An alternative approach has been put forward by Knill et al. [77], which requires only linear optical operations and measurements. However, this scheme is probabilistic and not very efficient in practice.
The scheme presented in this section allows for the realization of a deterministic entangling gate for photons using ultracold atoms in optical lattices. As explained in App. 2.2.1, this system consists of an ensemble of neutral atoms trapped by the periodic optical potential created by a standing wave. The resulting atom lattice is assumed to be prepared in a Mott insulating phase, in which the number of atoms in each site of the potential (i.e., in each of its minima) is approximately constant, and set to one [23, 24]. In the scheme described here, the photonic input state is mapped to a collective atomic state following light-matter interface schemes [14, 157–159, 241]. Once the input state is transferred to a collective state of the atomic system, the desired gate operation is performed by means of controlled atomic interactions. These controlled interactions due to collisions between atoms have been already used experimentally to create and manipulate highly entangled states, such as, for instance, cluster states [19,68,69,242,243]. As explained in App. 2.2.3, the controlled realization of collisions between atoms requires the ability to displace the

particles within the lattice depending on their internal state. The resulting entangled atomic state is then converted back to the photonic channel, and the protocol results in a deterministic two-qubit gate for photons. This way, the scheme combines the advantages of two successful experimental techniques that have been recently demonstrated, the techniques of quantum memories and repeater schemes on the one hand, and the ability to manipulate neutral atoms in a very clean and controllable environment on the other hand. It shows that atoms in optical lattices are not only suited to store quantum information, but also to process it at the same time.

4.3.2 Overview and main results

The gate operation realized by the scheme presented here transforms the photonic input state $|\Psi^{\text{in}}\rangle_L = \alpha|0\rangle_L + \beta|1\rangle_L + \gamma|2\rangle_L$, consisting of a a superposition of zero-, one-, or two-photon Fock states with corresponding coefficients α, β, and γ, into the output state $|\Psi^{\text{out}}\rangle_L = \alpha|0\rangle_L + i\beta|1\rangle_L + \gamma|2\rangle_L$. A phase i is applied if the parity of the photon number n is odd ($n = 1$), while no phase is applied in case of even parity ($n = 0$ or $n = 2$). Together with one-qubit rotations, this entangling operation is sufficient for universal quantum computation [244].

As outlined above, the quantum gate operation is implemented by mapping the input light state to an atomic ensemble, manipulating the resulting atomic state, and converting it back to a light state. More specifically, an atomic ensemble of N identical atoms possessing two internal states $|a\rangle$ and $|b\rangle$ is considered. The states $|a\rangle$ and $|b\rangle$ can for example be encoded in two different hyperfine ground states. All atoms are assumed to be initially prepared in state $|a\rangle$. The mapping of the light state to the ensemble can be realized by employing a quantum memory protocol that maps each incoming photon to a collective atomic excitation. This way, the one-photon Fock state $|1\rangle_L$ results in the collective atomic state $|1\rangle_A = \sum_{j=1}^{N} f_j |a\rangle_1 ... |b\rangle_j ... |a\rangle_N$ with $\sum_j^N |f_j|^2 = 1$. This state is a superposition of all possible N particle product states containing one atom in $|b\rangle$ and $N - 1$ atoms in $|a\rangle$ and represents one atomic excitation which is delocalized over the whole ensemble. The state containing two atomic excitations is defined in an analogous fashion. More generally, photonic Fock states $|n\rangle_L$ are mapped to collective atomic states with n excitations $|n\rangle_A$. The initial atomic state is therefore given by $|\Psi^{\text{in}}\rangle_A = \alpha|0\rangle_A + \beta|1\rangle_A + \gamma|2\rangle_A$.

In the next step, the quantum gate operation has to be applied to this state. As outlined below, a CNOT operation between two particles can be implemented by inducing a controlled collision between them. However, employing this tool includes the challenge to efficiently implement a nonlinear operation between collective states, using local interactions only. The following line of thoughts illustrates this difficulty. Using a naive approach, every atom has to interact with all other atoms in the ensemble, which would require $\mathcal{O}(N^2)$ operations. In a more sophisticated approach, a messenger atom could be chosen which interacts with all the other atoms in the sample. This procedure would still require $\mathcal{O}(N)$ controlled collisions, which is not experimentally feasible either. In contrast, the scheme put forward here requires only $\mathcal{O}(N^{1/3})$ interactions. This striking reduction is achieved by projecting the input state, which is shared by all N atoms in the ensemble, to a single qubit, which can be accessed and manipulated directly.

In order to perform the entangling gate, four kinds of basic operations are required, which are all within the experimental state of the art and do not require addressability of individual atoms. (1) *State dependent transport.* Atoms are displaced depending on their internal state using optical lattices with different polarizations [68, 69, 243] (see App. 2.2.2 for details). (2) *Population transfer between atomic states.* Coherent coupling of the two atomic levels can be achieved by driving Rabi oscillations. A $\pi/2$ pulse creates the coherent superposition $|a\rangle \mapsto (|b\rangle - |a\rangle)/\sqrt{2}$, $|b\rangle \mapsto (|b\rangle + |a\rangle)/\sqrt{2}$, while a π pulse inverts the atomic population. (3) *Collisional phase shift.* As described in App. 2.2.3, controlled collisions between particles in different states can be induced by spin dependent transport. If two particles occupy the same lattice site, a collisional phase $\phi_{\mathrm{col}} = \Delta E\ t_{\mathrm{int}}$ is accumulated [68, 69], where ΔE is the on–site interaction. By controlling the interaction time t_{int}, ϕ_{col} can be tuned. (4) *State-dependent phase shift.* A state-dependent single particle rotation can be obtained, for example, by applying a magnetic field. A detailed description of operational steps which have to be performed for realizing the desired gate is given in Sec. 4.3.3 and Sec. 4.3.4.

4.3.3 Processing of atomic states

As described in App. 2.2.3, controlled collisions can be utilized to manipulate a two-qubit state such that a phase π is introduced. This operation can be employed to implement a CNOT gate between two qubits. The key element used here is the displacement of control atoms in state $|b\rangle$ with respect to a set of target atoms which are prepared in state $|a\rangle$, such that collisions with the target qubits are induced[10] and the atoms located along its path are transferred to state $|b\rangle$. This tool is employed in two related methods, which lie at the heart of the proposed scheme.

Method (I): Creation of a d dimensional structure from a $(d-1)$- dimensional one

Starting from a control atom in $|b\rangle$ and an ensemble of target atoms in $|a\rangle$, a line of atoms in $|b\rangle$ can be produced. To this end, many CNOT operations are run in series, such that the control qubit in $|b\rangle$ acts successively on several target atoms in a row, which are accordingly transferred to state $|b\rangle$. The operational sequence, which has to be carried out is shown in Fig. 4.7. In Fig. 4.7a, the atomic ensemble, which is initially prepared in state $|a\rangle$, is shown as grey sphere, since the atomic sample occupies a spherical volume under typical experimental conditions. The black dot outside the sphere represents an isolated atom in state $|b\rangle$. Below, it is explained how such a configuration can be obtained. The atoms in the ensemble are the target qubits, while the isolated particle is the control qubit. First, a $\pi/2$ pulse is applied to the atomic ensemble transferring all target atoms to the

[10] For the realization of a CNOT gate, a control and a target atom are considered, which are for example placed along the $\hat{\mathbf{z}}$–axis at z_{c} and z_{t} (with $z_{\mathrm{t}} > z_{\mathrm{c}}$), respectively. First, a $\pi/2$ pulse is applied to the target atom $|a\rangle_{\mathrm{t}} \rightarrow (|b\rangle_{\mathrm{t}} - |a\rangle_{\mathrm{t}})/\sqrt{2}$. Then the $|b\rangle$ lattice is displaced along $\hat{\mathbf{z}}$, such that the control atom collides with the target atom and induces a π phase on $|a\rangle_{\mathrm{t}}$. Finally, the initial positions of the atoms are restored and a second $\pi/2$ pulse is applied to the target atom $(|b\rangle_{\mathrm{t}} + |a\rangle_{\mathrm{t}})/\sqrt{2} \rightarrow |b\rangle_{\mathrm{t}}$.

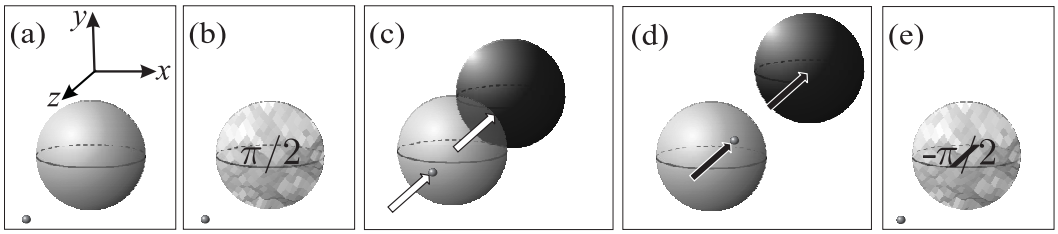

Figure 4.7: Creation of a line of atoms in $|b\rangle$. (a) A control atom in $|b\rangle$ is located outside an ensemble of atoms in $|a\rangle$. (b) A $\pi/2$ pulse is applied to the target atoms. (c) $|a\rangle$ and $|b\rangle$ components of the target qubits are separated spatially by a $|b\rangle$ lattice shift along $-\hat{\mathbf{z}}$. (d) The $|b\rangle$ lattice is further displaced along $-\hat{\mathbf{z}}$, such that the control atom in $|b\rangle$ interacts successively with the the $|a\rangle$ part of the target atoms along its path, each time leading to a collisional phase $\pi/2$. (e) Both lattice shifts are reversed such that all atoms are taken back to in their original positions. Then a second $\pi/2$ pulse is applied to the target qubits. Atoms that have interacted with the control atom are transferred to $|b\rangle$, while all other atoms in the ensemble are transferred back to $|a\rangle$.

superposition state $(|b\rangle - |a\rangle)/\sqrt{2}$ as shown in Fig. 4.7b. Then, the $|b\rangle$ lattice is displaced along $-\hat{\mathbf{z}}$, such that $|a\rangle$ and $|b\rangle$ components of the target qubits are separated spatially. This separation step is shown in Fig. 4.7c and has to be performed such that no collisional phases are accumulated. This can be done[11] by displacing the lattices first by half a lattice spacing along $\hat{\mathbf{x}}$ (or $\hat{\mathbf{y}}$) and then by a distance exceeding the length of the ensemble along $-\hat{\mathbf{z}}$. By displacing the $|b\rangle$ lattice further along $-\hat{\mathbf{z}}$ in the next step (compare Fig. 4.7d), collisions between the control atom and target atoms encountered on its path through the ensemble are induced. This way, the control atom interacts successively with all atoms along the indicated line, each time leading to a collisional phase $\phi_{\mathrm{col}} = \pi/2$. Both lattice shifts are reversed leaving all atoms in their original position. The affected target atoms are left in the state $(|b\rangle + |a\rangle)/\sqrt{2}$. In the last step shown in Fig. 4.7e, a $\pi/2$ pulse is applied to the target atoms. Since atoms, which are located on the path of the control qubit, have acquired a change of sign in the wave function, these atoms are transferred to state $|b\rangle$, while all other atoms in the ensemble are transferred back to state $|a\rangle$.
In an analogous fashion, a plane of atoms in state $|b\rangle$ can be produced using a line of control atoms instead of a single qubit. To this end, a line of control atoms in state $|b\rangle$ has to be swept through an ensemble of target atoms in $|a\rangle$. Following the steps described above, each control qubit in the line interacts with a line of atoms along its path, such that finally all target atoms located in this plane are transferred to $|b\rangle$.

[11] Alternatively, the lattice can be moved fast along $-\hat{\mathbf{z}}$. This way, the interaction time is very short and only a negligible collisional phase is accumulated. The displacement has to be done such that the atoms start and end up in their motional ground state [242, 245].

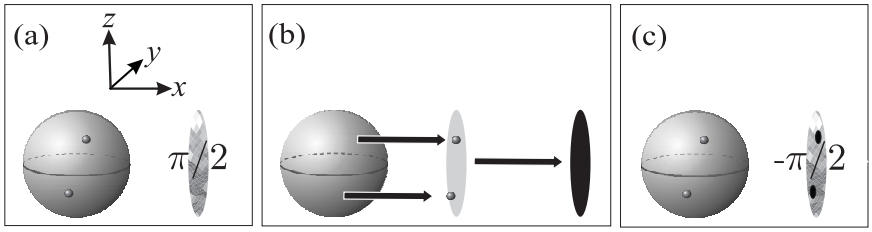

Figure 4.8: Mapping of excitations in the bulk to the plane. (a) A $\pi/2$ pulse is applied to the plane transferring all these qubits to the state $(|b\rangle - |a\rangle)/\sqrt{2}$. (b) The $|b\rangle$ lattice is shifted along $\hat{\mathbf{x}}$ such that atoms in $|b\rangle$ in the bulk interact with the $|a\rangle$ part of the plane. The time spent after each single site displacement is chosen such that a phase $\pi/2$ is accumulated if a collision occurs. Then this lattice movement is reversed such that the initial atomic positions are restored and each target atom which is located on the path of a control particle is in state $(|b\rangle + |a\rangle)/\sqrt{2}$. All other target atoms are still in state $(|b\rangle - |a\rangle)/\sqrt{2}$. (c) Finally the plane is subjected to another $\pi/2$ pulse, which transfers most of the atoms back to $|a\rangle$. Only atoms, taking part in a collision are transferred to $|b\rangle$.

Method (II): Mapping of collective excitations from an atomic ensemble of dimensionality d to a sample of dimensionality $d-1$

Fig. 4.8 illustrates how excitations in a three-dimensional ensemble can be mapped to a plane of particles. Fig. 4.8a shows an ensemble of atoms, where two atoms are in state $|b\rangle$, indicated by black dots. Note that collective excitations are delocalized. The state $|2\rangle_A$ corresponds to a superposition of all N-particle states with two atoms (at specific locations) in state $|b\rangle$. In this sense, Fig. 4.8 shows only one term of the superposition. Located next to the ensemble, a plane of particles in state $|a\rangle$ is shown. Both structures are separated in space but confined by the same optical lattice. Excitations in the ensemble can be mapped to excitations in the plane by using the atoms in the ensemble as control qubits acting on the target qubits in the plane, as described in the figure caption. Most atoms in the ensemble are in state $|a\rangle$ and do not induce any changes. However, in this example, two atoms in the ensemble are in state $|b\rangle$. Thus, collisions are induced if the $|b\rangle$ lattice is shifted along $\hat{\mathbf{x}}$ and the target atoms colliding with these control atoms along their paths through the plane are transferred to $|b\rangle$. This way, atoms in $|b\rangle$ are projected from the bulk to the plane. More precisely, this procedure leads to a mapping of a state with n atoms in $|b\rangle$ in the bulk to a state with n atoms in $|b\rangle$ in the plane, except if two atoms in $|b\rangle$ in the bulk are located in a line along $\hat{\mathbf{x}}$, leaving the corresponding target atom in $|a\rangle$ ($\mathrm{CNOT}^2 = 1$). In any case, an even (odd) number of excitations is mapped to an even (odd) number of excitations in the target object. This method allows for the stepwise reduction of the dimensionality of the problem. Collective excitations can be mapped from a plane to a line in an analogous fashion. Finally, excitations are mapped from a line to a single site ($d = 1$) and an odd number of excitations in the line transfers the target atom to state $|b\rangle$, while in case of an even number of excitations, this atom is left in state $|a\rangle$. Thus, the parity information is encoded in the state of a single atom.

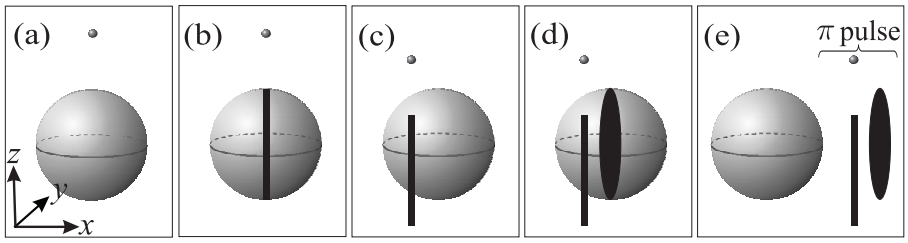

Figure 4.9: Initialization of the lattice. (a) A control atom in $|b\rangle$ is placed outside the ensemble. (b) The control qubit interacts successively with a row of target atoms in the ensemble, thus transferring them to state $|b\rangle$, as explained in Fig. 4.7. This way, a line of atoms in $|b\rangle$ is obtained, which is aligned along $\hat{\mathbf{z}}$. (c) The line is separated from the ensemble along $-\hat{\mathbf{y}}$. (d) The line of control qubits is now used to create a plane of atoms in $|b\rangle$. For this purpose, a $\pi/2$ pulse is applied to the ensemble, collisions are induced by a $|b\rangle$ lattice shift along $\hat{\mathbf{y}}$ and a $-\pi/2$ pulse is applied to the bulk. Since each control atom in the line leads to a line of atoms in $|b\rangle$, that is aligned along $\hat{\mathbf{y}}$, a plane in the $\hat{\mathbf{y}} - \hat{\mathbf{z}}$ plane is obtained. (e) The plane is separated from the ensemble by a $|b\rangle$ lattice shift along $\hat{\mathbf{x}}$, and a π pulse is applied, which leaves the atoms in the plane, the line, and the dot in state $|a\rangle$.

4.3.4 Quantum gate protocol

In this subsection, we introduce the main idea and describe the steps which have to be carried out in order to perform the desired quantum gate. We conclude this subsection by explaining the gate operation realized by this scheme based on its truth table.

Operation sequence

As explained above, the photonic input state is transferred to an atomic ensemble. Then, the gate operation is performed on the collective atomic input state, which is thereafter converted back to light. The main idea behind the processing of the delocalized atomic state is the stepwise mapping of collective excitations to structures of lower dimension. More specifically, collective excitations are first mapped from the three-dimensional Mott insulator to a plane of particles, then to a line, and finally, to a single atom. The whole scheme comprises two stages. During an initialization phase, the atoms are divided into four sets - the bulk, a plane, a line, and a dot - which are confined by the same optical lattice but spatially separated. Once this setup has been prepared, it can be used many times to perform gates. In the second phase, the gate protocol itself is performed. Below, the preparation of the setup is explained followed by a description of the processing stage.

Preparation of the lattice
The initialization protocol is summed up in Fig. 4.9. First, a single collective excitation is created in the ensemble, for example, by mapping a one-photon Fock state to the atomic sample by means of a light-atom interface scheme [14, 157–159, 241][12]. More specifically, after the absorption of the single photon, the atomic ensemble is in a superposition of all

[12] This can, for instance, be done employing heralded single photons from an EPR source. An atomic

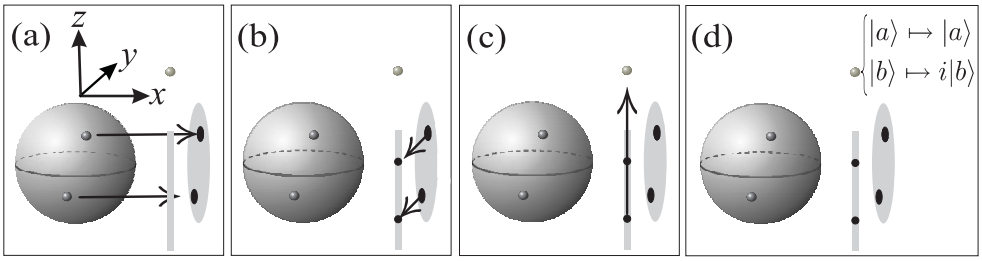

Figure 4.10: Quantum gate protocol transforming the input state $|\Psi^{\text{in}}\rangle_A = \alpha|0\rangle_A + \beta|1\rangle_A + \gamma|2\rangle_A$ into $|\Psi^{\text{out}}\rangle_A = \alpha|0\rangle_A + i\beta|1\rangle_A + \gamma|2\rangle_A$. (a) to (c) Excitations in the Mott insulator are successively mapped to structures of lower dimensionality resulting in a single atom in state $|a\rangle/|b\rangle$ in case of an even/odd number of excitations in the Mott insulator. (d) A state dependent phase is applied to the isolated particle such that $|1\rangle_A \mapsto i|1\rangle_A$. Subsequently steps (a) to (c) have to be reversed.

possible N particle product states with one atom in $|b\rangle$ and all other atoms in $|a\rangle$. Now, a $|b\rangle$ lattice shift is applied such that the (single) atom in state $|b\rangle$ is separated from the bulk of atoms in $|a\rangle$. This is a global operation acting on all atoms at the same time that affects only one atom (which is in state $|b\rangle$). In the next step, method (I) is applied to create a line of atoms in $|b\rangle$, using the isolated atom as control qubit[13]. Subsequently, this line is separated from the bulk and utilized to produce a plane of atoms in $|b\rangle$ employing the same method. Finally, the isolated atom, the line, and the plane are displaced by another global $|b\rangle$ lattice shift such that the constellation shown in Fig. 4.9e is obtained. Finally, a π pulse is applied to the plane, the line, and the dot transferring these atoms to state $|a\rangle$.

Quantum gate protocol.
The quantum gate protocol is summarized in Fig. 4.10. Once the light state is transferred to the bulk, the resulting collective atomic excitations are mapped to the plane of atoms by means of method (II). These excitations are mapped from the plane to the line in the next step in an analogous fashion. The projection sequence is completed by applying method (II) a third time and finally, mapping the excitations from the line to the single separated particle. This way, the parity of the number of excitations contained in the bulk is mapped to the dot, transferring the isolated atom to state $|b\rangle$ in case of one excitation, while it remains in state $|a\rangle$ otherwise. Now a state dependent phase shift is applied to the dot such that a phase $\pi/2$ is introduced if the atom is in state $|b\rangle$. This way, the phase i is only applied if an odd number of collective excitations has been initially present in the bulk and atomic states are transformed according to $|0\rangle_A \mapsto |0\rangle_A$, $|1\rangle_A \mapsto i|1\rangle_A$,

excitation can also be created by means of a weak coherent field together with a postselecting photon detection [157–159].

[13] If the path of the control atom is located at the edge of the cloud, short lines are produced. This can be avoided by focusing the light field, which is used in the first step of the preparation, to the center of the Mott insulator along $\hat{\mathbf{x}}$ and $\hat{\mathbf{y}}$. This way, the light field acts on a cylindrical volume centered at the center of the Mott insulator, restricting the deviation in length. Note that this procedure does not require individual addressing.

$|2\rangle_A \mapsto |2\rangle_A$. The described mapping sequence results in an entangled state of the bulk, the plane, the line, and the dot. In order to apply a light-matter interface protocol, which transfers the atomic state back to a photonic channel, the initial atomic state (up to the introduced phase) has to be restored. To this end, the previous steps have to be reversed. After converting the final atomic state to light, the setup is left in the original state and can be used again to perform a quantum gate operation.

Truth table

Now the truth table corresponding to the protocol is considered. After the mapping of the photonic state to the atomic ensemble, the bulk is in a state containing zero, one, or two collective excitations. Since a collective atomic state $|n\rangle_A$ is a superposition of atomic states with n atoms in $|b\rangle$ and $N-n$ atoms in $|a\rangle$, all possible configurations are included in this superposition. These possible initial atomic states of the bulk with n atoms in $|b\rangle$ located at certain lattice sites, corresponding to a configuration k are denoted by $|B_k^n\rangle_b$. $|P\rangle_p$ and $|L\rangle_l$ refer to the initial state of the plane and the line, respectively, where all atoms are in state $|a\rangle$. The three-step projection sequence of the protocol described above produces the map $|B_k^n\rangle_b|P\rangle_p|L\rangle_l|a\rangle_d \mapsto |B_k^n\rangle_b|P_k^{n'}\rangle_p|L_k^{n''}\rangle_l|a_n\rangle_d$. $|P_k^{n'}\rangle_p$ and $|L_k^{n''}\rangle_l$ denote the states of the plane and line after the excitations have been mapped and $|a_n\rangle_d$ describes the state of the dot with $a_0 = a_2 = a$ and $a_1 = b$. After applying the state dependent phase i and reversing all the previous steps, the protocol results in

$$|B_k^n\rangle_b|P\rangle_p|L\rangle_l|a\rangle_d \mapsto i^{n \bmod 2}|B_k^n\rangle_b|P\rangle_p|L\rangle_l|a\rangle_d. \tag{4.17}$$

The initial atomic state under consideration features not only a superposition of atoms in $|b\rangle$ at different positions in the ensemble, but also a superposition of different positions of the plane, the line, and the dot. This is due to the fact that the excitation created at the beginning of the initialization is delocalized and these positions depend on the initial position of the control atom in $|b\rangle$. However, for any term in the superposition, the final state differs only in a phase from the initial state. By adding the terms in Eq. (4.17) with respect to the positions of the excitations, k, and the positions of the plane, the line, and the dot, the desired quantum gate transformation is obtained. Note that the protocol does not rely on a coherent superposition of the different positions of the dot, the line, and the plane. It can also be run using a mixed state.

4.3.5 Performance of the quantum gate in the presence of noise

In this subsection, the main sources of errors of the scheme are analyzed. The specific design of the protocol minimizes decoherence and is optimized such that imperfections have only a small effect on the performance of the quantum gate despite the large number of particles involved. It has been carefully designed in order to minimize decoherence, first of all, by avoiding the presence of cat states in the internal atomic states, which would give rise to errors if few particles are lost. Apart from that, runtimes are very short such that decoherence has not much time to act. In particular, the time required to perform the scheme is essentially given by the time needed to run the collisional steps, since population transfers and separations can be done much faster. Each collisonal step

has to be performed along a whole ensemble length and requires therefore a time $t_{\rm int}N^{1/3}$, where $t_{\rm int}$ is the time spent in a single collision. Remarkably, the three dimensional problem scales like a one dimensional one in time, since the task of scanning N particles in a three dimensional lattice is accomplished by a one dimensional projection scheme.

In the following, transitions from $|a\rangle$ to $|b\rangle$ or to another trapped state affected by $|b\rangle$ lattice shifts are addressed and it is exemplified how a judicious choice of atomic levels allows one to sidestep this source of errors, while still being able to perform the operations that are necessary for the quantum gate. For example, by employing alkali atoms with nuclear spin 1/2, the atomic qubit can be encoded in hyperfine states of the $S_{1/2}$ shell by identifying $|a\rangle \equiv |F=1, m_F=-1\rangle$, and $|b\rangle \equiv |F=1, m_F=1\rangle$. A state dependent transport mechanism can be implemented by trapping $|F=1, m_F=-1\rangle$ and $|F=1, m_F=1\rangle$ by σ_- and σ_+ polarized light respectively, if the detuning of two off–resonant standing waves with different polarizations [68, 69] is chosen appropriately, Transitions $|a\rangle \mapsto |b\rangle$ cannot be induced by means of the off–resonant laser fields, since the state $|a\rangle$ corresponds to the nuclear magnetic quantum number $m_I=-1/2$, while the state $|b\rangle$ corresponds to $m_I=1/2$. $\pi/2$ or π pulses can be applied by means of resonant two-photon Raman or microwave transitions. Finally, the standing waves do induce transitions to the other trapped states $|F=1, m_F=0\rangle$ and $|F=0, m_F=0\rangle$. However, the optical potential experienced by these levels is given by the equally weighted sum of contributions from both polarizations. While shifting one lattice with respect to the other, the optical potential vanishes at some point, and these two levels are emptied, which ensures that they do not affect the protocol.
Among the other noise mechanisms, the most important ones are imperfect population transfer and dephasing of quantum states[14] between two $\pi/2$ pulses. The corresponding probability of error is proportional to the number of target atoms in the mapping steps $N^{2/3}$. This failure probability can be reduced by using an elongated atomic ensemble having a spatial extend L along the direction of the first lattice shift in the quantum gate protocol and a length $l < L$ along the other directions. In this case the probability of obtaining a wrong result is proportional to l^2.
The probability of error due to the remaining noise mechanism scales at worst like $N^{1/3}$, i.e. proportional to the runtime of the protocol. First, imperfections in the π pulse, which is performed at the end of the initialization of the lattice are considered. Since an imperfect population transfer leaves atoms in a superposition state, the $|b\rangle$ lattice should be emptied as an additional step of the initialization after the π pulse.
Another source of errors are occupation number defects. Only empty lattice sites have to be considered here, since double occupied sites can be avoided by choosing low filling factors. Holes in the plane and the line lead to a wrong result, if they are located at specific sites which interact with an atom in $|b\rangle$ in the course of the processing protocol.

[14] Inhomogeneous background fields are an important source of dephasing since they lead to uncontrolled relative phases β in superposition states $(|a\rangle + e^{i\beta}|b\rangle)/\sqrt{2}$ during the state dependent transport. Since all lattice shifts are reversed in the protocol, this effect can be suppressed by applying a single π pulse that swaps the levels $|a\rangle$ and $|b\rangle$ after each shift, before the atoms are transported back. This way, both components acquire the same phase. A π pulse has to be applied once each time the motion of the atoms is reversed, that is, only 6 times during the whole quantum gate protocol.

The failure probability due to defects which are initially present in the Mott insulator are given by the probability for a single site to be unoccupied, and does not depend on the size of the system. Holes can also be created as consequence of atomic transitions into untrapped states. This dynamical particle loss induces an error which scales like the duration of the gate, $N^{1/3}$. Another limiting factor are imperfect collisions. The phase acquired in each lattice shift during the collisional steps may differ from $\phi_{\mathrm{col}} = \pi$. However, as in the case of unoccupied lattice sites, the probability of obtaining a wrong result due to such an event is given by the probability on the single-site level. The fidelity of the scheme is also decreased by undesired collisional phases. The corresponding failure probability is proportional to $N^{1/3}$, since these phases are accumulated in one dimensional operations each covering one ensemble length. Finally, kinetic phases acquired by the atoms during lattice shifts do not play a role in the proposed scheme. Employing the common technique for state dependent transport, the nodes of two optical potentials forming standing waves are moved in opposite directions $V_{\pm}(x) = \cos^2(kx \pm \phi)$ for some wave vector k, spatial variable x and angle ϕ. Lattice shifts affect therefore both atomic species in the same way and lead only to global phases of the resulting quantum states.

Chapter 5

Number correlated states in Bose-Einstein condensates and optical cavities

This chapter is concerned with single atoms in high-finesse optical cavities (Sec. 5.1) and Bose-Einstein condensates interacting with freely propagating light (Sec. 5.2). Both sections focus on the creation and detection of correlations in the number basis. In Sec. 5.1, a multi-purpose cavity quantum electrodynamics setup is proposed and analyzed, which allows for the generation and purification of highly entangled photon number correlated states as well as for number-resolved nondestructive photon counting. In Sec. 5.2, the superradiant scattering of coherent light from an elongated BEC is studied. This process involves the creation of Einstein-Podolsky-Rosen (EPR) entanglement between atoms and light. Below, it is shown how this type of entanglement can be detected by means of particle number measurements and how this process can be used to create and distill inter-atomic entanglement by photon counting. The results presented in Sec. 5.1 and Sec. 5.2 have been published in [VI] and [VIII] respectively.

5.1 Quantum state engineering, purification, and photon counting in high finesse cavities

In this section, a multi-functional setup consisting of high finesse optical cavities, beam splitters and phase shifters is put forward and analyzed. The basic scheme projects arbitrary photonic two-mode input states onto the subspace spanned by the product of Fock states $|n\rangle|n\rangle$ with $n = 0, 1, 2, \ldots$. The proposed protocol does not allow for the conditional generation of highly entangled photon number states as resource for quantum information protocols, but provides also a possibility to test and hence purify this type of quantum states in a communication scenario, which is of great practical importance. This scheme is especially attractive as a generalization to many modes allows for distribution and purification of entanglement in networks. In an alternative working mode, the setup allows of quantum-nondemolition number resolved photodetection in the optical domain.

In Sec. 5.1.1, the proposal is introduced and related work and the state of the art are briefly reviewed. In Sec. 5.1.2, the central idea is explained and the main results are summarized. The nondestructive conditional projection of photonic states onto photon number correlated states is described in Sec. 5.1.3, in Sec. 5.1.4, it is shown that a modified version of the setup can act as a nondestructive photon number resolving detector, and in Sec. 5.1.5, the possibility to use the setup to detect, and thereby filter out losses is investigated.

5.1.1 State of the art and related work

Photons are attractive carriers of quantum information since the interactions of light with the surroundings are typically weak. However, for the same reason it is generally difficult to prepare, manipulate, and measure quantum states of light in a nondestructive way. As explained in Sec. 2.3, repeated interactions provide a method to increase the effective coupling strength between light and matter, and the backreflection of light in a cavity thus constitutes an interesting tool, in particular, because experiments are currently moving into the strong coupling regime [112–115].
Here, a versatile setup consisting of an array of cavities and passive optical elements (beam splitters and phase shifters) is proposed, which allows for quantum state engineering, quantum state purification, and nondestructive number resolving photon detection. The setup relies on two basic ingredients, the Hong-Ou-Mandel interference effect [246] generalized to input pulses containing an arbitrary number of photons and the possibility to project onto the subspace of even or the subspace of odd photon number states using cavity quantum electrodynamics in the strong coupling regime.
Regarding quantum state engineering, the basic setup provides a possibility to conditionally generate photon number correlated states. More specifically, the setup allows for the projection of an arbitrary photonic two mode input state onto the subspace S spanned by the state vectors $|n\rangle|n\rangle$ with $n = 0, 1, 2, \ldots$. The scheme is probabilistic and involves conditioning on a specific measurement outcome. The success probability equals the norm of the projection of the input state onto S and equals unity if the input state already lies in S. Therefore, the setup can be understood as a filter [247], which removes all undesired components of the quantum state and leaves the desired components unchanged. This way, it is for example possible to use two independent coherent states as input and obtain a photon number correlated state as output.
Photon number correlated states, for example Einstein-Podolsky-Rosen (EPR) entangled states [248], are an important resource for quantum teleportation [189, 199, 203, 211, 249], entanglement swapping [212, 250, 251], quantum key distribution [4, 213], and Bell tests [252, 253]. In practice, however, the applicability of these states is hampered by noise effects such as photon losses. Real-world applications require therefore entanglement purification. The proposed setup is very attractive for detection of losses and can in particular be used to purify photon number entangled states on site. If a photon number correlated state, for example an EPR state, is used as input, the desired state passes the setup with a certificate, while states which suffered from photon losses are detected and can be rejected.
Photon losses are a particlularly serious problem in quantum communication over long

distances. It is not only a very common source of decoherence which is hard to avoid, but also typically hard to overcome. The on-site purification protocol mentioned above can easily be adopted to a communication scenario such that it allows for the purification of a photon number correlated state after transmission to two distant parties.
Purification of two mode entangled states has been shown experimentally for qubits [254, 255] and in the continuous variable (CV) regime [256,257] (CV-entanglement purification is especially challenging [258–260]. Nevertheless, several proposals have been put forward to accomplish this task [261–266], and very recently Takahashi *et al.* succeeded in an experimental demonstration [267]). A special advantage of the scheme described here lies in the fact that it does not only allow for detection of arbitrary photon losses, but is also applicable to many modes such that entanglement can be distributed and purified in a network.
With a small modification, the basic setup can be used for number resolved photon detection. The ability to detect photons in a number resolved fashion is highly desirable in the fields of quantum computing and quantum communication. For example, linear optics quantum computation relies crucially on photon number resolving detectors [77,268,269]. Moreover, the possibility to distinguish different photon number states allows for conditional state preparation of nonclassical quantum states [270–272], and plays an important role in Bell experiments [251] and the security in quantum cryptographic schemes [273, 274]. Other applications include interferometry [275] and the characterization of quantum light sources [276,277].
Existing technologies for photon counting [278–291] such as avalanche photodiodes, cryogenic devices, and quantum dots typically have scalability problems and cannot reliably distinguish high photon numbers, destroy the quantum state of light in the detection process, or can not be applied in the optical domain. Here, a nondestructive number resolving photo detection scheme in the optical regime is presented. This quantum-nondemolition (QND) measurement of the photon number allows for subsequent use of the measured quantum state of light. An advantage of the counting device put forward here compared to other theoretical proposals for QND measurements of photon numbers [292–297] is the ability to detect arbitrarily high photon numbers with arbitrary resolution. The scheme is based on testing successively all possible prime factors and powers of primes and the resources needed therefore scale moderately with the (width and mean of the) photon number distribution. In particular, a very precise photon number measurement can be made even for high photon numbers by testing only few factors if the approximate photon number is known.

5.1.2 Overview and main results

The key-element of the proposed setup is the phase-flip gate introduced in Sec. 2.3.2. It allows one to use the internal state of a single atom in an optical cavity to control whether the phase of a light field is changed by π or not [121]. This gate is illustrated in Fig. 2.6 and can be used to prepare superpositions of coherent states [124]. To this end, the atom is initially prepared in the state $(|\uparrow\rangle + |\downarrow\rangle)/\sqrt{2}$, and the input field is chosen to be a coherent state $|\alpha\rangle$. After the interaction, the combined state of the atom and the light field is proportional to $|\alpha\rangle|\uparrow\rangle + |-\alpha\rangle|\downarrow\rangle \propto (|\alpha\rangle + |-\alpha\rangle)(|\uparrow\rangle + |\downarrow\rangle) + (|\alpha\rangle - |-\alpha\rangle)(|\uparrow\rangle - |\downarrow\rangle)$,

and a measurement of the atomic state in the basis $|\pm\rangle = (|\uparrow\rangle \pm |\downarrow\rangle)/\sqrt{2}$ projects the state of the light field onto the even $|\alpha\rangle + |-\alpha\rangle$ or the odd $|\alpha\rangle - |-\alpha\rangle$ superposition state. More generally, the input state $\sum_n c_n|n\rangle$, where $|n\rangle$ is an n-photon Fock state, is transformed into the output state $\sum_n (1/2 \pm (-1)^n/2)c_n|n\rangle$, i.e., the input state is either conditionally projected onto the subspace spanned by all even photon number states or the subspace spanned by all odd photon number states without destroying the state.

With this tool at hand, an arbitrary two-mode input state can be projected onto the subspace $S = \mathrm{span}(|n\rangle|n\rangle)$, $n = 0, 1, 2, \ldots$. If two modes interfere at a 50:50 beam splitter, a state of form $|n\rangle|n\rangle$ is transformed into a superposition of products of even photon number states. If a 50:50 beam splitter operation is applied to the input state, both of the resulting modes are conditionally projected onto the subspace of even photon number states. If a second 50:50 beam splitter operation is applied, the input state is thus unchanged if it already lies in S, but most other states do not pass the measurement test. To remove the final unwanted components, opposite phase shifts are applied to the two modes (which also leaves $|n\rangle|n\rangle$ unchanged) and the procedure is repeated (as shown in Fig. 5.1). For an appropriate choice of phase shifts, the desired state is obtained after infinitely many repetitions. In practice, however, a small number of iterations is typically sufficient. If, for instance, the input state is a product of two coherent states $|\alpha\rangle|\alpha\rangle$ with $|\alpha|^2 = 4$, the fidelity of the projection is 0.573 for one unit, 0.962 for two units, and 0.999998 for three units. The scheme is easily generalized to an M mode input state. In this case, first modes 1 and 2 are projected onto S, as well as modes 3 and 4, etc. Then modes 2 and 3 are projected on S, as well as modes 4 and 5 etc.

The setup can also be used as a device for photon number resolving measurements if the phases applied between the light-cavity interactions are chosen according to the new task. Each photon number state $|n\rangle$ sent through the array leads to a characteristic pattern of atomic states. As explained in Sec. 5.1.4, the photon number of an unknown state can be determined by testing the prime factors and powers of primes in the range of interest in subsequent parts of the array. The scheme scales thereby moderately in the resources. Three cavity pairs suffice for example for detecting any state which is not a multiple of three with a probability of 93.75%. However, in this basic version of the counting scheme, the tested photon state may leave each port of the last beam splitter with equal probability. Deterministic emission of the unchanged quantum state of light into a single spatial mode is rendered possible if one allows for entanglement of the atoms in different cavities before the interaction with the field (see Sec. 5.1.4). More generally, the proposed scheme allows for the determination of the difference in photon numbers of two input beams without changing the photonic state.

The correlations in photon number between two modes of states in S facilitate an interesting possibility to detect photon losses. To this end, the state is projected onto S a second time. If a photon loss has occurred, the state is most likely orthogonal to S, in which case a measurement outcome is obtained, which is not the one required for accepting the projection as successful. On the other hand, if no photon loss has occurred, the desired measurement outcome is obtained with certainty. Note that the loss of a single photon can always be detected by this method, and the state can thus be conditionally recovered with almost perfect fidelity if the probability for losses is sufficiently small. The robustness of the scheme can be improved even further, if a M-mode state is used. It

is then possible to detect all losses of up to $M-1$ photons, and even though it is M times more likely to lose one photon, the probability to lose one photon from each mode is approximately $(Mp)^M$, where p is the probability to lose one photon from one mode and $Mp \ll 1$ is assumed. In a situation where many photon losses are to be expected, photon number correlated states can be obtained with small probability but high fidelity. The different modes of a photon number correlated state can also be distributed to distant parties, while losses can be still checked for, provided that at least two modes are sent to each party. Since the proposed scheme can be used as a filter prior to the actual protocol, it has an important advantage compared to postselective schemes. If the tested entangled state is for example intended to be used for teleportation, the state to be teleported is not destroyed in the course of testing the photon number correlated resource state.
The dynamics in Fig. 2.6 requires strong coupling, a sufficiently slowly varying mode function of the input field, and a sufficiently low flux of photons. In order to quantify these requirements, a full multi-mode description of the interaction of the light with the cavity is provided in [VI] for the case of a coherent state input field. There, it is shown that the single atom cooperativity parameter should be much larger than unity, the mode function of the input field should be long compared to the inverse of the decay rate of the cavity, and the flux of photons in the input beam should not significantly exceed the rate of spontaneous emission events from an atom having an average probability of one half to be in the excited state. Moreover, the optimal shape of the mode function of the input field is derived in [VI] for the case when the mode function is only allowed to be nonzero in a finite time interval.

5.1.3 Nondestructive projection onto photon number correlated states

The proposed setup for the projection of an arbitrary two-mode input state onto S is sketched in Fig. 5.1. The field annihilation operators of the two input modes are denoted by a and b, respectively. The total transformation corresponding to one of the units (consisting of a beam splitter, a set of cavities, and a second beam splitter), conditioned on the detection of both atoms in state $|+\rangle$ after the interaction, is given by the operator $U^\dagger P U$, where

$$U = \exp\left[\frac{\pi}{4}\left(a^\dagger b - a b^\dagger\right)\right], \qquad P = \sum_{n=0}^{\infty}\sum_{m=0}^{\infty} |2n\rangle\langle 2n| \otimes |2m\rangle\langle 2m|. \tag{5.1}$$

As explained above, the Hong-Ou-Mandel effect ensures that $U^\dagger P U|n\rangle|n\rangle = |n\rangle|n\rangle$, while most other possible components of the input state are removed by means of the conditioning, for instance all components $|n\rangle|m\rangle$ with $n+m$ odd. There are, however, a few exceptions, since all states of the form $U^\dagger|2n\rangle|2m\rangle$, $n = 0, 1, 2, \ldots$, $m = 0, 1, 2, \ldots$, are accepted. The phase shifts between the $U^\dagger P U$ units are represented by the operator

$$U_\phi = \exp\left[i\phi\left(a^\dagger a - b^\dagger b\right)\right], \tag{5.2}$$

which leaves states of the form $|n\rangle|n\rangle$ unchanged, while states of the form $|n\rangle|m\rangle$ with $n \neq m$ acquire a phase shift. For a setup containing $N+1$ units, the complete conditional

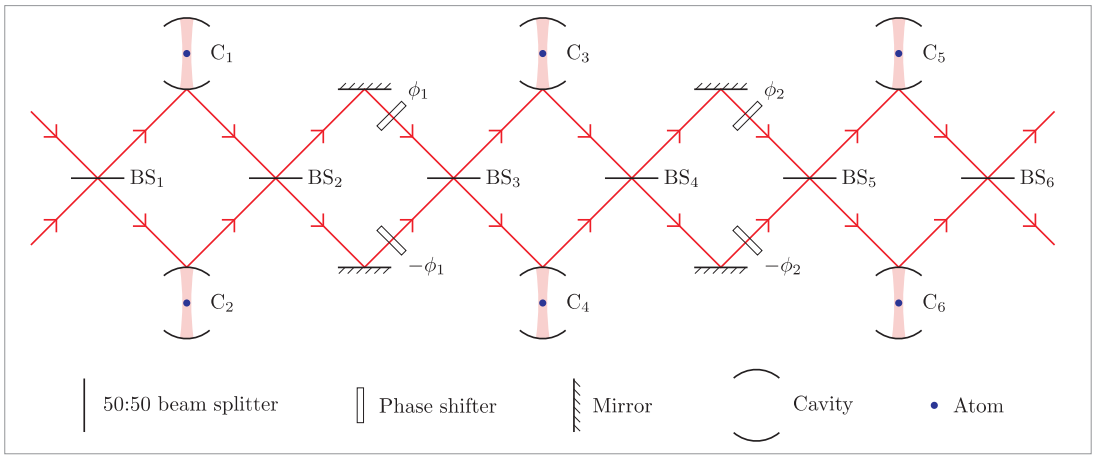

Figure 5.1: The first three units of the proposed setup for the conditional projection of an arbitrary two-mode input state onto the subspace spanned by the state vectors $|n\rangle|n\rangle$, $n = 0, 1, 2, \ldots$. All atoms are initially prepared in state $|+\rangle$. The desired projection occurs in the limit of infinitely many units conditioned on the detection of all atoms in state $|+\rangle$ after the interaction. As explained in the text, a small number of units will typically suffice in practice. For later reference, the beam splitters are labelled by BS_i and the cavities by C_i.

transformation is therefore represented by the operator

$$O_N = U^\dagger P U U_{\phi_N} U^\dagger P U \cdots U_{\phi_2} U^\dagger P U U_{\phi_1} U^\dagger P U = U^\dagger P U \prod_{i=1}^{N} \cos[\phi_i (a^\dagger a - b^\dagger b)], \tag{5.3}$$

where $U^\dagger P U$ in the last term commutes with the product of cosines. For $N \to \infty$, the product of cosines vanishes for all components of the input state with different numbers of photons in the two modes if, for instance, all the angles ϕ_i are chosen as an irrational number times π. The operators are here applied one after the other to the input state, which corresponds to the successive interactions of the light with the different components of the setup. Even though, the input pulses can be longer than the distance between the components such that different parts of the pulses interact with different components at the same time, if the state of the atoms is not measured before the interaction with the light field is completed. The setup using an array of cavities as in Fig. 5.1 can therefore be very compact even though the pulses are required to be long.[1]

In the following, the optimal choice of angles ϕ_i for achieving the projection onto S to a good approximation with a small number of units is addressed. To this end, the fidelity of the projection

$$F_N = \frac{|\langle \psi_N | \psi_\infty \rangle|^2}{\langle \psi_N | \psi_N \rangle \langle \psi_\infty | \psi_\infty \rangle} = \frac{\langle \psi_\infty | \psi_\infty \rangle}{\langle \psi_N | \psi_N \rangle} \tag{5.4}$$

[1] Note that it would also be possible to use a single pair of cavities and atoms repeatedly in a fold-on type of experiment. However in this case the compactness would be lost due to the need for long delay lines necessary to measure and re-prepare the atoms before they are reused.

is defined as the overlap between the unnormalized output state $|\psi_N\rangle = O_N|\psi_{\rm in}\rangle$ after $N+1$ units and the projection $|\psi_\infty\rangle$ of the input state $|\psi_{\rm in}\rangle$ onto the subspace S. The last equality follows from the fact that $|\psi_N\rangle = |\psi_\infty\rangle + |\psi_\perp\rangle$, where $|\psi_\perp\rangle$ lies in the orthogonal complement of S. Maximizing F_N for a given $|\psi_{\rm in}\rangle = \sum_n \sum_m c_{nm}|n\rangle|m\rangle$ thus corresponds to minimizing

$$\langle\psi_N|\psi_N\rangle = \sum_{n=0}^{\infty}\sum_{m=0}^{\infty} c_{nm} \prod_{i=1}^{N} \cos^2[\phi_i(n-m)] \times \langle\psi_{\rm in}|U^\dagger PU|n\rangle|m\rangle,$$

i.e., the optimal solution of the equation

$$\frac{\partial\langle\psi_N|\psi_N\rangle}{\partial\phi_j} = -\sum_{n=0}^{\infty}\sum_{m=0}^{\infty} c_{nm}\sin[2\phi_j(n-m)](n-m)\times\prod_{\substack{i=1\\ i\neq j}}^{N}\cos^2[\phi_i(n-m)]\langle\psi_{\rm in}|U^\dagger PU|n\rangle|m\rangle = 0.$$

A set of solutions valid for any input state can be obtained by requiring $\sin[2\phi_j(n-m)]\prod_{i\neq j}\cos^2[\phi_i(n-m)] = 0$ for all even values of $n-m$ (note that $U^\dagger PU|n\rangle|m\rangle = 0$ for $n+m$ odd). Within this set, the optimal solution is given by $\phi_j = 2^{-j}\times\pi/2$.[2] Even though this is not necessarily optimal with respect to maximizing F for a particular choice of input state, the angles $\phi_j = 2^{-j}\times\pi/2$ are used in the following, except if the input state satisfies the symmetry relations $c_{nm} = c_{mn}$. In this case, the operator $U^\dagger PU$ by itself removes all terms with $n-m = \pm2, \pm6, \pm10, \ldots$, i.e., the angles can be chosen as $\phi_j = 2^{-j}\times\pi/4$, and $|\psi_N\rangle$ only contains terms with $n-m = q2^{(N+2)}$, $q = 0, \pm1, \pm2, \ldots$. For instance, for $N = 2$, only terms with $n-m = 0, \pm16, \pm32, \ldots$ contribute.
In Fig. 5.2, the fidelity (5.4) for a product of two coherent states with amplitude α as input state is shown as a function of $|\alpha|^2$ for different numbers of units of the setup. Even for $|\alpha|^2$ as large as 10, the fidelity is still as high as 0.9961 for $N = 2$, and the required number of units is thus quite small in practice. The figure also shows the success probability $P_N = \langle\psi_N|\psi_N\rangle$ for $N\to\infty$. For instance, for $|\alpha|^2 = 10$ the experiment has to be repeated about 11 times on average before the desired measurement outcome is observed.

5.1.4 Photon number resolving measurement

In this section, it is shown how a photon number measurement can be implemented using a modified version of the setup introduced in the previous section. First, he key idea is explained and the basic photo-counting scheme is described. Then, this protocol is extended to allow for a QND measurement of photon numbers.

Number resolving detection scheme

In the following, the setup shown in Fig. 5.1 is analyzed considering a product of an n-photon Fock state in the lower port and a vacuum state in the upper port as input state.

[2] If one of the angles equals $2^{-j}\times\pi/2$, $j\in\{1,2,\ldots,N\}$, all terms with $n-m = 2^j\times(\pm1,\pm3,\pm5,\ldots)$ are removed from the input state according to (5.3). If all angles are chosen according to $\phi_j = 2^{-j}\times\pi/2$, it follows that $|\psi_N\rangle$ contains only terms with $n-m = q2^{(N+1)}$, $q = 0, \pm1, \pm2, \ldots$, which may be a useful property in practical applications of the scheme.

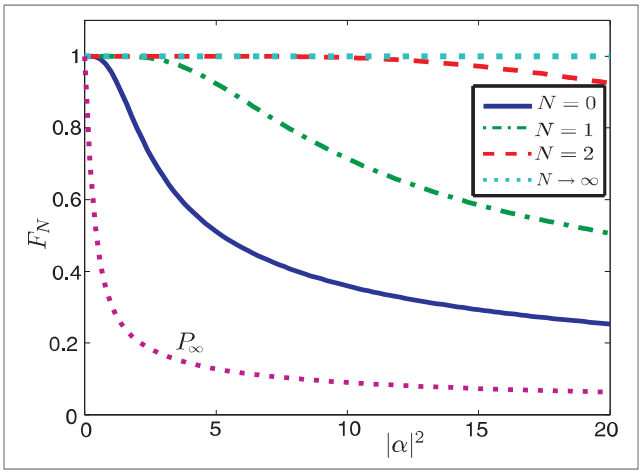

Figure 5.2: Projection fidelity (Eq. (5.4)) as a function of the expectation value of the number of photons in one of the input modes for $|\psi_{\text{in}}\rangle = |\alpha\rangle|\alpha\rangle$ and setups with one, two, three, and infinitely many units. The chosen angles are given by $\phi_j = 2^{-j} \times \pi/4$. The dotted line labelled P_∞ represents the probability to obtain the required measurement outcome, (i.e., all atoms in $|+\rangle$) after the interaction with the field in the limit of infinitely many units.

Since the setup contains a series of beam splitters, the definitions $A = (a^\dagger - b^\dagger)/\sqrt{2}$ and $B = (a^\dagger + b^\dagger)/\sqrt{2}$ are used in the following, such that $a^\dagger|0\rangle \to A|0\rangle$ and $b^\dagger|0\rangle \to B|0\rangle$ at beam splitters BS_1, BS_3, BS_5, ..., and $A|0\rangle \to a^\dagger|0\rangle$ and $B|0\rangle \to b^\dagger|0\rangle$ at beam splitters BS_2, BS_4, BS_6, ... As before, all atoms are assumed to be initially prepared in state $|+\rangle$ and measurements in the $|\pm\rangle$ basis after the interaction with the field are considered. If an n photon state is used as input, only two possible outcomes of the measurement of the atoms in the cavities labelled C_1 and C_2 in Fig. 5.1 can occur, depending on the parity of n. If n is even, the two atoms can only be in state $|++\rangle$ or $|--\rangle$. If n is odd, the atomic state after the interaction is $|-+\rangle$ or $|+-\rangle$. To describe the odd and even case at the same time, $|++\rangle, |-+\rangle$ is denoted by $|B_+\rangle$ and $|--\rangle, |+-\rangle$ by $|B_-\rangle$. A measurement of $|B_+\rangle$ indicates an even number of photons in the b-beam, while $|B_-\rangle$ indicates an odd number of photons.

To start with, the input state $|n\rangle|0\rangle = \frac{1}{\sqrt{n!}}(a^\dagger)^n|0\rangle|0\rangle$ is considered. After the beam splitter BS_1, the state has changed into $\frac{1}{\sqrt{n!}}\left(\frac{a^\dagger - b^\dagger}{\sqrt{2}}\right)^n |0\rangle|0\rangle$ and interacts with the two atoms in the cavities C_1 and C_2. By measuring the atoms in the $|\pm\rangle$ basis, the state is projected onto the subspace of an even or odd number of photons in the b path. The photon state after the measurement can be written as $|b_\pm\rangle := \frac{1}{\sqrt{2\ n!}}\left[\left(\frac{a^\dagger - b^\dagger}{\sqrt{2}}\right)^n \pm \left(\frac{a^\dagger + b^\dagger}{\sqrt{2}}\right)^n\right]|0\rangle|0\rangle = \frac{1}{\sqrt{2\ n!}}(A^n \pm B^n)|0\rangle|0\rangle$, where $|b_+\rangle(|b_-\rangle)$ is the state with an even (odd) number of b photons and corresponds to the measurement result $|B_+\rangle$ ($|B_-\rangle$). Note that this first measurement result is completely random. After BS_2 the state simplifies to $\frac{1}{\sqrt{2\ n!}}[(a^\dagger)^n \pm (b^\dagger)^n]|0\rangle|0\rangle$. Due to the phase shifters, the two modes pick up a relative phase of $2\phi_1 n$ such that the state is given by $\frac{1}{\sqrt{2\ n!}}[e^{i\phi_1 n}(a^\dagger)^n \pm e^{-i\phi_1 n}(b^\dagger)^n]|0\rangle|0\rangle$.

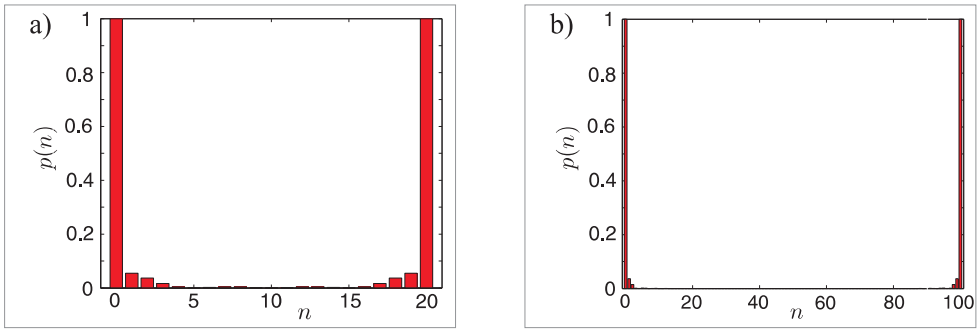

Figure 5.3: Number resolving photon detection. (a) Probabilities $p(n)$ (Eq. (5.5)) for $n_0 = 20$ and $N + 1 = 5$ resulting in $q = 94.49\%$ (Eq. (5.6)). For $N + 1 = 7$, $q = 99.66\%$. (b) Probabilities $p(n)$ for $n_0 = 100$ and $N + 1 = 8$ resulting in $q = 96.33\%$. For $N + 1 = 10$, $q = 99.95\%$.

Finally, after BS_3, the state $\frac{1}{\sqrt{2\ n!}}(e^{i\phi_1 n}A^n \pm e^{-i\phi_1 n}B^n)|0\rangle|0\rangle$ is obtained, which equals $\frac{1}{2\sqrt{2\ n!}}(e^{i\phi_1 n} \pm e^{-i\phi_1 n})(A^n + B^n)|0\rangle|0\rangle + \frac{1}{2\sqrt{2\ n!}}(e^{i\phi_1 n} \mp e^{-i\phi_1 n})(A^n - B^n)|0\rangle|0\rangle$. This state can be reexpressed as $(e^{i\phi_1 n} \pm e^{-i\phi_1 n})/2|b_+\rangle + (e^{i\phi_1 n} \mp e^{-i\phi_1 n})/2|b_-\rangle$. Hence, the result of measuring the atomic state in cavities C_3 and C_4 will be $|B_\pm\rangle$ with probability $p_+ = \cos(\phi_1 n)^2$ and $|B_\mp\rangle$ with probability $p_- = \sin(\phi_1 n)^2$. Since the state is again projected onto one of the two states $|b_\pm\rangle$, the same calculations can be repeated for all following steps.
While the first measurement result is completely random, all following measurement results depend on n and the previous measurement outcome. The probability that the $(i + 1)$-th measurement result is the same as the i-th result is given by $p_i = \cos(\phi_i n)^2$, and the probability that the measurement result changes (and the state changes from $|b_\pm\rangle$ to $|b_\mp\rangle$) is given by $\sin(\phi_i n)^2$. If the number of units is infinitely large (or sufficiently large) and all phases are chosen to equal ϕ, it is possible to infer the number of photons based on the relative frequency with which the measurement results switch between $|B_+\rangle$ and $|B_-\rangle$. This can be done with arbitrary precision for all photon numbers $n < \frac{\pi}{\phi}$. $n \approx \arccos(\sqrt{f})/\phi$, where $f = N_{\text{same}}/(N_{\text{same}} + N_{\text{different}})$ and N_{same} ($N_{\text{different}}$) is the number of cases, where the measurement outcome is the same (not the same) as the previous measurement outcome.
Measuring this relative frequency with a fixed small phase is not the optimal way to infer the photon number. Instead, the following procedure is proposed. In this improved protocol, a setup with a total of $N + 1$ units is used and the phases $\phi_i = 2^{i-1}\pi/n_0$, $i = 1, 2, \ldots, N$ are chosen for an arbitrary value of $n_0 \in \mathbb{N}$. Below, the probability $p(n)$ that all measurement results are the same,

$$p(n) = \prod_{i=1}^{N} p_i = \prod_{i=0}^{N-1} \cos\left(\frac{2^i \pi}{n_0} n\right)^2 . \tag{5.5}$$

is calculated. This probability is equal to one for all photon numbers that are a multiple of n_0. Otherwise, it tends to zero in the limit of infinitely many units. This way, it can be measured whether the photon number is a multiple of n_0. For example, for $n_0 = 3$ and

$N+1=3$, any state which is not a multiple of three can be detected with a probability of at least $q=93.75\%$ ($q=99.61\%$ for $N+1=5$), where

$$q := 1 - \max_{n\neq 0,n_0,2n_0,\ldots} p(n). \tag{5.6}$$

For $n_0=4$, already $N+1=3$ is sufficient to achieve $q=100\%$. For $n_0=5$ and $N+1=3$, $q=93.75\%$ is obtained, which increases to $q=99.61\%$ for $N+1=5$. In Fig. 5.3, $p(n)$ is shown for $n_0=20$ and $n_0=100$. The number N required to obtain a good result scales typically logarithmical with n_0, e.g. for $n_0=1000$ already $N+1=11$ is sufficient to reach $q=99.95\%$. Given an unknown state, all possible prime factors and powers of primes can be tested to identify the exact photon number. If, e.g., a state consisting of 0 to 10 photons is considered, the factors $n_0=2,3,4,5,7,8,9$ have to be tested (where the factor 2 does not need to be checked separately). 24 measurement results are sufficient to test all factors with a probability over 99%. If reliable photon number counting is required for n ranging from 0 to $n_{\max}$, for large $n_{\max}$, all primes and power of primes that are smaller than $n_{\max}$ need to be tested. This number can be bounded from above by $n_{\max}$. All $n_{\max}$ tests are required to work with high probability. To this end, each individual test needs to succeed with a probability better than $q \geq 1-1/n_{\max}$. It can be checked numerically that this is the case if $N=2\log(n_{\max})$, leading to a photon counting device with reliable photon detection up to $n_{\max}$ using an array consisting of less than $2n_{\max}\log(n_{\max})$ basic units. Note that this setup does not destroy the photonic input state but transforms $|n\rangle|0\rangle$ randomly into $\frac{1}{\sqrt{2}}[|n\rangle|0\rangle \pm |0\rangle|n\rangle]$, i.e., the photons leave the setup in a superposition of all photons taking either the a-path or the b-path. This state can not be transformed back into $|n\rangle|0\rangle$ by means of passive optical elements. The output state - a so-called $N00N$ state - is, however, a very valuable resource for applications in quantum information protocols and quantum metrology [298].

Nondestructive number resolving detection scheme

For a nondemolition version of the photon number measurement, the basic building block depicted in Fig. 5.4 is used. The atoms in the two upper cavities are initially prepared in an entangled state $|\phi_+\rangle = (|\uparrow\uparrow\rangle + |\downarrow\downarrow\rangle)/\sqrt{2}$, and the atoms in the lower cavities are also prepared in state $|\phi_+\rangle$. This can, for instance, be achieved via the parity measurement scheme put forward in [125]. During the interaction, the upper and the lower atoms stay in the subspace spanned by $|\phi_\pm\rangle = (|\uparrow\uparrow\rangle \pm |\downarrow\downarrow\rangle)/\sqrt{2}$. The state changes between $|\phi_+\rangle$ and $|\phi_-\rangle$ each time one of the two entangled cavities interacts with an odd number of photons. As in the previous subsection, $|B_\pm\rangle$ is defined to describe the even and the odd case at the same time. For n even, $|B_+\rangle = |\phi_+\rangle|\phi_+\rangle$ and $|B_-\rangle = |\phi_-\rangle|\phi_-\rangle$, while in the odd case, $|B_+\rangle = |\phi_-\rangle|\phi_+\rangle$ and $|B_-\rangle = |\phi_+\rangle|\phi_-\rangle$.
Using the same notation as before, the state is transformed as follows, when passing through the setup from left to right. The initial state is given by

$$|\psi_1\rangle = \frac{1}{\sqrt{n!}}(a^\dagger)^n|0\rangle|0\rangle|\phi_+\rangle|\phi_+\rangle.$$

After the first beam splitter,

$$|\psi_2\rangle = \frac{1}{\sqrt{n!}}A^n|0\rangle|0\rangle|\phi_+\rangle|\phi_+\rangle = \frac{1}{\sqrt{2}}(|b_+\rangle + |b_-\rangle)|\phi_+\rangle|\phi_+\rangle.$$

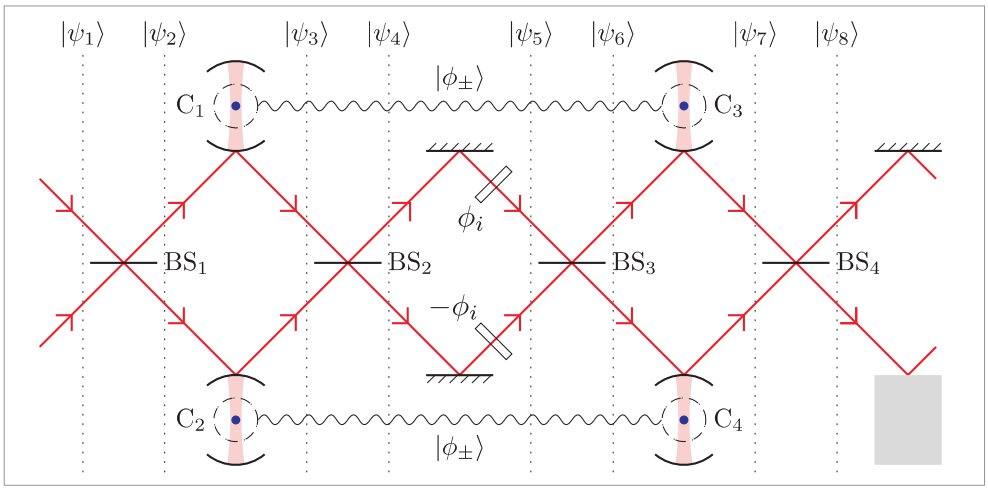

Figure 5.4: Basic building block of a nondemolition photon number resolving detection scheme. The dashed circles and the wavy lines indicate the entanglement between the atoms in cavities C_1 and C_3 and between the atoms in cavities C_2 and C_4. The gray box is either a cavity or a mirror. (In the latter case, the light may be sent as well directly from the cavities C_3 and C_4 to the first two cavities of the next block.)

The interaction with the first two cavities leads to

$$|\psi_3\rangle = \frac{1}{\sqrt{2}}|b_+\rangle|B_+\rangle + \frac{1}{\sqrt{2}}|b_-\rangle|B_-\rangle = \frac{1}{2\sqrt{n!}}(A^n+B^n)|0\rangle|0\rangle|B_+\rangle + \frac{1}{2\sqrt{n!}}(A^n-B^n)|0\rangle|0\rangle|B_-\rangle.$$

The second beam splitter transforms this state into

$$|\psi_4\rangle = \frac{1}{2\sqrt{n!}}\left\{[(a^\dagger)^n + (b^\dagger)^n]|0\rangle|0\rangle|B_+\rangle + [(a^\dagger)^n - (b^\dagger)^n]|0\rangle|0\rangle|B_-\rangle\right\}.$$

The two modes pick up a relative phase shift of $2\phi_i n$ at the phase shifters such that

$$|\psi_5\rangle = \frac{1}{2\sqrt{n!}}\left\{[e^{i\phi_i n}(a^\dagger)^n + e^{-i\phi_i n}(b^\dagger)^n]|0\rangle|0\rangle|B_+\rangle + [e^{i\phi_i n}(a^\dagger)^n - e^{-i\phi_i n}(b^\dagger)^n]|0\rangle|0\rangle|B_-\rangle\right\}.$$

After the third beam splitter,

$$\begin{aligned}|\psi_6\rangle &= \frac{1}{2\sqrt{n!}}\left[(e^{i\phi_i n}A^n + e^{-i\phi_i n}B^n)|0\rangle|0\rangle|B_+\rangle + (e^{i\phi_i n}A^n - e^{-i\phi_i n}B^n)|0\rangle|0\rangle|B_-\rangle\right] \\ &= \frac{1}{\sqrt{2}}\left(\cos(\phi_i n)|b_+\rangle|B_+\rangle + i\sin(\phi_i n)|b_-\rangle|B_+\rangle + i\sin(\phi_i n)|b_+\rangle|B_-\rangle + \cos(\phi_i n)|b_-\rangle|B_-\rangle\right).\end{aligned}$$

The interaction with the last two cavities transforms the states $|b_\pm\rangle|B_\pm\rangle$ into $|b_\pm\rangle|\phi_+\rangle|\phi_+\rangle$ and the states $|b_\pm\rangle|B_\mp\rangle$ into $|b_\pm\rangle|\phi_-\rangle|\phi_-\rangle$ independent on the parity of n. $|\psi_7\rangle$ is therefore transformed into

$$\begin{aligned}|\psi_7\rangle &= \frac{1}{\sqrt{2}}\cos(\phi_i n)\left(|b_+\rangle + |b_-\rangle\right)|\phi_+\rangle|\phi_+\rangle + \frac{i}{\sqrt{2}}\sin(\phi_i n)\left(|b_+\rangle + |b_-\rangle\right)|\phi_-\rangle|\phi_-\rangle \\ &= \frac{1}{\sqrt{n!}}A^n|0\rangle|0\rangle\left[\cos(\phi_i n)|\phi_+\rangle|\phi_+\rangle + i\sin(\phi_i n)|\phi_-\rangle|\phi_-\rangle\right],\end{aligned}$$

and after the last beam splitter,

$$|\psi_8\rangle = \frac{1}{\sqrt{n}}(a^\dagger)^n|0\rangle|0\rangle \otimes [\cos(\phi_i n)|\phi_+\rangle|\phi_+\rangle + i\sin(\phi_i n)|\phi_-\rangle|\phi_-\rangle] .$$

The photonic modes are now decoupled from the atomic state. The photons remain in state $|n\rangle|0\rangle$ after the final beam splitter, and the atoms carry information about the photon number. Note that $|\phi_+\rangle = (|++\rangle + |--\rangle)/\sqrt{2}$ and $|\phi_-\rangle = (|+-\rangle + |-+\rangle)/\sqrt{2}$. By measuring all atoms in the $|\pm\rangle$ basis one can easily distinguish between $|\phi_+\rangle$ and $|\phi_-\rangle$ based on the parity of the measurements. The probability to obtain $|\phi_+\rangle|\phi_+\rangle$ or $|\phi_-\rangle|\phi_-\rangle$ is given by $\cos(\phi n)^2$ and $\sin(\phi n)^2$ respectively. After the measurement, all photons leave the setup in beam a for both outcomes. The probability for measuring $|\phi_+\rangle|\phi_+\rangle$ equals the probability to observe a change in the measurement outcomes in the previous setup. Hence, the same procedure can be applied to a chain consisting of the demolition free blocks. If the parity information is to be inferred in each step, an additional cavity can be added at the end of each block as shown in Fig. 5.4.
More generally, the demolition free element leaves photonic input states $|\psi\rangle = \frac{1}{\sqrt{n!q!}}(a^\dagger)^n(b^\dagger)^q|0\rangle|0\rangle$, where n photons enter through the lower and q photons enter through the upper port, unchanged. A calculation analogous to the previous one shows that the atomic states $|\phi_+\rangle|\phi_+\rangle$ and $|\phi_-\rangle|\phi_-\rangle$ are obtained with probabilities $\cos(\phi_i(n-q))^2$ and $\sin(\phi_i(n-q))^2$ respectively. This way, one can test for photon number differences $n-q$ in two input states in the same fashion as for photon numbers in a single input beam described above. Similarly, two coherent input states $|\alpha\rangle|\alpha\rangle$ cab be projected onto generalized photon number correlated states $\sum_n c_n|n\rangle|n-d\rangle$ with fixed photon number difference $d = 0, 1, 2....$
In a realistic scenario one may be faced with photon losses. Both setups have a built-in possibility to detect the loss of one photon. In the first case, the parity of the total number of photons is obtained in every single measurement of a pair of atoms. If this parity changes in an element in the chain, it can be inferred that at least one photon has been lost. In the demolition free setup, the valid measurement results are restricted to $|\phi_+\rangle|\phi_+\rangle$ and $|\phi_-\rangle|\phi_-\rangle$. If $|\phi_-\rangle|\phi_+\rangle$ or $|\phi_+\rangle|\phi_-\rangle$ are measured, it can be inferred that a photon has been lost between the two pairs of cavities. In addition, the optional cavity at the end of each block provides an extra check.

5.1.5 Filtering out losses

Next, the possibility to use a comparison of the number of photons in the two modes to detect losses is investigated. As in Sec. 5.1.3, first the input state $|\psi_{\text{in}}\rangle = |\alpha\rangle|\alpha\rangle$ is considered and the proposed setup is used to project it onto the subspace S. Then two beam splitters with reflectivity R are used to model a fractional loss in both modes. After tracing out the reflected field, the proposed setup is used once more to project the state onto S. Fig. 5.5a displays the fidelity between the state obtained after the first projection onto S and the state obtained after the second projection onto S, the success probability for the second projection given that the first one is successful, and the purity of the state after the second projection. The second projection can be seen to recover the state obtained after the first projection with a fidelity close to unity even for losses of a few

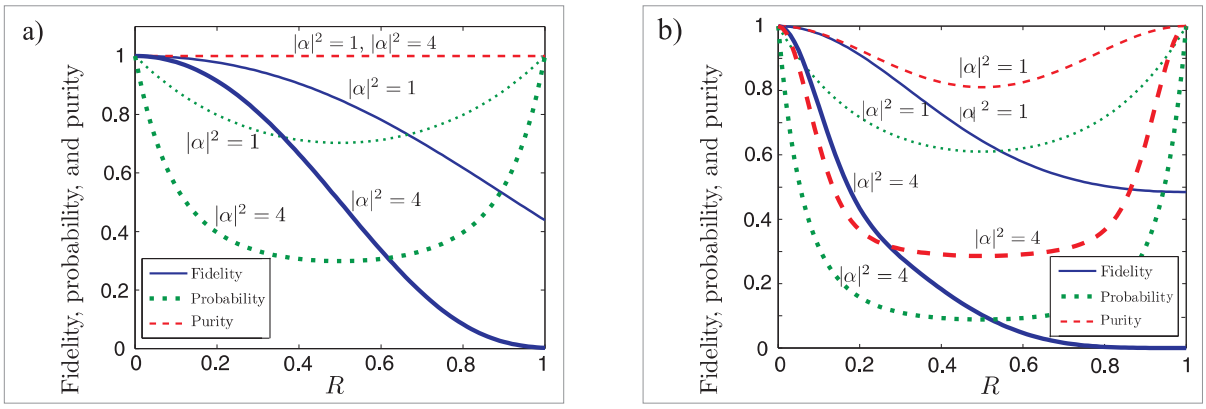

Figure 5.5: Filtering out losses. In panel a), the projection of the input state $|\psi_{\text{in}}\rangle = |\alpha\rangle|\alpha\rangle$ onto the subspace S followed by a fractional loss R in both modes and a second projection onto S is considered. In panel b), refers to the projection of the input state $|\psi_{\text{in}}\rangle = |\alpha\rangle|\alpha\rangle|\alpha\rangle|\alpha\rangle$ onto the subspace spanned by the vectors $|n\rangle|n\rangle|n\rangle|n\rangle$, $n = 0, 1, 2, \ldots$, followed by a fractional loss R in all four modes and a projection of modes 1 and 2 onto S and of modes 3 and 4 onto S. Both panels show the fidelity between the states obtained after the first and the second projection onto S, the probability of success for the second projection, given that the first one is successful, and the purity of the state after the second projection for two different values of $|\alpha|^2$.

percent. This is due to the fact that a loss of only one photon always leads to a failure of the second conditional projection. The main contribution to the fidelity decrease for small R is thus a simultaneous loss of one photon from both modes. It is also interesting to note that the final state is actually pure for all values of R, which is a consequence of the particular choice of input state. Finally, note that a single unit is sufficient to detect the loss of a single photon, and for small R only one unit is therefore required for the second projection in practice.
Now, a four mode input state $|\psi_{\text{in}}\rangle = |\alpha\rangle|\alpha\rangle|\alpha\rangle|\alpha\rangle$ is considered. As before, the setup is used to project this state onto the subspace spanned by the state vectors $|n\rangle|n\rangle|n\rangle|n\rangle$, $n = 0, 1, 2, \ldots$. Then a fractional loss of R is considered to occur in all modes. If two of the modes are sent to Alice and the two other modes are sent to Bob, the original projection can be recovered by projecting the former and the latter two modes onto S. The results are shown in Fig. 5.5b, and again the curves showing the fidelity and the purity are seen to be very flat and close to unity for small losses. This scheme allows one to distribute entanglement with high fidelity, but reduced success probability.

In conclusion, the setup put forward and studied in this section acts in many respects like a photon number filter and has several attractive applications for quantum technologies. Based on the ability to distinguish even and odd photon numbers using the interaction of the light field with a high finesse optical cavity, photonic two mode input states can be projected onto photon number correlated states. Naturally, this protocol is very well suited to detect losses and can in particular be adapted to purify photon number entangled

states in quantum communication. Deviations from ideal behavior such as finite length of the input pulses and limited coupling have been studied in [VI] to estimate for which parameters the idealized description is valid. The setup can be modified such that it is capable to perform a quantum-nondemolition measurement of photon numbers in the optical regime. The nondestructive photon counting device completes the versatile toolbox provided by the proposed scheme.

5.2 Detecting entanglement in two mode squeezed states by particle counting

In this section, an entanglement criterion for two mode squeezed states which relies on particle counting only is considered. The inequality analyzed here is optimal for the state under consideration and robust against particle losses. As it does not involve measurements of quadratures - which is typically very challenging for atomic modes - it renders the detection of atomic many-particle entanglement feasible in many different settings. Moreover, it bridges the gap between entanglement verification for qubits and criteria for continuous variables measured by homodyne detection. After publication of these results as e-print [VIII], Dr. C. Simon informed us that the entanglement criterion (5.9) presented in this work coincides with an inequality derived in a different context in [299] (see (Eq. (4)). In this article, the criterion has been derived in a different way and was used to quantify entanglement in photonic states which are generated by parametric down conversion in a cavity. Apart from the presentation and the analysis of the robustness of the inseparability criterion, our work includes additional material which is genuinely new (see Sec. 5.2.3). As outlined above, the application of the criterion is studied in the context of superradiant light scattering from Bose-Einstein condensates by considering the creation of entanglement between atoms and light as well as the possibility to create inter-atomic entanglement. In particular, a scheme for the creation of entanglement between two condensates in different momentum states is put forward, which takes advantage of leaving the Gaussian realm and features probabilistic entanglement distillation.

Below, we discuss the generation and detection of entanglement in two mode squeezed states in Sec. 5.2.1. In Sec. 5.2.2, we prove the inseparability criterion and study the influence of particle losses. In Sec. 5.2.3, we consider the creation of entanglement between atoms and light in superradiant Raman scattering and devise a scheme in which entanglement between a moving condensate and a condensate at rest is created and purified.

5.2.1 Generation and detection of entanglement in two mode squeezed states

Entanglement is a true quantum feature. Since the study of this peculiarity of physics holds not only the promise to acquire a deeper understanding of Nature, but paves also the way towards auspicious applications of quantum information science, the quest for

entanglement or inseparability criteria is a vigorous field of research[3]. In the most basic case, entanglement is shared between two parties, Alice and Bob, holding each a single particle. Bipartite entanglement of single pairs is well understood. Then again, entanglement between parties holding a a very large number of particles has been studied for Gaussian states with great success [252, 303]. Here, the natural question arises, how entanglement can be verified in the intermediate regime and how the two well studied cases of single pairs and Gaussian modes can be linked by an inseparability criterion for an arbitrary number of particles, which is not restricted to Gaussian states. Starting from this motivation, this section is concerned with the study of an inequality, which bridges the gap between inseparability criteria for a qubit and continuous variables. Moreover, from a practical point of view, this entanglement condition provides experimental feasibility and applicability in numerous settings.

More specifically, entanglement in two mode squeezed states (TMSS) can, in principle, be detected by means of a Gaussian inseparability criterion [304–309], which requires the measurement of variances in canonical quadratures. This can be conveniently performed for light modes, as was first demonstrated in [310, 311], as well as for multi-atom collective spin modes, as shown in [16]. However, in many cases involving multi-particle entanglement, homodyne measurement of atomic canonical variables which require an atomic "local oscillator" is not feasible.

This problem can be overcome by means of the practical entanglement condition studied in this section. Entanglement verification by means of this inequality requires particle number measurements only, rather than measurement of quadratures and can be used to detect N-particle entangled states of the form $|TMSS\rangle \otimes |TMSS\rangle$, which is attractive in view of many recent experiments, that offer the potential to generate this type of entanglement.

For example, superradiant scattering [136, 137] of laser light from a Bose-Einstein condensate has been observed recently [138, 141, 142, 147]. Superradiant scattering leads to highly directional emission of light from the atomic sample. This striking effect attracted considerable interest and it was shown theoretically that two mode squeezed states can be generated in this context [144, 312–316]. The entangled states created in this context are particularly interesting, since they represents the interspecies atom-light analogue of photonic twin beams generated in optical parametric down conversion, which play an essential role in many applications of quantum optics and quantum information theory. Despite the fact that the dynamics of the process and the resulting nonseparable state are well understood and the system is known to be a very promising candidate for entanglement generation [144, 312–317], entanglement could not be verified in this system[4]. Other examples can be found in many different setups, for example in entanglement production in spin exchange collisions in Bose-Einstein condensates [318, 319], the free electron laser [320], the creation of two mode squeezed states by dissociation [321–323] and entanglement production in colliding Bose-Einstein condensates [324–326] or four-wave mixing in matter waves in an optical lattice [327, 328]. While correlations could be observed,

[3] See [300] for a survey. For studies of separability of bipartite systems in arbitrary dimensions see for example [301] and [302].

[4] Nonclassical correlations have been studied, but since the quantum states produced in an experiment cannot be assumed to be pure, correlations do not imply the presence of entanglement.

multi-particle entanglement has not yet been detected in this context. This gap can be closed by means of the entanglement criterion studied in this section. As the Gaussian criterion [304–309], it can be understood as a local uncertainty relation [329, 330], with the difference that it involves a bound, which is given by expectation values of operators, rather than uncertainty limits represented by fixed numbers. The inequality is optimal for the state under consideration. Moreover it is robust against the sources of noise to be expected in a realistic setup and allows for successful detection of entanglement even for highly mixed states.

5.2.2 Inseparability criterion based on particle number measurements

As outlined above, the studied entanglement criterion is optimal for the state $|\Psi_1\rangle = |TMSS\rangle \otimes |TMSS\rangle$. In the Fock basis, this quantum state is given by

$$|\Psi_1\rangle = (1-\Lambda^2)\sum_{n=0}^{\infty}\Lambda^n|n\rangle|n\rangle \otimes \sum_{m=0}^{\infty}\Lambda^m|m\rangle|m\rangle, \tag{5.7}$$

where $\Lambda = \tanh(r)$ and $r \in \mathbb{C}$ is the squeezing parameter. The second and fourth ket refer to Alice's system, which is described by two modes with creation operators $a_+^\dagger$ and $a_-^\dagger$. Likewise, the first and third ket refer to Bob's system, which is described by two modes with creation operators $b_+^\dagger$ and $b_-^\dagger$. Using this notation, the state can be described in the Schwinger representation by introducing the Stokes operators S_x, S_y and S_z for Alice's system and J_x, J_y and J_z for Bob's. $\mathbf{S}$ is given by

$$\begin{aligned} S_x &= (n_{A,x} - n_{A,y})/2, \\ S_y &= (n_{A,+45} - n_{A,-45})/2, \\ S_z &= (n_{A,+} - n_{A,-})/2, \end{aligned} \tag{5.8}$$

and $\mathbf{J}$ is defined by analogous expressions. The number operators n carry subscripts for Alice's/Bob's system(A/B) and for the three different bases (x/y, $+45/-45$, $+/-$), where $n_{A,\pm} = a_\pm^\dagger a_\pm$ and $n_{B,\pm} = b_\pm^\dagger b_\pm$.

Entanglement criterion

The main characteristic feature of the two mode squeezed state $|\Psi_1\rangle$ is the correlation of particle numbers in Alice's and Bob's system. In contrast, any separable state satisfies a lower bound for the difference in particle numbers in different mutually independent bases. More precisely, any 2×2 - mode bipartite separable state, $\rho = \sum_i p_i\rho_i$, $\rho_i = \rho_i^A \otimes \rho_i^B$ (where $p_i \geqslant 0$ and $\sum_i p_i = 1$), satisfies the inequality

$$\langle (J_x - S_x)^2\rangle_\rho + \langle (J_y + S_y)^2\rangle_\rho + \langle (J_z - S_z)^2\rangle_\rho \geq \left(\langle n_A\rangle_\rho + \langle n_B\rangle_\rho\right)/2. \tag{5.9}$$

In the following, this entanglement criterion is proven. For any ρ_i, the left side of inequality (5.9) equals

$$\langle J_x^2 + J_y^2 + J_z^2\rangle_{\rho_i} + \langle S_x^2 + S_y^2 + S_z^2\rangle_{\rho_i} - 2\langle J_xS_x - J_yS_y + J_zS_z\rangle_{\rho_i}. \tag{5.10}$$

$\langle J_x^2 + J_y^2 + J_z^2\rangle_{\rho_i} = \langle (n_B/2)\,((n_B/2)+1)\rangle_{\rho_i}$, where $n_B = n_{B,+} + n_{B,-}$, and an analogous equality holds for the second term, as can be inferred from definition (5.8). Since ρ_i is assumed to be separable, the third term in expression (5.10) can be expressed as a product of two expectation values

$$-2\langle \mathbf{J}\ \tilde{\mathbf{S}}\rangle_{\rho_i} = -2\langle \mathbf{J}\rangle_{\rho_i}\langle \tilde{\mathbf{S}}\rangle_{\rho_i}$$

where $\tilde{\mathbf{S}} = \begin{pmatrix} S_x & -S_y & S_z \end{pmatrix}^T$. Using $\langle \mathbf{J}\rangle_{\rho_i} \leq \langle n_B/2\rangle_{\rho_i}$ and $\langle \tilde{\mathbf{S}}\rangle_{\rho_i} \leq \langle n_A/2\rangle_{\rho_i}$, it can be concluded that expression (5.10) is greater than or equal to

$$\left\langle \frac{n_B}{2}\left(\frac{n_B}{2}+1\right)\right\rangle_{\rho_i} + \left\langle \frac{n_A}{2}\left(\frac{n_A}{2}+1\right)\right\rangle_{\rho_i} - 2\left\langle \frac{n_B}{2}\right\rangle_{\rho_i}\left\langle \frac{n_A}{2}\right\rangle_{\rho_i}.$$

Since $\langle n_A/2\rangle_{\rho_i}\langle n_B/2\rangle_{\rho_i} = \langle n_A n_B/4\rangle_{\rho_i}$ for product states, this equation can be reexpressed as

$$\left\langle \left(\frac{n_B}{2} - \frac{n_A}{2}\right)^2\right\rangle_{\rho_i} + \left\langle \frac{n_B}{2} + \frac{n_A}{2}\right\rangle_{\rho_i} \geq \left\langle \frac{n_B}{2} + \frac{n_A}{2}\right\rangle_{\rho_i}.$$

As this is true for every ρ_i, the average $\langle (n_A + n_B)/2\rangle_\rho$ is a lower bound for the mixture $\rho = \sum_i p_i\rho_i$. This limitation imposed on convex mixtures of product states can be overcome if entanglement is involved. In particular,

$$\langle (J_x - S_x)^2\rangle_{|\Psi_1\rangle\langle\Psi_1|} + \langle (J_y + S_y)^2\rangle_{|\Psi_1\rangle\langle\Psi_1|} + \langle (J_z - S_z)^2\rangle_{|\Psi_1\rangle\langle\Psi_1|} = 0,$$

as the two mode squeezed state $|\Psi_1\rangle$ is a simultaneous eigenstate of $(J_x - S_x)$, $(J_y + S_y)$ and $(J_z - S_z)$ with common eigenvalue 0.

Implications of particle losses

In this subsection, the effect of particle losses on the performance of the entanglement criterion is analyzed. The influence of particle losses is modelled by a beam splitter transformation. Creation operators for atoms and light transform according to

$$a_\pm^\dagger \ \mapsto\ \sqrt{1-r_A}\,a_\pm^\dagger - i\sqrt{r_A}\ v_{A\pm}^\dagger, \qquad b_\pm^\dagger \mapsto \sqrt{1-r_B}\,b_\pm^\dagger - i\sqrt{r_B}\ v_{B\pm}^\dagger,$$

corresponding to a beamsplitter with reflectivity r_A for Alice's system and r_B for Bob's system. The quantum noise operators $v_{A\pm}^\dagger$, and $v_{B\pm}^\dagger$ obey canonical commutation relations for each mode and are mutually independent. For the target state $|\Psi_1\rangle$, the left side of condition (5.9) is transformed into

$$\frac{3}{2}\left((r_A - r_B)^2\mathrm{var}(n) + (r_A(1-r_A) + r_B(1-r_B))\,\langle n\rangle\right), \tag{5.11}$$

where $\langle n\rangle = \sinh^2(r)$ and $\mathrm{var}(n) = 2\sinh^4(r)$ is the variance of the particle number[5]. By applying the same beamsplitter transformation to the right side of inequality (5.9) one

[5] $\langle n\rangle$ denotes here the average number of particles in any of the considered modes $\langle n\rangle = \langle n_{A,+}\rangle_{|\Psi_1\rangle\langle\Psi_1|} = \langle n_{A,-}\rangle_{|\Psi_1\rangle\langle\Psi_1|} = \langle n_{B,+}\rangle_{|\Psi_1\rangle\langle\Psi_1|} = \langle n_{B,-}\rangle_{|\Psi_1\rangle\langle\Psi_1|}$.

obtains $(1-r_A)\langle n\rangle + (1-r_B)\langle n\rangle$. In case of symmetric losses $r_A = r_B = r$, successful entanglement verification requires therefore $r < 2/3$. Limitations imposed by particle losses which are different for Alice's and Bob's system are more restrictive, as they impair directly the symmetry-property to which the criterion is tailored to. For large particle numbers, the first term in expression (5.11) is likely to hinder the detection of entanglement. This problem can be resolved by introducing gain factors g_A and g_B for Alice and Bob, which characterize the amplification of measured signals

$$a_\pm^\dagger \;\mapsto\; \sqrt{g_A(1-r_A)}a_\pm^\dagger - i\sqrt{r_A}\; v_{A\pm}^\dagger, \qquad b_\pm^\dagger \mapsto \sqrt{g_B(1-r_B)}b_\pm^\dagger - i\sqrt{r_B}\; v_{B\pm}^\dagger.$$

In this situation, one obtains the result

$$\frac{3}{2}\left(g_B(1-r_B) - g_A(1-r_A)\right)^2 \mathrm{var}(n) + \frac{3}{2}\left(g_B r_B(1-r_B) + g_A r_A(1-r_A)\right)\langle n\rangle,$$

which has to be compared to $g_B(1-r_B)\langle n\rangle + g_A(1-r_A)\langle n\rangle$. g_B and g_A have to be optimized according to the experimental parameters. For large particle numbers, the quadratic term dominates such that the choice $g_A/g_B = (1-r_B)/(1-r_A)$ solves the problem of asymmetric losses and one obtains the condition $(r_A + r_B)/2 < 2/3$ for successful entanglement detection. Remarkably, this threshold does not depend on the degree of squeezing. If the probabilities for particle losses are known, atomic and photonic signals need not to be amplified, as it is sufficient to adjust the inequality accordingly.

5.2.3 Entanglement in superradiant scattering from Bose-Einstein condensates

As explained above, the entanglement criterion (5.9) can be applied in many different settings. Here, the verification of entanglement produced in superradiant scattering of laser light from a Bose-Einstein condensate is described. More specifically, a Bose-Einstein condensate, which is elongated along $\hat{z}$ and excited by a laser field propagating along the same direction is considered. The scattering interaction is assumed to be well within the superradiant regime, such that light is predominantly emitted along two endfire modes [312], along $\hat{z}$ and $-\hat{z}$, as shown in Fig. 5.6a. Atoms scattering photons along $-\hat{z}$ acquire a momentum kick of $2k$, where k is the wave vector of the incoming light field. These atoms are spatially separated from the BEC and form a new moving condensate. To begin with, only the endfiremode consisting of photons scattered along $-\hat{z}$ and atoms travelling along the $\hat{z}$ direction are considered.

Entanglement between atoms and light

Atoms are assumed to possess an internal level structure as shown in Fig. 5.6b. As was shown in [144], the dynamics of the superradiant process can be described by a two mode squeezing Hamiltonian $H_1 \propto a_+^\dagger b_+^\dagger + a_-^\dagger b_-^\dagger + H.C.$, where the creation operators $a_+^\dagger$ and $a_-^\dagger$ denote the scattered light fields in plus and minus polarization, while $b_+^\dagger$ and $b_-^\dagger$ are the creation operators for the respective atomic states. This leads to the generation of the two mode squeezed state $|\Psi_1\rangle$. The atom and photon numbers are correlated for

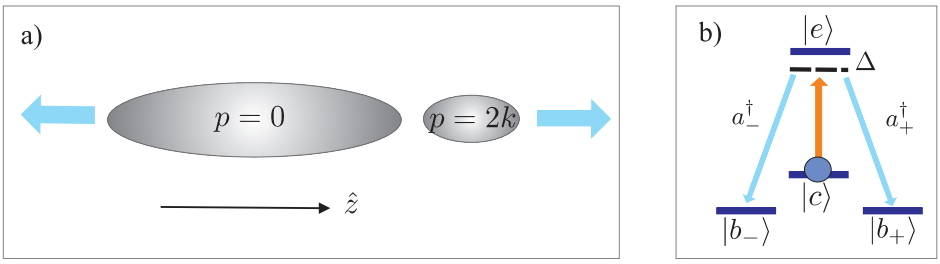

Figure 5.6: Setup and atomic levels considered for the creation of N-particle entanglement between atoms and light. a) Light propagating along $\hat{z}$ is scattered from an elongated condensate. Photons are scattered superradiantly into two endfiremodes, which correspond to scattering angles of 0 and π, as indicated by arrows. b) Off-resonant laser light couples to the transition $|c\rangle \rightarrow |e\rangle$, such that atoms, which are initially prepared in $|c\rangle$ are transferred to state or $|b_+\rangle$ or $|b_-\rangle$ via a Raman process and emit a photon in $+$ or $-$ polarization respectively.

each polarization and the inseparability of the produced quantum state can be verified according to criterion (5.9) by identifying Alice with the light field and Bob with the atomic system. In the considered physical setting, various sources of noise may impair the verification of entanglement. Apart from particle losses, which have been discussed in the previous section, undesired atomic transitions can degrade the reliability of the proposed criterion, for instance if atoms are scattered into states other than $|b_-\rangle$ and $|b_+\rangle$, while emitting photons in $+$ or $-$ polarization. These processes can be avoided by a suitable choice of atomic levels. As an example, typical alkali atoms used in BEC experiments, ^{87}Rb and ^{23}Na, with nuclear spin 3/2 are considered. By preparing the atomic sample in the $F = 1$, $m_F = 0$ ground state and inducing transitions to a manifold with $F' = 0$, $m_{F'} = 0$, atoms can only be scattered back to the $F = 1$ groundstate manifold, occupying the states $|F = 1, m_F = -1\rangle \equiv |b_-\rangle$ and $|F = 1, m_F = +1\rangle \equiv |b_+\rangle$, while transitions to other states are forbidden due to the selection rule $\Delta(F) = 1$. However, undesired atomic transitions can still be mediated by interatomic collisions. The effect of transitions from $|b_+\rangle$ or $|b_-\rangle$ to other states is already included in the consideration of particle losses above, but the creation of a pair of atoms in these two states without the production of the corresponding photon pair should be avoided. This can be done by applying electromagnetic fields imposing Stark shifts on the internal levels such that such a transition is prohibited by energy conservation.

The measurement of Stokes operators of light required for the verification of entanglement can be performed in a standard fashion [172, 241, 260]. The measurement of the atomic collective spin component J_z can be done by counting atoms in the final states $|b_+\rangle$, $|b_-\rangle$ using resonant absorptive imaging. The measurement of the spin components $J_{x,y}$ can be performed by applying suitable radio-frequency $\pi/2$ pulses to the final atomic states before imaging.

Entanglement between two condensates

The correlations between atoms and light, that are generated in the process described above, can be used to create entanglement between two condensates. To this end, both endfire modes are considered. The full Hamiltonian is given by

$$H_2 \propto a^\dagger_{+I} b^\dagger_{+I} + a^\dagger_{-I} b^\dagger_{-I} + a^\dagger_{+II} b^\dagger_{+II} + a^\dagger_{-II} b^\dagger_{-II} + H.C.\ ,$$

where the subscript I refers to the backward scattered light and and the moving condensate, while the subscript II refers to forward scattered light and the condensate at rest. After the interaction, the backward scattered light field and the moving condensate are in a two mode squeezed state as well as the light field scattered in forward direction and the part of the condensate at rest, which is transferred to state $|b_+\rangle$ or $|b_-\rangle$,

$$|\Psi_2\rangle = (1-\Lambda)^4 \sum_{n=0}^{\infty} \Lambda^n |n\rangle|n\rangle \otimes \sum_{j=0}^{\infty} \Lambda^j |j\rangle|j\rangle \otimes \sum_{m=0}^{\infty} \Lambda^m |m\rangle|m\rangle \otimes \sum_{l=0}^{\infty} \Lambda^l |l\rangle|l\rangle,$$

where the first and second term refer to atom-photons pairs in plus and minus polarization which are described by creation operators labelled with the subscript I while the third and fourth term refer to atom-photons pairs in plus and minus polarization which are described by creation operators labelled with the subscript II.
The part of the resting condensate which has been transferred to the state $|b_+\rangle$ or $|b_-\rangle$ can be entangled with the moving condensate by means of entanglement swapping, i.e. by measuring EPR operators for each polarization of light modes using homodyne detection. However, this procedure leads to degradation of entanglement if non-maximally entangled states are involved, and a distillation step has to be performed afterwards to obtain a more useful resource state. It has been shown that continuous variable entanglement cannot be distilled using Gaussian operations only [172, 259, 260][6]. In the following, a scheme which relies on photon counting rather than Gaussian measurements and exhibits probabilistic entanglement distillation is put forward. More specifically, the moving and resting condensates are entangled by combining the forward and backward scattered light modes at a beamsplitter and measuring the photon numbers at both output ports. This has to be done for each polarization separately. The scheme is explained for the + polarized part of the light field. Analogous expressions hold for the − polarized part.
The application of a balanced beamsplitter transformation $a^{in}_{+I} \rightarrow (a^{out}_{+I} + a^{out}_{+II})/\sqrt{2}$, $a^{in}_{+II} \rightarrow (a^{out}_{+I} - a^{out}_{+II})/\sqrt{2}$, where a^{in}_{+I}/a^{in}_{+II} and $a^{out}_{+I}/a^{out}_{+II}$ denote annihilation operators of the light fields at the input and output ports of the beamsplitter respectively, to state (5.7) results in

$$\begin{aligned} |\Psi_1^{BS}\rangle \;=\; & (1-\Lambda^2) \sum_{n,m=0}^{\infty} \Lambda^{n+m} \frac{1}{\sqrt{n!m!}} 2^{\frac{-(n+m)}{2}} \sum_{i=0}^{n} \sum_{j=0}^{m} \binom{n}{i} \binom{m}{j} (-1)^j \\ & \sqrt{(i+j)!(n+m-i-j)!}|n, i+j\rangle|m, n+m-i-j\rangle. \end{aligned}$$

[6] Distillation of entanglement in two mode squeezed states requires at least one non-Gaussian element as for example employed in [67, 264–266, 331].

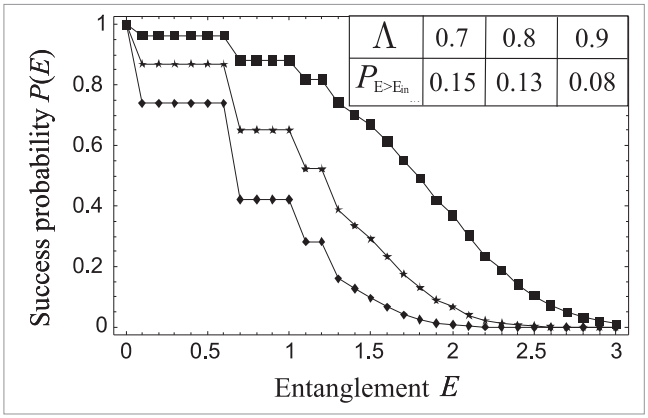

Figure 5.7: Success probability versus entanglement which can be produced by means of the proposed scheme for different values of Λ. Diamonds: $\Lambda = 0.7$, stars: $\Lambda = 0.8$, squares: $\Lambda = 0.9$. The inset shows the probability of obtaining at least as much entanglement as was present in the input state $|\Psi_1\rangle$.

The probability of detecting N_I photons at the first and N_{II} photons at the second output port of the beamsplitter is given by $P_{N_I,N_{II}} = (1-\Lambda^2)\Lambda^{N_I+N_{II}}$. Such an event results in the quantum state

$$|\Psi_{N_I,N_{II}}\rangle \;=\; \sum_{n=0}^{N} k_{N_I,N_{II}}(n)\; |n, N-n\rangle,$$

where $N = N_I + N_{II}$ denotes the total number of detected photons. The coefficients $k_{N_I,N_{II}}(n)$ are given by

$$k_{N_I,N_{II}}(n) = 2^{\frac{-N}{2}}(-1)^{N_I}\sqrt{\frac{N_{II}!}{N_I!}}\sqrt{\frac{(N-n)!}{n!}}\frac{1}{(N_{II}-n)!}\;{}_2F_1(-n,-N_I,N_{II}-n+1;-1),$$

where ${}_2F_1(a,b,c;z)/(c-1)!$ is the regularized hypergeometric function. This state describes pairs of atoms in $|b_+\rangle$ in the moving condensate and at rest, which are referred to in the first and second ket respectively. For certain measurement outcomes this state is more entangled than $|\Psi_1\rangle$, such that the state can be purified by postselection. Fig. 5.7 shows the success probability versus the produced entanglement given by the von Neumann entropy of the reduced density matrix of the resulting atomic state $E(N_I,N_{II}) = \sum_{n=0}^{\infty} k^2_{N_I,N_{II}}(n)\ln\left(k^2_{N_I,N_{II}}(n)\right)$ for different values of Λ. Note that the initial state, which contains infinitely many terms, is truncated by the measurement process. This way, states with entanglement close to the maximal degree of entanglement in the corresponding subspace can be produced. For example, for $N_I = 1$ and $N_{II} = 0$, the maximally entangled state $|\Psi\rangle = (|1,0\rangle + |1,0\rangle)/\sqrt{2}$ is created. By considering the light field in $+$ as well as in $-$ polarization, the resulting atomic state can be detected by criterion (5.9) after performing the local transformations $n_{+II} \mapsto N - n_{+II}$ and $n_{-II} \mapsto N' - n_{-II}$. In this case, **J** refers to atomic operators at rest and **S** describes the moving condensate.

Chapter 6

Conclusions and outlook

In this Thesis, we proposed several novel protocols for applications in quantum information science and explored new directions based on the use of light-matter interface techniques and engineered dissipation.

We investigated two different platforms for the implementation of quantum interfaces, atomic vapor at room temperature and ultracold atoms in optical lattices. We considered ensembles of ultracold atoms for the implementation of an entangling gate for photons (Sec. 4.3) and for the realization of a novel spectroscopy method which allows one to probe dynamical correlations in strongly interacting systems (Sec. 4.2). The latter protocol introduces the use of quantum memories to the field of quantum simulations of many-body systems and opens up new possibilities for the investigation and engineering of complex dynamics. This type of scheme could also be used to monitor a system non-destructively and act back on it conditioned on the result of the measurement. Due to the use of a quantum memory, the correlations in the system are preserved during the time delay which is necessary to read out the quantum state and perform certain unitary operations for feedback. This way, interesting dynamics could be steered and non-equilibrium phenomena could be studied. Applying concepts developed in quantum information science, such as quantum memory techniques, for the study of correlated quantum many-body systems is a very promising route. Both fields have a natural overlap which allows for interdisciplinary work and cross-fertilization.
The former protocol uses the interactions and control available in atomic systems to manipulate photonic states by means of light-matter interface schemes. Such an approach can find many more useful applications for the engineering of photonic states [168]. Recently developed techniques for the single-site resolved manipulation of ultracold atoms in optical lattices [107–109], will allow for the precise control of the spin waves, to which photonic states are mapped and released from. In turn, the mapping of suitable photonic states to matter can be a very valuable tool for the manipulation of atomic systems.

We also discussed an application of light-matter interface schemes for the second platform mentioned above, atomic vapor at room temperature. In Sec. 4.1, we analyzed a protocol for the faithful teleportation of a quantum state between two atomic ensembles.

The performance of this and related protocols could be improved by realizing samples with a higher optical depth. Possible routes towards this goal include the use of micro-fabricated cells and low-finesse optical cavities, which would render many more applications of ensemble-based interface schemes in quantum information science possible. In particular, the development of a robust, integrated and scalable room temperature atom-light interface and its incorporation into a hybrid multi-facet quantum network with other relevant quantum systems, such as nano-mechanical oscillators and electronic circuits is a promising future direction. Micro-size room temperature atomic quantum memories in spin-protecting micro-cells appear to be excellent candidates for this task. The light-matter interface schemes discussed here for atomic ensembles are based on quadratic interactions and measurements, which preserve the Gaussian character of quantum states. However, important tasks such as the distillation of entanglement and hence its distribution over large distances by means of quantum repeater schemes require non-Gaussian elements. It would be therefore very interesting and important to devise experiments involving atomic ensembles at room temperature which leave the Gaussian realm, for example by including single photon detections.

Regarding the second aspect of the research line followed here, engineered dissipation, we introduced two different types of protocols. We proposed a new method for the dissipative generation of robust steady state entanglement (Sec. 3.1) and novel schemes for the distillation and distribution of steady state entanglement over long distances (Sec. 3.2). The first scheme is very concrete and a specific physical implementation has been worked out in detail. The ideas put forward here have been implemented using gas samples at room temperature, such that theory and experiment could go hand in hand. In contrast, the protocols for dissipative entanglement distillation and distribution are very abstract and specific implementations of the ideas and concepts developed in this proof-of-principle study are yet to be explored. Using dissipation for quantum state engineering and other tasks related to quantum information science represents a paradigm shift. Exploring and exploiting all advantages of dissipative approaches will require both, devising new protocols which are capable of generating and processing steady states as well as finding realistic and practical ways of implementing the required coupling of physical systems to a bath. The results presented here provide starting points for future research in this new and promising direction.

The overall guiding theme of this Thesis is the endeavor to understand and to use quantum correlations in the context of light-matter interactions. The study of the behavior of quantum systems can lead to both, interesting applications and new technologies as well as a deeper understanding of nature. Quantum mechanics gives rise to many phenomena which we are only beginning to understand.

Appendix A

Quantum Information Theory

The quantum world is governed by laws which are in many ways very different from those of classical mechanics. Since some effects are unlike anything encountered in daily live, they can appear counterintuitive and are difficult to comprehend by applying common sense and everyday experience. Interestingly, the behavior of quantum particles includes aspects which can be understood as new possibilities and as restrictions at the same time. The superposition principle allows for example for a plethora of quantum interference effects and imposes at the same time fundamental restrictions on the distinguishability of quantum states and on the creation of identical copies as stated by the no-cloning theorem [10]. Moreover, quantum systems can exhibit correlations which are stronger than any correlations allowed in a classical world. The correlations present in entangled states are fundamentally distinct from classical ones and can yield markedly different results. Entangled states can violate Bell inequalities[1] [253, 341] and lead to observations that can not be described by standard classical models.

The laws and peculiarities of quantum mechanics have a profound impact on the way information can be processed. In the field of quantum information science, this interesting topic is studied with the twofold aim to understand and harness quantum systems. As outlined below, quantum states can for instance be used for fast factoring algorithms [1, 2] or for unconditionally secure communication [4, 5]. Apart from that, quantum effects will become important for information technologies in the future, if the miniaturization of devices reaches molecular or even atomic length scales. These considerations show that the recognition that "information is physical" [342, 343] has important implications. However, also the reverse insight that "physics is information" has been proven to yield relevant advances in physics. The quantum information perspective on quantum physics, the notion of entanglement and similar concepts as well as methods and tools developed in this context (see e.g. App. A.3) can add important contributions to other fields, such as the study of strongly correlated systems and condensed matter physics.

[1] Bell inequalities provide a possibility to test quantum mechanics experimentally against theories which are based on local (hidden) variables and have first been first introduced by John Bell in 1964 [253]. Since then, the study of Bell inequalities has evolved into a vigorous field of research and many different experiments have been performed [332–337, 337–340].

In this appendix, we give a brief introduction to quantum information science. Since this is a rapidly developing research area with many different aspects and various cross links to other fields, we address only few major directions. In the following we consider the fields of quantum computing (App. A.1), quantum communications (App. A.2) and quantum simulations (App. A.3). Apart from these three areas, several other subfields exist, which are concerned with fundamental tests of quantum mechanics, high-precision measurements and sensing, random number generators, entanglement theory, new numerical methods to describe quantum systems and other interesting aspects of QIS.

A.1 Quantum computing

As outlined above, the implications of the laws of quantum mechanics for information processing render quantum computers capable of performing tasks beyond the possibilities accessible by classical means.
A quantum computer could evaluate a function for several input values in a coherent superposition. The possibility to access a whole range of values at the same time "in parallel", allows one to quickly infer global properties of functions (such as their periodicity). This principle is exploited by the quantum Fourier transform, the quantum analogue of the classical discrete Fourier transform. It lies at the heart of many quantum computation schemes such as Deutsch's algorithm [344], the Deutsch-Jozsa algorithm [345,346], Shor's algorithms for facturing and computing the discrete logarithm [1,2], the estimation of the eigenvalues of a unitary operator [347] and phase estimation [3]. Deutsch's algorithm and the Deutsch-Jozsa algorithm are early examples, demonstrating that quantum computers can be more powerful than classical ones[2]. Together with Simon's algorithm [348] they were the basis for Shor's algorithms for factoring and the computation of the discrete logarithm. These algorithms provide quantum solutions to problems which are believed not to be efficiently solvable classically[3] and are also of high practical relevance. A quantum device able to factor efficiently large numbers would allow one to break RSA cryptosystems [349], which are the most widely used public-key cryptosystems to date. Similarly, other cryptosystems are based on the assumption that the discrete logarithm is hard to compute[4]. Later, a unified view to these and related algorithms has been found by noting that Simon's and Shor's algorithms mentioned above as well as many other related algorithms which provide an exponential speedup are special instances of the hidden subgroup problem [347,350].

[2] The Deutsch-Jozsa algorithm provides an efficient deterministic solution to Deutsch's problem: a binary function $f(x)$, takes the numbers 0 to $2^n - 1$ as input and is known to be either balanced (i.e. yielding the result 1 for precisely half of the possible input values and else 0) or constant (i.e. yielding the same results for all inputs). By means of the Deutsch-Jozsa algorithm, the problem to decide whether $f(x)$ is balanced or constant can be solved using only one evaluation of the function, while a classical deterministic strategy would require in the worst case $2^n/2 - 1$ queries.

[3] Using Shor's algorithm, the time required to find the prime factors of an N-digit integer scales polynomial in N, which is exponentially faster than any known classical algorithm. However, the question whether efficient classical algorithms for factoring exist is still an open problem.

[4] As explained in Sec. A.2, quantum information science does not only pose a potential threat to secure communication, -it also opens up a new route towards cryptography, where privacy is guaranteed by the laws of nature.

A different class of quantum algorithms was discovered in 1995 by Lov Grover [351, 352], who invented a general search algorithm which requires only $O(\sqrt{N})$ queries to find a marked element in an unsorted list with N items (a classical search would require $O(N)$ queries). The problem of unstructured data base search is very common and has a very wide range of applicability including the speedup of solutions to NP-complete problems. By combining Grover's search algorithm with a quantum Fourier transform, it is possible to determine whether a search problem has a solution or not. Using this method, - quantum counting - the number of solutions of a search problem can be estimated much more quickly than possible classically [353].
Recent progress[5] includes for example algorithms for solving sets of linear equations [354] and quantum metropolis sampling [355]. Using the former algorithm, features of solutions of linear equations can be estimated much faster than could be done on a classical computer. The latter algorithm allows for the computation of properties of equilibrated quantum systems by preparing ground and Gibbs states on a quantum computer. Another interesting direction of current research is based on quantum walks [356]. Using this approach, efficient algorithms for the quantum simulation of Hamiltonian dynamics [357], the evaluation of NAND formulas [358–361] and specific oracle problems, which cannot be solved classically with high probability in subexponential time [362] have been found recently.

Small scale implementations of quantum algorithms have already been experimentally realized. Shor's algorithm has already been implemented using nuclear magnetic resonance (NMR) [363]. In this experiment, the factorization of the integer 15 has been demonstrated using a seven-qubit quantum computer. A related algorithm for order finding has been implemented in a similar experiment using five qubits [364]. The Deutsch-Jozsa algorithm has been implemented (involving two qubits), using trapped ions [365] and superconducting devices [366]. Experimental implementations of Grover's database-search algorithm include two-qubit realizations using NMR [367, 368], photons [369], ions [370] and solid state systems [366] as well as three qubit NMR realizations [371]. A related (quantum fetching) algorithm has been implemented using seven qubits [372]. Scaling quantum computing schemes up represents an enormous challenge, due to the difficulty to control large quantum systems. It has been shown that quantum computing is possible in the presence of noise and imperfections: the quantum fault-tolerance theorem states that errors can be suppressed efficiently at the cost of a polynomial overhead in computation, if the level of noise in a quantum system can be reduced below a constant threshold value [3]. However, even though controlling the errors in large scale quantum computation is possible in principle, it is extremely difficult. From a theoretical perspective, quantum algorithms are extremely interesting, in particular in view of fundamental questions. The question which problems can be solved efficiently on a quantum computer and how quantum information processing relates to classical computing is actively investigated. Practically, other applications of quantum information science such as quantum communication (Sec. A.2) or quantum simulations (Sec. A.3) are much closer in reach.

[5] See http://math.nist.gov/quantum/zoo.

A.2 Quantum communication

Playing on the peculiar properties of quantum systems opens up a plethora of intriguing possibilities for the realization of communication tasks. The field of quantum communication is concerned with protocols which yield a quantum advantage compared with their classical counterparts or enable tasks that are impossible classically. Such schemes include protocols for superdense coding [373], quantum secret sharing [374,375], quantum digital signatures [376], quantum fingerprinting [377], unclonable encryption [378], conference key agreements [379], quantum coin tossing [4] and quantum money [380].

Quantum cryptography [381], the art of expanding a secret key, is a particularly active area and first (prototype) quantum cryptosystems are already commercially available and distributed by the companies id Quantique, MagiQ Technologies, SmartQuantum and Quintessence Labs. Most classical cryptosystems used today, such as the widely used RSA [349] public-key cryptosystem, rely on the unproven computational assumption that certain functions are hard to compute (moreover, important systems such as RSA could be broken by a quantum computer as discussed in Sec. A.1). Quantum cryptography, in contrast, offers unconditional security. Any message can be safely encrypted using one-time pads [382], i.e. by adding an element of a random key to each bit (or symbol) of the text. This method is unbreakable but requires a secret random key of the length N, where N is the number of bits used in the text. Quantum mechanics offers several possibilities to expand a small key (which is used for authentication[6]).
The first quantum key distribution (QKD) schemes have been devised by Stephen Wiesner [380] and Charles Bennett and Gilles Brassard who introduced the paradigmatic BB84 protocol [4] in 1984. These protocols rely on the fact that any attempt of an eavesdropper to copy, measure or manipulate quantum states that are transmitted between two parties can be detected. Due to the impossibility to clone unknown quantum states [10], cryptographic protocols can be designed such that a third party is unable to attain information on the key without leaving a trace which reveals that secrecy is compromised. QKD schemes can also be formulated in terms of entangled states [385, 386]. In this case, a secret key is established by distributing an entangled state between two parties - Alice and Bob. The correlations in the resulting shared quantum state, which serves as resource for the key can be tested, e.g. by means of Bell inequalities. This type of scheme relies on a fundamental trade-off known as "monogamy of entanglement" [387, 388]. The amount of entanglement shared between Alice and Bob translates directly into an upper bound on the amount of information a third party can have on the shared quantum state. If two qubits are in a maximally entangled state, none of them can be correlated with a third one. In general, QKD schemes rely on the principle, that an upper bound on the information of a potential eavesdropper can be given for each sufficiently small error rate associated with the transmission of quantum states [389]. If the knowledge on the key of a potential eavesdropper is sufficiently small, classical protocols for privacy amplification can be applied in order to achieve an arbitrary high level of secrecy.

[6] The keys required for authentication can be much shorter than the message to be authenticated. Efficient secure authentication can be done using the Wigman-Carter scheme [383, 384].

Today, there exists a large variety of advanced protocols for QKD, which can be formulated using discrete or continuous variables. QKD protocols can be realized by means of very different techniques which may, for example, use any two nonorthogonal states [390], employ a 6-state coding-scheme [391, 392], or utilize even orthogonal states. Recent progress in the development of new QKD systems includes the invention of decoy state protocols [393], phase shift keying protocols [381] and Gaussian-modulated coherent-state systems [394], which resort to continuous variables.

The first experimental implementation of a key distribution system has been realized in 1992, when the BB84 protocol has been used to generate a secret key over 30cm at rate of 10 bits per second [395]. Shortly after, a key could be established over 19 km using an optical fiber [396]. In a first demonstration out of the lab, a QKD protocol has been performed over 23km [397] (and later 76km [398]) under the Lake Geneva. In 2004, a secret key has even be generated over 150km using commercial telecom fibers.
In spite of these impressive advances, the realization of quantum communication schemes (in general) using present technology is fundamentally limited by the absorption length of silica fibers, which is on the order of hundred kilometers. Due to the uncertainty principle, classical strategies for signal amplification cannot be used, since they would destroy the quantum properties of the transmitted light states. Therefore, quantum repeater schemes[7] [155] have been devised which allow for the distribution of highly entangled states over large distances. These entangled states can in turn be used to teleport quantum states [189] with high fidelity rather than transmitting quantum states directly. The realization of quantum repeaters is a very important challenge of current research and relies crucially on reliable light-matter interfaces and quantum memories.
Free space links to satellites could provide an alternative route towards global quantum communication in future. Entanglement has been distributed over an optical free space link between two Canary Islands and a quantum cryptographic key has been generated bridging 144km [401, 402]. Due to the decreasing density of the atmosphere with increasing height, the efficiency demonstrated in this experiment corresponds to the one required for ground-to-satellite communication. Global satellite-based quantum communication is a visionary long-term goal of current research. Other future directions and challenges include for example the investigation of quantum networks. The European project SECOQC[8] aims at providing a basis for long-range secure communication in a network by combining QKD with classical network design and cryptography. The first demonstration of a working quantum network took place in 2008 in Vienna. The realization of QKD systems in a network setting has also been demonstrated in 2010 in Tokyo[9]. Apart from this experimentally driven line of research, the investigation of quantum networks represents also a very interesting field of research from a more

[7] In quantum repeater schemes, a large distance is divided into short segments, over which entanglement can be distributed directly. The entangled links can be pair wise connected by entanglement swapping [251, 399], which doubles the length of the entangled links. The inevitable degradation of entanglement during this procedure is compensated by the subsequent application of an entanglement distillation protocol [179, 400]. By iterating this routine, a single long-range entangled link of high quality is obtained.
[8] See http://www.secoqc.net
[9] See http://www.uqcc2010.org/highlights/index.html

theoretical perspective. It has for instance been discovered recently that quantum networks exhibit properties which differ in a surprising way from the effects encountered in classical complex networks [403].

A.3 Quantum simulations

A quantum simulator is a well controlled quantum system which can be used for the simulation of other quantum systems. As explained below, this idea encompasses universal as well as special purpose simulators. The latter concept aims at the emulation of a specific quantum system of interest by another one. This way, models which are believed to give rise to certain phenomena can be tested in a controlled way and with much less resources than by known classical simulation techniques. There are two types of generic applications. The first one is the investigation of phenomena which cannot be observed directly in experiments. Quantum simulators can for example be used to study phenomena originating in the interplay of gravitational and quantum effects such as the generation of Hawking radiation in the vicinity of black holes [404–408]. The second application concerns the exploration of systems where no simple theoretical description is available and the quantities of interest cannot be calculated classically. In this regard, quantum simulators provide a promising route towards the understanding of quantum many-body systems. Due to the exponential growth of the underlying Hilbert space, the classical simulation of quantum systems quickly becomes intractable for large particle numbers. If no simplifying model exists (for example in strongly correlated systems), a general quantum system can only be simulated if it is very small (the description of a system consisting of 40 qubits is already beyond current capabilities [409]).
In terms of technological applications, the simulation of quantum many-body systems can pave the way for discovering and devising new materials. Moreover, the simulation of molecular structures and chemical reactions can play an important role in the design of new chemicals and drugs. In terms of fundamental research, quantum simulations (QS) are expected to provide new results and insights into very relevant problems in condensed matter physics and are a promising tool for exploring dynamics and non-equilibrium physics.

Historically, the idea of QS has been introduced in 1982 by Richard Feynman [7]. Later, Seth Lloyd and others developed this concept further and formulated the conditions under which QS can be performed efficiently on a universal quantum computer [8]. The key concept put forward in this context is the simulation of time evolutions by means of Trotterization. This method is based on the fact that any system consistent with special and general relativity evolves according to local interactions. Any physically relevant Hamiltonian can therefore be written as a sum of local terms. The time evolution according to such a Hamiltonian can be approximated by the Trotter-Suzuki decomposition [410, 411], i.e., by dividing the time interval to be simulated into small discrete time steps. For each small time step, the evolution can be approximated using unitary gates which involve few particles. This simulation scales efficiently with the number of operations and the overall error can be made as small as required by using

sufficiently small time steps. This method is sometimes referred to as "digitial" quantum simulation as opposed to the "analogue" quantum simulation mentioned above, where the Hamiltonian of the system is controlled such that it acts in correspondence to the Hamiltonian to be simulated.

By now, QS has become a vigorous and fast developing research field [409, 412] and several proof-of-concept experiments have been performed using different approaches. The furthest developed systems in this respect are trapped ions and ultracold atoms in optical lattices. Quantum simulations using trapped ions [413] profit from the very high degree of control available in this system. Scaling ion-based simulation schemes up is difficult, but possible in principle [414]. It has been shown that trapped ions can be used to simulate spin systems [415, 416] and important models in solid state physics such as the Bose-Hubbard model [417]. Experimental realizations of quantum simulations in this system include the simulation of quantum phase transitions [418, 419], the Klein paradox [420], the Dirac equation [421] and the Ising system [422]. Neutral atoms in optical lattices [20, 21, 242] constitute a very clean system which has the advantage that a large number of particles are involved and can be manipulated in parallel. Moreover, techniques for single-site resolved imaging and manipulation have recently been developed. This system is therefore a very promising platform for realizing a special-purpose device for the simulation of a large quantum system. There exists a plethora of proposals for simulation schemes which are based on ultracold atoms in optical lattices. Important experimental advances include the observation of the quantum phase transition from a superfluid to a Mott-insulator [23, 24] and the simulation of a 1D Tonks-Girardeau gas [423]. Other systems have also already acted as testbed for quantum simulations. Nuclear magnetic resonance systems [424] have been used to simulate three-body (Heisenberg-)interaction Hamiltonians [425], pairing Hamiltonians [426] and many-body Fermi systems [427] and photons served as simulators for molecules [428] and Heisenberg Hamiltonians [429]. Moreover, atoms in coupled cavity arrays [430], polar molecules [431] or solid state systems such as quantum dots [432] and nitrogen vacancy centers in diamond [433] are promising candidates for QS.

On the theoretical side, recent interesting results related to lattice gauge theories, open quantum systems, quantum chemistry and interacting fermions in general have been reported, as will be briefly explained in the following. The study of interacting fermions is of central interest in many fields such as quantum chemistry and solid state physics. However, interacting fermions are extremely difficult to simulate classically, since the symmetry of fermionic wave function leads to the so called "sign problem", which limits classical methods such as Monte Carlo algorithms to systems of small size. In contrast, fermionic systems can be simulated efficiently using quantum algorithms, which are not impaired by the sign problem [434]. The QS of interacting electrons can lead to a better understanding of important phenomena such as high-temperature superconductivity and the fractional quantum Hall effect. As mentioned above, quantum effects are also very important for molecular reactions, but unfortunately the corresponding calculations based on the full Schrödinger equation are infeasible if many electrons are involved [409]. The study of dynamics and properties of molecular reactions can

therefore profit greatly from quantum simulations. In [435], it has been shown for a concrete example, that quantum simulations are a valuable tool to calculate molecular energies. These results demonstrate that a quantum simulation algorithm using 30 to 100 qubits can already exceed the limitations of classical computing for practically relevant applications. Another interesting line of recent research is the investigation and simulation of open quantum systems. The simulation of systems interacting with an environment is important for the study of quantum noise and dissipative phenomena and plays a central role in the modelling of quantum processes under realistic conditions. In [59], a universal open system simulator has been demonstrated in a system of trapped ions.

Lattice gauge theories are another important field of application for quantum simulations [436–439]. Lattice gauge theories are used in many areas of physics. In particular the field of quantum chromodynamics, which relies on extensive lattice quantum field theory calculations, could be advanced through efficient simulation techniques. Cold atoms in optical lattices are a promising candidate system for the implementation of this type of simulation. Several schemes for the emulation of quantum field theories using cold atoms have already been put forward [440–442] including a protocol for the simulation of Dirac fermions interacting with dynamical fields [443].

Quantum simulations represent one of the most important areas of QIS. Even modest-size quantum simulators have a wide range of relevant applications in many fields of science and are much closer in reach than the realization of a universal quantum computer. Proof-of-principle demonstrations have already been experimentally realized and the next important step will be the demonstration of a quantum simulation which outperforms classical devices. Special purpose quantum simulators are at the forefront of this endeavor.

Appendix B

Dissipatively driven entanglement: supplementary material

This appendix provides additional material supplementing Sec. 3.1. In App. B.1, we emphasize characteristic differences between the entangling scheme which is proposed and analyzed here and standard protocols for the creation of entanglement. Moreover, we explain and highlight special features of the dissipative method . In App. B.2, we show that the steady state of the dissipative evolution considered in Sec. 3.1 is unique. App. B.3 and App. B.4 complement Sec. 3.1.3. More specifically, App. B.3 and App. B.4 contain details of the derivation of the complete master equation describing the entangling dynamics and the detailed calculation of the corresponding amount of entanglement which can be generated respectively. App. B.5 concerns the extension of the scheme to multi-level systems discussed in Sec. 3.1.4. In the last part of this appendix (App. B.6), we consider the realization of the proposed scheme in ^{133}Cs ensembles and calculate (implementation-independent) limits on the amount of produced entanglement, which arise due to undesired radiative transitions.

B.1 Comparison of dissipative entanglement generation with other methods

There exists a large variety of methods for creating entanglement between two quantum systems. In particular, several methods have been devised and demonstrated for entangling atomic ensembles. Even though some schemes share similarities with the new method presented here, they are fundamentally different. In the following this is explained in detail and the features of dissipative entanglement generation are highlighted by comparing the scheme put forward here with previous approaches.

In standard approaches [12, 16, 66, 67, 157–161, 444–446], two atomic ensembles A and B are prepared in specific pure states $|a\rangle_{\mathrm{A}}$, and $|b\rangle_{\mathrm{B}}$. An additional system, E, which typically corresponds to certain modes of the electromagnetic field, is also initialized in a specific state, for example the vacuum $|0\rangle_{\mathrm{E}}$. For appropriately chosen external parameters such as the frequency and polarization of applied laser fields, the interaction

of system E with A and B gives rise to an entangled state $|\Psi\rangle = U|a,b\rangle_{\mathrm{A,B}}|0\rangle_E$. If system E is measured, e.g. using a beam splitter and single-photon detectors, or by means of homodyne detection, the state of systems A and B is projected onto an entangled state, $|\Phi(e)\rangle_{\mathrm{A,B}}$. This state depends on the outcome of the measurement e. If no measurement is performed (which corresponds to averaging with respect to the possible measurement outcomes[1]) the resulting state is not entangled. For instance, the DLCZ protocol [67] yields a separable state if the photons emitted by the ensembles are not detected.

Dissipative methods can be described as follows. $|a\rangle_{\mathrm{A}}$, $|b\rangle_{\mathrm{B}}$, and $|0\rangle_{\mathrm{E}}$ denote again the initial states of systems A, B and E respectively. Due to the interaction of system E with A and B, the state $|\Psi(t)\rangle = U(t)|a,b\rangle_{A,B}|0\rangle_E$ is created, where the dependence of the resulting quantum state on the time t is explicitly indicated. Under ideal conditions, i.e. if systems A and B do not couple to other environments, the interaction of A and B with E can be engineered such that the atomic system evolves towards an entangled state. In contrast to the schemes described above, the implementation of this entangling dynamics does not require measurements on system E. This type of behavior can occur if system E possesses an infinite number of degrees of freedom, such that a non-unitary dynamics drives the system towards a fixed state. Due to this property, E is typically referred to as environment and the corresponding interaction with systems A and B is referred to as dissipative process. Dissipative phenomena of this kind are best described by means of master equations. To this end, the environment is traced out and an equation for the reduced density operator of systems A and B, ρ, is derived as described in Sec. 3.1. In the presence of other environments, the dissipation induced by the coupling of A and B to system E can still create entanglement with a life time, which exceeds the decoherence times due to these extra noise sources significantly, if the corresponding (uncontrolled) coupling is sufficiently weak. Note further, that typically, noise processes can be included in the master equation description as it is done here (see Sec. 3.1).

In the experiment described in Sec. 3.1.5, entanglement induced by dissipation has been observed. In particular, in contrast to previous approaches entanglement is obtained without using measurements on the quantum state of the environment[2]. Furthermore, systems A and B remain entangled for 40ms. This entanglement life-time is at least by a factor 16 longer than the decoherence time induced by other noise sources. It has been experimentally verified that in the absence of the dissipative process, the measured entanglement life time is limited to 2.5ms due to the remaining noise sources such as collisions or inhomogeneities of the applied magnetic fields.

Dissipative methods exhibit another distinctive feature, which is present in the

[1] A measurement yielding the result e, produces the quantum state ρ_e. The situation where no measurement is performed corresponds to the situation where the measurement result is unknown. The resulting mixed state is given by $\tilde{\rho} = \sum_e P(e)\rho_e$, where $P(e)$ is the probability to obtain the measurement result e and the sum $\sum_e$ runs over all possible measurement results.

[2] In the experiment, the light field is measured continuously due to technical reasons. However, the measurement results are not used in the set of experiments leading to the results shown in Fig. 3.5d in the main text. As explained above, this corresponds to a situation where the measurement outcomes are not known or, equivalently, no measurement is performed.

two–level model discussed in Sec. 3.1.3, but not in the multilevel description corresponding to the actual experiment. For long times $t \to \infty$, systems A and B decouple from the environment E, $|\Psi(t)\rangle \to |\Phi\rangle_{A,B}|E(a,b,t)\rangle_E$ under ideal conditions, i.e. in the absence of additional noise sources. Remarkably, the desired state $|\Phi\rangle_{A,B}$ is reached irrespective of the initial state of systems A and B which can be highly mixed. Moreover, except for an initial waiting time, no special timing is required. This behavior is again due to the fact that E possesses an infinite number of degrees of freedom, which guarantees that revival effects are not present. This way, entropy is transferred from the system to the environment, which drives A and B into a particular steady state, which depends only on the engineered coupling.

In contrast, the state of systems A and B depends not only crucially on the measurement outcome but also on the initial states states $|a\rangle$ and $|b\rangle$ if standard approaches as described above are used. For example, if the DLCZ protocol is applied starting from the initial state $\rho^{\text{in}} = (|1\rangle\langle 1| + |0\rangle\langle 0|)/2$, corresponding to an equal mixture of states which contain one or zero excitations of the atomic collective modes, the resulting state is not entangled.

Using dissipative methods, a mixed but still entangled steady state can be reached even in the presence of additional noise sources, as long as the coupling of A and B to other environments is sufficiently weak compared to the engineered dissipative processes. This opens up the possibility to keep systems A and B entangled for arbitrarily long times.

The main reason, why the atomic system in the experiment described in Sec. 3.1.5 does not display dissipatively generated entanglement in a steady state is depopulation of the relevant two-level subsystem due to spontaneous emission which transfers the atoms into other Zeeman levels. The depopulation of the relevant levels can be avoided by applying strong repump fields, which transfer atoms back. However, these additional fields introduce additional decoherence processes which inhibit the creation of entanglement in a steady state. This problem can be circumvented by increasing the optical depth of the atomic ensembles such that the entangling dissipation process prevails over the noise processes induced by the repump fields and dominates the dynamics. In the experiment described here, an alternative approach has been devised and implemented, which enables the continuous creation of event-ready entanglement which persists for arbitrarily long times and allows one to realize entanglement life times for more than an hour, which exceeds the entanglement live times ever achieved in any system by several orders of magnitude.
The presence of noise and, in particular, noise effects due to repump fields prevent the decoupling of systems A and B from the environment E in the steady state ρ_{ss}. In contrast to the ideal case described above, atoms and light are entangled for long times $t \to \infty$. This implies that, if the environment can be accessed and measured, information on the atomic state ρ_{ss} can be obtained which results in an increase in its pureness and accordingly an improvement in the generated entanglement. By performing continuous measurements on E yielding the results $e(t)$, the atomic state $\rho[e]$ is produced, which may be entangled even though ρ_{ss} was not. The experimental realization of this approach is described in Sec. 3.1.5. The orresponding results are shown in Fig. 3.5d.

B.2 Steady state entanglement for bosonic modes

In the following, it is shown that the two mode squeezed state $\rho_{\rm TMS} = |\Psi_{\rm TMS}\rangle\langle\Psi_{\rm TMS}|$, with $\tilde{A}|\Psi_{\rm TMS}\rangle = \tilde{B}|\Psi_{\rm TMS}\rangle = 0$, is the unique steady state of the time evolution described by the Master equation

$$\begin{aligned} d_t\rho(t) &= \kappa_A\left(\tilde{A}\rho(t)\tilde{A}^\dagger - \tilde{A}^\dagger\tilde{A}\rho(t)/2 - \rho(t)\tilde{A}^\dagger\tilde{A}/2\right) \\ &+ \kappa_B\left(\tilde{B}\rho(t)\tilde{B}^\dagger - \tilde{B}^\dagger\tilde{B}\rho(t)/2 - \rho(t)\tilde{B}^\dagger\tilde{B}/2\right). \end{aligned}$$

As stated in Sec. 3.1.2, the bosonic mode operators a and b ($[a, a^\dagger] = [b, b^\dagger] = 1$) can be transformed into the non-local operators $\tilde{A}$ and $\tilde{B}$ by the unitary operation

$$\begin{aligned} \tilde{A} &= UaU^\dagger = \mu\, a + \nu\, b^\dagger, \\ \tilde{B} &= UbU^\dagger = \mu\, b + \nu\, a^\dagger. \end{aligned}$$

Since unitary transformations preserve commutation relations, $[\tilde{A}, \tilde{A}^\dagger] = [\tilde{B}, \tilde{B}^\dagger] = 1$ with $\mu^2 - \nu^2 = 1$. By inserting these expressions in the equation above and defining $\rho_U = U^\dagger\rho U$ one finds

$$\begin{aligned} d_t\rho_U(t) = {} & \kappa_A\big(a\rho_U(t)a^\dagger - a^\dagger a\rho_U(t)/2 - \rho_U(t)a^\dagger a/2\big) \\ & + \kappa_B\big(b\rho_U(t)b^\dagger - b^\dagger b\rho_U(t)/2 - \rho_U(t)b^\dagger b/2\big). \end{aligned} \tag{B.1}$$

This is a master equation for two modes coupled to a bath with temperature $T = 0$. The steady state is the vacuum[3] $|0,0\rangle\langle 0,0|$, with $a|0,0\rangle = b|0,0\rangle = 0$. Hence, inverting the unitary transformation yields the unique steady state $U|0,0\rangle = |\Psi_{\rm TMS}\rangle$.

For bosonic modes, the amount of entanglement can be quantified by means of the violation of a local uncertainty relation in terms of quadratures [304, 305]. For entangled states

$$\mathrm{var}(x_+) + \mathrm{var}(p_-) < 1,$$

where $x_+ = (x_{\rm a} + x_{\rm b})/\sqrt{2}$, $p_- = (p_{\rm a} - p_{\rm b})/\sqrt{2}$ and $x_{\rm a} = \left(a + a^\dagger\right)/\sqrt{2}$ and $p_{\rm a} = -i\left(a - a^\dagger\right)/\sqrt{2}$ (analogous expressions hold for $x_{\rm b}$ and $p_{\rm b}$). In particular, $\mathrm{var}(x_+) + \mathrm{var}(p_-) = (\mu - \nu)^{-2} = e^{-2r}$, for two mode squeezed states with squeezing parameter r.

For large, strongly polarized atomic ensembles, collective spins can be described by bosonic modes $\frac{1}{\sqrt{N_I}}\sum_{i=1}^{N_I}\sigma_{I,i} \approx a$, $\frac{1}{\sqrt{N_{II}}}\sum_{i=1}^{N_{II}}\sigma_{II,i} \approx b$ using the Holstein-Primakoff-approximation [89]. In this case, $\xi < 1$ (see Sec. 3.1.2) is equivalent to the criterion $\mathrm{var}(x_+) + \mathrm{var}(p_-) < 1$.

[3] Eq. (B.1) yields $d_t\langle a^\dagger a\rangle = -\kappa_A\langle a^\dagger a\rangle$ and $d_t\langle b^\dagger b\rangle = -\kappa_B\langle b^\dagger b\rangle$. Hence, $\langle a^\dagger a\rangle_\infty = \langle b^\dagger b\rangle_\infty = 0$ in the steady state.

B.3 Derivation of the master equation

In this appendix, the master equation for creating entanglement between two atomic ensembles at room temperature discussed in Sec. 3.1.3 is derived in detail. The master equation for atomic ground states, Eq. (B.6) is derived. In the latter, thermal motion of atoms is included and the effective decay rates are calculated. It is shown that in the setup under consideration, the resulting master equation can be assumed to be real, since imaginary parts play only a minor role.

B.3.1 Master equation for atomic ground state levels $|\uparrow\rangle$ and $|\downarrow\rangle$

Light and matter are assumed to interact as described in Sec. 3.1.3. The full Hamiltonian is considered including undesired transitions[4] and without applying the rotating wave approximation for quantum fields. It is given by $H = H_{\rm L} + H_{\rm A} + H_{\rm int}$, where $H_{\rm L} = \int dk\ (\omega_k - \omega_L)\, a_k^\dagger a_k$ is the Hamiltonian of the free light field and $H_{\rm A}$ accounts for atomic energies in the rotating frame. $H_{\rm A} = H_{\rm A,I} + H_{\rm A,II}$ with $H_{\rm A,I} = \sum_i (\Delta_{\uparrow,I}|e_\uparrow\rangle_{I,i}\langle e_\uparrow| + \Delta_{\downarrow,I}|e_\downarrow\rangle_{I,i}\langle e_\downarrow|)$ and $H_{\rm A,II} = \sum_i (\Delta_{\uparrow,II}|e_\uparrow\rangle_{II,i}\langle e_\uparrow| + \Delta_{\downarrow,II}|e_\downarrow\rangle_{II,i}\langle e_\downarrow|)$. Here, the detunings $\Delta_{\uparrow,I/II}$ and $\Delta_{\downarrow,I/II}$ have been introduced, which correspond to diagonal transitions $|\downarrow\rangle \to |e_\uparrow\rangle$ and $|\uparrow\rangle \to |e_\downarrow\rangle$ respectively in the first/second ensemble. In the setup illustrated in Fig. 3.1, $\Delta_{\uparrow,I} = -\Delta_{\uparrow,II} = \Delta - \Omega$ and $\Delta_{\downarrow,I} = -\Delta_{\downarrow,II} = \Delta + \Omega$. The interaction Hamiltonian $H_{\rm int} = H_{\rm cl} + H_{\rm qu}$ consists of a classical part $H_{\rm cl}$, which accounts for transitions induced by the driving field and a quantum part $H_{\rm qu}$, which involves quantized field operators. The Hamiltonian describing the interaction of light with the first atomic ensemble is governed by the Hamiltonian

$$
\begin{aligned}
H_{\rm int,I} &= H_{\rm cl,I} + H_{\rm qu,I}, \sigma_{e_\uparrow\uparrow,I,i} \qquad\qquad (B.2)\\
H_{\rm cl,I} &= \Omega_{\rm probe} \sum_{i=1}^{N} e^{i\mathbf{k}_L\mathbf{r}_i} \left(|e_\uparrow\rangle_{I,i}\langle\downarrow| + |e_\downarrow\rangle_{I,i}\langle\uparrow|\right) + H.C.,\\
H_{\rm qu,I} &= \sum_{i=1}^{N}\sum_{\mathbf{k}}\sum_{\hat\lambda_{\mathbf{k}}=1}^{2} g_{\mathbf{k}} e^{i\mathbf{k}\mathbf{r}_i} a_{\mathbf{k}} (|e_\downarrow\rangle_{I,i}\langle\downarrow| e^{i\Omega t} + |e_\uparrow\rangle_{I,i}\langle\uparrow| e^{-i\Omega t}\\
&\quad + |\downarrow\rangle_{I,i}\langle e_\downarrow| e^{-i\Omega t} e^{-2i\omega_L t} + |\uparrow\rangle_{I,i}\langle e_\uparrow| e^{i\Omega t} e^{-2i\omega_L t}) + H.C.,\\
&\quad + \sum_{i=1}^{N}\sum_{\mathbf{k}}\sum_{\hat\lambda_{\mathbf{k}}=1}^{2} \check{g}_{\mathbf{k}} e^{i\mathbf{k}\mathbf{r}_i} a_{\mathbf{k}} (|e_\uparrow\rangle_{I,i}\langle\downarrow| + |e_\downarrow\rangle_{I,i}\langle\uparrow|\\
&\quad + |\downarrow\rangle_{I,i}\langle e_\uparrow| e^{-2i\omega_L t} + |\uparrow\rangle_{I,i}\langle e_\downarrow| e^{-2i\omega_L t}) + H.C.,
\end{aligned}
$$

where $\hat\lambda_{\mathbf{k}}$ specifies the two orthogonal polarizations of the light mode with wave vector $\mathbf{k}$. $g_{\mathbf{k}} = \hat{\mathbf{e}}_{\mathbf{k}} \cdot \mathbf{p}\sqrt{\frac{\omega_k}{2\epsilon_0 V}}$ is the coupling strength of desired transitions involving the quantum field, while $\check{g}_{\mathbf{k}}$ is the coupling strength corresponding to undesired transitions. $\hat{\mathbf{e}}_{\mathbf{k}}$ is the unit polarization vector, V is the quantization volume of the electromagnetic field, ϵ_0 the vacuum permittivity and $\mathbf{p}$ is the transition matrix element

[4] Undesired radiative transitions $|\uparrow\rangle \to |\uparrow\rangle$ and $|\downarrow\rangle \to |\downarrow\rangle$ involve the emission of a photon but no change of the internal atomic state. These processes are not explicitly shown in Fig. 3.1.

of transitions $|e_\uparrow\rangle \rightarrow |\downarrow\rangle$ and $|e_\downarrow\rangle \rightarrow |\uparrow\rangle$. $H_{\rm int} = H_{\rm int,I} + H_{\rm int,II}$. $H_{\rm int,II}$ is given by an expression analogous to Eq. (B.2), where subscripts are changed accordingly ($I \rightarrow II$).

Based on this Hamiltonian, a master equation for the reduced atomic density matrix $\rho(t)$ is derived using the approximation of independent rates of variation and assuming Born-Markov dynamics as explained in Sec. 3.1.3. For quantumoptical systems, assuming Markov dynamics is an excellent approximation, since the typical (optical) frequencies $\omega_{\rm opt}$ are much larger than the decay rates and correlations in the light field disappear on a time scale $\tau_c \propto \omega_{\rm opt}^{-1}$ which is much faster than the atomic dynamics. One obtains

$$d_t\rho(t) = -i[H_{cl}, \rho(t)] + \mathcal{L}_{\rm qu}\rho(t),$$

where $\mathcal{L}$ is a Lindblad operator corresponding to the quantum part of the interaction $H_{\rm qu}$. This master equation consists of three parts

$$d_t\rho(t) = L(\rho(t))_{\rm ens.I} + L(\rho(t))_{\rm ens.II} + L(\rho(t))_{\rm inter\text{-}ens.}\ . \tag{B.3}$$

The first and second term $L(\rho(t))_{\rm ens.I}$ and $L(\rho(t))_{\rm ens.II}$ include only terms referring to the first and second ensemble respectively, while the third term $L(\rho(t))_{\rm inter\text{-}ens.}$ summarizes all terms combining operators acting on both samples. The first term is given by

$$\begin{aligned} L(\rho(t))_{\rm ens.I} &= -i[H_{cl,I}, \rho(t)] \\ &+ \frac{1}{2}\sum_{i,j} \mathcal{J}_{ij}^{I,I} |\uparrow\rangle_{I,i}\langle e_\uparrow|\rho(t)|e_\uparrow\rangle_{I,j}\langle\uparrow| \\ &+ \frac{1}{2}\sum_{i,j} \check{\mathcal{J}}_{ij}^{I,I} |\downarrow\rangle_{I,i}\langle e_\uparrow|\rho(t)|e_\uparrow\rangle_{I,j}\langle\downarrow| \\ &+ \ \ldots\ , \end{aligned} \tag{B.4}$$

where the approximation $\omega_L \gg \Omega$ has been used, which is very well justified for optical frequencies, and neglected fast oscillating terms which appear in the standard derivation [165], if photonic modes in the upper and lower sideband are not treated as independent baths[5]. $\mathcal{J}_{ij}^{I,I} = \mathcal{J}_{ji}^{I,I}$ is a complex decay rate associated with desired transitions, while $\check{\mathcal{J}}_{ij}^{I,I} = \check{\mathcal{J}}_{ji}^{I,I}$ is the rate of undesired transitions. For the simple model discussed in Sec.3.1.3 we have $\check{\mathcal{J}}_{ij}^{I,I} = 2\mathcal{J}_{ij}^{I,I}$. Imaginary single particle terms $Im\left(\mathcal{J}_{ii}^{I,I}\right)$ (Lamb shifts) are absorbed in the detunings as explained in Sec. 3.1.3. The second term $L(\rho(t))_{\rm ens.II}$ is given by an analogous expression with changed subscripts $I \mapsto II$.

The last term in Eq. (B.3) can be written as sum $L(\rho(t))_{\rm inter\text{-}ens.} = L(\rho(t))_{\rm inter\text{-}ens.}^{I,II} +$

[5] If the upper and lower sideband are not treated as independent baths, cross terms appear, which rotate fast (with frequency $\pm 2\Omega$) compared to the single-bath terms, (which do not rotate in this picture). These cross terms can be neglected in a rotating wave approximation if $\Omega \gg \Gamma_{\rm atomic}$.

$L(\rho(t))^{II,I}_{\text{inter-ens.}}$. The first part is given by

$$\begin{aligned} L(\rho(t))^{I,II}_{\text{inter-ens.}} &= \frac{1}{2}\sum_{i,j}\mathcal{J}^{I,II}_{ij}|\uparrow\rangle_{I,i}\langle e_\uparrow|\rho(t)|e_\downarrow\rangle_{II,j}\langle\downarrow| \\ &+ \frac{1}{2}\sum_{i,j}\mathcal{J}^{I,II}_{ij}|\downarrow\rangle_{I,i}\langle e_\downarrow|\rho(t)|e_\uparrow\rangle_{II,j}\langle\uparrow| \\ &+ \frac{1}{2}\sum_{i,j}\check{\mathcal{J}}^{I,II}_{ij}|\uparrow\rangle_{I,i}\langle e_\downarrow|\rho(t)|e_\uparrow\rangle_{II,j}\langle\downarrow| \\ &+ \frac{1}{2}\sum_{i,j}\check{\mathcal{J}}^{I,II}_{ij}|\downarrow\rangle_{I,i}\langle e_\uparrow|\rho(t)|e_\downarrow\rangle_{II,j}\langle\uparrow| \\ &+ \ldots \end{aligned} \tag{B.5}$$

and $L(\rho(t))^{II,I}_{\text{inter-ens.}}$ is given by an analogous expression with changed subscripts ($I \to II$). Decay rates appearing in inter-ensemble terms differ from single-ensemble rates $\mathcal{J}^{I,I}_{ij} = \mathcal{J}^{II,II}_{ij}$

$$\mathcal{J}^{I,II}_{ij} = e^{-i\mathbf{kR}}\mathcal{J}^{I,I}_{ij},\ \mathcal{J}^{II,I}_{ij} = e^{+i\mathbf{kR}}\mathcal{J}^{I,I}_{ij}$$

where $\mathbf{R}$ is the distance between the two ensembles. In order to obtain compact expressions, the simplified notation $\mathcal{J}_{ij}$ is used for single ensemble or inter-ensemble rates depending to which samples the indices i and j refer. Moreover, the convention $\mathbf{r}_{ij} = \mathbf{r}_i - \mathbf{r}_j - \mathbf{R}$ is used if the atom with index j is located in the second ensemble. (However, in App. B.3.2, it is shown that the distance between the ensembles does not play a role in the setting considered here.) Using this notation, $\mathcal{J}_{ij}$ is given by

$$\mathcal{J}_{ij} = \int d\mathbf{k}\sum_{\hat{\lambda}_\mathbf{k}=1}^{2} g^2(\mathbf{k})e^{i\mathbf{k}(\mathbf{r}_i-\mathbf{r}_j)}\int_0^\infty d\tau(e^{-i(\omega_k-\omega_L)\tau}+e^{-i(\omega_k+\omega_L)\tau}),$$

where the sum over light modes was changed into an integral $\sum_\mathbf{k} \to \frac{V}{(2\pi)^3}\int d\mathbf{k}$. The prefactor is absorbed in the coupling constant $g(\mathbf{k}) = \sqrt{V/(2\pi)^3}\, g_\mathbf{k}$ whenever an integral over light modes is used. The second term in the expression in brackets ($e^{-i(\omega_k+\omega_L)\tau}$) stems from counter-rotating terms in the Hamiltonian and would not appear if the rotating wave approximation had been applied. Using the identity $\int_0^\infty e^{i\omega\tau} = \pi\delta(\omega) + i\mathcal{P}(1/\omega)$, where $\mathcal{P}$ is the principal value, one obtains

$$\begin{aligned} Re(\mathcal{J}_{ij}) &= \pi\int d\mathbf{k}\sum_{\hat{\lambda}_\mathbf{k}=1}^{2} g^2(\mathbf{k})e^{i\mathbf{k}(\mathbf{r}_i-\mathbf{r}_j)}\delta(\omega_k-\omega_L), \\ Im(\mathcal{J}_{ij}) &= i\mathcal{P}\left(\int d\mathbf{k}\sum_{\hat{\lambda}_\mathbf{k}=1}^{2} g^2(\mathbf{k})e^{i\mathbf{k}(\mathbf{r}_i-\mathbf{r}_j)}\left(\frac{1}{\omega_L-\omega_k}+\frac{1}{\omega_L+\omega_k}\right)\right), \end{aligned}$$

These rates can be calculated as shown in [166] (compare Eqs. (3.8) and (3.9)).

Now, a master equation for the reduced density matrix of atomic ground states $\mathbb{P}_g\rho(t)\mathbb{P}_g$ is derived by applying the projector $\mathbb{P}_g = \bigotimes_{i,j=1}^{N} (|\uparrow\rangle_{I,i}\langle\uparrow| + |\downarrow\rangle_{I,i}\langle\downarrow|) \otimes (|\uparrow\rangle_{II,j}\langle\uparrow| + |\downarrow\rangle_{II,j}\langle\downarrow|)$ to the differential equation $d_t\rho(t) = L(\rho(t))_{\text{ens.I}} + L(\rho(t))_{\text{ens.II}} + L(\rho(t))_{\text{inter-ens.}}$ using Eqs. (B.4) and (B.5). Excited states are eliminated under the condition $\Delta_{\uparrow,I/II}, \Delta_{\downarrow,I/II} >> \Gamma_{\text{atomic}}$, using $d_t\mathbb{P}_e\rho(t)\mathbb{P}_g = d_t\mathbb{P}_g\rho(t)\mathbb{P}_e = d_t\mathbb{P}_e\rho(t)\mathbb{P}_e = 0$, where $\mathbb{P}_e = \mathbb{1} - \mathbb{P}_g$. Moreover, it is assumed that terms corresponding to states with two or more excitations, for example terms of the type $\mathbb{P}_e^{(2)}\rho(t)\mathbb{P}_g$, are negligible compared to terms corresponding to states where at most one atom is in an excited state like $\mathbb{P}_e^{(1)}\rho(t)\mathbb{P}_g$. $\mathbb{P}_e^{(1)} = \sum_{i=1}^{N} \mathbb{P}_{e,I,i} \otimes \mathbb{P}_{g,II} + \sum_{j=1}^{N} \mathbb{P}_{g,I} \otimes \mathbb{P}_{e,II,j}$ with $\mathbb{P}_{e,i,I/II} = \bigotimes_{i=1}^{N} \left(|e_\uparrow\rangle_{I/II,i}\langle e_\uparrow| + |e_\downarrow\rangle_{I/II,i}\langle e_\downarrow|\right)$. $\mathbb{P}_e^{(2)}$ is defined analogously. In the following the resulting reduced density matrix of atomic ground states $\mathbb{P}_g\rho(t)\mathbb{P}_g$ is denoted by $\rho(t)$. One obtains

$$
\begin{aligned}
d_t\rho(t) \;=\; & \frac{\Omega_{\text{probe}}}{2} \sum_{i,j} e^{-i\mathbf{k}_L(r_j - r_i)} (\\
& \mathcal{J}_{ij} \left(\frac{\sigma_{I,i}}{\Delta_{\uparrow,I}} + \frac{\sigma_{II,j}^\dagger}{\Delta_{\downarrow,II}} \right) \rho(t) \left(\frac{\sigma_{I,i}^\dagger}{\Delta_{\uparrow,I}} + \frac{\sigma_{II,j}}{\Delta_{\downarrow,II}} \right) \\
& + \mathcal{J}_{ij} \left(\frac{\sigma_{II,i}}{\Delta_{\uparrow,II}} + \frac{\sigma_{I,j}^\dagger}{\Delta_{\downarrow,I}} \right) \rho(t) \left(\frac{\sigma_{II,i}^\dagger}{\Delta_{\uparrow,II}} + \frac{\sigma_{I,j}}{\Delta_{\downarrow,I}} \right) \\
& + \check{\mathcal{J}}_{ij} \left(\frac{\sigma_{\downarrow\downarrow,I,i}}{\Delta_{\uparrow,I}} + \frac{\sigma_{\uparrow\uparrow,II,j}^\dagger}{\Delta_{\downarrow,II}} \right) \rho(t) \left(\frac{\sigma_{\downarrow\downarrow,I,i}}{\Delta_{\uparrow,I}} + \frac{\sigma_{\uparrow\uparrow,II,j}^\dagger}{\Delta_{\downarrow,II}} \right) \\
& + \check{\mathcal{J}}_{ij} \left(\frac{\sigma_{\downarrow\downarrow,II,i}}{\Delta_{\uparrow,II}} + \frac{\sigma_{\uparrow\uparrow,I,j}^\dagger}{\Delta_{\downarrow,I}} \right) \rho(t) \left(\frac{\sigma_{\downarrow\downarrow,II,i}}{\Delta_{\uparrow,II}} + \frac{\sigma_{\uparrow\uparrow,I,j}^\dagger}{\Delta_{\downarrow,I}} \right)) \\
& + \;\; \ldots \,,
\end{aligned}
$$

where the abbreviations $\sigma_{\uparrow\uparrow,I/II,i} = |\uparrow\rangle_{I/II,i}\langle\uparrow|$ and $\sigma_{\downarrow\downarrow,I/II,i} = |\downarrow\rangle_{I/II,i}\langle\downarrow|$ were used. Terms with prefactors $1/\Delta^3$ have been neglected since it is assumed that detunings are large. AC-Stark shifts

$$
d_t\rho(t)|_{\text{AC Stark}} = -i\Omega_{\text{probe}} \sum_{i=1}^{N} \left[\frac{\sigma_{\uparrow\uparrow,I,i}}{\Delta_{\downarrow,I}} + \frac{\sigma_{\downarrow\downarrow,I,i}}{\Delta_{\uparrow,I}}, \rho(t) \right] + i\Omega_{\text{probe}} \sum_{i=1}^{N} \left[\frac{\sigma_{\uparrow\uparrow,II,i}}{\Delta_{\downarrow,I}} + \frac{\sigma_{\downarrow\downarrow,II,i}}{\Delta_{\uparrow,I}}, \rho(t) \right]
$$

are absorbed in the detunings. Using the definitions $\mu_{I/II} = \pm\frac{\Delta+\Omega}{2\sqrt{\Delta\Omega}}$, $\nu_{I/II} = \pm\frac{\Delta-\Omega}{2\sqrt{\Delta\Omega}}$ and $J_{ij} = \mathcal{J}_{ij}\ 2\Omega_{\text{probe}}\sqrt{\Delta\Omega}/\left(\Delta^2 - \Omega^2\right)$, one obtains

$$
\begin{aligned}
d_t\rho(t) = & \frac{1}{2} \sum_{i,j=1}^{N} e^{-i\mathbf{k}_L(\mathbf{r}_j - \mathbf{r}_i)} J_{ij} \left(A_i\rho(t)A_j^\dagger + B_i\rho(t)B_j^\dagger \right) \\
& + \frac{1}{2} \sum_{i,j=1}^{N} e^{-i\mathbf{k}_L(\mathbf{r}_j - \mathbf{r}_i)} \check{J}_{ij} \left(C_i\rho(t)C_j^\dagger + D_i\rho(t)D_j^\dagger \right) \\
& + \ldots
\end{aligned}
\tag{B.6}
$$

with

$$\begin{aligned} A_i &= \mu_I\ \sigma_{I,i} + \nu_{II}\ \sigma^\dagger_{II,i}, \\ B_i &= \mu_{II}\ \sigma_{II,i} + \nu_I\ \sigma^\dagger_{I,i}, \\ C_i &= \mu_I\ \sigma_{\downarrow\downarrow,I,i} + \nu_{II}\ \sigma_{\uparrow\uparrow,II,i}, \\ D_i &= \mu_{II}\ \sigma_{\downarrow\downarrow,II,i} + \nu_I\ \sigma_{\uparrow\uparrow,I,i}. \end{aligned}$$

The expressions in the main text are obtained by introducing a unified notation (compare Eq. (3.8)), which absorbs the relative sign μ_I/μ_{II} in atomic operators referring to the second ensemble $\sigma_{II} \to \mathrm{sgn}(\mu_I \mu II)\sigma_{II}$.

B.3.2 Master equation including atomic motion

In the following, thermal motion of particles is included by treating atomic positions as classical random variables. The master equation for atomic ground states (B.6) is considered. As outlined in Sec. 3.1.3, random atomic positions can be taken into account by introducing averaged coefficients in the master equation. Averaged rates $\langle J_{ij}\rangle$ are calculated assuming Gaussian distributions with width L for atomic positions in the two ensembles. First, the rate corresponding to moving particles in a single ensemble is calculated. Below it is shown that for inter-ensemble rates the same result is obtained for the setup and range of parameters considered here.

$$\begin{aligned} \langle J_{ij}\rangle &= \frac{1}{\pi^3 L^6}\int d\mathbf{r}\int d\acute{\mathbf{r}}\, e^{i\mathbf{k}_L(\mathbf{r}-\acute{\mathbf{r}})-\frac{r^2+\acute{r}^2}{L^2}}\left(\gamma(\mathbf{r}-\acute{\mathbf{r}})+ig(\mathbf{r}-\acute{\mathbf{r}})\right), \\ &= \frac{1}{(2\pi)^{3/2}\,L^3}\int d\mathbf{r}_-\, e^{i\mathbf{k}_L\mathbf{r}_- - \frac{\mathbf{r}_-^{\,2}}{2L^2}}\left(\gamma(\mathbf{r}_-)+ig(\mathbf{r}_-)\right), \end{aligned} \tag{B.7}$$

where the variable transformation $\mathbf{r}_+ = \mathbf{r} + \acute{\mathbf{r}}$, $\mathbf{r}_- = \mathbf{r} - \acute{\mathbf{r}}$ was made in the second step. The single particle rate is given by $J_{ii} = \Gamma$ (Lamb shifts are absorbed in the detunings). Now, averaged rates $\langle J_{ij}\rangle$ with $i \neq j$ need to be determined. Firstly, the real part and then the imaginary part of the averaged decay rate $\langle J_{ij}\rangle$ is considered.

The real part $\Gamma_{ij} = Re\left(\langle J_{ij}\rangle\right)$ is calculated by inserting Eq. (3.8) into Eq. (B.7) and fixing $\hat{\mathbf{p}} = \hat{\mathbf{x}}$ and $\hat{\mathbf{k}}_\mathbf{L} = \hat{\mathbf{z}}$. $\Gamma_{ij} = \Gamma_{ij,A} + \Gamma_{ij,B}$ is a sum of two contributions corresponding to the first and the second line in Eq. (3.8). The first term is given by

$$\Gamma_{ij,A} = \frac{3\Gamma}{\sqrt{2\pi}L^3}\int_0^\infty dr_- r_-^2 e^{-\frac{r_-^2}{2L^2}}\ \frac{\sin(k_L r_-)}{k_L r_-}\left(\frac{\sin(k_L r_-)}{k_L r_-} + \frac{\cos(k_L r_-)}{(k_L r_-)^2} - \frac{\sin(k_L r_-)}{(k_L r_-)^3}\right). \tag{B.8}$$

The integrand of this expression tends to zero in the limit $r_- \to 0$. This can for example be seen by expanding the integrand for small values $r_- \ll 1$, $r_-^2 e^{-\frac{r_-^2}{2L^2}}\ \frac{\sin(k_L r_-)}{k_L r_-}\left(\frac{\sin(k_L r_-)}{k_L r_-} + \frac{\cos(k_L r_-)}{(k_L r_-)^2} - \frac{\sin(k_L r_-)}{(k_L r_-)^3}\right) = \frac{2}{3}r_-^2 + \mathcal{O}(r_-^4)$. Hence the dominant contribution in the limit $k_L L \gg 1$ stems from the first term in brackets $\sin(k_L r_-)/(k_L r_-)$. The other two terms in brackets decay faster in the interatomic distance r_- and lead only

to corrections on the order of $1/(k_L L)^4$. For $k_L L \gg 1$,

$$\Gamma_{ij,A} = \frac{3\Gamma}{\sqrt{2\pi}L^3}\int_0^\infty dr_- r_-^2 e^{-\frac{r_-^2}{2L^2}}\,\frac{\sin(k_L r_-)^2}{(k_L r_-)^2} = \frac{3}{4}\Gamma\frac{1}{(k_L L)^2}\left(1-e^{-2k_L L}\right),$$

which can be approximated by $\Gamma_{ij,A} = \frac{3}{4}\Gamma\frac{1}{(k_L L)^2}$. The second part

$$\Gamma_{ij,B} = \frac{3\Gamma}{\sqrt{2\pi}L^3}\int_0^\infty dr_- r_-^2 e^{-\frac{r_-^2}{2L^2}}\left(\frac{\cos(k_L r_-)}{(k_L r_-)^2}-\frac{\sin(k_l r_-)}{(k_L r_-)^3}\right)\left(\frac{\sin(k_L r_-)}{k_L r_-}+\frac{3\cos(k_L r_-)}{(k_L r_-)^2}-\frac{3\sin(k_L r_-)}{(k_L r_-)^3}\right),$$

is negligible compared to the first part $\Gamma_{ij,A}$ in the asymptotic limit $k_L L \to \infty$. Its integrand tends to zero for $r_- \to 0$ (expansion for $r_- \ll 1$ yields $k_L^2 r_-^4/45 + \mathcal{O}(r_-^5)$) and contains only terms proportional to $\cos(k_L r_-)\sin(k_L r_-)/(k_L r_-)^x$, $\cos(k_L r_-)^2/(k_L r_-)^x$ and $\sin(k_L r_-)^2/(k_L r_-)^x$ with $x \geq 1$. These types of terms have been neglected in Eq. (B.8) or decay even faster in r_-. Since $\Gamma_{ij,B}$ is negligible compared to $\Gamma_{ij,A}$, $\Gamma_{ij} = \Gamma\frac{3}{4(k_L L)^2}$ is used.

Next, the imaginary part $G_{ij} = Im\left(\langle J_{ij}\rangle\right)$ is calculated by inserting Eq. (3.9) into Eq. (B.7). As before, the two contributions $G_{ij} = G_{ij,A} + G_{ij,B}$ corresponding to the first and the second line in Eq. (3.9) are considered separately. The integrand of the first part

$$G_{ij,A} = -\frac{3\Gamma}{\sqrt{2\pi}L^3}\int_0^\infty dr_- r_-^2 e^{-\frac{r_-^2}{2L^2}}\,\frac{\cos(k_L r_-)}{k_L r_-}\left(\frac{\sin(k_L r_-)}{k_L r_-}+\frac{\cos(k_L r_-)}{(k_L r_-)^2}-\frac{\sin(k_L r_-)}{(k_L r_-)^3}\right),$$

tends to zero for $r_- \to 0$ (expansion for $r_- \ll 1$ yields $2r_-/(3k_L) + \mathcal{O}(r_-^3)$) and features a rapidly oscillating term proportional to $\sin(k_L r_-)\cos(k_L r_-)$ in the integral, which leads to a contribution which scales with $1/(k_L L)^3$. The other terms proportional to $\cos^2(k_L L)/(k_L L)^3$ and $\cos(k_L L)\sin(k_L L)/(k_L L)^3$ are again of the type discussed and neglected before. Hence it is well justified to assume that $G_{ij,I} \ll \Gamma_{ij,I}$. The integrand of the second part

$$G_{ij,B} = \frac{3\Gamma}{\sqrt{2\pi}L^3}\int_0^\infty dr_- r_-^2 e^{-\frac{r_-^2}{2L^2}}\left(\frac{\sin k_L r_-)}{(k_L r_-)^2}+\frac{\cos(k_L r_-)}{(k_L r_-)^3}\right)\left(\frac{\sin(k_L r_-)}{k_L r_-}+\frac{3\cos(k_L r_-)}{(k_L r_-)^2}-\frac{3\sin(k_L r_-)}{(k_L r_-)^3}\right),$$

also tends to zero for $r_- \to 0$ (expansion for $r_- \ll 1$ yields $-r_-/(15k_L) + \mathcal{O}(r_-^3)$) and contains only one term which has not been considered so far. The term in the integrand proportional $\sin(k_L r_-)^2/(k_L r_-)$ leads to to a contribution which decays with $\log(k_L L)/(k_L L)^3$ in the asymptotic limit $k_L L \to \infty$. The imaginary part of the averaged decay rate $\langle J_{ij}\rangle$ is therefore negligible compared to the real part.

The distance between the two atomic samples does not play a role in the setting under consideration. In the limit $k_L \gg R/L^2$, averaged single ensemble rates equal averaged inter-ensemble rates $\langle J_{ij}\rangle = \langle J_{ij}\rangle^{I,I} = \langle J_{ij}\rangle^{I,II}$. In the following, the calculation of the inter-ensemble value $\Gamma_{ij,A}^{I,II}$ is outlined. Analogous arguments can be used compute $\Gamma_{ij,B}^{I,II}$, $G_{ij,A}^{I,II}$, and $G_{ij,B}^{I,II}$.

Inter-ensemble rates are obtained by averaging atomic positions with respect to Gaussian distributions centered at the origin and a distance R apart respectively

$$\begin{aligned}\Gamma_{ij}^{I,II} &= \frac{1}{\pi^3 L^6}\int d\mathbf{r}\int d\acute{\mathbf{r}} e^{i\mathbf{k}_L(\mathbf{r}-\acute{\mathbf{r}})} e^{\frac{-r^2}{L^2}} e^{\frac{-(\acute{\mathbf{r}}-\mathbf{R})^2}{L^2}}\gamma(\mathbf{r}-\acute{\mathbf{r}}),\\ &= \frac{1}{(2\pi)^3 L^6}\int d\mathbf{r}_+\int d\mathbf{r}_- e^{i\mathbf{k}_L\mathbf{r}_-} e^{\frac{-(\mathbf{r}_-+\mathbf{R})^2}{2L^2}} e^{\frac{-(\mathbf{r}_+-\mathbf{R})^2}{2L^2}}\gamma(\mathbf{r}_-),\\ &= \frac{1}{(2\pi)^{3/2} L^3}\int d\mathbf{r}_- e^{i\mathbf{k}_L\mathbf{r}_-} e^{\frac{-(\mathbf{r}_-+\mathbf{R})^2}{2L^2}}\gamma(\mathbf{r}_-),\end{aligned}$$

where the variable transformation $\mathbf{r}_+ = \mathbf{r}+\acute{\mathbf{r}}$, $\mathbf{r}_- = \mathbf{r}-\acute{\mathbf{r}}$ was made, as before. By inserting Eq. (3.8) and neglecting the dipole factor $(\hat{\mathbf{x}}\cdot(\mathbf{r}-\acute{\mathbf{r}})/|\mathbf{r}-\acute{\mathbf{r}}|)^2$, which does not play a role for the distance under consideration[6], one obtains

$$\begin{aligned}\Gamma_{ij}^{I,II} &= \frac{3\Gamma}{2(2\pi)^{3/2} L^3}\int d\mathbf{r}_-\; e^{i\mathbf{k}_L\mathbf{r}_-} e^{\frac{-(\mathbf{r}_-+\mathbf{R})^2}{2L^2}}\frac{\sin(k_L r_-)}{k_L r_-},\\ &= \frac{3\Gamma}{2\sqrt{2\pi}L^3}\int_0^\infty dr_- r_-^2\frac{\sin(k_L r_-)}{k_L r_-}\int_0^\pi d\theta\sin(\theta) e^{ik_L r_-\cos(\theta)} e^{\frac{-1}{2L^2}\left(r_-^2+R^2+2r_- R\cos(\theta)\right)},\\ &= \frac{3\Gamma}{2\sqrt{2\pi}L^3 k_L}\int_0^\infty dr_-\sin(k_L r_-) e^{\frac{-\left(r_-^2+R^2\right)}{2L^2}}\int_{-r_-}^{r_-} dx e^{-ik_L x} e^{\frac{Rx}{L^2}}.\end{aligned}$$

In the last step, the integral over θ was transformed using the variable transformation $x = -\cos(\theta) r_-$. The integral over x can be directly evaluated yielding

$$\begin{aligned}\Gamma_{ij}^{I,II} &= \frac{3\Gamma}{2\sqrt{2\pi}L^3 k_L\left(ik_L - R/L^2\right)}\int_0^\infty dr_-\sin(k_L r_-) e^{\frac{-\left(r_-^2+R^2\right)}{2L^2}}\left(e^{ik_L r_- - \frac{Rr_-}{L^2}} - e^{-ik_L r_- + \frac{Rr_-}{L^2}}\right),\\ &= \frac{3\Gamma}{2\sqrt{2\pi}L^3 k_L\left(ik_L - R/L^2\right)}\int_{-\infty}^\infty dr_-\sin(k_L r_-) e^{\frac{-(r_-+R)^2}{2L^2}} e^{ik_L r_-}.\end{aligned}$$

As next step, the variable transformation $\tilde{r} = r_- + R$ is made such that

$$\begin{aligned}\Gamma_{ij}^{I,II} &= \frac{3\Gamma}{2\sqrt{2\pi}L^3 k_L\left(ik_L - R/L^2\right)}\int_{-\infty}^\infty d\tilde{r}\sin\left(k_L(\tilde{r}-R)\right),\\ &\quad e^{\frac{-\tilde{r}^2}{2L^2}} e^{ik_L(\tilde{r}-R)}\\ &= \frac{3\Gamma}{4\sqrt{2\pi}L^3 k_L\left(-k_L - iR/L^2\right)}\int_{-\infty}^\infty d\tilde{r} e^{\frac{-\tilde{r}^2}{2L^2}},\\ &\quad (e^{2ik_L(\tilde{r}-R)} - 1),\\ &= \frac{3\Gamma}{4\left(L^2 k_L^2 + ik_L R\right)}\left(1 - e^{-2k_L^2 L^2 - 2ik_L R}\right)\end{aligned}$$

which yields $\Gamma_{ij}^{I,II} = \Gamma\frac{3}{4(k_L L)^2}$ for $k_L \gg R/L^2$ and $k_L L \gg 1$.

[6] The dipole term $(\hat{\mathbf{p}}\cdot\hat{\mathbf{r}}_{ij})^2)$ leads to contributions which decay quickly in the interatomic distance. The corresponding terms in Eq. (B.8) (the second and third term in brackets) are also negligible in the calculation of the single-ensemble rate $\Gamma_{ij,A}$.

B.4 Time evolution of entanglement in a two-level model

In this appendix, the amount of entanglement produced $\xi(t)$ (compare Eq. (3.3)) is calculated for the model described in Sec. 3.1.3. The first part of this appendix B.4.1 covers the derivation of $\xi(t)$ based on the full master equation (3.11). The second part B.4.2 contains explanations concerning Eq. (3.11).

B.4.1 Time evolution of entanglement

In the following, the time evolution of entanglement $\xi(t)$ is calculated. To this end, the single-ensemble variance of transverse spin components $\mathrm{var}(J_z) = \langle J_z^2\rangle - \langle J_z\rangle^2$, the inter-ensemble product of transverse spins $\langle J_{z,I}J_{z,II}\rangle$ and finally the mean value of the longitudinal spin $\langle J_x\rangle$ is calculated.

First, $d_t\langle J_z^2\rangle_t$ is calculated. The dissipative evolution described by Eq. (3.11) leads to

$$d_t\langle J_z^2\rangle \;=\; -\tilde{\Gamma}\langle J_z^2\rangle - \frac{2d}{N}\Gamma\langle J_z^2 J_x\rangle + \frac{N}{4}\tilde{\Gamma} + \frac{d\Gamma}{N}\langle J_x^2\rangle\big(\mu^2+\nu^2\big).$$

Applying the decorrelation approximation $\langle J_zJ_x\rangle \approx \langle J_z\rangle\langle J_x\rangle$ [7] for mean values of products of transverse and longitudinal spin yields

$$d_t\langle J_z^2\rangle \;=\; -\Big(\tilde{\Gamma}+d\Gamma P_2(t)\Big)\langle J_z^2\rangle + \frac{N}{4}\Big(\tilde{\Gamma}+d\Gamma P_2(t)^2\big(\mu^2+\nu^2\big)\Big)$$

and similarly

$$d_t\langle J_y^2\rangle \;=\; -\Big(\tilde{\Gamma}+d\Gamma P_2(t)\Big)\langle J_y^2\rangle + \frac{N}{4}\Big(\tilde{\Gamma}+d\Gamma P_2(t)^2\big(\mu^2+\nu^2\big)\Big)$$

where $\langle J_x\rangle = \frac{N}{2}P_2(t)$ and $\langle J_x^2\rangle \approx \langle J_x\rangle^2 = \frac{N^2}{4}P_2(t)^2$ were used. The latter approximation leads only to an error of the order [8] $\mathcal{O}\left(\frac{1}{N}\right)$. Next, the mean values of the transverse spin components are computed using the same approximations.

$$d_t\langle J_{y/z}\rangle_t \;=\; -\frac{1}{2}\Big(\tilde{\Gamma}+d\Gamma P_2(t)\Big)\langle J_{y/z}\rangle_t,$$

with $\langle J_{y/z}\rangle_{t=0} = 0$. The mean values can therefore be ignored when calculating single ensemble variances $\mathrm{var}(J_{y/z})$.

[7] For perfectly polarized ensembles $\langle J_zJ_x\rangle = \langle J_z\rangle\langle J_x\rangle$. The decorrelation approximation is justified as long as only a small number of collective (coherent) excitations is created in the atomic sample. In practice, the degree of squeezing, which can be produced in atomic samples is small, such that the decorrelation approximation is a reasonable assumption for the settings considered here.

[8] Initially, $\langle J_x^2\rangle|_{t=0} = \langle J_x\rangle^2|_{t=0}$. The time evolution of $\langle J_x^2\rangle$ is given by $d_t\langle J_x^2\rangle = -2\left(\Gamma_{\mathrm{cool}}+\Gamma_{\mathrm{heat}}\right)\langle J_x^2\rangle + \frac{N}{2}\left(\Gamma_{\mathrm{cool}}+\Gamma_{\mathrm{heat}}\right) + N\left(\Gamma_{\mathrm{cool}}-\Gamma_{\mathrm{heat}}\right)\langle J_x\rangle$. Hence, $\langle J_x^2\rangle_\infty - \langle J_x\rangle_\infty^2 = \frac{N}{4} + \langle J_x\rangle_\infty$ (compare Eq. (3.12)) in the steady state and the error is by a factor N smaller than $\langle J_x^2\rangle$ for all times.

The time derivatives of inter-ensemble products of transverse spins are given by

$$d_t\langle J_{z,I}J_{z,II}\rangle = -\left(\tilde{\Gamma}+d\Gamma P_2(t)\right)\langle J_{z,I}J_{z,II}\rangle + \frac{N}{2}\mu\nu d\Gamma P_2(t)^2,$$
$$d_t\langle J_{y,I}J_{y,II}\rangle = -\left(\tilde{\Gamma}+d\Gamma P_2(t)\right)\langle J_{y,I}J_{y,II}\rangle - \frac{N}{2}\mu\nu d\Gamma P_2(t)^2,$$

where $\langle J_{x,I}J_{x,II}\rangle \approx \langle J_{x,I}\rangle\langle J_{x,II}\rangle$ has been used. For $N \gg 1$, this is a very good approximation, since collective effects on populations are suppressed by a factor d/N. Therefore, the time evolution of longitudinal spins is only determined by single-particle terms, which do not lead to correlations between the two ensembles. Hence, the variances of the non-local operators $J_{y,\pm} = \left(J_{y,I} \pm J_{y,II}\right)/\sqrt{2}$ and $J_{z,\pm} = \left(J_{z,I} \pm J_{z,II}\right)/\sqrt{2}$ evolve according to

$$\begin{aligned} d_t\mathrm{var}\left(J_{y,\pm}\right) &= -\left(\tilde{\Gamma}+d\Gamma P_2(t)\right)\mathrm{var}\left(J_{y,\pm}\right) + \frac{N}{4}\left(\tilde{\Gamma}+d\Gamma P_2(t)^2\left(\mu\mp\nu\right)^2\right), \\ d_t\mathrm{var}\left(J_{z,\pm}\right) &= -\left(\tilde{\Gamma}+d\Gamma P_2(t)\right)\mathrm{var}\left(J_{z,\pm}\right) + \frac{N}{4}\left(\tilde{\Gamma}+d\Gamma P_2(t)^2\left(\mu\pm\nu\right)^2\right), \end{aligned}$$

such that

$$\mathrm{var}\left(J_{y,\pm}\right)_\infty = \mathrm{var}\left(J_{z,\mp}\right)_\infty = \frac{N}{4}\frac{\tilde{\Gamma}+d\Gamma P_{2,\infty}^2\left(\mu\mp\nu\right)^2}{\tilde{\Gamma}+d\Gamma P_{2,\infty}}$$

in the steady state. The variances $\mathrm{var}\left(J_{y,+}\right)$ and $\mathrm{var}\left(J_{z,-}\right)$ are squeezed, while $\mathrm{var}\left(J_{y,-}\right)$ and $\mathrm{var}\left(J_{z,+}\right)$ are anti-squeezed. Now, the time evolution of the longitudinal spin

$$d_t|\langle J_x\rangle| = -\frac{N}{2}\left(\Gamma_{\mathrm{heat}}-\Gamma_{\mathrm{cool}}\right) - \left(\Gamma_{\mathrm{heat}}+\Gamma_{\mathrm{cool}}\right)|\langle J_x\rangle|,$$

is considered, which yields directly

$$|\langle J_x\rangle|_\infty = \frac{N}{2}\,\frac{\Gamma_{\mathrm{cool}}-\Gamma_{\mathrm{heat}}}{\Gamma_{\mathrm{cool}}+\Gamma_{\mathrm{heat}}} = \frac{N}{2}P_{2,\infty}$$

for $t \to \infty$.

Collective effects have an negligible effect on the time evolution of the polarization. $P_2(t)$ evolves due to single-particle effects only and hence much slower than $\mathrm{var}\left(J_{y,\pm}\right)$ and $\mathrm{var}\left(J_{z,\pm}\right)$ for samples with high optical depth. In this case, the solution for $\xi(t) = \mathrm{var}\left(J_{z,+}\right)/P_2(t)$ can be cast in a simple analytical form

$$\xi(t) = \frac{1}{P_2(t)}e^{-\left(\tilde{\Gamma}+d\Gamma P_2(t)\right)t} + \frac{1}{P_2(t)}\frac{\tilde{\Gamma}+d\Gamma P_2(t)^2\left(|\mu|-|\nu|\right)^2}{\tilde{\Gamma}+d\Gamma P_2(t)}\left(1-e^{-\left(\tilde{\Gamma}+d\Gamma P_2(t)\right)t}\right).$$

B.4.2 Full master equation

In the following, the form of Eq. (3.11) is discussed and explained, in particular on the absence of collective noise terms.

The probe fields considered in Sec. 3.1.3 are off-resonant and it has been shown in the main text that collective contributions feature an enhancement factor which renders them the dominant decay mechanism for samples with high optical depth. As is shown in Sec. 3.1.3, it can be advantageous to apply also resonant laser light (pump fields). In contrast to off-resonant fields, collective contributions are negligible compared to single-particle terms for resonant light in the situation considered here. Unlike off-resonant collective rates, resonant collective rates are much slower than the corresponding single-particle rates for samples with high optical depth, which is an effect well known and harnessed in electromagnetically induced transparency [447–450]. The single particle decay rate after adiabatic elimination of excited states is given by $\Gamma_{res} = \frac{\Omega^2_{\rm pump}}{\gamma_{\rm LW}}$, where $\Omega_{\rm pump}$ is the Rabi frequency of the applied laser field and $\gamma_{\rm LW}$ is the natural line width of excited levels. Coherent effective effects lead to an enhancement factor d in the denominator. Intuitively, this effect can be understood by noting that emitted resonant photons are reabsorbed in an optically thick medium.

Due to atomic motion in ensembles at room temperature, spectral lines are Doppler broadened. Therefore off-resonant contributions of pump fields to the master equation with a detuning on the order of the Doppler width $\delta_{\rm Doppler}$ are taken into account. A calculation along the lines of the derivation shown in Sec. B.4.1 shows that these terms are negligible compared to their single-atom counterparts. More specifically, collective terms corresponding to a detuning $\delta_{\rm Doppler}$ lead to decay rates proportional to $\frac{\Omega^2_{\rm pump}}{\delta_{\rm Doppler}}\gamma_{\rm LW}d = \frac{\Omega^2_{\rm pump}}{\gamma_{\rm LW}d}\left(\frac{\gamma_{\rm LW}d}{\delta_{\rm Doppler}}\right)^2$ with $|\delta_{\rm Doppler}| >> \gamma_{\rm LW}d$, while single particle resonant terms lead to decay rates proportional to $\frac{\Omega^2_{\rm pump}}{\gamma_{\rm LW}}$.

Finally, Eq. (3.11) does not include collective terms, corresponding to radiative processes which do not change the internal atomic state, since they do not have an effect on the amount of entanglement generated. A master equation corresponding to the terms omitted in Eq. (3.10)

$$d_t\rho(t) \;=\; d\frac{\check{\Gamma}}{2}C\rho(t)C^\dagger + d\frac{\check{\Gamma}}{2}D\rho(t)D^\dagger + \dots\,,$$

with operators $C = \sum_i \left(\mu\ \sigma_{\downarrow\downarrow,I,i} + \nu\ \sigma_{\uparrow\uparrow,II,i}\right)$ and $D = C = \sum_i \left(\mu\ \sigma_{\downarrow\downarrow,II,i} + \nu\ \sigma_{\uparrow\uparrow,I,i}\right)$ leads to $d_t\xi(t) = 0$. Since $d_t\langle J_y\rangle = -\frac{d\check{\Gamma}}{2N}\langle J_y\rangle$, $d_t\langle J_z\rangle = -\frac{d\check{\Gamma}}{2N}\langle J_z\rangle$, and $d_t\langle J_x\rangle = 0$, $\langle J_y\rangle = \langle J_z\rangle = 0$ and $\langle J_z\rangle = N/2$ for all times. The time derivatives of single-ensemble variances for transverse spin components is given by

$$\begin{aligned} d_t\langle J_y^2\rangle &= \check{\Gamma}\frac{d}{N}\left(\mu^2+\nu^2\right)\left(-\langle J_y^2\rangle + \langle J_z^2\rangle\right), \\ d_t\langle J_z^2\rangle &= \check{\Gamma}\frac{d}{N}\left(\mu^2+\nu^2\right)\left(\langle J_y^2\rangle - \langle J_z^2\rangle\right), \end{aligned}$$

such that $\langle J_y^2\rangle = \langle J_z^2\rangle = N/4$, for all times. Accordingly, $\langle J_{y,I}J_{y,II}\rangle = \langle J_{z,I}J_{z,II}\rangle = 0$ for all times since

$$d_t\langle J_{y,I}J_{y,II}\rangle \;=\; -2\frac{d}{N}\hat{\Gamma}\mu\nu\langle J_{z,I}J_{z,II}\rangle,$$

$$d_t\langle J_{z,I}J_{z,II}\rangle \;=\; 2\frac{d}{N}\hat{\Gamma}\mu\nu\langle J_{y,I}J_{y,II}\rangle.$$

The processes under consideration do not create entanglement unlike the terms in Eq. (3.10) with jump operators A and B. As shown above, they do not degrade entanglement either. Collective terms corresponding to far off-resonant radiative transitions $|\uparrow\rangle \to |e_\downarrow\rangle \to |\uparrow\rangle$, $|\downarrow\rangle \to |e_\uparrow\rangle \to |\downarrow\rangle$ do not introduce random phases and preserve coherence. The emitted photon does not reveal information about the internal atomic state, since it is emitted into the laser mode. Terms with jump operators C and D lead only to very small correction terms proportional to $1/N$ and can be ignored.

B.5 Generation of steady state entanglement in alkali atoms

In this appendix, the generation of dissipatively driven entanglement in multi-level systems is considered based on the model described in Sec. 3.1.4.

Taking three ground state levels $|\uparrow\rangle$, $|\downarrow\rangle$ and $|h\rangle$ into account, the evolution of the reduced atomic density matrix can be described by the master equation

$$\begin{aligned}
d_t\rho(t) \;=\;& d\Gamma A\rho(t)A^\dagger + d\Gamma B\rho(t)B^\dagger \\
&+\; \Gamma_{\downarrow\uparrow}\sum_{i=1}^{N}\left(\sigma_{I,i}\rho(t)\sigma_{I,i}^\dagger + \sigma_{II,i}\rho(t)\sigma_{II,i}^\dagger\right) \\
&+\; \Gamma_{\uparrow\downarrow}\sum_{i=1}^{N}\left(\sigma_{I,i}^\dagger\rho(t)\sigma_{I,i} + \sigma_{II,i}^\dagger\rho(t)\sigma_{II,i}\right) \\
&+\; \Gamma_{\not\downarrow h}\sum_{i=1}^{N}\left(|h\rangle_{I,i}\langle\uparrow|\rho(t)|\uparrow\rangle_{I,i}\langle h| + |h\rangle_{II,i}\langle\uparrow|\rho(t)|\uparrow\rangle_{II,i}\langle h|\right) \\
&+\; \Gamma_{h\not\uparrow}\sum_{i=1}^{N}\left(|\uparrow\rangle_{I,i}\langle h|\rho(t)|h\rangle_{I,i}\langle\not\uparrow| + |\not\uparrow\rangle_{II,i}\langle h|\rho(t)|h\rangle_{II,i}\langle\not\uparrow|\right) \\
&+\; \Gamma_{\not\downarrow h}\sum_{i=1}^{N}\left(|h\rangle_{I,i}\langle\downarrow|\rho(t)|\downarrow\rangle_{I,i}\langle h| + |h\rangle_{II,i}\langle\downarrow|\rho(t)|\downarrow\rangle_{II,i}\langle h|\right) \\
&+\; \Gamma_{h\not\downarrow}\sum_{i=1}^{N}\left(|\downarrow\rangle_{I,i}\langle h|\rho(t)|h\rangle_{I,i}\langle\not\downarrow| + |\not\downarrow\rangle_{II,i}\langle h|\rho(t)|h\rangle_{II,i}\langle\not\downarrow|\right) \\
&+\; \Gamma_{\not\uparrow\uparrow}\sum_{i=1}^{N}\left(|\uparrow\rangle_{I,i}\langle\uparrow|\rho(t)|\uparrow\rangle_{I,i}\langle\uparrow| + |\uparrow\rangle_{II,i}\langle\uparrow|\rho(t)|\uparrow\rangle_{II,i}\langle\uparrow|\right) \\
&+\; \Gamma_{\not\downarrow\downarrow}\sum_{i=1}^{N}\left(|\downarrow\rangle_{I,i}\langle\downarrow|\rho(t)|\downarrow\rangle_{I,i}\langle\downarrow| + |\downarrow\rangle_{II,i}\langle\downarrow|\rho(t)|\downarrow\rangle_{II,i}\langle\downarrow|\right),
\end{aligned} \tag{B.9}$$

where Γ_{ab} is the single-particle rate for the transition $|a\rangle \to |b\rangle$. As in Sec. 3.1.3, collective terms due to resonant pump fields, as well as collective dephasing terms are omitted (see

App. B.4.2). Collective terms involving the level $|h\rangle$ are also insignificant for $N >> 1$, as long as the number of coherent collective excitations is small.

In order to compute the amount of entanglement produced, the variance of the nonlocal operator $J_{y,+,2} = (J_{y,I} + J_{y,II})_2 / \sqrt{2}$ is considered. (The subscript "2" emphasizes that these quantities are defined with respect to the two-level subsystem $\{|\uparrow\rangle, |\downarrow\rangle\}$.) A calculation analogous to the two-level derivation in App. B.4.1 shows that $\langle J_{y,I}\rangle_2 = \langle J_{y,II}\rangle_2 = 0$ for all times. Therefore $\mathrm{var}\,(J_y)_2 = \langle J_y^2\rangle_2$. For simplicity, it is assumed that both ensembles are identical $\langle J_{y,I}^2\rangle_2 = \langle J_{y,II}^2\rangle_2 = \langle J_y^2\rangle_2$.
According to Eq. (B.9), the time derivative of the single-ensemble variance $\langle J_y^2\rangle_2$ is given by

$$d_t\langle J_y^2\rangle_2 \;=\; -\left(\bar{\Gamma} + d\Gamma\frac{N_2(t)}{N}P_2(t)\right)\langle J_y^2\rangle_2 + \Gamma\frac{N_2(t)}{4} + d\Gamma\frac{1}{4}\frac{N_2(t)}{N}P_2(t)^2\left(\mu^2+\nu^2\right),$$

where the decay rate $\bar{\Gamma}$, the number of atoms in the relevant two-level subsystem $\{|\uparrow\rangle, |\downarrow\rangle\}$, $N_2(t)$ and the corresponding polarization $P_2(t)$ are defined in Sec. 3.1.4. $N = \sum_i (|\uparrow\rangle_i\langle\uparrow| + |\downarrow\rangle_i\langle\downarrow| + |h\rangle_i\langle h|)$ is the total number of atoms in one ensemble and $N_2(0) = N$. Note that repump fields, which transfer atoms from $|h\rangle$ to $|\uparrow\rangle$ or $|\downarrow\rangle$ (corresponding to terms with prefactors Γ_{hg} and Γ_{hs} in Eq. (B.9)), do not contribute to $\bar{\Gamma}$.

Inter-ensemble correlations $\langle J_{y,I}J_{y,II}\rangle_2$ evolve according to

$$d_t\langle J_{y,I}J_{y,II}\rangle_2 \;=\; -\left(\bar{\Gamma} + d\Gamma\frac{N_2(t)}{N}P_2(t)\right)\langle J_{y,I}J_{y,II}\rangle_2 - d\Gamma\frac{1}{2}\frac{N_2(t)}{N}P_2(t)^2\mu\nu.$$

Hence, the time evolution of $\mathrm{var}\,(J_{y,+})_2 = \langle J_y^2\rangle_2 + \langle J_{y,I}J_{y,II}\rangle_2$ is given by

$$d_t\langle J_{y,+}^2\rangle_2 \;=\; -\left(\bar{\Gamma} + d\Gamma\frac{N_2(t)}{N}P_2(t)\right)\langle J_{y,+}^2\rangle_2 + \bar{\Gamma}\frac{N_2(t)}{4} + d\Gamma\frac{1}{4}\frac{N_2(t)}{N}P_2(t)^2\left(\mu-\nu\right)^2 \quad \text{(B.10)}$$

Analogously,

$$d_t\langle J_{z,-}^2\rangle_2 = -\left(\bar{\Gamma} + d\Gamma\frac{N_2(t)}{N}P_2(t)\right)\langle J_{z,-}^2\rangle_2 + \bar{\Gamma}\frac{N_2(t)}{4} + d\Gamma\frac{1}{4}\frac{N_2(t)}{N}P_2(t)^2\left(\mu-\nu\right)^2. \quad \text{(B.11)}$$

Since the evolution of $N_2(t)$ and $P_2(t)$ is known from equations (3.15), $\Sigma_{J,2} = \langle J_{y,+}^2\rangle_2 + \langle J_{z,-}^2\rangle_2$ can be directly calculated yielding a complicated expression. However, as explained in Sec. 3.1.3 and Sec. 3.1.4, $N_2(t)$ and $P_2(t)$ can be considered to change slowly compared to the fast entangling dynamics. In this case, (B.11) leads to the simple and convenient expression (3.16) used in Sec. 3.1.4.

B.6 Implementation in room temperature ^{133}Cs vapors

In this appendix, the results derived in Sec. 3.1.4 are applied to a specific example and the generation of entanglement between two ^{133}Cs ensembles at room temperature

is considered. The parameters used in the following take values consistent with the experiments reported in [VII], [16]. The approximate calculation outlined below provides a rough estimate of the entanglement that can be produced.
In the following $\hat{\mathbf{y}}$-polarized probe light which propagates along $\hat{\mathbf{z}}$ and interacts in succession with two ensembles in a magnetic field which is oriented along $\hat{\mathbf{x}}$ is considered. The laser field is assumed to be blue detuned by $\Delta = 700$MHz with respect to the $6S_{1/2}(F = 4) \rightarrow 6P_{3/2}(F = 5)$ transition (D2 line). Fig. 2.2 depicts the relevant parts of the atomic level schemes in both samples and illustrates the atomic transitions due to the light-matter interaction induced by the applied laser field. Initially, all atoms are pumped to state $|\uparrow\rangle$. The restriction of the analysis to the three levels $|\uparrow\rangle$, $|\downarrow\rangle$ and $|h\rangle$ in the presence of strong pump fields, as described in Sec. 3.1.4 for $\hat{\mathbf{x}}$-polarized probe light is also valid for this configuration, as the rates of transitions from level $|\uparrow\rangle$ to states with $m_F = \pm 2$ occur at rates which are two orders of magnitude smaller than transitions within the sub-system under consideration. ($\Gamma_{|4,4\rangle\rightarrow|4,2\rangle} = 0.03\ \Gamma_{|4,4\rangle\rightarrow|4,3\rangle}$ and $\Gamma_{|4,4\rangle\rightarrow|3,2\rangle} = 0.02\ \Gamma_{|4,4\rangle\rightarrow|4,3\rangle}$).

In order to calculate the experimentally measurable steady state entanglement using Eq. (3.19) for a given optical depth d and parameters μ and ν, $N_2(t)$, $P_2(t)$ and $\bar{\Gamma}$ need to be computed. $N_2(t) = N_\uparrow(t) + N_\downarrow(t)$ and $P_2(t) = (N_\uparrow(t) - N_\downarrow(t))/N_2(t)$ are readily obtained from Eq. (3.15), if the rates for all transitions are known. As the probe field is assumed to be off-resonant, probe induced rates Γ_{ab} for transitions $|a\rangle \rightarrow |b\rangle$ are calculated using the formula $\Gamma_{ab}^{\mathrm{probe}} = \Omega^2_{\mathrm{probe}} |\sum_l \frac{c_l^{\mathrm{ab}}}{\Delta_l^{\mathrm{ab}}}|^2 \gamma_{\mathrm{LW}}$, where the sum runs over all exited levels $|e_l\rangle$ contributing to a particular transitions (for example the states $|5,3\rangle$, $|4,3\rangle$ and $|3,3\rangle$ in $6^2P_{3/2}$, if $\Gamma_{\uparrow\downarrow} = \Gamma\nu^2$ is computed). Δ_l^{ab} is the detuning for each contributing level, γ_{LW} the natural line width of excited levels and $c_l^{\mathrm{ab}} = \langle j_b, m_b; j_{L_2}, m_{L_2} | j_{e_l}, m_{e_l}\rangle \langle j_{e_l}, m_{e_l} | j_a, m_a; j_{L_1}, m_{L_1}\rangle$ is the product of the corresponding Clebsch-Gordan coefficients. j_x and m_x refer to the total angular momentum and magnetic quantum number of the atomic state $|x\rangle$ and $j_{L_{1/2}}$ and $j_{L_{1/2}}$ refer to the absorbed and emitted photons involved in the process. Pump, or repump induced transitions are resonant and involve to a good approximation only one level. Hence the corresponding rates[9] are given by $\Gamma_{\mathrm{ab}}^{\mathrm{pump}} = \frac{\Omega^2_{\mathrm{pump}}}{\gamma_{\mathrm{LW}}} c^2_{\mathrm{pump}}\ k$ and $\Gamma_{\mathrm{ab}}^{\mathrm{repump}} = \frac{\Omega^2_{\mathrm{repump}}}{\gamma_{\mathrm{LW}}} c^2_{\mathrm{repump}}\ k$ respectively, where $k = \frac{\Gamma}{\delta\mathrm{Doppler}} = \frac{5\mathrm{MHz}}{380\mathrm{MHz}}$. Here, pumping resonant with respect to the level $|4,4\rangle$ in $6P_{1/2}$ (D_1 line) and pump fields resonant with respect to the level $|4,4\rangle$ in $6P_{3/2}$ (D_2 line) are considered. (The decay rates are approximately the same $\gamma_{D_1} \approx \gamma_{D_2} = \gamma_{\mathrm{LW}}$.) Having expressions for $N_2(t)$, $P_2(t)$ as well as $\bar{\Gamma} = \Gamma_{\uparrow\downarrow} + \Gamma_{\downarrow\uparrow} + \Gamma_{\uparrow h} + \Gamma_{\downarrow h} + \Gamma_{\uparrow\uparrow} + \Gamma_{\downarrow\downarrow} + r$ at hand, the amount of entanglement which can be produced in this particular setting can be calculated. Results are shown in Fig. 3.3 and are discussed in Sec. 3.1.4. As the three-level description becomes inaccurate if too many atoms are transferred from state $|\uparrow\rangle$ to state $|\downarrow\rangle$, both plots show results for the optimal (that is minimal) pump power which guarantees a fraction of at least 95% of all atoms in the relevant two-level

[9] The correction factor k takes into account that due to the Doppler broadening of atoms moving at room temperature only a fraction $k = \frac{\gamma_{\mathrm{LW}}}{\delta_{\mathrm{Doppler}}}$ of all atoms in the cell is on resonance with the applied field. The Doppler width is given by $\delta_{\mathrm{Doppler}} = \frac{\nu}{c}\left(\frac{2k_BT}{m\ln 2}\right)^{1/2}$, where $c/\nu = \lambda$ is the wavelength of the applied light field, k_B is the Boltzmann constant, T is the temperature and m is the atomic mass.

subsystem in state $|\uparrow\rangle$ for all times. Besides the need for sufficient pump fields, repumping of atoms from $F = 3$ to $F = 4$ is required. If strong pump but no repump fields are applied, no entangled state can be reached, as for $t \to \infty$, all atoms are transferred to level $|h\rangle$.

Appendix C

Dissipative quantum repeaters: supplementary material

In this appendix, the results presented in Sec. 3.2 are explained in more detail. In the following, two dissipative distillation schemes are discussed. Scheme I (see Sec. C.1) is suited for settings where a dissipative processes is available which produces entangled steady states, that are close to pure states. If only very mixed steady states are available as input, scheme II is preferable, (which is explain in detail in Sec. C.4). In Sec. C.2, the notion of continuous exchange of classical information between two parties is introduced in the master equation formalism and it is shown that arbitrary LOCC channels can be realized using local dissipation and classical communication. In Sec. C.3, it is explained how the continuous protocols used here can be made robust against noise. Finally, in Sec. C.5, the dissipative quantum repeater scheme put forward in the main text is analyzed.

C.1 Scheme I: Dissipative entanglement distillation for source states close to pure states

In this section, two variants of scheme I are explained[1]. In Sec. C.1.1, a protocol, which allows for dissipative entanglement distillation without communication is discussed. Sec. C.1.2 is concerned with a related protocol, which includes classical communication. Both protocols produce Bell-diagonal steady states which can further distilled using scheme II presented in Sec. C.4.

C.1.1 Dissipative entanglement distillation without communication

In this subsection, the setup illustrated in Fig. 3.8a is considered. The dissipative dynamics driving the two systems s_1 and s_2 is physically motivated and can be implemented by coupling the systems located at Alice's and Bob's side to a common bath, for example

[1] The variant of scheme I without communication is fundamentally different from scheme II, which is presented in Sec. C.4 and cannot not be formulated in terms of master equations of the form $\dot{\rho} \propto (T(\rho) - \rho)$, where $T(\rho)$ is a LOCC channel.

the vacuum modes of the electromagnetic field [163, 451, 452]. The entanglement which can be attained per single copy is limited for a given dissipative process. Moreover these systems are subject to noise. Still, it is possible to use these two copies as resource for creating a single highly entangled pair in target system $\mathcal{T}$. In the absence of undesired processes, the dynamics described by the master equation $\dot{\rho} = \gamma\left(\mathfrak{L}^A(\rho) + \mathfrak{L}^B(\rho)\right)$ (see main text) drives systems s_1 and s_2 into the state

$$|\psi\rangle^{\otimes 2} \propto |00\rangle_{s_1}|00\rangle_{s_2} - \lambda\left[|00\rangle_{s_1}|11\rangle_{s_2} + |11\rangle_{s_1}|00\rangle_{s_2}\right] + \lambda^2|11\rangle_{s_1}|11\rangle_{s_2}.$$

Alice and Bob share a maximally entangled state $|\Psi_0\rangle = \left(|00\rangle_{s_1}|11\rangle_{s_2} + |11\rangle_{s_1}|00\rangle_{s_2}\right)/\sqrt{2}$ in a subspace with one excitation on each side. Scheme I is based on the extraction of entanglement from this subspace and its subsequent transfer to the target system by means of the flip operation $\mathbb{F} = \sum_{i,j} |j_{\mathcal{T}}\hat{i}_{\mathrm{s}}\rangle\langle i_{\mathcal{T}}\hat{j}_{\mathrm{s}}|$, where $|\hat{0}_{\mathrm{s}}\rangle = |0_{\mathrm{s}_1}1_{\mathrm{s}_2}\rangle$ and $|\hat{1}_{\mathrm{s}}\rangle = |1_{\mathrm{s}_1}0_{\mathrm{s}_2}\rangle$. Systems s_1 and s_2 are permanently driven back to an entangled state. In contrast to standard distillation protocols for pure states [400], the presence of this strong process leads to a substantial decrease in the entanglement if the flip operations on Alice's and Bob's side are not applied simultaneously. Hence, the coordination of their actions, e.g., using fast classical communication, seems to be essential. Surprisingly, the desired dynamics can be realized in the absence of communication or predefined correlations using local unitary evolutions.

This is possible by exploiting the symmetry of the maximally entangled state $|\Psi_0\rangle$. More specifically, $|\Psi_0\rangle$ is invariant under any unitary operation of the form $U \otimes \bar{U}$, while less entangled pure states are not. $\bar{U}$ denotes the complex conjugate of U. Such an operation can be implemented without communication as the time evolution of a sum of local Hamiltonians $H = H_A \otimes \mathbb{I} - \mathbb{I} \otimes \bar{H}_B$. Here, the flip operation is used such that the corresponding master equation is given by

$$\begin{aligned}
\dot{\rho} &= \gamma\left(\mathfrak{L}^{A_{\mathrm{s}_1}}(\rho) + \mathfrak{L}^{B_{\mathrm{s}_1}}(\rho) + \mathfrak{L}^{A_{\mathrm{s}_2}}(\rho) + \mathfrak{L}^{B_{\mathrm{s}_2}}(\rho)\right) \\
&+ i\delta_{\mathbb{F}}\left[\mathbb{F} \otimes \mathbb{I} - \mathbb{I} \otimes \mathbb{F}, \rho\right] \\
&+ \varepsilon_{\mathrm{c}}\left(\mathfrak{L}^{a_{\mathrm{s}_1}}(\rho) + \mathfrak{L}^{b_{\mathrm{s}_1}}(\rho) + \mathfrak{L}^{a_{\mathrm{s}_2}}(\rho) + \mathfrak{L}^{b_{\mathrm{s}_2}}(\rho)\right) \\
&+ \varepsilon_{\mathrm{h}}\left(\mathfrak{L}^{a^\dagger_{\mathrm{s}_1}}(\rho) + \mathfrak{L}^{b^\dagger_{\mathrm{s}_1}}(\rho) + \mathfrak{L}^{a^\dagger_{\mathrm{s}_2}}(\rho) + \mathfrak{L}^{b^\dagger_{\mathrm{s}_2}}(\rho)\right) \\
&+ \varepsilon_{\mathrm{d}}\left(\mathfrak{L}^{a^\dagger_{\mathrm{s}_1} a_{\mathrm{s}_1}}(\rho) + \mathfrak{L}^{b^\dagger_{\mathrm{s}_2} b_{\mathrm{s}_2}}(\rho)\right),
\end{aligned}$$

where $a = \sigma^-_{\mathrm{Alice}}$ and $b = \sigma^-_{\mathrm{Bob}}$. The first line corresponds to the entangling dissipative process (described by nonlocal jump operators A and B) acting on the two source systems as explained in the main text. The second line describes the unitary coupling of the target system to the entangled subspace of the two source systems and the last three lines represent undesired processes. More specifically, dephasing at a rate ϵ_{d} as well as noise terms, which create (annihilate) excitations locally at the heating (cooling) rate ϵ_{h} (ϵ_{c}) are included. Note that the noise types considered here also include depolarizing noise. The target system itself is assumed to be protected (below, a variant of this scheme is described, which includes classical communication and can be made robust against noise acting on the target system).

A disadvantage of the unitary evolution employed here lies in the fact that the source system is subject to a back-action of the target state, which depends on the quantum state of $\mathcal{T}$. Accordingly, the evolution of the source systems is highly dependent on the state of the target pair. It remains an open question, whether schemes, similar to the one described in Sec. C.3 can be used to render this protocol robust against errors on the target system, or whether this is a special feature of protocols including classical communication.

C.1.2 Distillation using scheme I including classical communication

In this subsection, the setup illustrated in Fig. 3.8b is considered. As explained in Sec. C.1.1, the dissipative entangling process acting on the source systems s_1 and s_2 has the property that Alice and Bob share a maximally entangled state if the resulting steady state is projected onto the subspace with one excitation on each side. Ideally, this quantum state is then transferred to the target system $\mathcal{T}$ by means of the flip operation defined above. Below, a classical communication channel is introduced, which allows Alice and Bob to coordinate their actions such that flip operations on both sides can be performed in a synchronized fashion if both sides have successfully accomplished a projection onto the relevant subspace with one excitation. As explained in Sec. C.2, Lindblad terms of the form $\mathfrak{L}^{T_{\text{LOCC}}}(\rho) = (T_{\text{LOCC}}(\rho) - \rho)$, where T_{LOCC} is an arbitrary LOCC channel[2], can be realized by means of local dissipative processes and classical communication.
As explained in Sec. C.3, this protocol is resistent against target errors if it is coupled to sufficiently many blocks of source pairs. For simplicity, the basic protocol is explained here in the absence of target errors, which corresponds to the limit of using infinitely many source blocks (entanglement distillation for a finite number of source blocks and finite error rates is analyzed in Sec. C.3 and Sec. C.5). Classical communication allows for the implementation of the scheme outlined above. The LOCC distillation operation corresponding to this process, $T_{\mathbb{F}}$, is given by

$$\begin{aligned} T_{\mathbb{F}}(\rho) &= \mathbb{F}_{\text{A}} \otimes \mathbb{F}_{\text{B}} \rho \mathbb{F}_{\text{A}} \otimes \mathbb{F}_{\text{B}} + P_A \otimes \ P_B^{\perp} \rho P_A \otimes P_B^{\perp} \\ &+ \ P_A^{\perp} \otimes P_B \rho P_A^{\perp} \otimes P_B + P_A^{\perp} \otimes P_B^{\perp} \rho P_A^{\perp} \otimes P_B^{\perp}, \end{aligned}$$

where $P = |0_{s_1} 1_{s_2}\rangle\langle 0_{s_1} 1_{s_2}| + |1_{s_1} 0_{s_2}\rangle\langle 1_{s_1} 0_{s_2}|$ is the projector onto the subspace with one excitation, and $P^{\perp} = \mathbb{1} - P$ the projector onto the subspace with zero or two excitations. Note that only the first term has an effect on the target system. The flip operation leads to a back-action on the source system, which depends on the state of $\mathcal{T}$.
In order to simplify the discussion in Sec. C.3, a slightly modified version of this protocol is introduced here, $T'_{\mathbb{F}}(\rho)$, which does not exhibit a state-dependent back-action. This can

[2] LOCC channels are completely positive trace preserving maps that can be realized by means of Local Operations and Classical Communication.

be achieved by applying a twirl [181, 182] on the target system prior to the flip operation

$$\begin{aligned} T'_{\mathbb{F}}(\rho) &= \sum_{ij=0}^{3} \frac{1}{16} \mathbb{F}_{\mathrm{A}} \otimes \mathbb{F}_{\mathrm{B}} U_{ij} \rho U_{ij}^{\dagger} \mathbb{F}_{\mathrm{A}} \otimes \mathbb{F}_{\mathrm{B}} + P_A \otimes P_B^{\perp} \rho P_A \otimes P_B^{\perp} \\ &+ P_A^{\perp} \otimes P_B \rho P_A^{\perp} \otimes P_B + P_A^{\perp} \otimes P_B^{\perp} \rho P_A^{\perp} \otimes P_B^{\perp}. \end{aligned}$$

$U_{ij} = \sigma_i^A \otimes \sigma_j^B$ is a unitary operation acting on the target system only, where σ_i denote the four Pauli matrices and σ_0 is the identity. Due to the twirl, this protocol features an enhanced back-action on the source, which is independent from the target. It turns out that the performance of this protocol is qualitatively the same as shown in Fig. 3.9 in the main text. The total master equation is then given by

$$\begin{aligned} \dot{\rho} &= \gamma \left(\mathfrak{L}^{A_{\mathrm{s}_1}}(\rho) + \mathfrak{L}^{B_{\mathrm{s}_1}}(\rho) + \mathfrak{L}^{A_{\mathrm{s}_2}}(\rho) + \mathfrak{L}^{B_{\mathrm{s}_2}}(\rho) \right) \\ &+ \delta_{\mathbb{F}} \left(T'_{\mathbb{F}}(\rho) - \rho \right) \\ &+ \varepsilon_{\mathrm{c}} \left(\mathfrak{L}^{a_{\mathrm{s}_1}}(\rho) + \mathfrak{L}^{b_{\mathrm{s}_1}}(\rho) + \mathfrak{L}^{a_{\mathrm{s}_2}}(\rho) + \mathfrak{L}^{b_{\mathrm{s}_2}}(\rho) \right) \\ &+ \varepsilon_{\mathrm{h}} \left(\mathfrak{L}^{a_{\mathrm{s}_1}^{\dagger}}(\rho) + \mathfrak{L}^{b_{\mathrm{s}_1}^{\dagger}}(\rho) + \mathfrak{L}^{a_{\mathrm{s}_2}^{\dagger}}(\rho) + \mathfrak{L}^{b_{\mathrm{s}_2}^{\dagger}}(\rho) \right) \\ &+ \varepsilon_{\mathrm{d}} \left(\mathfrak{L}^{a_{\mathrm{s}_1}^{\dagger} a_{\mathrm{s}_1}}(\rho) + \mathfrak{L}^{b_{\mathrm{s}_2}^{\dagger} b_{\mathrm{s}_2}}(\rho) \right), \end{aligned}$$

where $a = \sigma^-_{\mathrm{Alice}}$ and $b = \sigma^-_{\mathrm{Bob}}$.

C.2 Classical dissipative channels and dissipative LOCC

Classical channels are easier to realize experimentally than their quantum counterparts and can for example be implemented using optical fibers. Since classical channels are insufficient for the generation of quantum correlations, long-range links can be established over large distances using the toolkit of classical error-correction. The class of LOCC operations, i.e. quantum operations that can be performed using local operations and classical communication, is of essential importance in quantum information theory, especially in the context of entanglement distillation protocols.

In this section, the notion of classical channels is introduced in the framework of dissipative quantum information processing. This allows for the formulation of generalized LOCC operations in a continuous dissipative setting, which includes a wide range of continuous distillation protocols.

C.2.1 Classical dissipative channels

To start with, a dissipative classical communication channel is introduced.
Both parties, Alice and Bob, each have access to a d-dimensional system which is used exclusively for classical communication (see. Fig. C.1). The master equation

$$\dot{\rho} = \Gamma \left(\sum_i \langle i_{\mathrm{c_A}} | \rho_{\mathrm{Alice}} | i_{\mathrm{c_A}} \rangle | 0_{\mathrm{c_A}} i_{\mathrm{c_B}} \rangle \langle 0_{\mathrm{c_A}} i_{\mathrm{c_B}} | - \rho \right) \equiv \Gamma \mathfrak{C}_{\mathrm{A} \to \mathrm{B}}(\rho)$$

Figure C.1: Realization of a classical dissipative channel.

describes a one-way classical communication channel. States referring to the communication system at Alice's and Bob's side are labelled by subscripts $\mathrm{c_A}$ and $\mathrm{c_B}$ respectively. Alice's communication system is continuously measured in the computational basis yielding the quantum state $|i_{\mathrm{c_A}}\rangle$ with probability $\langle i_{\mathrm{c_A}}|\rho_{\mathrm{Alice}}|i_{\mathrm{c_A}}\rangle$ and reset to the state $|0_{\mathrm{c_A}}\rangle$, while the communication system on Bob's side is set to the measurement outcome. This process can be written in the form

$$\dot{\rho} = \Gamma\mathfrak{C}_{\mathrm{A}\to\mathrm{B}}(\rho) \equiv \Gamma(T(\rho) - \rho),$$

where the completely positive map $T(\rho)$ is an entanglement breaking operation [453], which maps any state to a separable one. The solution of this master equation $\rho(t)$ is given by

$$\rho(t) = \rho(0)e^{-\Gamma t} + \underbrace{\int_0^t d\tau T(\rho(\tau))e^{\Gamma(\tau-t)}}_{\text{separable}}.$$

The second term is separable, since $T(\rho)$ is entanglement breaking. Accordingly, the classical channel introduced above does not produce entanglement. Moreover any entanglement present in the state $\rho(0)$ is exponentially suppressed.

C.2.2 Generation of Lindblad operators of the form $T(\rho) - \rho$

In the following, it is proven that any dissipative time evolution which satisfies a master equation of the form $\dot{\rho} = \gamma(T(\rho) - \rho)$ can be designed by means of local dissipative processes in combination with the classical communication channels introduced above in the limit of high rates Γ. The basic setup is sketched in Fig. C.2. Alice and Bob hold a bipartite system, which is referred to as the main system. In addition both parties have access to several classical communication channels and can apply dissipative dynamics acting on the classical channels and their part of the main system. This setting allows for a wider class of dissipative evolutions on the main system which includes dissipative LOCC processes. In particular the following is stated.
Let $T(\rho)$ be any LOCC map. Let $\mathfrak{L}(\rho)$ be any bounded Lindblad operator, i.e., $\max_\rho \|\mathfrak{L}(\rho)\| = 1$, acting on the main system at a rate γ. Let Alice and Bob have access to classical communication channels as described above. If both parties can apply any dissipative process of Lindblad form on their side, an effective dissipative time evolution on the main system satisfying the master equation

$$\dot{\rho} = \gamma\mathfrak{L}(\rho) + \delta\,(T'(\rho) - \rho) \tag{C.1}$$

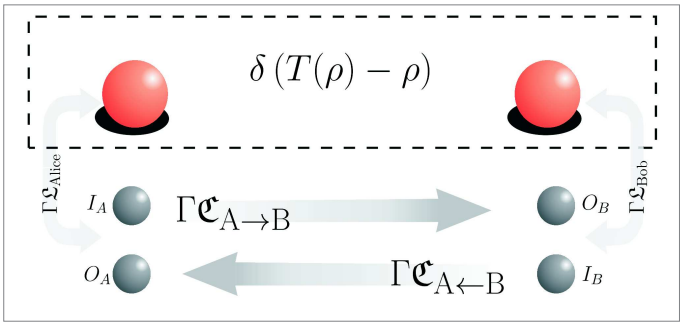

Figure C.2: Using local dissipative processes and fast classical communication, arbitrary LOCC channels can be implemented in a continuous fashion.

after an initial waiting time of the order $\frac{1}{\delta}$ can be realized. The completely positive operator $T'(\rho)=T(\rho)+\mathcal{O}(\sqrt{\alpha})$ is an imperfect realization of $T(\rho)$ up to an error $\mathcal{O}(\sqrt{\alpha})$, which vanishes for small $\alpha=\frac{\gamma'}{\Gamma}$, where $\gamma'=\gamma+\delta$. $\mathcal{O}(f(\alpha))$ denotes any hermitian (time and state dependent) operator with a trace norm scaling with $f(\alpha)$ in the limit $\alpha\to 0$. Since $\max_\rho \|\mathfrak{L}(\rho)\|=1$, the strength of the process is completely encoded in γ. $\mathfrak{L}(\rho)$ can include a dissipative LOOC map itself, as discussed at the end of this section. The error $\mathcal{O}(\sqrt{\alpha})$ of the LOCC map is small for $\alpha\ll 1$. A time evolution satisfying Eq. (C.1) can be either obtained by starting from certain initial conditions, or after an initial waiting time on the order of $\frac{1}{\delta}$, during which no external control is required. If $\Gamma\gg\gamma+\delta$ ($\alpha\ll 1$), the system evolves approximately according to $\dot\rho=\gamma\mathfrak{L}(\rho)+\delta\,(T(\rho)-\rho)$.

Note, that LOOC operations are extremely hard to parameterize. It is known, that they can be written as a separable superoperator $T(\rho)=\sum_i A_i\otimes B_i\rho A_i^\dagger\otimes B_i^\dagger$, but not every separable superoperator is a LOCC map. Practically, a general LOCC map can only be characterized by fixing the number of communication rounds between Alice and Bob and to specifying the exact operations that Alice and Bob perform in each round. The most general operation Alice and Bob can apply is a positive operator valued measurement (POVM). This covers any completely positive map as well as measurements, unitary evolutions, etc. A POVM is specified by a number of Kraus operators A_i, corresponding to the possible measurement outcomes i, where the normalization condition $\sum_i A_i^\dagger A_i=\mathbb{I}$ guaranties that the probabilities for the different possible outcomes add up to 1.
The following situation is considered. Alice performs a first POVM A_i and sends her result i to Bob. Bob chooses a POVM B_j^i depending on Alice's result i. Subsequently, he sends the result j to Alice, who chooses her next POVM A_k^{ij} which may depend on all previous measurement results. This procedure can be repeated many times. This corresponds to the application of the operation

$$T(\rho)=\sum_{i_0,j_0,i_1,j_1,\ldots,i_r,j_r} X_{i_0,j_0,i_1,j_1,\ldots,i_r,j_r}\rho X^\dagger_{i_0,j_0,i_1,j_1,\ldots,i_r,j_r},$$

where each Kraus operator is of the form

$$X_{i_0,j_0,i_1,j_1,\ldots,i_r,j_r}=B_{j_n}^{i_0,j_0,i_1\ldots i_n}\ldots B_{j_1}^{i_0,j_0,i_1}A_{i_1}^{i_0,j_0}B_{j_0}^{i_0}A_{i_0}$$

and represent one possible set of measurements outcomes $i_0, j_0, i_1, j_1, \ldots, i_r, j_r$ for all r POVM measurements. Due to this lack of a concise notation for a general LOCC map, a complete proof of this statement would be lost in notation and it would be hard for the reader to understand the main idea of the proof. The setting is therefore restricted to LOCC maps with one communication round, i.e., Alice sends one message to Bob and Bob can send an answer back to Alice once. A generalization of the following proof to a LOCC map with a finite number of communication rounds m is straight forward and will be discussed below.

Let $T(\rho)$ denote a LOCC map with one round of communication. This map can be realized in the following way:

- Alice applies a POVM measurement with Kraus operators A_i, obtains the measurement result i and sends it to Bob.
- Bob performs a POVM measurement B_j^i, which can depend on i, and sends the result j to Alice. Since it is assumed that Alice is memoryless, Bob also sends the measurement outcome of Alice's measurement i.
- In the last step, Alice can apply any completely positive map T_{ij} on her side. This map can depend on both, i and j.

Note, that $T_{ij}(\rho) = \sum_k C_k^{ij} \rho (C_k^{ij})^\dagger$ is also a POVM map with Kraus operators C_k^{ij} , where the measurement results k are not used. Let Alice and Bob have n different measurement results for each POVM, where n can be upper bounded by the square of the dimension of the system. For typical distillation protocols on qubits, $n = 2$. Note that all indices for Kraus operators run from 1 to n, and do not start with 0. This choice allows for a shorter notation later on (the index 0 is reserved for indicating that the classical channel is operable). The basic setup is illustrated in Fig. C.2. Alice and Bob have access to classical one-way communication channels labelled $C1$ and $C2$. $C1$ and $C2$ can be used to send information from Alice to Bob and vice versa respectively. Apart from these classical channels, Alice and Bob hold a system subject to a dissipative evolution described by the Lindblad operator $\mathfrak{L}(\rho)$. In the following, this system is referred to as the main system. The first classical channel needs to store all possible measurement outcomes obtained by Alice, whereas the second one needs to store the measurement results obtained by both, Alice and Bob. It is therefore assumed that $C1$ and $C2$ are $n+1$ and $n'+1 = n^2+1$ dimensional systems respectively. Note, that the state $|0\rangle$ will be used to indicate that the channel input or output is "empty", while the states $|1\rangle, \ldots, |n\rangle$ represent n possible measurement results of Alice and the states $|1\rangle, \ldots, |n'\rangle$ encode the n^2 different measurement results obtained by Alice and Bob. The corresponding master equation is given by

$$\dot{\rho} = \gamma \mathfrak{L}(\rho) + \Gamma \mathfrak{C}_{\mathrm{A}\to\mathrm{B}}(\rho) + \Gamma \mathfrak{C}_{\mathrm{A}\leftarrow\mathrm{B}}(\rho),$$

where $\gamma\mathfrak{L}(\rho)$ is a process acting on the main system only. The time scales for classical communication Γ^{-1} are assumed to be sufficiently long such that retardation effects can be

ignored. The four systems used for classical communication are denoted by I_a, I_b, O_a, O_b as shown in Fig. C.2. I and O stand for "Input" and "Output".
As a next step, local Lindblad operators are added, which correspond to the application of a LOCC map depending on the registers of the classical channels. The following three terms are added, one for each step of the protocol outlined above. The first term is given by

$$\delta \sum_{i=1,k=0} \mathfrak{L}^{A_i \otimes |i\rangle\langle k|_{I_a}}(\rho),$$

where A_i acts on Alice's part of the main system and $|i\rangle\langle 0|_{I_a}$ on Alice's side of the first classical system, i.e., the input system of the first classical channel. Note, that the short hand notation $\mathfrak{L}^A(\rho) = \gamma\left(A\rho A^\dagger - \frac{1}{2}\left(\rho A^\dagger A + A^\dagger A\rho\right)\right)$ which was already introduced in the main text is used here. This corresponds to the first step of the realization of the LOCC map. Alice performs a POVM and writes the measurement result onto the input system of the classical channel. As second term, the Lindblad operator

$$\Gamma \sum_{ji=1,xy=0} \mathfrak{L}^{B_j^i \otimes |0\rangle\langle i|_{O_b} \otimes |j,i\rangle\langle x,y|_{I_b}}(\rho)$$

is added, where B_j^i acts on Bob's part of the main system, $|0\rangle\langle i|_{O_b}$ on the output of the first classical channel and $|j,i\rangle\langle x,y|_{I_b}$ on the input of the second channel. Note, that the second channel can store both values i and j at the same time. $|j,i\rangle$ stands for any encoding of i,j in the n^2+1 dimensional state space, where the label zero is reserved for indicating the status of the channel. The summation over x,y starts from zero, i.e., includes the reserved zeros term as well as the n^2 possible measurement results. Bob only carries out a POVM measurement, if he receives the message i via $C1$. Afterwards he writes i,j onto the classical channel. Note that the sum over xy implies that Bob overwrites any previous state of the classical communication system. The last term to be added is given by

$$\Gamma \sum_{jik=1} \mathfrak{L}^{C_k^{ij} \otimes |0\rangle\langle i,j|_{O_a}}(\rho),$$

where C_k^{ij} acts on Alice's quantum system with $T_{ij}(\rho) = \sum_k C_k^{ij} \rho {C_k^{ij}}^\dagger$ and $|0\rangle\langle i,j|_{O_a}$ act on the output of the second classical channel. Alice receives the message ij and reacts by applying T_{ij} to complete the LOCC map. The sum starts from $ij=1$, i.e., Alice acts only if a message has arrived. She does not act if the register is empty ($|0\rangle$). Hence, the total master equation is given by

$$\begin{aligned} \dot{\rho} &= \gamma\mathfrak{L}(\rho) + \Gamma\mathfrak{C}_{\mathrm{A}\to\mathrm{B}} + \Gamma\mathfrak{C}_{\mathrm{A}\leftarrow\mathrm{B}} + \delta \sum_{i=1,k=0} \mathfrak{L}^{A_i \otimes |i\rangle\langle k|_{I_a}}(\rho) \\ &+ \Gamma \sum_{ji=1,xy=0} \mathfrak{L}^{B_j^i \otimes |0\rangle\langle i|_{O_b} \otimes |j,i\rangle\langle xy|_{I_a}}(\rho) + \Gamma \sum_{jik=1} \mathfrak{L}^{C_k^{ij} \otimes |0\rangle\langle i,j|_{O_a}}(\rho). \end{aligned} \tag{C.2}$$

The basic idea can be described as follows. The term in the second line starts the process of realizing $T(\rho)$ at a rate δ (Alice performs the first step). The following steps are performed

with a high rate Γ, such that the state of the quantum system stays approximately constant during the time needed to complete the whole operation. So, practically, the whole LOCC map $T(\rho)$ is applied at once at a rate δ.
In the following, this will be proven rigorously by considering the effective evolution of the main systems after tracing out the classical channels. The reduced state of the main system can be written as

$$\rho_M = \sum_{ijkl} \rho_{ijkl},$$

with $\rho_{ijkl} = \langle i_{I_a} j_{O_b} k_{I_b} l_{O_a} | \rho | i_{I_a} j_{O_b} k_{I_b} l_{O_a} \rangle$, where i, j (k, l) denote the computational bases for $C1$ ($C2$). The indices are arranged such that their order corresponds to the order in the communication cycle. i refers to the input of Alice's side, j to the output on Bob's side, k to the input on Bob's side and l to the output on Alice's side. A system of differential equations for all ρ_{ijkl} can be derived using $\dot{\rho}_{ijkl} = \langle i_{I_a} j_{O_b} k_{I_b} l_{O_a} | \dot{\rho} | i_{I_a} j_{O_b} k_{I_b} l_{O_a} \rangle$ and Eq. (C.2). The desired terms $\rho_{0000}, \rho_{i000}, \rho_{0i00}, \rho_{00(ij)0}, \rho_{000(ij)}$ evolve according to

$$\dot{\rho}_{0000} = \gamma \mathfrak{L}(\rho_{0000}) - \delta \rho_{0000} + \Gamma \sum_{xy=1} T_{ij}(\rho_{000(xy)}), \tag{C.3}$$

$$\dot{\rho}_{i000} = \gamma \mathfrak{L}(\rho_{i000}) - (\Gamma + \delta) \rho_{i000} + \delta \sum_{k=0} A_i \rho_{k000} A_i^\dagger + \Gamma \sum_{xy=1} T_{xy}(\rho_{i00(xy)}), \tag{C.4}$$

$$\dot{\rho}_{0i00} = \gamma \mathfrak{L}(\rho_{0i00}) - (\Gamma + \delta) \rho_{0i00} + \Gamma \sum_{k=0} \rho_{ik00} + \Gamma \sum_{xy=1} T_{xy}(\rho_{0i0(xy)}), \tag{C.5}$$

$$\dot{\rho}_{00(ij)0} = \gamma \mathfrak{L}(\rho_{00(ij)0}) - (\Gamma + \delta) \rho_{00(ij)0} + \Gamma \sum_{xy=0} B_j^i \rho_{0i(xy)0} B_j^{i\dagger} + \Gamma \sum_{xy=0} T_{xy}(\rho_{00(ij)(xy)}), \tag{C.6}$$

$$\dot{\rho}_{000(ij)} = \gamma \mathfrak{L}(\rho_{000(ij)}) - (\Gamma + \delta) \rho_{000(ij)} + \Gamma \sum_{xy=0} \rho_{00(ij)(xy)}. \tag{C.7}$$

All other terms correspond to small errors. In the first step of the proof it is shown that after an initial waiting time, only the states $\rho_{0000}, \rho_{i000}, \rho_{0i00}, \rho_{00(ij)0}, \rho_{000(ij)}$ are significantly populated, while the population of all other states is small. In the next step it is shown that $\rho_M \approx \rho_{0000}$. In the following the short-hand notation $\rho_0 := \rho_{0000}$ is used.

Bounds for occupation probabilities

Below, the probabilities $p_{ijkl} = \mathrm{tr}(\rho_{ijkl})$ are used. A system of differential equations $\dot{p}_{ijkl} = \mathrm{tr}(\dot{\rho}_{ijkl})$ for these probabilities can be derived by from the differential equations for ρ_{ijkl}. Traceless terms such as $\gamma \mathfrak{L}(\rho)$ and T_{ij} do no longer appear.
Moreover, $p_{000X}, \ldots, p_{XXX0}, p_{XXXX}$ are defined as the sum of p_{ijkl}, where all indices marked with X are summed from 1 to n, n', in order to remove the dependence on the Kraus operators by virtue of their normalization condition ($\sum_{i=1}^{n} A_i^\dagger A_i = \mathbb{I}$). A successful application of the LOCC map corresponds to the series $p_{X000}, p_{0X00}, p_{00X0}, p_{000X}, p_{0000}$ (similarly to a X-excitation which created on the first index, travels to the right and disappears in the end). p_{0000} takes high values, while the other probabilities are on the order of $\frac{\delta}{\Gamma}$, which indicates that this process is fast. However, the situation considered here

does not correspond to this ideal case because Alice can start a new round before the last one is finished, which gives rise to probabilities which are denoted by indices with more than one X, e.g. $p_{XX00}, p_{X0X0}, \ldots$ which results in an incorrect realization of the LOCC map. Since the complete solution is not of interest here, but only upper and lower bounds, the system is further simplified by defining the probabilities $p_{0000}, p_{X\Xi\Xi\Xi}, p_{0X\Xi\Xi}, p_{00X\Xi}$ and p_{000X}, which cover all possible events. X indicates that the corresponding index is different from zero. Therefore, the summation runs from 1 to n, n'. Ξ stands for an arbitrary value, i.e., the summation starts from zero. These five quantities include also non-ideal processes, with two or more X entries which correspond an errors and evolve according to

$$\begin{aligned}
\dot{p}_{0000} &= -\delta p_{0000} + \Gamma p_{000X}, \\
\dot{p}_{000X} &= -(\delta+\Gamma) p_{000X} + \Gamma p_{00X\Xi}, \\
\dot{p}_{00X\Xi} &= -(\delta+\Gamma) p_{00X\Xi} + \Gamma p_{0X\Xi\Xi}, \\
\dot{p}_{0X\Xi\Xi} &= -(\delta+\Gamma) p_{0X\Xi\Xi} + \Gamma p_{X\Xi\Xi\Xi}, \\
\dot{p}_{X\Xi\Xi\Xi} &= -\Gamma p_{X\Xi\Xi\Xi} + \delta(p_{0000} + p_{000X} + p_{00X\Xi} + p_{0X\Xi\Xi}).
\end{aligned}$$

The solution shows that the steady state (ss) with

$$p^{\mathrm{ss}}_{0000} = \frac{\Gamma^4}{(\Gamma+\delta)^4},\ p^{\mathrm{ss}}_{000X} = \frac{\delta\Gamma^3}{(\Gamma+\delta)^4},\ p^{\mathrm{ss}}_{00X\Xi} = \frac{\delta\Gamma^2}{(\Gamma+\delta)^3},\ p^{\mathrm{ss}}_{0X\Xi\Xi} = \frac{\delta\Gamma}{(\Gamma+\delta)^2},\ p^{\mathrm{ss}}_{X\Xi\Xi\Xi} = \frac{\delta}{(\Gamma+\delta)} \quad \text{(C.8)}$$

is reached[3] up to an error smaller than $\mathcal{O}(\alpha^2)$ after a time of the order of $\frac{1}{\delta}$. In the steady state, $p^{\mathrm{ss}}_{0000} = 1 - 4\frac{\delta}{\Gamma} + \mathcal{O}(\frac{\delta^2}{\Gamma^2})$. Next, bounds for $p_{X000}, p_{0X00}, p_{00X0}, p_{000X}$ are derived. According to Eq. (C.4), $\dot{p}_{X000} = -\Gamma p_{X000} + \delta p_{0000} + \Gamma p_{X00X}$. Assuming that p^{ss}_{0000} is reached after a time t',

$$\begin{aligned}
p_{X000}(t) &= e^{-\Gamma(t-t')} p_{X000}(t') + \int_{t'}^{t} d\tau e^{\Gamma(\tau-t)} \left(\frac{\delta\Gamma^4}{(\Gamma+\delta)^4} + \Gamma p_{X00X} \right), \\
&= e^{-\Gamma(t-t')} p_{X000}(t') + (1 - e^{-\Gamma(t-t')}) \frac{\delta\Gamma^3}{(\Gamma+\delta)^4} + h(t,t'),
\end{aligned}$$

where $h(t,t') \geq 0$ is a positive function since $p_{X00X} \geq 0$. Hence, doubling the initial waiting time guarantees $p_{X000} \geq \frac{\delta\Gamma^3}{(\Gamma+\delta)^4}$. According to Eq. (C.5), $\dot{p}_{0X00} = -(\Gamma+\delta) p_{0X00} + \Gamma p_{X000} + \Gamma p_{XX00} + \Gamma p_{0X0X}$. By integration, using the bound for p_{X000} and assuming that the contributions from p_{0X0X} and p_{XX00} sum up to a positive function it can be concluded that $\frac{\delta\Gamma^4}{(\Gamma+\delta)^5} \leq p_{0X00}$ is fulfilled after waiting for another period on the order of $\frac{1}{\delta}$. Similarly, one obtains $\frac{\delta\Gamma^5}{(\Gamma+\delta)^6} \leq p_{00X0}$ and $\frac{\delta\Gamma^6}{(\Gamma+\delta)^7} \leq p_{000X}$. Since $p_{0000} + p_{X000} + p_{0X00} + p_{00X0} + p_{000X} \geq 1 - \frac{12\delta^2}{\Gamma^2}$, any probability with more than two X entries is smaller than $\frac{12\delta^2}{\Gamma^2}$. In summary,

$$\frac{\delta}{\Gamma} - 7\frac{\delta^2}{\Gamma^2} \leq p_{X000}, p_{0X00}, p_{00X0}, p_{000X} \leq \frac{\delta}{\Gamma},$$

after a time of the order $\frac{1}{\delta}$, where the upper bounds are found using Eq. (C.8). Hence, a steady state is reached where states labelled with one (more than one) X are occupied with probability $O(\alpha)$ ($O(\alpha^2)$).

[3] The slowest term converges as $\mathcal{O}\left(\frac{t^3\delta\Gamma^3}{(\Gamma+\delta)} e^{-t(\Gamma+\delta)}\right)$. After an initial waiting time of the order of $\frac{1}{\delta}$ the steady state is reached up to an error of the order $\mathcal{O}\left(\alpha^{-2} e^{-\alpha^{-1}}\right)$.

Differential equation for ρ_0

The evolution of $\rho_0 \equiv \rho_{0000}$ is governed by Eq. (C.3). After a period of the order $\frac{1}{\delta}$, $\dot{\rho}_0 = \gamma' \mathcal{O}(1+\alpha)$, since $\|\rho_{000X}\| = \frac{\delta}{\Gamma} + \mathcal{O}(\alpha^2)$. Hence, for $\alpha \ll 1$, ρ_0 is approximately constant on time scales that are short compared to γ' . In order to obtain an equation which depends only on ρ_0, the differential equations for $\rho_{i000}, \rho_{0i00}, \rho_{00(ij)0}$ and $\rho_{000(ij)}$ are successively solved. According to Eq. (C.4),

$$\dot{\rho}_{i000} = -\Gamma \rho_{i000} + \delta A_i \rho_0 A_i^\dagger + \mathfrak{N},$$

where $\mathfrak{N} = \gamma \mathfrak{L}(\rho_{i000}) - \delta \rho_{i000} + \delta \sum_k A_i \rho_{k000} A_i^\dagger + \Gamma \sum_{xy=1} T_{xy}(\rho_{i00(xy)})$, which is bounded by $\gamma' \mathcal{O}(\alpha)$. For the first three terms $p_{X000} = \mathcal{O}(\alpha)$ is used. The last term can be bounded by $p_{X00X} = \mathcal{O}(\alpha^2)$, such that

$$\rho_{i000}(t) = \rho_{i000}(0) e^{-\Gamma t} + \int_0^t d\tau e^{\Gamma(\tau - t)} \left(\delta A_i \rho_0 A_i^\dagger + \mathfrak{N} \right).$$

The integral $\int_0^t d\tau e^{\Gamma(\tau-t)} \mathfrak{N}$ can be bounded by $\mathcal{O}(\alpha^2)$. The initial term is suppressed by $e^{-\Gamma t}$ and therefore smaller than $\mathcal{O}(\alpha^2)$ after the initial waiting time. Hence,

$$\rho_{i000}(t) \;=\; \mathcal{O}(\alpha^2) + \delta \int_0^t d\tau e^{\Gamma(\tau-t)} A_i \rho_0 A_i^\dagger. \tag{C.9}$$

Since the integral is mainly determined by terms close to $\tau = t$ and ρ_0 varies little on small time intervals, ρ_0 can be assumed to be constant. To prove this, the integral

$$\int_0^t X(\tau, t) d\tau = \int_0^{t'} X(\tau, t) d\tau + \int_{t'}^t X(\tau, t) d\tau \tag{C.10}$$

is considered, where $X(\tau, t) = e^{\Gamma(\tau - t)} A_i \rho_0 A_i^\dagger$ and $t' = t - \frac{1}{\sqrt{\Gamma \gamma'}} = t - \frac{1}{\gamma'} \sqrt{\alpha}$. Since $\frac{1}{\gamma'}$ is the typical time during which ρ_0 changes, it is nearly constant during the interval (t, t'). Since $\dot{\rho}_0 = \mathcal{O}(\gamma'(1+\alpha))$,

$$\rho_0(t'') = \rho_0(t) + \int_t^{t''} d\tau \dot{\rho}_0(\tau) = \rho_0(t) + \mathcal{O}(\sqrt{\alpha}) \tag{C.11}$$

for any $t'' \in [t', t]$. The integral from 0 to t' in Eq. (C.10) is suppressed at least by a factor $e^{-\sqrt{\frac{1}{\alpha}}} < \alpha$ ($A_i \rho_0 A_i^\dagger$ is on the order of one). Inserting Eq. (C.11) in Eq. (C.9) and using $\delta \int_{t'}^t d\tau e^{\Gamma(\tau - t)} = \frac{\delta}{\Gamma}(1 - e^{-\sqrt{\alpha^{-1}}})$ with $e^{-\sqrt{\alpha^{-1}}} < \alpha$ yields

$$\rho_{i000}(t) \;=\; \frac{\delta}{\Gamma} A_i \rho_0(t) A_i^\dagger + \frac{\delta}{\Gamma} \mathcal{O}(\sqrt{\alpha}), \tag{C.12}$$

which shows that for small α, Alice applies her first POVM with high accuracy.
Next, the evolution of ρ_{0i00} is considered (see Eq. (C.5)),

$$\dot{\rho}_{0i00} = -\Gamma \rho_{0i00} + \Gamma \rho_{i000} + \mathfrak{N}, \tag{C.13}$$

where $\mathfrak{N}$ can be bounded by $\gamma'\mathcal{O}(\alpha)$ using $p_{0X00} = \mathcal{O}(\alpha)$, $p_{XX00} = \mathcal{O}(\alpha^2)$ and $p_{0X0X} = \mathcal{O}(\alpha^2)$. Inserting Eq. (C.12) yields $\rho_{0i00}(t) = \rho_{0i00}(0)e^{-\Gamma t} + \int_0^t d\tau e^{\Gamma(\tau-t)}\left(\delta A_i\rho_0(\tau)A_i^\dagger + \delta\mathcal{O}(\sqrt{\alpha}) + \mathfrak{N}\right)$. As before, the integral over $\mathfrak{N}$ and the first term can be bounded by $\mathcal{O}(\alpha^2)$ after a waiting time. If the remaining integral is split as in Eq. (C.10), one obtains one part, where ρ_0 is nearly constant and one vanishing part. The main error is again due to expression (C.11), leading to

$$\rho_{0i00}(t) = \frac{\delta}{\Gamma}A_i\rho_0(t)A_i^\dagger + \frac{\delta}{\Gamma}\mathcal{O}(\sqrt{\alpha}). \tag{C.14}$$

Hence, for small α, sending classical information to Bob causes only marginal errors on the main system.
Next, the evolution of $\rho_{00(ij)00}$ is considered (Eq. (C.6)),

$$\dot{\rho}_{00(ij)0} = -\Gamma\rho_{00(ij)0} + \Gamma B_j^i\rho_{0i00}B_j^{i\dagger} + \mathfrak{N},$$

where $\mathfrak{N}$ can be bounded by $\gamma' O(\alpha)$ such that

$$\rho_{00(ij)0}(t) = \frac{\delta}{\Gamma}B_j^iA_i\rho_0(t)A_i^\dagger B_j^{i\dagger} + \frac{\delta}{\Gamma}\mathcal{O}(\sqrt{\alpha}),$$

which corresponds to a process, where Bob applies his part of the POVM and writes i, j onto his classical input register. Similarly, Eq. (C.7) leads to

$$\rho_{000(ij)}(t) = \frac{\delta}{\Gamma}B_j^iA_i\rho_0(t)A_i^\dagger B_j^{i\dagger} + \frac{\delta}{\Gamma}\mathcal{O}(\sqrt{\alpha}),$$

which corresponds to a transfer of the classical measurement results i, j back onto Alice's side. Finally, these results can be applied for calculating ρ_0,

$$\dot{\rho}_0 = \gamma\mathfrak{L}(\rho_0) - \delta\rho_0 + \Gamma\sum_{ij}T_{ij}(\rho_{000(ij)}) = \gamma\mathfrak{L}(\rho_0) - \delta\left(T'(\rho_0) - \rho_0\right).$$

The operation $T'(\rho) \equiv T(\rho_0) + \mathcal{O}(\sqrt{\alpha})$ represents a noisy version of the desired LOCC map $T(\rho)$. The undesired contribution can be suppressed by choosing the parameter α small, that is, by choosing Γ large enough. The rate Γ is only limited by the speed of light. If the time evolution resulting from the local error rates and the dissipative process is fast compared to time it takes to transfer classical communication from Alice to Bob, additional errors have to be taken into account. In this case the parameter $\gamma' = \gamma + \delta$ could be choosen to be small in order to obtain a small value of α, but this would require more sophisticated methods for protection against noise.
In principle, the time evolution of $\rho_M = \sum\rho_{ijkl}$ would be of interest. But since this state is (up to an error of $\mathcal{O}(\alpha)$) close to ρ_0, it's evolution is dominated by this contribution and other terms can be ignored. More formally, one could calculate $\dot{\rho}_M = \sum\dot{\rho}_{ijkl}$ by calculating the remaining terms $\dot{\rho}_{ijkl}$, but all remaining terms are on the order of $\mathcal{O}(\alpha)$ and therefore negligible.

The generalization to more than one round of communication is straight forward. By summing over the indices of the corresponding Kraus-operators, one obtains equations for the probabilities, which are independent of the POVMs applied in the protocol. From these equations it can be concluded that only the relevant state responsible for the application of the LOCC is populated, while all others are suppressed by a factor of order α^2 after an initial waiting time. By successive integration as shown above, the desired approximation for $\dot{\rho}$ is obtained.
For an increasing number of communication rounds, the errors add up, such that the requirements on the parameter α become more severe. At some point, the speed of light becomes a limiting factor and restricts this method to a regime with small noise terms and retardation effects have to be included. However, many distillation protocols only require a small amount of rounds to reach high fidelities and sometimes even one-way communication (half a round) is sufficient [179, 183].
After the initial waiting time, the term $\delta(T'(\rho) - \rho)$ is bounded by $\delta\mathcal{O}(1)$, such that another term of the same form can be added. This way several terms of this type can be included which gives rise to the master equation $\sum_k \delta(T'_k(\rho) - \rho)$.

C.3 Stabilization of dissipative distillation schemes against errors acting on the target system

In this section, it is shown how the distillation schemes presented in Sec. C.1.2 and Sec. C.4 can be made robust against noise acting on the target system. The same method for stabilization against errors is applicable for both protocols and a wide range of other dissipative schemes, which include classical communication. The basic idea is illustrated in Fig. 3.10a. A dissipative protocol is run using m blocks of source systems in parallel, which are all coupled individually to the same target system. This way, a boost effect on the desired dynamics of the target system can be achieved, while the back-action on the source pairs remains unchanged. If sufficiently many source systems are provided, the dynamics on the target system is dominated completely by the desired dynamics. First, the application of this method is explained for schemes of the type described in Sec. C.4 and Sec. C.5. Then the stabilization of scheme I is discussed.
To start with, a target system $\mathcal{T}$ and a source block consisting of n pairs are considered. An entangling dissipative process described by the Lindblad operator $\delta\mathfrak{L}(\rho)$ acts on each source pair separately such that each of them is individually driven into an entangled steady state ρ_s. The effective master equation for the target system, which is obtained by tracing out the source system, is given by

$$\dot{\rho}_{\mathcal{T}} = \delta\mathfrak{L}_S(\rho_{\mathcal{T}}),$$

where the Lindblad operator $\mathfrak{L}_S(\rho_{\mathcal{T}})$ may be time dependent. It does not depend on the state of $\mathcal{T}$ but only on the state of the source system as indicated by the subscript S. Accordingly, the convergence speed at which $\mathfrak{L}_S(\rho_{\mathcal{T}})$ converges to a constant operator is given by the rate at which the source system reaches a steady state. The convergence rate of the source system is limited by the rate δ at which the flip operation mapping the quantum states of the source system to $\mathcal{T}$ is performed (see Sec. C.1 and Sec. C.4).

It is assumed that m identical source systems $S_1, \ldots, S_m$ are individually coupled to a single source system $\mathcal{T}$ through the Lindblad operator $\delta \sum_{i=1}^{m} \mathfrak{L}(\rho_{\mathcal{T},S_i})$, where $\mathfrak{L}(\rho_{T,S_i})$ is a Lindblad operator acting on $\mathcal{T}$ and the ith source system (see Fig. 3.10a for a schematic overview). These operators are assumed to be identical $\mathfrak{L}_{S_i} = \mathfrak{L}_S$, such that the dynamics of the target system is governed by the reduced master equation

$$\dot{\rho}_{\mathcal{T}} = \delta \sum_i \mathfrak{L}_{S_i}(\rho_{\mathcal{T}}) = m\delta \mathfrak{L}_S(\rho_{\mathcal{T}}).$$

This is not generally the case, since the m source systems are coupled to each other through the target system. Due to this indirect coupling, the source systems may evolve differently in time and can reach different steady states, which can be disadvantageous for the evolution of the target system. This is for example the case for the scheme described in Sec. C.1.1 which does not include classical communication.
It can be shown that $\mathfrak{L}_{S_i}(\rho_{\mathcal{T}}) = \mathfrak{L}_S(\rho_{\mathcal{T}})$, if there is no state dependent back-action of $\mathcal{T}$ on the source systems. In this case, the evolution of the reduced density matrix of each source block is independent from the time evolution of the other blocks. This property can be guaranteed by re-initializing the source systems after each swap operation in a standard state, for example the identity (strict equality requires in principle also that all source systems start from the same initial state. However, different initial states have only an effect on the time evolution in the beginning. The following discussions are only concerned with the steady state of the system, which is independent of the initial conditions). Scheme I including classical communication (see Sec. C.1.2) exhibits a weak state dependent back-action. As explained in the end of Sec. C.1.2, this can be avoided by applying a twirl [181, 182] on the target system prior to each flip operation. Hence, the stabilization method outlined above is directly applicable to this modified version of the scheme[4].
By boosting the desired dynamics on the target system, arbitrary high error rates ϵ can be tolerated. For $m\delta \gg \varepsilon$, the dynamics governed by the master equation

$$\dot{\rho}_T = m\delta \mathfrak{L}_s(\rho_T) + \varepsilon \mathfrak{L}_{\text{noise}}(\rho_T)$$

is dominated by the first term and the steady state is arbitrarily close to the original steady state. In the specific case, where the process $\mathfrak{L}_s(\rho_{\mathcal{T}}) = \text{tr}(\rho_{\mathcal{T}})\rho_{\mathcal{T},s} - \rho$ driving the target system into the steady state $\rho_{\mathcal{T},s}$ is counteracted by depolarizing noise ($\text{tr}(\rho_{\mathcal{T}})\mathbb{I} - \rho_{\mathcal{T}}$), the time evolution described by

$$\dot{\rho}_{\mathcal{T}} = m\delta(\text{tr}(\rho_{\mathcal{T}})\rho_{\mathcal{T},s} - \rho) + \varepsilon(\text{tr}(\rho_{\mathcal{T}})\mathbb{I} - \rho_{\mathcal{T}})$$

leads to the steady state $\rho'_{\mathcal{T},s} = \frac{m\delta\rho_{\mathcal{T},s} + \varepsilon\mathbb{I}}{m\delta + \varepsilon}$, which can be easily verified by solving the equation $\dot{\rho}_{\mathcal{T}} = 0$. This state is reached exponentially fast with a rate $m\delta + \varepsilon$. The same result holds for local depolarizing noise acting on Alice's and Bob's system (see Sec. C.4.1) if the steady state $\rho_{\mathcal{T},s}$ is a Werner state. A master equation of this type is solved exactly in the next section.

[4] It can be shown that this back-action has only a small effect on the steady state of the source system, and that this effect does not accumulate if many source systems are coupled to $\mathcal{T}$. The strict avoidance of a state depended back-action is enforced only for the sake of clarity.

C.4 Scheme II: dissipative entanglement distillation for Werner states

In this section, a second dissipative distillation scheme is introduced, which does not rely on entangling processes producing steady states, which are close to pure states, as scheme I presented in Sec. C.1. Here, a very general model for Werner states [181, 182] is analyzed, which can be solved exactly. Werner states are of the simple form $\rho_{\mathrm{W}}(f) = f\Omega+(1-f)(\mathbb{I}-\Omega)/3$, and are characterized in terms of their fidelity f, which is given by the overlap with the maximally entangled state Ω. Any quantum state can be transformed into a Werner state by twirling [181, 182] without a loss of fidelity. Since a Werner-twirl is a LOCC map, a dissipative protocol can be constructed, which corresponds to the continuous application of a twirl operation on a given system and mapping of the resulting state to a new pair acting as target system $\mathcal{T}$ by means of a continuous flip procedure (compare Sec. C.4.2).
This way, any dissipative process can be modified such that it can be described in terms of a Werner Lindblad operator $E_f(\rho_{\mathcal{T}})$ as used in above and Sec. C.5, where f is the steady state fidelity of the underlying process. In this sense, the Werner model used here is very general and can be applied in many situations.

C.4.1 Dissipative entangling model process for a single source pair

A dissipative model process, which produces an arbitrary Werner state as steady state can be modelled by considering two processes, which generate the steady states Ω and $\mathbb{1}$ respectively, where $\mathbb{1} = \mathbb{I}/4$ denotes the normalized identity. Let $|\psi_i\rangle$ denote the four Bell-states, where $|\psi_0\rangle = (|00\rangle + |11\rangle)/\sqrt{2}$, and σ_i the Pauli matrices, where σ_0 is the identity. A master equation which leads to the steady state $\Omega = |\Psi_0\rangle\langle\Psi_0|$ can be constructed using the four jump operators $Q_i = |\psi_0\rangle\langle\psi_i|$, which give rise to the Lindlbad term

$$Q(\rho) = \sum_i \mathfrak{L}^{Q_i}(\rho) = \mathrm{tr}(\rho)\Omega - \rho.$$

Similarly, a master equation which leads to the steady state $\mathbb{1}$ is obtained using the jump operators $W_{ij} = \sigma_i \otimes \sigma_j$, which give rise to the Lindblad term

$$W(\rho) = \sum_{ij} \mathfrak{L}^{W_{ij}}(\rho) = \mathrm{tr}(\rho)\mathbb{1} - \rho.$$

Hence, the Werner state $\rho_W(f)$ with fidelity f is the steady state of the time evolution governed by the master equation

$$E_f(\rho) = fQ(\rho) + \frac{1-f}{3}(3W(\rho) - Q(\rho)) = \mathrm{tr}(\rho)\rho_W - \rho.$$

The Lindblad term $E_f(\rho)$ will be used in the following to model the basic entangling process acting on the source systems.

Local depolarizing noise acting on Alice's (Bob's) side is included using the jump operators $S_i = \mathbb{I}_A \otimes \sigma_i$ ($S_i = \sigma_i \otimes \mathbb{I}_B$), such that the corresponding Lindblad terms are given by

$$\begin{aligned} N_{\text{Alice}}(\rho) &= \sum_i \mathfrak{L}^{S_i}_{\text{Alice}} = \rho_{\text{A}} \otimes \mathbb{1}_B - \rho, \\ N_{\text{Bob}}(\rho) &= \sum_i \mathfrak{L}^{S_i}_{\text{Bob}} = \mathbb{1}_A \otimes \rho_{\text{B}} - \rho, \end{aligned}$$

where ρ_{A} (ρ_{B}) is the reduced density matrix corresponding to Alice's (Bob's) system and $\mathbb{1}_A$ ($\mathbb{1}_B$) the normalized identity $\mathbb{I}/2$ on Alice's (Bob's) system. This process describes the continuous replacement of the state on Alice's (Bob's) side by the completely mixed state. The total master equation

$$\dot{\rho} = \gamma E_f(\rho) + \frac{\varepsilon}{2} N(\rho), \tag{C.15}$$

where $N(\rho) = N_{\text{Alice}}(\rho) + N_{\text{Bob}}(\rho)$, describes the basic entangling process including local noise. This type of equation will be used frequently in the following sections, as it also describes also the evolution of the target systems once the corresponding source systems have reached the steady state.

The steady state of the time evolution described by Eq. (C.15) is a Werner state

$$\rho_s = \frac{\gamma \rho_{\text{W}}(f) + \varepsilon \mathbb{1}}{\gamma + \varepsilon} \tag{C.16}$$

with reduced fidelity $f_s = \frac{\gamma f + \varepsilon \frac{1}{4}}{\gamma + \varepsilon}$. The general time dependent solution of the master equation (C.15) is of the form

$$\rho(t) = \rho_0 g_0(t) + \rho_1 g_1(t) + \rho_2 g_2(t) + \rho_3 g_3(t), \tag{C.17}$$

where ρ_0 is any initial state, $\rho_1 = \frac{1}{2}(\rho_{0,\text{A}} \otimes \mathbb{1}_B + \mathbb{1}_A \otimes \rho_{0,\text{B}})$, $\rho_2 = \rho_{\text{W}}(f)$ and $\rho_3 = \mathbb{1} = \mathbb{1}_A \otimes \mathbb{1}_B$. $\rho_{0,\text{A}}$ and $\rho_{0,\text{B}}$ are the reduced density matrices of the initial state ρ_0 at Alices and Bobs side. The functions g_i are given by

$$\begin{aligned} g_0(t) &= e^{-\gamma' t}, \\ g_1(t) &= 2\left(e^{-\gamma'' t} - e^{-\gamma' t}\right), \\ g_2(t) &= \frac{\gamma}{\gamma'}(1 - e^{-\gamma' t}), \\ g_3(t) &= \frac{2\gamma}{\gamma'}\left(e^{-\gamma' t} - e^{\gamma'' t}\right) + \frac{\varepsilon}{\gamma'}(e^{\gamma' t} - 2e^{\gamma'' t} + 1), \end{aligned} \tag{C.18}$$

where $\gamma' = \gamma + \varepsilon$ and $\gamma'' = \gamma + \varepsilon/2$. Note, that the terms which depend on the initial state of the system, i.e. ρ_0 and ρ_1, are suppressed exponentially fast. The system reaches the steady state given by Eq. (C.16) exponentially fast with a rate of at least $\gamma + \frac{\varepsilon}{2}$.

In order to verify that Eqs. (C.17) and (C.18) are a solution of Eq. (C.15), Eq. (C.17) can be used as ansatz. The master equation gives rise to a set of differential equations for the functions g_i with initial conditions $g_0 = 1$ and $g_i = 0$,

$$\begin{aligned} \dot{g}_0 &= -(\gamma+\varepsilon)g_0, \\ \dot{g}_1 &= -(\gamma+\frac{\varepsilon}{2})g_1 + \varepsilon g_0, \\ \dot{g}_2 &= -\varepsilon f_2 + \gamma(g_0+g_1+g_2+g_3), \\ \dot{g}_3 &= -\gamma g_3 + \frac{\varepsilon}{2}g_1 + \varepsilon g_2. \end{aligned} \tag{C.19}$$

Below, the initial condition $\rho_0 = \mathbb{1}$ will be considered frequently. In this case the solution simplifies to

$$\rho(t) = \rho_s + (\mathbb{1} - \rho_s)e^{-(\gamma+\varepsilon)t}. \tag{C.20}$$

C.4.2 Steady state entanglement distillation acting on n source systems

In the following, n systems which are subject to the basic entangling process $\gamma E_f(\rho) + \frac{\varepsilon}{2}N(\rho)$ and are driven into the steady state ρ_s as described in Sec. C.4.1 are considered. These qubit pairs act as source systems for a LOCC distillation operation T_D, which distills one potentially higher entangled state from these copies. The resulting quantum state is mapped to a target pair $\mathcal{T}$ and each source system is re-initialized in the state $\mathbb{1}$. T_D is not specified at this point - the solution derived in this section holds for any n to 1 distillation protocol. To start with, deterministic protocols are considered. These results are generalized at the end of this section such that probabilistic schemes are also covered. Note that the complete re-initialization of the source systems represents the worst-case situation regarding the back-action of the target system onto the source pairs. This choice allows one to solve the model exactly and to provide a lower bound for dissipative distillation schemes of this type.

The continuous distillation procedure explained above is described by the master equation

$$\dot{\rho} = \sum_{i=1}^{n} \Big(\gamma E_f(\rho) + \frac{\varepsilon}{2}N(\rho)\Big)_i + \delta_D(T_D(\rho) - \rho), \tag{C.21}$$

where $(X(\rho))_i$ stands for the dissipative process $X(\rho)$ acting on the ith source system. In the following, the time evolution and the steady state of the target system are determined. The reduced master equation for $\mathcal{T}$ depends on the steady state of the reduced source system. Therefore, the dynamics on the source system is solved first. Since the back-action of $\mathcal{T}$ on the source system does not depend on the quantum state of $\mathcal{T}$, the time evolution of the source pairs can be considered independently from the target system. For clarity, the reduced states of source and target system are denoted by σ and $\rho_{\mathcal{T}}$ respectively in this section. The reduced master equation for the n source systems is given

by

$$\dot{\sigma} = \sum_{i=1}^{n} \left(\gamma E_f(\sigma) + \frac{\varepsilon}{2} N(\sigma) \right)_i + \delta_D (\mathrm{tr}(\sigma)\, \mathbb{1}^{\otimes n} - \sigma). \tag{C.22}$$

The solution of the homogeneous master equation which describes the entangling dynamics for n independent source systems

$$\dot{\sigma}_* (\sigma_0, t) = \sum_{i=1}^{n} \left(\gamma E_f(\sigma_*(\sigma_0, t)) + \varepsilon N(\sigma_*(\sigma_0, t)) \right)_i ,$$

is already known (see Sec. C.4.1) if the initial state is a product state. $\sigma_*(\sigma_0, t)$ denotes the solution of the homogeneous master equation with initial condition $\sigma_*(\sigma_0, t = 0) = \sigma_0$. The solution of the inhomogeneous master equation Eq. (C.22) is given by

$$\begin{aligned} \sigma(t) &= \sigma_*(\sigma_0, t) e^{-\delta_D t} + \delta_D \int_0^t d\tau \sigma_*(\mathbb{1}^{\otimes n}, t-\tau) e^{-\delta_D (t-\tau)}, \\ &= \sigma_*(\sigma_0, t) e^{-\delta_D t} + \delta_D \int_0^t d\tau \sigma_*(\mathbb{1}^{\otimes n}, \tau) e^{-\tau \delta_D}, \end{aligned}$$

with arbitrary initial condition $\sigma(0) = \sigma_0$. This solution can be easily verified by considering the time derivative

$$\dot{\sigma}(t) = -\delta_D \sigma(t) + e^{-\delta_D t} \dot{\sigma}_*(\sigma_0, t) + e^{-\delta_D t} \partial_t \left[\delta_D \int_0^t d\tau \sigma_*(\mathbb{1}^{\otimes n}, t-\tau) e^{\tau \delta_D} \right].$$

Using $\partial_t \int_0^t g(\tau) f(t-\tau) = f(0) g(t) + \int_0^t g(\tau) \dot{f}(t-\tau)$ and $\sigma_*(\mathbb{1}^{\otimes n}, 0) = \mathbb{1}^{\otimes n}$, one obtains

$$\dot{\sigma}(t) = -\delta_D \sigma(t) + e^{-\delta_D t} \dot{\sigma}_*(\sigma_0, t) + \delta_D \mathbb{1}^{\otimes n} + e^{-\delta_D t} \partial_t \left[\delta_D \int_0^t d\tau \dot{\sigma}_*(\mathbb{1}^{\otimes n}, t-\tau) e^{\tau \delta_D} \right],$$

which yields Eq. (C.22). The steady state

$$\sigma_s = \delta_D \int_0^\infty d\tau \sigma_*(\mathbb{1}^{\otimes n}, \tau) e^{-\delta_D \tau} \tag{C.23}$$

is reached exponentially fast with a rate of at least δ_D. The homogeneous solution $\sigma_*(\mathbb{1}^{\otimes n}, \tau)$ is given by the tensor product of the solution for a single source pair (C.20),

$$\sigma_*(\mathbb{1}^{\otimes n}, t) = (\rho_s + (\mathbb{1} - \rho_s) e^{-(\gamma+\varepsilon)t})^{\otimes n},$$

such that Eq. (C.23) can be further simplified

$$\sigma_s = \int_0^1 dx (\rho_s + (\mathbb{1} - \rho_s) x^{\frac{\gamma+\varepsilon}{\delta_D}})^{\otimes n}. \tag{C.24}$$

Next, the dynamics of the target system $\mathcal{T}$ is considered. It is described by the time dependent master equation

$$\dot{\rho}_{\mathcal{T}} = \delta_D \left(T_D(\sigma(t)) - \rho_{\mathcal{T}} \right),$$

which is solved by

$$\rho_T(t) = \rho_T(0)e^{-\delta_D t} + \int_0^t d\tau \delta_D T_D(\sigma(t))e^{-\delta_D(t-\tau)}$$

with steady state $T_D(\sigma_s)$. The corresponding steady state fidelity can be inferred by integrating over the fidelities that are obtained if a standard distillation protocol is applied such that

$$f_{\text{out}}(f_s) \equiv f_{\text{out}}(f,\varepsilon) = \int_0^1 dx f_D(f_s + (\frac{1}{4} - f_s)x^{\frac{\gamma+\varepsilon}{\delta_D}})^{\otimes n},$$

where Eq. (C.24) was used.
So far, it has been assumed, that the underlying distillation protocol T_D is deterministic, such that a distilled state is available whenever it is applied. However, many distillation protocols of interest are probabilistic, i.e., they only succeed some probability $P(\rho)$. If a probabilistic distillation protocol is used, the corresponding map T_D is defined in such a way, that a flip operation is only performed when the distillation was successful, which leads to a state dependent rate in the master equation

$$\dot{\rho}_T = \delta_D P(\sigma(t)) \left(T_D(\sigma(t)) - \rho_T\right).$$

Accordingly, the target system is driven into the same steady state as discussed above with a reduced rate. Once the time evolution of the source system has reached a steady state, the dynamics of the target system is determined by the master equation

$$\dot{\rho}_T = \delta_D P(\sigma_s) \left(\text{tr}(\rho_T)\rho_s' - \rho_T\right) = \delta_D p E_{f_{\text{out}}}(\rho_T),$$

where ρ_s' is the distilled steady state of the source system. Since ρ_s' is a Werner state, the target system can act as one of n new source systems which drive a new target system into an even more entangled state. This way, the distillation protocol can be iterated in a nested form.

C.5 Continuous quantum repeaters

The ability to distribute entangled states of high quality over long distances is of vital importance for quantum communication and quantum network related applications in general. As opposed to classical information, quantum information cannot be cloned. Therefore, classical repeater schemes are not applicable in this context and quantum repeater schemes which respect the coherence of quantum states are required [66,67,155]. In quantum repeater protocols, entanglement is first distributed over short distances L_0 with high accuracy. Then neighboring pairs are connected by a teleportation procedure [189] (entanglement swapping [251, 399]) such that entangled links which span a distance $2L_0$ are obtained. In the next step, two neighboring links of length $2L_0$ are connected by entanglement swapping, resulting in entangled pairs which span a distance $4L_0$. This way, an entangled link of length $L = L_0 2^k$ can be established in k iteration steps (compare Fig. 3.11 in the main text). However, for non-maximally entangled states, entanglement

swapping leads to a considerable degradation in the fidelity of the resulting quantum state. Since the distributed entanglement decreases dramatically every time the length of the entangling links is doubled, it can not be distributed over large distances this way. Therefore an entanglement distillation protocol has to be applied after every entanglement swapping procedure before proceeding to the next stage.
In the following, a continuous dissipative quantum repeater scheme is described, which combines continuous swap and distillation processes in order to generate long-range entangled steady states, while entangling dissipative processes are only required over short distances. To this end, a continuous swap operation is introduced in Sec. C.5.1. In Sec. C.5.2 it is explained how this method can be combined with the distillation scheme presented above (Sec. C.4) such that a high-quality entangled link can be established over a large distance as steady state of a continuous dissipative evolution. A specific example concludes this proof-of-principle study.

C.5.1 Continuous entanglement swapping

The basic setup for entanglement swapping consists of three nodes aligned on a line, operated by Alice, Bob and Charlie, where Alice and Bob as well as Bob and Charlie share an entangled pair, while the distance between Alice and Charlie is too large for generating an entangled state of high quality (see Fig. 3b in the main text). By performing a teleportation procedure, which requires the measurement of the two qubits at Bob's node and classical communication to Alice and Charlie, as well as local operations on their sides, an entangled link can be established between Alice and Charlie [251].
In the setting considered here, Alice and Bob as well as Bob and Charlie each hold a source pair which is subject to the basic dissipative entangling mechanism considered in Sec. C.4, such both pairs are individually driven into the steady state ρ_s. This dynamics is described by the Lindblad term $\gamma_{\mathrm{sw}} \sum_{i=1}^{2} \left(E_f(\rho)\right)_i = \gamma_{\mathrm{sw}} \sum_{i=1}^{2} (\mathrm{tr}(\rho)\rho_W - \rho)_i$. As illustrated in Fig. 3.10b in the main text, the source pairs are coupled to a pair of target qubits shared between Alice and Charlie through the term $\delta_{\mathrm{sw}} \left(T_{\mathrm{sw}}(\rho) - \rho\right)$, where the completely positive map T_{sw} corresponds to a flip operation which maps the state resulting from the entanglement swapping procedure to a target system and re-initializes the source systems in the state[5] $\mathbb{1} \otimes \mathbb{1}$. Hence, the total master equation is given by

$$\dot{\rho} = \gamma_{\mathrm{sw}} \sum_{i=1}^{2} \left(E_f(\rho) + \frac{\varepsilon}{2} N(\rho) \right)_i + \delta_{\mathrm{sw}} \left(T_{\mathrm{sw}}(\rho) - \rho \right)$$

and the reduction to the source systems σ yields

$$\dot{\sigma} = \gamma_{\mathrm{sw}} \sum_{i=1}^{2} \left(E_f(\rho) + \frac{\varepsilon}{2} N(\rho) \right)_i + \delta_{\mathrm{sw}} \left(\mathrm{tr}(\sigma) \mathbb{1} \otimes \mathbb{1} - \sigma \right).$$

[5] The channel $T_{\mathrm{sw}}(\rho)$ corresponds to a three-partite LOCC map. The results in Sec. C.4 hold for bi-partite LOCC terms of the form $T(\rho) - \rho$ and can easily be extended to multi-partite operations. The continuous realization of the swap scheme is already covered by the derivation for bi-partite LOCC operations presented above, since this protocol can be considered as an effective bi-partite scheme in which Alice and Charlie are treated as one party. Here, a classical one-way channel is used to send two copies of a message at the same time. One copy is sent to Alice and the other one is sent to Charlie.

The solution of this differential equation (compare Sec. C.4.2)

$$\sigma(t)=\sigma_*(\sigma_0,t)e^{-\delta_{\rm sw}t}+\delta_{\rm sw}\int_0^t d\tau\sigma_*(\mathbb{1}^{\otimes 2},t-\tau)e^{-\delta_{\rm sw}(t-\tau)},$$

where $\sigma_*(\sigma_0,t)$ is the homogeneous solution with initial condition $\sigma(t=0)=\sigma_0$, shows that the steady state

$$\sigma_s=\int_0^1 dx(\rho_s+(\mathbb{1}-\rho_s)x^{\frac{\gamma_{\rm sw}+\varepsilon}{\delta_{\rm sw}}})^{\otimes 2}, \tag{C.25}$$

where $\rho_s=\frac{\gamma_{\rm sw}\rho_W(f)+\varepsilon\mathbb{1}}{\gamma_{\rm sw}+\varepsilon}$, is reached exponentially fast with a rate of at least $\delta_{\rm sw}$.
The time dependent master equation governing the dynamics of the target system is given by

$$\dot\rho=\delta_{\rm sw}(T_{\rm sw}(\sigma(t))-\rho_T), \tag{C.26}$$

where $T_{\rm sw}(\sigma_s)$ is the steady state of this evolution. According to Eq. (C.25), the steady state fidelity is given by

$$f_{\rm sw}(f,\varepsilon)\equiv f_{\rm sw}(f_s)=\int_0^1 dxF\left(f_s+(\frac{1}{4}-f_s)x^{\frac{\gamma_{\rm sw}+\varepsilon}{\delta_{\rm sw}}}\right).$$

f_s is the fidelity of the state ρ_s and $F(f)=(1-2f+4f^2)/3$ is the output fidelity of the swap protocol for two input states with fidelity f. A short calculation shows that

$$f_{\rm sw}(f,\varepsilon)\equiv f_{\rm sw}(f_s)=2\gamma_{\rm sw}^2\frac{\left(\frac{1}{3}(1-2f_s+4f_s^2)-\frac{1}{4}\right)+\frac{1}{4}}{(2\gamma_{\rm sw}+\delta_{\rm sw})(\gamma_{\rm sw}+\delta_{\rm sw})}\ , \tag{C.27}$$

where f is the fidelity of the state ρ_W and $f_s=\frac{\gamma_{\rm sw}f+\varepsilon\frac{1}{4}}{\gamma_{\rm sw}+\varepsilon}$. As discussed in Sec. C.3, the scheme can be made robust against noise processes acting on the target system by using m copies of the source systems and coupling them all to the same target state.

C.5.2 Creation of long-range, high-quality steady state entanglement

The continuous swap operation introduced above (Sec. C.5.1), the dissipative distillation protocol explained in Sec. C.4 and the method for stabilization against errors acting on target systems (Sec. C.3) are the basic building blocks for the dissipative quantum repeater scheme illustrated in Fig. C.3. To begin with, the distance L over which an entangled link has to be established is divided into 2^k segments of length L_0, as in standard repeater schemes. At each intermediate node, many qubits are supplied which are subject to local depolarizing noise acting at a rate ε. Each source pair constituting an elementary link of length L_0 is assumed to be individually driven into a steady state ρ_s of high fidelity by means of an entangling dissipative process of the type discussed in Sec. C.4.1, $\gamma E_{f_I}(\rho)$, with high initial steady state fidelity f_I and a rate γ, which is large compared to the noise rate ϵ. Note that this assumption can also be satisfied starting from dissipative processes

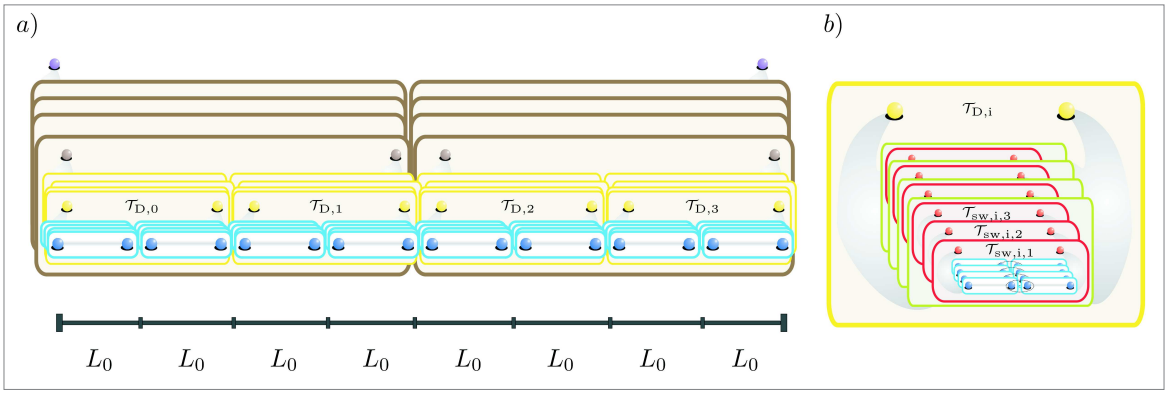

Figure C.3: Dissipative quantum repeater architecture. a) Concatenation of elementary steps, in which the distance over which entanglement is distributed is doubled. b) Illustration of a single iteration step including entanglement swapping and -distillation.

leading to a steady state with low fidelity and low γ, if distillation and boost processes are applied as discussed above. In the following, an iteration step of the repeater protocol which acts on 2^r entangled source systems, which each span a distance l with fidelity f_l, and produces entangled links of the length $2l$ with fidelity f_{2l}, such that $f_{2l} \geq f_l$ is considered. This is illustrated in Fig. C.3, where the entangled source pairs of length l are shown in blue and the yellow target pairs of length $2l$ are depicted in yellow. Each iteration step consist of the following subroutines, which are illustrated in Fig. C.3b:

- Neighboring source pairs of length l (blue) are connected via a continuous swap operation. The resulting quantum states are written onto target pairs $\mathcal{T}_{\mathrm{sw},i}$ (red). In order to achieve a boost-effect on the targets, this protocol is run on m source systems in parallel.

- A block of n such pairs $\mathcal{T}_{\mathrm{sw},i,j}$, $j = 1, \ldots, n$, acts as source system (green) for an distillation process, which maps the resulting quantum state to new target system $\mathcal{T}_{\mathrm{D},i}$ (yellow).

- m of these blocks (green) are needed to achieve a high fidelity of the quantum state of the target systems (yellow).

This iteration step results in entangled links (yellow) which span twice the initial distance and feature a high fidelity as well as a high convergence rate once all source systems have reached the steady state.

In the following, $\delta_D = \delta_{sw} = \frac{\gamma}{m}$ is considered for simplicity (these parameters can be optimized for a given distillation protocol). The individual levels of the repeater scheme converge seriatim from bottom to top to a steady state. For example, once the source systems of length l (blue) are in a steady state, the reduced master equation for the target system of length $2l$ (yellow) becomes time independent and this system reaches a steady state too. It is assumed, that all source pairs of length l (blue) are driven by a

time independent master equation of the type discussed in Sec. C.4.2, $\dot{\rho} = \gamma E_f(\rho)$ once all underlying systems have reached the steady state. The reduced master equation for the target system $\mathcal{T}_{\mathrm{sw},i}$ (red)

$$\dot{\rho}_{\mathcal{T}_{\mathrm{sw}},i} = \delta m E_{f_{sw}(f_I,\varepsilon)}(\rho_{\mathcal{T}_{\mathrm{sw}},i}) + \frac{\varepsilon}{2} N(\rho_{\mathcal{T}_{\mathrm{sw}},i}) + \delta \left(\mathbb{1}^{\otimes n} - \rho_{\mathcal{T}_{\mathrm{sw}},i}\right)$$

includes local polarizing noise as introduced in Sec. C.4.1 and the back-action of the distillation scheme. Note, that the rate of the entangling process, $\delta m = \gamma$ is again high, due to the boost on the target system. The entangling process acting on the target systems of the distillation procedure $\mathcal{T}_D, i$ (yellow), $E_{f_{\mathcal{T}_{\mathrm{sw}}}}(\rho_{\mathcal{T}_{\mathrm{D}}})$ is determined by the steady state fidelity $f_{\mathcal{T}_{\mathrm{sw}}} := f_{sw}(f_I, \varepsilon)$.
A wide range distillation protocols for Werner states [454] can be used in a continuous form as demonstrated in Sec. C.4 (below a specific example is discussed). As explained there, a distillation protocol corresponds to a completely positive map T_D which is described by a Linblad term $\delta_{\mathrm{D}} (T_D(\rho) - \rho)$. The distillation process is applied continuously for each entangled link and the resulting highly entangled qubit state is flipped to new target pairs $\mathcal{T}_{\mathrm{D},i}$ spanning the same length l.
Here, a distillation procedure is considered which acts on n entangled source systems and distills one potentially higher entangled pair. Hence, for each of the 2^{r-1} links, n copies $\mathcal{T}_{\mathrm{sw},ij}$, $i \in \{1, 2^{r-1}\}$, $j \in \{1, n\}$ have to be supplied. This situation is sketched in Fig. C.3b, where the target systems $\mathcal{T}_{\mathrm{sw},ij}$ (red), driven by the source pairs (blue), are used as resource for creating a highly entangled steady state of the new target pair (yellow). One source block (shown in green) is sufficient for entanglement distillation, but several of them running in parallel are needed to boost the desired dynamics on the target system. This way, each target pair $\mathcal{T}_{\mathrm{D},i}$ is driven at a rate $m\delta_{\mathrm{D}} = \gamma$ and the total effective master equation for the target systems of the distillation protocol is given by

$$\dot{\rho}_{\mathcal{T}_D} = m\delta_D E_{f_{\mathcal{T}_{\mathrm{D}}}}(\rho) + \frac{\varepsilon}{2} N(\rho).$$

Hence, the resulting steady state fidelity is

$$f_{\mathcal{T}_{\mathrm{D}}} = (f_D(f_{\mathcal{T}_{\mathrm{sw}}})) = (f_D(f_{\mathrm{sw}}(f_I, \varepsilon)))\,,$$

where $f_D(f_{\mathcal{T}_{\mathrm{sw}}})$ is the entanglement distilled from source systems with steady state fidelity $f_{\mathcal{T}_{\mathrm{sw}}}$. In order to iterate this process, $f_{\mathcal{T}_{\mathrm{D}}} \geq f_I$, is required which can always be achieved using a strong entanglement distillation (large n) and high entangling rates[6] γ.
The next iteration step begins with another continuous entangling swapping procedure. Here, the target systems of the distillation scheme act as source systems for the entanglement swapping operation.
Since the total distance L has been divided into 2^k segments ($L = L_0 2^k$), the protocol has to be iterated k times. As explained above, each iteration stage requires $2m^2 n$ qubit

[6] The error rate ε does not play an important role in this consideration, since the effect of noise on the target systems can be rendered negligible for large rates γ, without changing the scaling of the protocol. This implies that more resource are needed to achieve this rate γ for the initial stage of the repeater protocol, i.e., the number of resources may be multiplied by a large factor, but the scaling with the length remains unchanged.

pairs such that in total $(2m^2n)^k$ source systems are needed. Hence the resources scale with $(L/L_0)^{\log_2(2m^2n)}$ in the distance. The estimate of the required resources is restricted to the number of used qubit pairs, since the other resources scale polynomial in this quantity. As specific example, the distribution of an entangled state such that each repeater stage starts with and results in links with fidelity $f = 0.96$ is considered. The considered setting involves noise acing at a rate $\epsilon = 0.05$, distillation based on $n = 16$ source systems (the distillation protocol is described below) and stabilization of the target pairs by means of $m = 50$ copies of the underlying source blocks and $\gamma \approx 70$. In this example, the required resources scale with $(L/L_0)^{16.4}$.

The entanglement distillation scheme used here is a four-to-one distillation protocol for Werner states [454] which is applied two times in a nested fashion. Starting from four source states s_1, s_2, s_3, s_4 with fidelity f_{in}, the following operations are performed. First, a bilateral $\text{CNOT}_{s_1 \to s_2}$ operation is applied to the first two pairs (where s_1 is the control and s_2 the target qubit) and s_2 is measured in the computational basis. Then, a Hadamard transformation is performed on both qubits of s_1. Subsequently, a bilateral $\text{CNOT}_{s_1 \to s_3}$ operation is applied to the first and third pair (where s_1 is the control and s_3 the target qubit) and s_3 is measured in the computational basis. The measurement obtained on Alice's and Bob's side are compared. If their measurement results coincide, the resulting state s_1 is the desired higher entangled state. If not, the "safety-copy" s_4 is used instead. In this event, distillation was not successful and the fidelity has not been increased, but in any case an entangled pair is available. The fidelity of the resulting state is given by

$$f_{out}\left(f_{in}\right) = \frac{\left(1+g\right)\left(1+7g^2\right)}{16P_{\text{succ}}},$$

where $g = \left(4f_{in} - 1\right)/3$ and $P_{\text{succ}} = \left(1 + g^2 + 2g^3\right)/4$ is the success probability of this protocol. In the example above, this protocol is applied twice in a concatenated fashion. The second application of the scheme is run using the output states of the first one as input such that $f_D(f_{in}) = f_{out}\left(f_{out}\left(f_{in}\right)\right)$.

An estimate of the convergence speed of the presented repeater scheme concludes this section. To start with, the elementary pairs constituting the entangled links on the lowest level of the scheme are considered. These systems reach the steady state up to a certain high accuracy after a time t_0. After this time, the dynamics of all systems on the next level is governed to a good approximation by a time independent master equation and converge with high accuracy to the steady state after another time period of length t_0 has elapsed. Convergence of all k levels of the repeater scheme requires therefore a waiting time kt_0. Since the number of levels used in the scheme scale only logarithmical with the distance, a very moderate scaling of the convergence time with the distance is obtained. Note, that once the whole system is in a steady state, removal of the final long-range entangled pair does not have an effect on the underlying systems which remain in steady state. The repeater protocol put forward here is based on continuous LOCC maps, which represent a particular subset of possible dissipative schemes. A distillation protocol, which does not fall into this class (and does not require communication) has

also been presented. However, also the set of dissipative processes assisted by classical communication includes other types of schemes not covered here, which are yet to be explored.

Appendix D

Quantum teleportation: supplementary material

In the following, we provide details and derivations of the results presented in Sec. 4.1 as well as additional figures. In App. D.1, we derive the input-output relations, which relate the photonic and atomic variables before and after the scattering interaction. App. D.2 regards the special case, where a QND interaction is used for teleportation and contains a discussion of different strategies for increasing the fidelity of the basic protocol introduced in Sec. 4.1.3. App. D.3 is concerned with the non-QND case and provides details complementing the analysis of the experimental feasibility of the teleportation scheme in Sec. 4.1.4.

D.1 Input-output relations

In this appendix, we derive the input-output relations used in Sec. 4.1, assuming a general quadratic interaction between atoms and light. The QND case is obtained as special case in the limit where the parameter Z which characterizes the imbalance between the active and the passive component of the light-matter interaction tends to infinity $Z^2 \to \infty$ (compare Sec. 4.1). In App. D.1.1, we derive the input-output relations for the ideal case. In App. D.1.2, we include transverse atomic decay.

D.1.1 Input-output relations in the ideal case

In the following, we derive the input-output relations used in Sec. 4.1.4 in a one-dimensional model assuming a pointlike atomic ensemble located at $z = 0$. As explained in Sec. 2.1.1, the light field is described in terms of spatially localized modes $x_L(z)$, $p_L(z)$ (see Eq. (2.1)). Due to the finite bandwith of the classical field b, the corresponding canonical commutation relation involves a Dirac delta function with a finite width of the order of c/b, $[x_L(z), p_L(\acute{z})] = ic\delta_b(z - \acute{z})$. Light and atoms interact according to the Hamiltonian $H = H_A + H_L + H_{int}$, where

$$H_A = \frac{\Omega}{2}\left(x_A^2 + p_A^2\right), \qquad H_{int} = \frac{\kappa}{\sqrt{T}}\left(p_A p_L(0) + \frac{1}{Z^2} x_A x_L(0)\right). \tag{D.1}$$

H_{int} corresponds to a predominatly passive interaction (compare Sec. 2.1.2). For simplicity, we discuss this case in the following. The corresponding active variant is obtained by considering $Z^2 \to -Z^2$. H_L represents the free propagation of the light field. The action of this Hamiltonian on the quadratures of the light field results in $\frac{d}{dt}x_L(z) = -c\frac{d}{dz}x_L(z)$. We obtain the Heisenberg equations

$$\begin{aligned}
\frac{d}{dt}x_A(t) &= \Omega p_A + \frac{\kappa}{\sqrt{T}}p_L(0,t), \\
\frac{d}{dt}p_A(t) &= -\Omega x_A - \frac{1}{Z^2}\frac{\kappa}{\sqrt{T}}x_L(0,t), \\
\left(\frac{d}{dt} + c\frac{d}{dz}\right)x_L(r,t) &= \frac{\kappa}{\sqrt{T}}p_A(t)\delta_b(z), \\
\left(\frac{d}{dt} + c\frac{d}{dz}\right)p_L(r,t) &= -\frac{\kappa}{\sqrt{T}Z^2}x_A(t)\delta_b(z).
\end{aligned}$$

and perform the variable transformation $\xi = ct - z$. The new light field variables are denoted by a bar, $\bar{x}_L(\xi,t) = x_L(ct-\xi,t)$. As explained in Sec. 2.1.3, the variable ξ labels the localized light modes of the pulse and represents a coordinate system which is fixed to the light pulse, starting with $\xi = 0$ at the front and ending with $\xi = cT$, as illustrated in Fig. 2.3. In a rotating frame with

$$\begin{pmatrix} \tilde{x}_A(t) \\ \tilde{p}_A(t) \end{pmatrix} = \begin{pmatrix} \cos(\Omega t) & -\sin(\Omega t) \\ \sin(\Omega t) & \cos(\Omega t) \end{pmatrix} \begin{pmatrix} x_A(t) \\ p_A(t) \end{pmatrix},$$

the new Maxwell-Bloch equations read

$$\begin{aligned}
\frac{d}{dt}\tilde{x}_A(t) &= \frac{\kappa}{\sqrt{T}}\left(\cos(\Omega t)\bar{p}_L(ct,t) + \frac{1}{Z^2}\sin(\Omega t)\bar{x}_L(ct,t))\right), \qquad \text{(D.2)} \\
\frac{d}{dt}\tilde{p}_A(t) &= \frac{\kappa}{\sqrt{T}}\left(\sin(\Omega t)\bar{p}_L(ct,t) - \frac{1}{Z^2}\cos(\Omega t)\bar{x}_L(ct,t)\right), \\
\frac{d}{dt}\bar{x}_L(r,t) &= \frac{\kappa}{\sqrt{T}}\left(-\sin(\Omega t)\tilde{x}_A(t) + \cos(\Omega t)\tilde{p}_A(t)\right)\delta_b(ct-\xi), \qquad \text{(D.3)} \\
\frac{d}{dt}\bar{p}_L(r,t) &= -\frac{\kappa}{\sqrt{T}Z^2}\left(\cos(\Omega t)\tilde{x}_A(t) + \sin(\Omega t)\tilde{p}_A(t)\right)\delta_b(ct-\xi).
\end{aligned}$$

In order to solve this set of differential equations, the equations for the light field (D.2) are integrated, which yields

$$\begin{pmatrix} \bar{x}_L(\xi,t) \\ \bar{p}_L(\xi,t) \end{pmatrix} = \begin{pmatrix} \bar{x}_L(\xi,0) \\ \bar{p}_L(\xi,0) \end{pmatrix} + \Theta_b(\xi - ct)\frac{\kappa}{\sqrt{T}}L_{\mathrm{P}}(-\Omega,t)\begin{pmatrix} \tilde{x}_A(t) \\ \tilde{p}_A(t) \end{pmatrix}, \qquad \text{(D.4)}$$

where

$$L_{\mathrm{P}}(-\Omega,t) = \begin{pmatrix} -\sin(\Omega t) & \cos(\Omega t) \\ -\frac{1}{Z^2}\cos(\Omega t) & -\frac{1}{Z^2}\sin(\Omega t) \end{pmatrix}.$$

Note that the Heaviside function $\Theta_b(ct-\xi)$ is a smooth step function, since the Dirac delta function which appears in the Heisenberg equations $\delta_b(ct-\xi)$, has a width of the

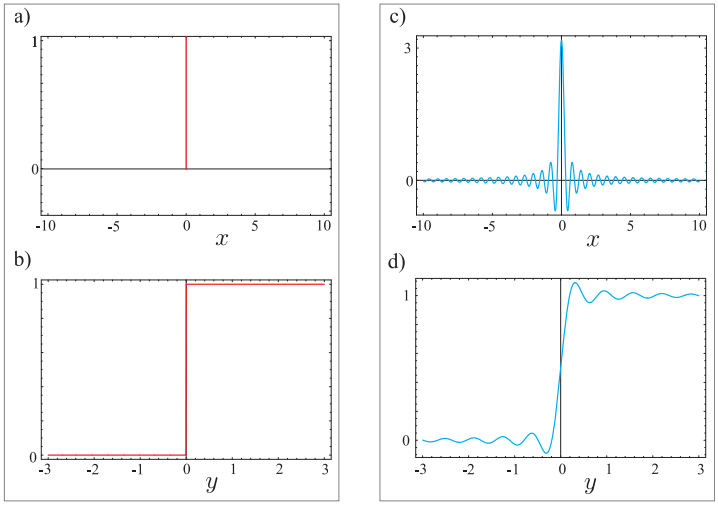

Figure D.1: a) Dirac delta function $\delta(x)$ b) Heaviside function $\Theta(y)$ c) Approximate delta function $f_a(x) = \frac{1}{2\pi}\int_{-a}^{+a} e^{i\omega x} d\omega$, $(a = 10)$. d) Smooth step function $\int_{-\infty}^{y} f_a(x)dx$, $(a = 10)$.

order b/c. In the following, the tilde on atomic operators is omitted in order to simplify the notation. By inserting the expressions for $\bar{x}_L(\xi, t)$ and $\bar{p}_L(\xi, t)$ given by Eq. (D.4) into the differential equation for the atomic variables (D.3),

$$\begin{aligned}\frac{d}{dt}\begin{pmatrix} x_A(t) \\ p_A(t) \end{pmatrix} &= \frac{\kappa}{\sqrt{T}} A_{\mathrm{P}}(-\Omega, t) \begin{pmatrix} \bar{x}_L(ct, t) \\ \bar{p}_L(ct, t) \end{pmatrix}, \\ &= \frac{\kappa}{\sqrt{T}} A_{\mathrm{P}}(-\Omega, t) \begin{pmatrix} \bar{x}_L(ct, 0) \\ \bar{p}_L(ct, 0) \end{pmatrix} + \Theta_b(0)\frac{\kappa^2}{T} A_{\mathrm{P}}(-\Omega, t) L_{\mathrm{P}}(-\Omega, t) \begin{pmatrix} x_A(t) \\ p_A(t) \end{pmatrix},\end{aligned}$$

is obtained, where

$$A_{\mathrm{P}}(-\Omega, t) = \begin{pmatrix} \frac{1}{Z^2}\sin(\Omega t) & \cos(\Omega t) \\ -\frac{1}{Z^2}\cos(\Omega t) & \sin(\Omega t) \end{pmatrix}.$$

Using $A_{\mathrm{P}}(-\Omega, t) L_{\mathrm{P}}(-\Omega, t) = -\frac{1}{Z^2}\mathbb{1}$ (where $\mathbb{1}$ is the unit matrix) yields

$$\frac{d}{dt}\begin{pmatrix} x_A(t) \\ p_A(t) \end{pmatrix} = \frac{\kappa}{\sqrt{T}} A_{\mathrm{P}}(-\Omega, t) \begin{pmatrix} \bar{x}_L(ct, 0) \\ \bar{p}_L(ct, 0) \end{pmatrix} - \frac{\kappa^2}{2Z^2 T} \begin{pmatrix} x_A(t) \\ p_A(t) \end{pmatrix},$$

such that

$$\begin{pmatrix} x_A(t) \\ p_A(t) \end{pmatrix} = e^{\frac{-\kappa^2}{2Z^2}} \begin{pmatrix} x_A^{in} \\ p_A^{in} \end{pmatrix} + \frac{\kappa}{\sqrt{T}} \int_0^t d\tau e^{\frac{-\kappa^2(t-\tau)}{2Z^2 T}} A_{\mathrm{P}}(-\Omega, \tau) \begin{pmatrix} \bar{x}_L(c\tau, 0) \\ \bar{p}_L(c\tau, 0) \end{pmatrix}, \tag{D.5}$$

and accordingly

$$\begin{pmatrix} x_A^{out} \\ p_A^{out} \end{pmatrix} = e^{-\frac{\kappa^2}{2Z^2}} \begin{pmatrix} x_A^{in} \\ p_A^{in} \end{pmatrix} + \sqrt{1 - e^{-\frac{\kappa^2}{Z^2}}} \begin{pmatrix} x_{\mathrm{r(P)},+}^{in} \\ p_{\mathrm{r(P)},+}^{in} \end{pmatrix},$$

where

$$\begin{pmatrix} x^{in}_{\mathrm{r(P)},\pm} \\ p^{in}_{\mathrm{r(P)},\pm} \end{pmatrix} = \frac{1}{2}\left(\left(Z+\frac{1}{Z}\right)\begin{pmatrix} x^{in}_{us,\pm} \\ p^{in}_{us,\pm} \end{pmatrix}+\left(Z-\frac{1}{Z}\right)\begin{pmatrix} p^{in}_{ls,\pm} \\ x^{in}_{ls,\pm} \end{pmatrix}\right),$$

and

$$\begin{aligned}\begin{pmatrix} x^{in}_{us,\pm} \\ p^{in}_{us,\pm} \end{pmatrix} &= \frac{\kappa}{Z\sqrt{T}}\frac{1}{N_\pm}\int_0^T d\tau e^{\pm\frac{\kappa^2\tau}{2Z^2T}} R(\tau)\begin{pmatrix} \bar{p}_L(c\tau,0) \\ -\bar{x}_L(c\tau,0) \end{pmatrix}, \\ \begin{pmatrix} p^{in}_{ls,\pm} \\ x^{in}_{ls,\pm} \end{pmatrix} &= \frac{\kappa}{Z\sqrt{T}}\frac{1}{N_\pm}\int_0^T d\tau e^{\pm\frac{\kappa^2\tau}{2Z^2T}} R(\tau)\begin{pmatrix} \bar{p}_L(c\tau,0) \\ \bar{x}_L(c\tau,0) \end{pmatrix}\end{aligned}$$

with

$$N_+ = \sqrt{e^{\frac{\kappa^2}{Z^2}}-1}, \quad N_- = \sqrt{1-e^{-\frac{\kappa^2}{Z^2}}}, \quad R(\tau) = \begin{pmatrix} \cos(\Omega\tau) & -\sin(\Omega\tau) \\ \sin(\Omega\tau) & \cos(\Omega\tau) \end{pmatrix}.$$

The input-output relations for the light field are derived in an analogous fashion.

$$\begin{aligned}\begin{pmatrix} x^{out}_{\mathrm{r(P)},-} \\ p^{out}_{\mathrm{r(P)},-} \end{pmatrix} &= \frac{\kappa}{\sqrt{T}}\frac{1}{N_-}\int_0^T dt e^{-\frac{\kappa^2 t}{2Z^2T}} A_{\mathrm{P}}(-\Omega,\tau)\begin{pmatrix} \bar{x}_L(ct,T) \\ \bar{p}_L(ct,T) \end{pmatrix}, \\ &= \begin{pmatrix} x^{in}_{\mathrm{r(P)},-} \\ p^{in}_{\mathrm{r(P)},-} \end{pmatrix} + \frac{\kappa^2}{T}\frac{1}{N_-}\int_0^T dt e^{-\frac{\kappa^2 t}{2Z^2T}} A_{\mathrm{P}}(-\Omega,\tau) L_{\mathrm{P}}(-\Omega,\tau)\begin{pmatrix} x_A(t) \\ p_A(t) \end{pmatrix}, \\ &= \begin{pmatrix} x^{in}_{\mathrm{r(P)},-} \\ p^{in}_{\mathrm{r(P)},-} \end{pmatrix} - \frac{\kappa^2}{Z^2T}\frac{1}{N_-}\int_0^T dt e^{-\frac{\kappa^2 t}{Z^2T}}\begin{pmatrix} x^{in}_A \\ p^{in}_A \end{pmatrix} \\ &+ \frac{\kappa^2}{Z^2T}\frac{1}{N_-}\int_0^T dt\int_0^t d\tau e^{-\frac{\kappa^2 t}{2Z^2T}} e^{-\frac{\kappa^2(t-\tau)}{2Z^2T}} A_{\mathrm{P}}(-\Omega,\tau)\begin{pmatrix} \bar{x}_L(c\tau,0) \\ \bar{p}_L(c\tau,0) \end{pmatrix},\end{aligned}$$

where Eq. (D.5) has been used in the last step. Accordingly,

$$\begin{pmatrix} x^{out}_{\mathrm{r(P)},-} \\ p^{out}_{\mathrm{r(P)},-} \end{pmatrix} = -\sqrt{1-e^{-\frac{\kappa^2}{Z^2}}}\begin{pmatrix} x^{in}_A \\ p^{in}_A \end{pmatrix} + e^{-\frac{\kappa^2}{2Z^2}}\begin{pmatrix} x^{in}_{\mathrm{r(P)},+} \\ p^{in}_{\mathrm{r(P)},+} \end{pmatrix}.$$

Input-output relations for the upper and lower sideband modes are given by

$$\begin{aligned}\begin{pmatrix} x^{out}_{us,+} \\ p^{out}_{us,+} \end{pmatrix} &= \left(1+\frac{\alpha_I(1+\frac{1}{Z^2})}{\sqrt{2}}\right)\begin{pmatrix} x^{in}_{us,+} \\ p^{in}_{us,+} \end{pmatrix} - \frac{\kappa^2(1+\frac{1}{Z^2})}{2Z\sqrt{e^{\frac{\kappa^2}{Z^2}}-1}}\begin{pmatrix} x^{in}_A \\ p^{in}_A \end{pmatrix} + \frac{\alpha_I(1-\frac{1}{Z^2})}{\sqrt{2}}\begin{pmatrix} p^{in}_{ls,+} \\ x^{in}_{ls,+} \end{pmatrix} \\ &+ \frac{\beta_I}{\sqrt{2}}\left((1+\frac{1}{Z^2})\begin{pmatrix} x^{in}_{us,+,\perp} \\ p^{in}_{us,+,\perp} \end{pmatrix} + (1-\frac{1}{Z^2})\begin{pmatrix} p^{in}_{ls,+,\perp} \\ x^{in}_{ls,+,\perp} \end{pmatrix}\right), \\ \begin{pmatrix} p^{out}_{ls,+} \\ x^{out}_{ls,+} \end{pmatrix} &= \left(1+\frac{\alpha_{II}(1-\frac{1}{Z^2})}{\sqrt{2}}\right)\begin{pmatrix} p^{in}_{ls,+} \\ x^{in}_{ls,+} \end{pmatrix} + \frac{\kappa^2(1-\frac{1}{Z^2})}{2Z\sqrt{e^{\frac{\kappa^2}{Z^2}}-1}}\begin{pmatrix} x^{in}_A \\ p^{in}_A \end{pmatrix} + \frac{\alpha_{II}(1-\frac{1}{Z^2})}{\sqrt{2}}\begin{pmatrix} x^{in}_{us,+} \\ p^{in}_{us,+} \end{pmatrix} \\ &+ \frac{\beta_{II}}{\sqrt{2}}\left((1+\frac{1}{Z^2})\begin{pmatrix} x^{in}_{us,+,\perp} \\ p^{in}_{us,+,\perp} \end{pmatrix} + (1-\frac{1}{Z^2})\begin{pmatrix} p^{in}_{ls,+,\perp} \\ x^{in}_{ls,+,\perp} \end{pmatrix}\right)\end{aligned}$$

and

$$\begin{pmatrix} x^{out}_{us,-} \\ p^{out}_{us,-} \end{pmatrix} = \left(1 - \frac{1}{4}(Z+\frac{1}{Z})^2\right)\begin{pmatrix} x^{in}_{us,-} \\ p^{in}_{us,-} \end{pmatrix} - \frac{1}{4}(Z^2 - \frac{1}{Z^2})\begin{pmatrix} p^{in}_{ls,-} \\ x^{in}_{ls,-} \end{pmatrix} - \frac{1}{2}(Z+\frac{1}{Z})\sqrt{1-e^{-\frac{\kappa^2}{z^2}}}\begin{pmatrix} x^{in}_{A} \\ p^{in}_{A} \end{pmatrix}$$
$$+ \frac{1}{2}(Z+\frac{1}{Z})e^{-\frac{\kappa^2}{2z^2}}\left(\frac{Z+\frac{1}{Z}}{2}\begin{pmatrix} x^{in}_{us,+} \\ p^{in}_{us,+} \end{pmatrix} + \frac{Z-\frac{1}{Z}}{2}\begin{pmatrix} p^{in}_{ls,+} \\ x^{in}_{ls,+} \end{pmatrix}\right),$$
$$\begin{pmatrix} p^{out}_{ls,-} \\ x^{out}_{ls,-} \end{pmatrix} = \left(1 + \frac{1}{4}(Z-\frac{1}{Z})^2\right)\begin{pmatrix} p^{in}_{ls,-} \\ x^{in}_{ls,-} \end{pmatrix} + \frac{1}{4}(Z^2 - \frac{1}{Z^2})\begin{pmatrix} x^{in}_{us,-} \\ p^{in}_{us,-} \end{pmatrix} + \frac{1}{2}(Z-\frac{1}{Z})\sqrt{1-e^{-\frac{\kappa^2}{z^2}}}\begin{pmatrix} x^{in}_{A} \\ p^{in}_{A} \end{pmatrix}$$
$$- \frac{1}{2}(Z-\frac{1}{Z})e^{-\frac{\kappa^2}{2z^2}}\left(\frac{Z+\frac{1}{Z}}{2}\begin{pmatrix} x^{in}_{us,+} \\ p^{in}_{us,+} \end{pmatrix} + \frac{Z-\frac{1}{Z}}{2}\begin{pmatrix} p^{in}_{ls,+} \\ x^{in}_{ls,+} \end{pmatrix}\right),$$

where

$$\alpha_I = \frac{(1+\frac{1}{Z^2})Z^2}{2\sqrt{2}}\frac{\frac{\kappa^2}{Z^2} - (e^{\frac{\kappa^2}{Z^2}}-1)}{e^{\frac{\kappa^2}{Z^2}}-1}, \quad \alpha_I^2 + \beta_I^2 = -\frac{(1+\frac{1}{Z^2})^2 Z^4}{8(e^{\frac{\kappa^2}{Z^2}}-1)}\left(\frac{\kappa^4}{Z^4} + 2\frac{\kappa^2}{Z^2} - 2(e^{\frac{\kappa^2}{Z^2}}-1)\right),$$
$$\alpha_{II} = -\frac{(1-\frac{1}{Z^2})Z^2}{2\sqrt{2}}\frac{\frac{\kappa^2}{Z^2} - (e^{\frac{\kappa^2}{Z^2}}-1)}{e^{\frac{\kappa^2}{Z^2}}-1}, \quad \alpha_{II}^2 + \beta_{II}^2 = -\frac{(1-\frac{1}{Z^2})^2 Z^4}{8(e^{\frac{\kappa^2}{Z^2}}-1)}\left(\frac{\kappa^4}{Z^4} + 2\frac{\kappa^2}{Z^2} - 2(e^{\frac{\kappa^2}{Z^2}}-1)\right).$$

If two atomic ensembles in antiparallel oriented magnetic fields are used, as in the setup for dissipative entanglement generation, the situation is simplified, since backaction modes cancel. In this case, the atomic input output relations are given by

$$\begin{pmatrix} x^{out}_{A,+} \\ p^{out}_{A,-} \end{pmatrix} = e^{-\frac{\kappa^2}{2Z^2}}\begin{pmatrix} x^{in}_{A,+} \\ p^{in}_{A,-} \end{pmatrix} + Z\sqrt{1-e^{-\frac{\kappa^2}{Z^2}}}\begin{pmatrix} p^{in}_{\cos,+} \\ p^{in}_{\sin,+} \end{pmatrix},$$
$$\begin{pmatrix} x^{out}_{A,-} \\ p^{out}_{A,+} \end{pmatrix} = e^{-\frac{\kappa^2}{2Z^2}}\begin{pmatrix} x^{in}_{A,-} \\ p^{in}_{A,+} \end{pmatrix} + \frac{1}{Z}\sqrt{1-e^{-\frac{\kappa^2}{Z^2}}}\begin{pmatrix} x^{in}_{sin,+} \\ -x^{in}_{cos,+} \end{pmatrix},$$

where

$$\begin{pmatrix} x^{in}_{sin,\pm} \\ x^{in}_{cos,\pm} \end{pmatrix} = \frac{\sqrt{2}\kappa}{\sqrt{T}ZN_{\pm}}\int_0^T e^{\pm\frac{\kappa^2 t}{2Z^2T}}\begin{pmatrix} \sin(\Omega t)\bar{x}_L(ct,0) \\ \cos(\Omega t)\bar{x}_L(ct,0) \end{pmatrix}. \tag{D.6}$$

The input-output relations for arbitrarily modulated sine and cosine modes of the light field (see Eq. (2.6)) are given by

$$\begin{pmatrix} x^{out}_{h,sin} \\ x^{out}_{h,cos} \end{pmatrix} = \begin{pmatrix} x^{in}_{h,sin} \\ x^{in}_{h,cos} \end{pmatrix} + \frac{\kappa}{T}\int_0^T dt h(t) e^{\frac{-\kappa^2 t}{2Z^2T}}\begin{pmatrix} x^{in}_{A,-} \\ p^{in}_{A,+} \end{pmatrix} - \frac{\kappa^2\sqrt{2}}{T^{\frac{3}{2}}Z^2}\int_0^T dt\int_0^t d\tau h(t) e^{\frac{-\kappa^2(t-\tau)}{2Z^2T}}\begin{pmatrix} \sin(\Omega\tau)\bar{x}_L(c\tau,0) \\ \cos(\Omega\tau)\bar{x}_L(c\tau,0) \end{pmatrix},$$
$$\begin{pmatrix} p^{out}_{h,sin} \\ p^{out}_{h,cos} \end{pmatrix} = \begin{pmatrix} p^{in}_{h,sin} \\ p^{in}_{h,cos} \end{pmatrix} + \frac{\kappa}{TZ}\int_0^T dt h(t) e^{\frac{-\kappa^2 t}{2Z^2T}}\begin{pmatrix} p^{in}_{A,-} \\ -x^{in}_{A,+} \end{pmatrix} - \frac{\kappa^2\sqrt{2}}{T^{\frac{3}{2}}Z^2}\int_0^T dt\int_0^t d\tau h(t) e^{\frac{-\kappa^2(t-\tau)}{2Z^2T}}\begin{pmatrix} \sin(\Omega\tau)\bar{p}_L(c\tau,0) \\ \cos(\Omega\tau)\bar{p}_L(c\tau,0) \end{pmatrix}.$$

In the special case of exponentially falling read out modes

$$\begin{pmatrix} x^{out}_{sin,-} \\ x^{out}_{cos,-} \end{pmatrix} = e^{-\frac{\kappa^2}{2Z^2}}\begin{pmatrix} x^{in}_{sin,-} \\ x^{in}_{cos,-} \end{pmatrix} + Z\sqrt{1-e^{-\frac{\kappa^2}{Z^2}}}\begin{pmatrix} x^{in}_{A,-} \\ p^{in}_{A,+} \end{pmatrix},$$
$$\begin{pmatrix} p^{out}_{sin,-} \\ p^{out}_{cos,-} \end{pmatrix} = e^{-\frac{\kappa^2}{2Z^2}}\begin{pmatrix} p^{in}_{sin,-} \\ p^{in}_{cos,-} \end{pmatrix} + \frac{1}{Z}\sqrt{1-e^{-\frac{\kappa^2}{Z^2}}}\begin{pmatrix} p^{in}_{A,-} \\ -x^{in}_{A,+} \end{pmatrix},$$

is obtained.

D.1.2 Input-output relations including transverse atomic decay

In the following, transverse atomic decay at a constant rate η/T is included. More specifically, atomic decay is modelled in the form of beamsplitter losses with vacuum input. Including this type of noise, the differential equations for the atomic variables read[1]

$$\begin{aligned}
\frac{d}{dt}x_A(t) &= -\frac{\eta}{2T}x_A(t)+\frac{\kappa}{\sqrt{T}}\left(\cos(\Omega t)\bar{p}_L(ct,t)+\frac{1}{Z^2}\sin(\Omega t)\bar{x}_L(ct,t)\right)+\sqrt{\frac{\eta}{T}}f_{x_A}(t),\\
\frac{d}{dt}p_A(t) &= -\frac{\eta}{2T}p_A(t)+\frac{\kappa}{\sqrt{T}}\left(\sin(\Omega t)\bar{p}_L(ct,t)-\frac{1}{Z^2}\cos(\Omega t)\bar{x}_L(ct,t)\right)+\sqrt{\frac{\eta}{T}}f_{p_A}(t),\\
\frac{d}{dt}\bar{x}_L(r,t) &= \frac{\kappa}{\sqrt{T}}\left(-\sin(\Omega t)x_A(t)+\cos(\Omega t)p_A(t)\right)\delta_b(ct-\xi),\\
\frac{d}{dt}\bar{p}_L(r,t) &= -\frac{\kappa}{\sqrt{T}Z^2}\left(\cos(\Omega t)x_A(t)+\sin(\Omega t)p_A(t)\right)\delta_b(ct-\xi),
\end{aligned}$$

with $[f_{x_A}(t), f_{p,A}(\acute{t})] = \delta(t-\acute{t})$ and $\mathrm{var}(f_{x_A}(t)) = \mathrm{var}(f_{p_A}(t)) = 1/2$. Inserting the expressions for $\bar{x}_L(\xi,t)$ and $\bar{p}_L(\xi,t)$ given by Eq. (D.4) into the differential equation for the atomic variables results in

$$\begin{aligned}
\frac{d}{dt}\begin{pmatrix}x_A(t)\\p_A(t)\end{pmatrix} &= -\frac{\eta}{2T}\begin{pmatrix}x_A(t)\\p_A(t)\end{pmatrix}+\frac{\kappa}{\sqrt{T}}A_{\mathrm{P}}(-\Omega,t)\begin{pmatrix}\bar{x}_L(ct,t)\\\bar{p}_L(ct,t)\end{pmatrix}+\sqrt{\frac{\eta}{T}}\begin{pmatrix}f_{x_A}(t)\\f_{p_A}(t)\end{pmatrix},\\
&= \frac{\kappa}{\sqrt{T}}A_{\mathrm{P}}(-\Omega,t)\begin{pmatrix}\bar{x}_L(ct,0)\\\bar{p}_L(ct,0)\end{pmatrix}-\left(\frac{\kappa^2}{2Z^2T}+\frac{\eta}{2T}\right)\begin{pmatrix}x_A(t)\\p_A(t)\end{pmatrix}+\sqrt{\frac{\eta}{T}}\begin{pmatrix}f_{x_A}(t)\\f_{p_A}(t)\end{pmatrix},
\end{aligned}$$

such that

$$\begin{aligned}
\begin{pmatrix}x_A(t)\\p_A(t)\end{pmatrix} &= e^{-\left(\frac{\kappa^2}{Z^2}+\eta\right)\frac{t}{2T}}\begin{pmatrix}x_A^{in}\\p_A^{in}\end{pmatrix}+\frac{\kappa}{\sqrt{T}}\int_0^t d\tau e^{-\left(\frac{\kappa^2}{Z^2}+\eta\right)\frac{t-\tau}{2T}}A_P(-\Omega,\tau)\begin{pmatrix}\bar{x}_L(c\tau,0)\\\bar{p}_L(c\tau,0)\end{pmatrix}\\
&+ \sqrt{\frac{\eta}{T}}\int_0^t d\tau e^{-\left(\frac{\kappa^2}{Z^2}+\eta\right)\frac{t-\tau}{2T}}\begin{pmatrix}f_{x_A}(t)\\f_{p_A}(t)\end{pmatrix}.
\end{aligned}$$

Using $\gamma_{\mathrm{P}} = \frac{\kappa^2}{Z^2}+\eta$,

$$\begin{pmatrix}x_A^{out}\\p_A^{out}\end{pmatrix} = e^{\frac{-\gamma_{\mathrm{P}}}{2}}\begin{pmatrix}x_A^{in}\\p_A^{in}\end{pmatrix}+\frac{\kappa}{Z\sqrt{\gamma_{\mathrm{P}}}}\sqrt{1-e^{-\gamma_{\mathrm{P}}}}\begin{pmatrix}x^{in}_{\mathrm{r(P)},+,\eta}\\p^{in}_{\mathrm{r(P)},+,\eta}\end{pmatrix}+\sqrt{\frac{\eta}{\gamma_P}}\sqrt{1-e^{-\gamma}}\begin{pmatrix}F^{in}_{x_A,+,\eta}\\F^{in}_{p_A,+,\eta}\end{pmatrix} \quad \text{(D.7)}$$

is obtained, where

$$\begin{aligned}
\begin{pmatrix}x^{in}_{\mathrm{r(P)},\pm,\eta}\\p^{in}_{\mathrm{r(P)},\pm,\eta}\end{pmatrix} &= \sqrt{\frac{\gamma_{\mathrm{P}}}{T}}\frac{Z}{N_{\pm,\eta}}\int_0^T dt e^{\frac{\pm\gamma_{\mathrm{P}}t}{2T}}A_{\mathrm{P}}(-\Omega,t)\begin{pmatrix}\bar{p}_L(c\tau,0)\\\bar{x}_L(c\tau,0)\end{pmatrix}\\
&= \frac{1}{2}\left(\left(Z+\frac{1}{Z}\right)\begin{pmatrix}x^{in}_{us,\pm,\eta}\\p^{in}_{us,\pm,\eta}\end{pmatrix}+\left(Z-\frac{1}{Z}\right)\begin{pmatrix}p^{in}_{ls,\pm,\eta}\\x^{in}_{ls,\pm,\eta}\end{pmatrix}\right),
\end{aligned}$$

[1] As before, the passive variant of the interaction given by Eq. (D.1) is discussed. The input-output relations for the active case can be derived analogously with $Z^2 \to -Z^2$.

with $N_{+,\eta} = \sqrt{e^{\gamma_P} - 1}$, $N_{-,\eta} = \sqrt{1 - e^{-\gamma_P}}$ and

$$\begin{pmatrix} x^{in}_{us,\pm,\eta} \\ p^{in}_{us,\pm,\eta} \end{pmatrix} = \sqrt{\frac{\gamma_P}{T}} \frac{1}{N_{\pm,\eta}} \int_0^T d\tau e^{\pm \frac{\gamma_P \tau}{2T}} R(\tau) \begin{pmatrix} \bar{p}_L(c\tau, 0) \\ -\bar{x}_L(c\tau, 0) \end{pmatrix},$$
$$\begin{pmatrix} p^{in}_{ls,\pm,\eta} \\ x^{in}_{ls,\pm,\eta} \end{pmatrix} = \sqrt{\frac{\gamma_P}{T}} \frac{1}{N_{\pm,\eta}} \int_0^T d\tau e^{\pm \frac{\gamma_P \tau}{2T}} R(\tau) \begin{pmatrix} \bar{p}_L(c\tau, 0) \\ \bar{x}_L(c\tau, 0) \end{pmatrix},$$

and exponentially modulated noise modes $F_{x_A,+,\eta}$, $F_{p_A,+,\eta}$ (with $[F_{x_A,+,\eta}, F_{p_A,+,\eta}] = i$) as defined in Sec. 4.1.4. The input-output relations for the light field (Eq. (4.7) in the main text) are derived in an analogous fashion.

D.2 Improved QND teleportation schemes

This appendix is concerned with strategies aiming at the improvement of the performance of the basic QND teleportation protocol introduced in Sec. 4.1.3. In App. D.2.1 the use of squeezed light, the measurement of higher order backaction modes and the application of a double pass scheme [98–100] are discussed. App. D.2.2 is concerned with the use of time dependent coupling strength and suitable readout modes and provides the basis for the analysis in Sec. 4.1.3.

D.2.1 Use of squeezed light, measurement of backaction modes and application of a double pass scheme

As shown in Sec. 4.1.3, the optimal fidelity of the QND teleportation scheme cannot be attained for couplings restricted to realistic values. However, obtaining high fidelities for limited couplings can be rendered possible, for example, by using squeezed light. Below, three different strategies are discussed.

QND teleportation using squeezed light

If the variance of the x-quadrature of the light field can be reduced to $\Delta(x_{squ})^2 = \frac{1}{4}\Delta(x_{coh})^2$, the optimal teleportation fidelity can be attained even for $\kappa = 1.0$. For more moderate degrees of squeezing, the optimal average fidelity cannot be achieved for the values of κ considered here, but the use of squeezed light still leads to an improvement. Figure D.2a shows the average teleportation fidelity for -3dB of squeezing and limited couplings. Fig. D.2b shows the fidelity for -3dB of squeezing and 6dB antisqueezing. The shown fidelities are calculated as follows. Considering squeezed variances of the light field $\Delta(x_{sin})^2 = \Delta(x_{cos})^2 = \frac{1}{2}e^{-r}$ and $\Delta(p_{sin})^2 = \Delta(p_{cos})^2 = \Delta(p_{sin,1})^2 = \Delta(p_{cos,1})^2 = \frac{1}{2}e^{r}$, where r is the squeezing parameter, the atomic variances corresponding to Bob's ensemble after the feedback operation are given by

$$\begin{aligned} \begin{pmatrix} \Delta(x^{fin}_{B,squ})^2 \\ \Delta(p^{fin}_{B,squ})^2 \end{pmatrix} &= \frac{1}{2} \begin{pmatrix} (1 - \frac{\kappa_1 g_{sin}}{\sqrt{2}})^2 \\ (1 + \frac{\kappa_1 g_{cos}}{\sqrt{2}})^2 \end{pmatrix} + \frac{1}{2} \begin{pmatrix} \frac{\kappa_2^2 g_{sin}^2}{2} \\ \frac{\kappa_2^2 g_{cos}^2}{2} \end{pmatrix} + \frac{1}{2} e^{-r} \begin{pmatrix} g_{sin}^2 \\ g_{cos}^2 \end{pmatrix} \\ &+ \frac{1}{2} e^{r} \left(\frac{\kappa_1^2 + \kappa_2^2}{4\sqrt{3}} \right)^2 \begin{pmatrix} g_{sin}^2 \\ g_{cos}^2 \end{pmatrix} + \frac{1}{2} e^{r} \begin{pmatrix} (\frac{\kappa 1}{\sqrt{2}} - g_{sin} \frac{\kappa_1^2 + \kappa_2^2}{4})^2 \\ (\frac{\kappa 1}{\sqrt{2}} + g_{cos} \frac{\kappa_1^2 + \kappa_2^2}{4})^2 \end{pmatrix}, \end{aligned}$$

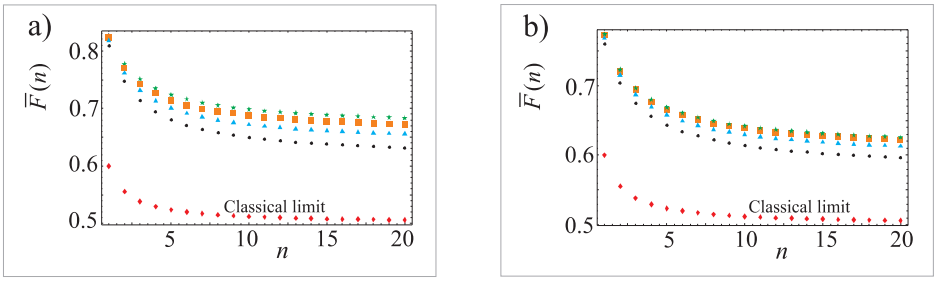

Figure D.2: Average teleportation fidelity $\bar{F}(n)$ versus width of the distribution of input states n, using squeezed light. The lowest (red) line in each panel represents the classical limit. The other lines show the optimized average fidelity for restricted couplings and correspond to $\kappa^2_{max} = 1.69$ (green stars), $\kappa^2_{max} = 1.44$ (orange squares), $\kappa^2_{max} = 1.21$ (blue triangles) and $\kappa^2_{max} = 1.0$ (black dots). In panel a) squeezing up to -3dB is considered. In panel b) noisy squeezing of -3dB with 6dB antisqueezing is considered.

while the averages remain unchanged. The resulting average fidelity is maximized with respect to r, g_{sin}, g_{cos}, κ_1 and κ_2 ($\kappa_1/2$ denote the coupling strength corresponding the first/second light-matter interaction and $g_{sin/cos}$ are the gainfactors characterizing the feedback of $x_{sin/cos}$ onto x_B/p_B as explained in Sec. 4.1.3). The values for κ_1 and κ_2 are restricted as specified in the figure caption. In order to obtain plot D.2a, the constraint $r < \frac{3\ln(10)}{10}$ was added in the optimization. For plot D.2b, the variances

$$\begin{pmatrix} \Delta(x^{fin}_{B,squ})^2 \\ \Delta(p^{fin}_{B,squ})^2 \end{pmatrix} = \frac{1}{2}\begin{pmatrix} (1-\frac{\kappa_1 g_{sin}}{\sqrt{2}})^2 \\ (1+\frac{\kappa_1 g_{cos}}{\sqrt{2}})^2 \end{pmatrix} + \frac{1}{2}\begin{pmatrix} \frac{\kappa_2^2 g_{sin}^2}{2} \\ \frac{\kappa_2^2 g_{cos}^2}{2} \end{pmatrix} + \frac{1}{2}e^{-r}\begin{pmatrix} g_{sin}^2 \\ g_{cos}^2 \end{pmatrix} + \frac{1}{2}e^{\acute{r}}\left(\frac{\kappa_1^2+\kappa_2^2}{4\sqrt{3}}\right)^2\begin{pmatrix} g_{sin}^2 \\ g_{cos}^2 \end{pmatrix} + \frac{1}{2}e^{\acute{r}}\begin{pmatrix} (\frac{\kappa 1}{\sqrt{2}} - g_{sin}\frac{\kappa_1^2+\kappa_2^2}{4})^2 \\ (\frac{\kappa 1}{\sqrt{2}} + g_{cos}\frac{\kappa_1^2+\kappa_2^2}{4})^2 \end{pmatrix},$$

with $\acute{r} = \frac{6\ln(10)}{10}$ were used. The results indicate that the use of squeezed light allows one to circumvent the problem posed by the dramatic decrease of the teleportation fidelities if the coupling strength is limited to realistic values. However since this strategy requires a squeezed light source, it involves a substantial experimental overhead.

QND teleportation involving the measurement of higher order backaction modes

The fidelity can also be increased, if the p-quadratures of the 1st order backaction mode of the light field, $p_{sin,1}$ and $p_{cos,1}$, can be measured in addition to x_{sin} and x_{cos} (note that the 0st and 1st order backaction modes are independent $[x_{sin}, p_{sin,1}] = 0$). More specifically, the final input-output relations for Bob's variables after feedback of the measurement results for x_{sin}, x_{cos}, $p_{sin,1}$ and $p_{cos,1}$ with respective gain factors g_{sin}, g_{cos}, G_{sin} and G_{cos}

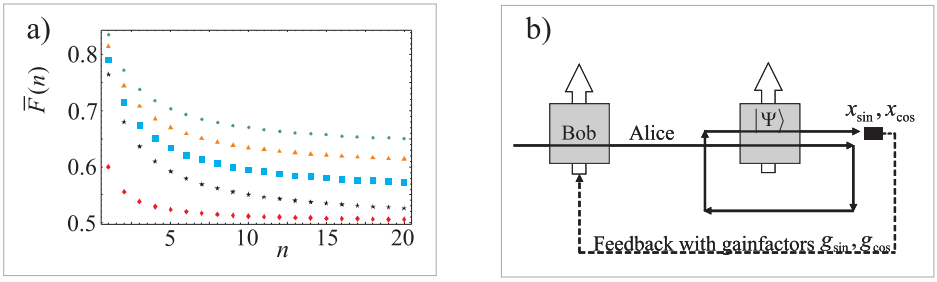

Figure D.3: Improved QND teleportation schemes a) Average teleportation fidelity $\bar{F}(n)$ versus width of the distribution of input states n for limited couplings if $p_{sin,1}$, $p_{cos,1}$, x_{sin} and x_{cos} can be measured. The lowest (red) line represents the classical limit. The other curves show the fidelities for $\kappa^2_{max} = 1.69$ (green stars), $\kappa^2_{max} = 1.44$ (orange squares), $\kappa^2_{max} = 1.21$ (blue triangles) and $\kappa^2_{max} = 1.0$ (black dots). b) Setup for the double pass teleportation scheme described in the text.

read

$$\begin{aligned}
\begin{pmatrix} x_B^{fin} \\ p_B^{fin} \end{pmatrix} &= \begin{pmatrix} x_B^{out} \\ p_B^{out} \end{pmatrix} + \begin{pmatrix} g_{sin}\ \tilde{x}_{sin}^{out} \\ g_{cos}\ \tilde{x}_{cos}^{out} \end{pmatrix} + \begin{pmatrix} G_{cos}\ \tilde{p}_{cos,1}^{out} \\ G_{sin}\ \tilde{p}_{sin,1}^{out} \end{pmatrix} \\
&= \begin{pmatrix} (1-\frac{\kappa_1 g_{sin}}{\sqrt{2}})\ x_B^{in} \\ (1+\frac{\kappa_1 g_{cos}}{\sqrt{2}})\ p_B^{in} \end{pmatrix} + \begin{pmatrix} -\frac{\kappa_2 g_{sin}}{\sqrt{2}}\ x_V^{in} \\ \frac{\kappa_2 g_{cos}}{\sqrt{2}}\ p_V^{in} \end{pmatrix} + \begin{pmatrix} g_{sin} x_{sin}^{in} \\ g_{cos} x_{cos}^{in} \end{pmatrix} + \begin{pmatrix} (\frac{\kappa 1}{\sqrt{2}} - g_{sin}\frac{\kappa_1^2+\kappa_2^2}{4})\ p_{cos}^{in} \\ (\frac{\kappa 1}{\sqrt{2}} + g_{cos}\frac{\kappa_1^2+\kappa_2^2}{4})\ p_{sin}^{in} \end{pmatrix} \\
&+ \begin{pmatrix} (-g_{sin}\frac{\kappa_1^2+\kappa_2^2}{\sqrt{3}\ 4} + G_{cos})\ p_{cos,1}^{in} \\ (g_{cos}\frac{\kappa_1^2+\kappa_2^2}{\sqrt{3}\ 4} + G_{sin})\ p_{sin,1}^{in} \end{pmatrix}.
\end{aligned}$$

Optimally, G_{sin} and G_{cos} are chosen such that the last term in the equation is zero and the average fidelities shown in Fig. D.3a are obtained. This strategy yields a significant improvement, however the simultaneous measurement of x_{sin}, and $p_{sin,1}$ is technically very demanding. In current experiments [14–16, 18, 95, 452] either the x-quadrature of the light field or the p-quadrature is measured by homodyne detection. Different modulation functions can be analyzed in a second (postprocessing) step of the data. The simultaneous measurement of of x_{sin}, and $p_{sin,1}$ would require the measurement of both, the x-quadrature of the light field as well as the p-quadrature. Due to the different modulation functions, x_{sin}, and $p_{sin,1}$ are independent observables in principle, but they cannot be measured at the same time using the detection methods which are currently used.

QND teleportation using a double pass scheme

Alternatively, the attainable teleportation fidelity can be increased by employing a double pass scheme [98–100] as shown in Fig. D.3b. More specifically, a situation is considered in which the laser pulse passes the right ensemble completely before it reenters the sample again, such that it does not encounter itself inside the atomic ensemble. The input-output relations for Bob's ensemble after the interaction with the light field are the same as in the basic protocol discussed in Sec. 4.1.3. The input-output relations for the quadratures

of the light field after the third (final) pass $\acute{x}^{out}_{cos}$, $\acute{x}_{sin}$ are given by

$$\begin{pmatrix} \acute{x}^{out}_{cos} \\ \acute{x}^{out}_{sin} \end{pmatrix} = \begin{pmatrix} x^{in}_{cos} \\ x^{in}_{sin} \end{pmatrix} + \frac{\kappa_1}{\sqrt{2}} \begin{pmatrix} p^{in}_B \\ -x^{in}_B \end{pmatrix} + \sqrt{2}\kappa_2 \begin{pmatrix} p^{in}_V \\ -x^{in}_V \end{pmatrix} + \frac{\kappa_1^2+4\kappa_2^2}{4} \begin{pmatrix} p^{in}_{sin} \\ -p^{in}_{cos} \end{pmatrix} + \frac{\kappa_1^2+2\kappa_2^2}{\sqrt{3}\ 4} \begin{pmatrix} p^{in}_{sin,1} \\ -p^{in}_{cos,1} \end{pmatrix}.$$

As in the basic protocol, $\acute{x}_{sin}$ and $\acute{x}_{cos}$ are measured after the last pass, and fed back onto Bob's ensemble. In this case,

$$\begin{aligned} \begin{pmatrix} x^{fin}_B \\ p^{fin}_B \end{pmatrix} &= \begin{pmatrix} x^{out}_B \\ p^{out}_B \end{pmatrix} + \begin{pmatrix} g_{sin}\ \acute{x}^{out}_{sin} \\ g_{cos}\ \acute{x}^{out}_{cos} \end{pmatrix} \\ &= \begin{pmatrix} (1-\frac{\kappa_1 g_{sin}}{\sqrt{2}})\ x^{in}_B \\ (1+\frac{\kappa_1 g_{cos}}{\sqrt{2}})\ p^{in}_B \end{pmatrix} + \begin{pmatrix} -\kappa_2 g_{sin}\sqrt{2}\ x^{in}_V \\ \kappa_2 g_{cos}\sqrt{2}\ p^{in}_V \end{pmatrix} + \frac{\kappa_1^2+2\kappa_2^2}{\sqrt{3}\ 4} \begin{pmatrix} -g_{sin}\ p^{in}_{cos,1} \\ g_{cos}\ p^{in}_{sin,1} \end{pmatrix} \\ &+ \begin{pmatrix} g_{sin}\ x^{in}_{sin} \\ g_{cos}\ x^{in}_{cos} \end{pmatrix} + \begin{pmatrix} (\frac{\kappa 1}{\sqrt{2}} - g_{sin}\frac{\kappa_1^2+4\kappa_2^2}{4})\ p^{in}_{cos} \\ (\frac{\kappa 1}{\sqrt{2}} + g_{cos}\frac{\kappa_1^2+4\kappa_2^2}{4})\ p^{in}_{sin} \end{pmatrix} \end{aligned}$$

is obtained. Note that this scheme does not correspond to the basic protocol with $\kappa_2 \to 2\kappa_2$. This is due to the fact that atomic contributions corresponding to the right ensemble (x_V, p_V) are enhanced by a factor 2 ($\kappa_2 \to 2\kappa_2$), while contributions from the higher order backaction modes of the light fields are only enhanced by a factor $\sqrt{2}$ ($\kappa_2^2 \to 2\kappa_2^2$). Moreover, contributions proportional to p_{sin}, p_{cos}, which have been stored in the atoms during the first round are mapped to the light field, when it enters the right ensemble the second time. The resulting optimized average fidelity is shown in Fig. D.4. As shown in Fig. D.4b, the double pass scheme performs better than the single pass scheme for restricted couplings. In this comparison, the total coupling strength is fixed, that is, in the double pass scheme, only $\kappa^2_{2,max}/2$ is available for each of the two rounds.

Rather than applying a double pass scheme as outlined above, two individual pulses of light can be sent consecutively through the two atomic ensembles which is easier to realize experimentally. Using this simpler procedure, a higher fidelity can by achieved by means of the two pass scheme compared to a strategy, where only one long single pass (corresponding to twice the coupling strength used in each previous pass) is sent through the ensembles. This is due to the fact that two different parameter sets (couplings and feedback gains) can be chosen in the first case. In the following section this is investigated in more general terms by allowing for arbitrarily shaped light pulses and arbitrary feedback-functions.

D.2.2 Input-output relations for a single cell in a magnetic field for a time dependent coupling strength and an arbitrary readout mode

This appendix complements Sec. 4.1.3, where it is shown that a judicious choice of slowly varying functions modulating the coupling strengths and the readout modes can lead to a substantial improvement of the performance of the QND teleportation protocol (see Sec. 4.1.2). In the following, the input-output relations for a single cell in a magnetic field

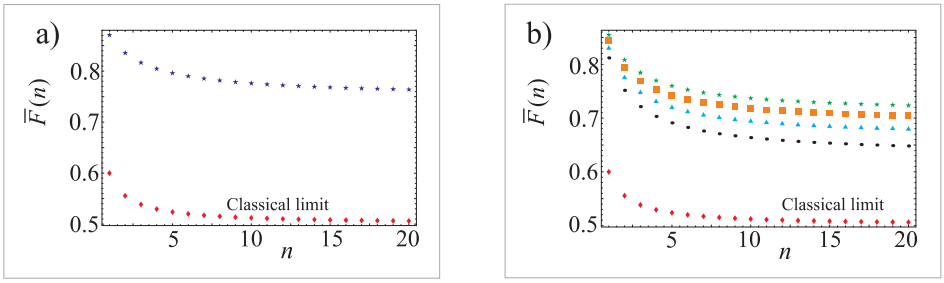

Figure D.4: Average teleportation fidelity $\bar{F}(n)$ versus width of the distribution of input states n for the double-pass scheme shown in Fig. D.3b. The lowest (red) curve in each panel reperesents the classical limit. a) The upper curve depicts the optimized average fidelity in the ideal case. b) Optimized average fidelity for restricted couplings. The four topmost curves correspond to $\kappa^2_{1,max} = 1.69$, $\kappa^2_{2,max} = 1.69/2$ (green stars), $\kappa^2_{1,max} = 1.44$, $\kappa^2_{2,max} = 1.44/2$ (orange squares), $\kappa^2_{1,max} = 1.21$, $\kappa^2_{2,max} = 1.21/2$ (blue triangles) and $\kappa^2_{1,max} = 1.0$, $\kappa^2_{2,max} = 0.5$ (black dots).

are derived for a time dependent coupling strength and light modes with arbitrary envelope functions. To this end, a time depending coupling strength $\kappa(t) = \kappa f(t)$ is considered, where the function $f(t)$ describing the temporal profile is assumed to be normalized such that

$$\frac{1}{T}\int_0^T f(t)^2 dt = 1.$$

T is the duration of the light pulse. The corresponding Maxwell Bloch equations are obtained by evaluating the Heisenberg equations using $H = H_A + H_L + H_{int}$, where $H_A = \frac{\Omega}{2}(x_A^2 + p_A^2)$, H_L is the free Hamiltonian of the light field and the time-dependent interaction Hamiltonian H_{int} is given by

$$H_{int} = \frac{\kappa(t)}{\sqrt{T}} p_A p_L.$$

In the rotating frame (using the variable transformation $\xi = ct - r$, as explained in Sec. D.1.1) the solution to this set of equations is given by

$$\begin{aligned}
x_A(t) &= x_A(0) + \frac{\bar{\kappa}}{\sqrt{T}}\int_0^T d\tau f(\tau)\cos(\Omega\tau) p_L(c\tau, 0), \\
p_A(t) &= p_A(0) + \frac{\bar{\kappa}}{\sqrt{T}}\int_0^T d\tau f(\tau)\sin(\Omega\tau) p_L(c\tau, 0), \\
x_L(\xi, t) &= x_L(\xi, 0) + \frac{\bar{\kappa}}{\sqrt{T}} f(\xi/c)[-\sin(\Omega\xi/c) x_A(\xi/c) \\
&\quad + \cos(\Omega\xi/c) p_A(\xi/c)] \\
p_L(\xi, t) &= p_L(\xi, 0),
\end{aligned}$$

It is assumed that the function $f(t)$ varies on a time scale much slower than the Larmor frequency Ω. The duration of the pulse measured in Larmor periods ΩT is considered to

be large $(\Omega T)^{-1} \ll 1$. For a pulse length of the order of ms and Larmor frequencies of the order of MHz (as in the experimental setup reported in [14–16, 18, 95, 452]) this is very well justified. In particular, the approximations

$$\int_0^T d\tau f(\tau)\sin^2(\Omega\tau) = \int_0^T d\tau f(\tau)\cos^2(\Omega\tau) \simeq \frac{1}{2}\int_0^T d\tau f(\tau),$$
$$\int_0^T d\tau f(\tau)\sin(\Omega\tau)\cos(\Omega\tau) \simeq 0$$

are used in the following. This yields directly

$$\begin{pmatrix} x_B^{out} \\ p_B^{out} \end{pmatrix} = \begin{pmatrix} x_B^{in} \\ p_B^{in} \end{pmatrix} + \frac{\kappa}{\sqrt{2}} \begin{pmatrix} p_{f,cos}^{out} \\ p_{f,sin}^{out} \end{pmatrix}, \tag{D.8}$$

where the time dependence of the coupling strength has been absorbed in the definition of the light modes

$$\begin{aligned} p_{f,cos}^{in} &= \sqrt{\frac{2}{T}} \int_0^T d\tau f(\tau)\cos(\Omega\tau) p_L(c\tau, 0), \\ p_{f,sin}^{in} &= \sqrt{\frac{2}{T}} \int_0^T d\tau f(\tau)\sin(\Omega\tau) p_L(c\tau, 0). \end{aligned}$$

Analogous expressions hold for $x_{f,sin}$ and $x_{f,cos}$. After the scattering interaction, the light field is read out according to some profile $h(t)$. More specifically,

$$\begin{aligned} \begin{pmatrix} x_{h,sin}^{out} \\ x_{h,cos}^{out} \end{pmatrix} &= \sqrt{\frac{2}{T}} \int_0^T d\tau h(\tau) \begin{pmatrix} \sin(\Omega\tau) \\ \cos(\Omega\tau) \end{pmatrix} x_L(c\tau, T), \\ &= \begin{pmatrix} x_{h,sin}^{in} \\ x_{h,cos}^{in} \end{pmatrix} + \frac{\kappa}{\sqrt{2}T} \int_0^T d\tau f(\tau)h(\tau) \begin{pmatrix} -x_A^{in} \\ p_A^{in} \end{pmatrix} + \frac{\kappa^2}{\sqrt{2}T^{3/2}} \int_0^T d\tau \int_0^\tau d\acute{\tau} f(\tau)h(\tau)f(\acute{\tau}) \begin{pmatrix} -\cos(\Omega\acute{\tau}) p_L(c\acute{\tau}, 0) \\ \sin(\Omega\acute{\tau}) p_L(c\acute{\tau}, 0) \end{pmatrix}, \\ &= \begin{pmatrix} x_{h,sin}^{in} \\ x_{h,cos}^{in} \end{pmatrix} + \frac{\kappa}{\sqrt{2}T} \int_0^T d\tau f(\tau)h(\tau) \begin{pmatrix} -x_A^{in} \\ p_A^{in} \end{pmatrix} + \frac{\kappa^2}{\sqrt{2}T^{3/2}} \int_0^T d\acute{\tau} \int_{\acute{\tau}}^T d\tau f(\tau)h(\tau)f(\acute{\tau}) \begin{pmatrix} -\cos(\Omega\acute{\tau}) p_L(c\acute{\tau}, 0) \\ \sin(\Omega\acute{\tau}) p_L(c\acute{\tau}, 0) \end{pmatrix}. \end{aligned}$$

The last term can be decomposed into a part proportional to $(p_{f,cos}^{in}, p_{f,sin}^{in})^T$ and an orthogonal mode

$$\frac{\kappa^2}{\sqrt{2}T^{3/2}} \int_0^T d\acute{\tau} f(\acute{\tau}) \begin{pmatrix} -\cos(\Omega\acute{\tau}) \\ \sin(\Omega\acute{\tau}) \end{pmatrix} p_L(c\acute{\tau}, 0) \int_{\acute{\tau}}^T d\tau f(\tau)\acute{f}(\tau) = \alpha \begin{pmatrix} -p_{f,cos}^{in} \\ p_{f,cos}^{in} \end{pmatrix} + \beta \begin{pmatrix} -p_{f,cos,1}^{in} \\ p_{f,cos,1}^{in} \end{pmatrix}.$$

The coefficients α and β can be calculated using the conditions $[x_{f,cos}, \alpha p_{f,cos}^{in} + \beta p_{f,cos,1}^{in}] = i\alpha$ and $[x_{f,cos,1}^{in}, p_{f,cos,1}^{in}] = i$, yielding

$$\begin{pmatrix} x_{h,sin}^{out} \\ x_{h,cos}^{out} \end{pmatrix} = \begin{pmatrix} x_{h,sin}^{in} \\ x_{h,cos}^{in} \end{pmatrix} + \frac{\kappa}{\sqrt{2}T} \int_0^T d\tau f(\tau)h(\tau) \begin{pmatrix} -x_A^{in} \\ p_A^{in} \end{pmatrix} + \alpha \begin{pmatrix} -p_{f,cos}^{in} \\ p_{f,sin}^{in} \end{pmatrix} + \beta \begin{pmatrix} -p_{f,cos,1}^{in} \\ p_{f,sin,1}^{in} \end{pmatrix},$$

where the coefficients α and β are given by the expressions

$$\begin{aligned} \alpha &= \frac{\kappa^2}{2T} \int_0^T d\acute{\tau} f(\acute{\tau})^2 \, \frac{1}{T} \int_{\acute{\tau}}^T d\tau f(\tau)h(\tau), \\ \beta^2 &= \frac{\kappa^4}{4T} \int_0^T d\acute{\tau} f(\acute{\tau})^2 \, \left(\frac{1}{T} \int_{\acute{\tau}}^T d\tau f(\tau)h(\tau) \right)^2 - \alpha^2. \end{aligned}$$

The quality of the state transfer depends therefore on the overlap of the function $f(t)$, which is used to modulate the input field and the function $h(t)$ which is used for the readout of the light field after the interaction. For $\frac{1}{T}\int d\tau f(\tau)h(\tau) = 0$, no mapping of atomic quadratures onto the light field and vice vera can be observed.

D.3 Non-QND teleportation

This appendix complements Sec. 4.1.4. In App. D.3.1, we derive the input-output relations for the setup involving parallel oriented magnetic fields in the ideal case. In App. D.3.2, we deirive the equations which lead to the final input-output relations for the non-QND teleportation in the antiparallel setup including noise.

D.3.1 Non-QND teleportation in the ideal case for antiparallel oriented magnetic fields

For antiparallel oriented magnetic fields, the input-output relations can be derived as follows. If the light-matter interactions involving the first and second ensemble are the same,

$$H_{1/2} = \frac{\kappa}{\sqrt{T}}\left(p_{B/V}\; p_L(0) \pm \frac{1}{Z^2} x_{B/V}\; x_L(0)\right) \mp \frac{\Omega}{2}\left(x_{B/V}^2 + p_{B/V}^2\right) + H_L, \tag{D.9}$$

where the upper (lower) sign corresponds to a predominantly passive (active) interaction. Step (i) of the teleportation protocol explained in Sec. 4.1.2 results in

$$\begin{aligned}
\begin{pmatrix} x_B(t) \\ p_B(t) \end{pmatrix} &= e^{\frac{\mp\kappa^2 t}{2Z^2T}} \begin{pmatrix} x_B^{in} \\ p_B^{in} \end{pmatrix} + \frac{\kappa}{\sqrt{T}} \int_0^t d\tau e^{\frac{\mp\kappa^2(t-\tau)}{2Z^2T}} A_{\mathrm{P/A}}(\Omega,\tau) \begin{pmatrix} \bar{x}_L(c\tau,0) \\ \bar{p}_L(c\tau,0) \end{pmatrix}, \\
\begin{pmatrix} x_{h,sin}^{out} \\ x_{h,cos}^{out} \end{pmatrix} &= \begin{pmatrix} x_{h,sin}^{in} \\ x_{h,cos}^{in} \end{pmatrix} + \frac{\kappa}{\sqrt{2}T} \int_0^T dt h(t) e^{\frac{\mp\kappa^2 t}{2Z^2T}} \begin{pmatrix} x_B^{in} \\ p_B^{in} \end{pmatrix} \\
&+ \frac{\kappa^2}{\sqrt{2}T^{\frac{3}{2}}} \int_0^T dt \int_0^t d\tau h(t) e^{\frac{\mp\kappa^2(t-\tau)}{2Z^2T}} A_{\mathrm{P/A}}(\Omega,\tau) \begin{pmatrix} \bar{x}_L(c\tau,0) \\ \bar{p}_L(c\tau,0) \end{pmatrix},
\end{aligned} \tag{D.10}$$

step (ii) leads to

$$\begin{aligned}
\begin{pmatrix} x_V(t) \\ p_V(t) \end{pmatrix} &= e^{\frac{\mp\kappa^2 t}{2Z^2T}} \begin{pmatrix} x_V^{in} \\ p_V^{in} \end{pmatrix} + \frac{\kappa}{\sqrt{T}} \int_0^t d\tau e^{\frac{\mp\kappa^2(t-\tau)}{2Z^2T}} A_{\mathrm{P/A}}(-\Omega,\tau) \begin{pmatrix} \bar{x}_L(c\tau,0) \\ \bar{p}_L(c\tau,0) \end{pmatrix}, \\
\begin{pmatrix} \tilde{x}_{h,sin}^{out} \\ \tilde{x}_{h,cos}^{out} \end{pmatrix} &= \begin{pmatrix} x_{h,sin}^{in} \\ x_{h,cos}^{in} \end{pmatrix} + \frac{\kappa}{\sqrt{2}T} \int_0^T dt h(t) e^{\frac{\mp\kappa^2 t}{2Z^2T}} \begin{pmatrix} x_B^{in} - x_V^{in} \\ p_B^{in} + p_V^{in} \end{pmatrix} \\
&\mp \frac{\kappa^2\sqrt{2}}{T^{\frac{3}{2}}Z^2} \int_0^T dt \int_0^t d\tau h(t) e^{\frac{\mp\kappa^2(t-\tau)}{2Z^2T}} \begin{pmatrix} \sin(\Omega\tau)\bar{x}_L(c\tau,0) \\ \cos(\Omega\tau)\bar{x}_L(c\tau,0) \end{pmatrix},
\end{aligned}$$

and the final atomic state after the feedback operation is given by

$$\begin{aligned}\begin{pmatrix} x_B^{fin} \\ p_B^{fin} \end{pmatrix} &= \frac{\kappa}{\sqrt{2}T}\int_0^T dt h(t) e^{\frac{\mp\kappa^2 t}{2Z^2T}} G_- \begin{pmatrix} x_V^{in} \\ p_V^{in} \end{pmatrix} + \left(e^{\frac{\mp\kappa^2}{2Z^2}}\mathbb{1} + \frac{\kappa}{\sqrt{2}T}\int_0^T dt h(t) e^{\frac{\mp\kappa^2 t}{2Z^2T}} G_+ \right) \begin{pmatrix} x_B^{in} \\ p_B^{in} \end{pmatrix} \\ &+ G_+ \begin{pmatrix} x_{g,sin}^{in} \\ x_{g,cos}^{in} \end{pmatrix} + \frac{\kappa}{\sqrt{T}}\int_0^T dt e^{\frac{\mp\kappa^2(T-t)}{2Z^2T}} \begin{pmatrix} \cos(\Omega t)\bar{p}_L(ct,0) \\ -\sin(\Omega t)\bar{p}_L(ct,0) \end{pmatrix} \\ &\mp \frac{\kappa}{\sqrt{T}Z^2}\int_0^T d\tau \left(e^{\frac{\mp\kappa^2(T-\tau)}{2Z^2T}}\mathbb{1} + \frac{\kappa\sqrt{2}}{T}\int_\tau^T dt h(t) e^{\frac{\mp\kappa(t-\tau)}{2Z^2T}} G_+ \right) \begin{pmatrix} \sin(\Omega\tau)\bar{x}_L(c\tau,0) \\ \cos(\Omega\tau)\bar{x}_L(c\tau,0) \end{pmatrix}.\end{aligned}$$

If the light-matter interactions involving the first and second ensemble are of different type

$$\begin{aligned} H_1 &= \frac{\kappa}{\sqrt{T}}\left(p_B p_L(0) \mp \frac{1}{Z^2} x_B\ x_L(0) \right) - \frac{\Omega}{2}\left(x_B^2 + p_B^2 \right) + H_L, \\ H_2 &= \frac{\kappa}{\sqrt{T}}\left(p_V\ p_L(0) \pm \frac{1}{Z^2} x_V\ x_L(0) \right) + \frac{\Omega}{2}\left(x_V^2 + p_V^2 \right) + H_L, \end{aligned} \tag{D.11}$$

where the upper (lower) sign corresponds to an active-passive (passive-active) configuration. Step (i) of the teleportation scheme discussed in 4.1 is described by Eq. (D.10), with $Z^2 \to -Z^2$. Step (ii) results in

$$\begin{aligned}\begin{pmatrix} x_V(t) \\ p_C(t) \end{pmatrix} &= e^{\frac{\mp\kappa^2 t}{2Z^2T}} \begin{pmatrix} x_V^{in} \\ p_V^{in} \end{pmatrix} \pm 2\sinh\left(\frac{\kappa^2 t}{2Z^2T}\right) \begin{pmatrix} x_B^{in} \\ -p_B^{in} \end{pmatrix} + \frac{\kappa}{\sqrt{T}}\int_0^t d\tau e^{\frac{\pm\kappa^2(t-\tau)}{2Z^2T}} A_{\mathrm{P/A}}(-\Omega,\tau) \begin{pmatrix} \bar{x}_L(c\tau,0) \\ \bar{p}_L(c\tau,0) \end{pmatrix}, \\ \begin{pmatrix} \tilde{x}_{h,sin}^{out} \\ \tilde{x}_{h,cos}^{out} \end{pmatrix} &= \begin{pmatrix} x_{h,sin}^{in} \\ x_{h,cos}^{in} \end{pmatrix} + \frac{\kappa}{T\sqrt{2}}\int_0^T dt h(t) e^{\frac{\mp\kappa^2 t}{2Z^2T}} \begin{pmatrix} x_B^{in} - x_V^{in} \\ p_B^{in} + p_V^{in} \end{pmatrix},\end{aligned}$$

and after the feedback operation (step (iii))

$$\begin{aligned}\begin{pmatrix} x_B^{fin} \\ p_B^{fin} \end{pmatrix} &= \frac{\kappa}{\sqrt{2}T}\int_0^T dt h(t) e^{\frac{\mp\kappa^2 t}{2Z^2T}} G_- \begin{pmatrix} x_V^{fin} \\ p_V^{fin} \end{pmatrix} + \left(e^{\frac{\pm\kappa^2}{2Z^2}}\mathbb{1} + \frac{\kappa}{\sqrt{2}T}\int_0^T dt h(t) e^{\frac{\mp\kappa^2 t}{2Z^2T}} G_+ \right) \begin{pmatrix} x_B^{fin} \\ p_B^{fin} \end{pmatrix} \\ &+ \int_0^T dt \left(\pm\frac{\kappa}{\sqrt{T}Z^2} e^{\frac{\pm\kappa^2(T-t)}{2Z^2T}}\mathbb{1} + \sqrt{\frac{2}{T}} h(t) G_+ \right) \begin{pmatrix} \sin(\Omega t)\bar{x}_L(c\tau,0) \\ \cos(\Omega t)\bar{x}_L(c\tau,0) \end{pmatrix} \\ &+ \frac{\kappa}{\sqrt{T}}\int_0^T dt e^{\frac{\pm\kappa^2(T-t)}{2Z^2T}} \begin{pmatrix} \cos(\Omega t)\bar{p}_L(ct0) \\ -\sin(\Omega t)\bar{p}_L(ct0) \end{pmatrix}\end{aligned}$$

is obtained. For antiparallel magnetic fields, the classical limit can be surpassed for all possible combinations (passive-passive, active-active, passive-active and active-passive) for $Z = 2.5$ in the ideal case, but the teleportation fidelities are well below the fidelities that can be reached using the parallel setup discussed in the main text.

D.3.2 Non-QND teleportation for parallel magnetic fields including transverse atomic decay

In this appendix, Eq. (4.8) and Eq. (4.9) in Sec. 4.1.4 are derived. If a predominantly passive interaction is employed and a constant decay of the transverse atomic spin state

at a rate η/T is assumed as discussed in App. D.1.2, the input-output relations for Bob's ensemble and the light field corresponding to step (i) of the teleportation protocol correspond to Eq. (D.7) and Eq. (4.7) respectively. The active variant is obtained by considering $Z^2 \to -Z^2$. If the same interaction is used twice in succession, step (ii) of the teleportation protocol results in

$$\begin{aligned}\begin{pmatrix} x_V^{out} \\ p_V^{out} \end{pmatrix} &= e^{-\frac{\gamma_{\mathrm{A/P}} t}{2T}} \begin{pmatrix} x_V^{in} \\ p_V^{in} \end{pmatrix} + \sqrt{\frac{\eta}{T}} \int_0^t d\tau e^{-\frac{\gamma_{\mathrm{A/P}}(t-\tau)}{2T}} \begin{pmatrix} f_{x_V}(\tau) \\ f_{p_V}(\tau) \end{pmatrix} \pm \frac{\kappa^2 t}{Z^2 T} e^{-\frac{\gamma_{\mathrm{A/P}} t}{2T}} \begin{pmatrix} x_B^{in} \\ p_B^{in} \end{pmatrix} \\ &+ \frac{\kappa}{\sqrt{T}} \int_0^t d\tau e^{-\frac{\gamma_{\mathrm{A/P}}(t-\tau)}{2T}} \left(1 \pm \frac{\kappa^2}{Z^2 T}(t-\tau)\right) A_{\mathrm{A/P}}(\Omega,\tau) \begin{pmatrix} \bar{x}_L(c\tau,0) \\ \bar{p}_L(c\tau,0) \end{pmatrix} \\ &\pm \frac{\kappa^2 \sqrt{\eta}}{Z^2 T^{\frac{3}{2}}} \int_0^t d\tau (t-\tau) e^{-\frac{\gamma_{\mathrm{A/P}}(t-\tau)}{2T}} \begin{pmatrix} f_{x_B}(\tau) \\ f_{p_B}(\tau) \end{pmatrix},\end{aligned}$$

$$\begin{aligned}\begin{pmatrix} \tilde{x}_{h,sin}^{out} \\ \tilde{x}_{h,cos}^{out} \end{pmatrix} &= \begin{pmatrix} x_{h,sin}^{in} \\ x_{h,cos}^{in} \end{pmatrix} + \frac{\kappa}{\sqrt{2}T} \int_0^T dt h(t) e^{-\frac{\gamma_{\mathrm{A/P}} t}{2T}} \begin{pmatrix} x_V^{in} \\ p_V^{in} \end{pmatrix} \\ &+ \frac{\kappa\sqrt{\eta}}{\sqrt{2}T^{\frac{3}{2}}} \int_0^T dt \int_0^t d\tau h(t) e^{-\frac{\gamma_{\mathrm{A/P}}(t-\tau)}{2T}} \begin{pmatrix} f_{x_V}(\tau) \\ f_{p_V}(\tau) \end{pmatrix} \\ &+ \frac{\kappa}{\sqrt{2}T} \int_0^T dt h(t) e^{-\frac{\gamma_{\mathrm{A/P}} t}{2T}} \left(1 \mp \frac{\kappa^2 t}{Z^2 T}\right) \begin{pmatrix} x_B^{in} \\ p_B^{in} \end{pmatrix} \\ &+ \frac{\kappa\sqrt{\eta}}{\sqrt{2}T^{\frac{3}{2}}} \int_0^T dt \int_0^t d\tau h(t) e^{-\frac{\gamma_{\mathrm{A/P}}(t-\tau)}{2T}} \left(1 \pm \frac{\kappa^2 (t-\tau)}{Z^2 T}\right) \begin{pmatrix} f_{x_B}(\tau) \\ f_{p_B}(\tau) \end{pmatrix} \\ &+ \frac{\kappa^2}{\sqrt{2}T^{\frac{3}{2}}} \int_0^T dt \int_0^t d\tau h(t) e^{-\frac{\gamma_{\mathrm{A/P}}(t-\tau)}{2T}} \left(2 \pm \frac{\kappa^2 (t-\tau)}{Z^2 T}\right) A_{\mathrm{A/P}}(\Omega,\tau) \begin{pmatrix} \bar{x}_L(c\tau,0) \\ \bar{p}_L(c\tau,0) \end{pmatrix},\end{aligned}$$

where the upper (lower) sign corresponds to a setting where the active (passive) variant is employed (in both interactions). These expressions give rise to Eq. (4.8). Finally, we consider the case, where different types of interactions are used in step (i) and step (ii). If first a predominantly active/passive and then a mainly passive/active interaction is used,

$$\begin{aligned}\begin{pmatrix} x_V^{out} \\ p_V^{out} \end{pmatrix} &= e^{-\frac{\gamma_{\mathrm{P/A}} t}{2T}} \begin{pmatrix} x_V^{in} \\ p_V^{in} \end{pmatrix} + \frac{\kappa}{\sqrt{T}} \int_0^t d\tau e^{-\frac{\gamma_{\mathrm{P/A}}(t-\tau)}{2T}} A_{\mathrm{P/A}}(\Omega,\tau) \begin{pmatrix} \bar{x}_L(c\tau,0) \\ \bar{p}_L(c\tau,0) \end{pmatrix} \\ &+ \sqrt{\frac{\eta}{T}} \int_0^t d\tau e^{-\frac{\gamma_{\mathrm{P/A}}(t-\tau)}{2T}} \begin{pmatrix} f_{x_V}(\tau) \\ f_{p_V}(\tau) \end{pmatrix},\end{aligned}$$

$$\begin{aligned}\begin{pmatrix} \tilde{x}_{h,sin}^{out} \\ \tilde{x}_{h,cos}^{out} \end{pmatrix} &= \begin{pmatrix} x_{h,sin}^{in} \\ x_{h,cos}^{in} \end{pmatrix} + \frac{\kappa}{\sqrt{2}T} \int_0^T dt h(t) \left(e^{-\frac{\gamma_{\mathrm{A/P}} t}{2T}} \begin{pmatrix} x_B^{in} \\ p_B^{in} \end{pmatrix} + e^{-\frac{\gamma_{\mathrm{P/A}} t}{2T}} \begin{pmatrix} x_V^{in} \\ p_V^{in} \end{pmatrix} \right) \\ &+ \frac{\sqrt{\eta}\kappa}{\sqrt{2}T^{\frac{3}{2}}} \int_0^T d\tau \int_\tau^T dt h(t) \left(e^{-\frac{\gamma_{\mathrm{A/P}}(t-\tau)}{2T}} \begin{pmatrix} f_{x_B}(\tau) \\ f_{p_B}(\tau) \end{pmatrix} + e^{-\frac{\gamma_{\mathrm{P/A}}(t-\tau)}{2T}} \begin{pmatrix} f_{x_V}(\tau) \\ f_{p_V}(\tau) \end{pmatrix} \right) \\ &+ \frac{\kappa^2}{\sqrt{2}T^{\frac{3}{2}}} \int_0^T d\tau \int_\tau^T dt h(t) \left(e^{\frac{-\gamma_{\mathrm{A/P}}(t-\tau)}{2T}} A_{\mathrm{A/P}}(\Omega,\tau) + e^{\frac{-\gamma_{\mathrm{P/A}}(t-\tau)}{2T}} A_{\mathrm{P/A}}(\Omega,\tau) \right) \begin{pmatrix} \bar{x}_L(c\tau,0) \\ \bar{p}_L(c\tau,0) \end{pmatrix}\end{aligned}$$

is obtained, which gives rise to Eq. (4.9).

Thank

First and foremost, I would like to thank Ignacio Cirac for his support and for the great gifts I received over the last years in the form of ideas, advice, guidance, support, challenge and inspiration. I'm very grateful for the opportunities he provided me with.
I am also deeply thankful to Eugene Polzik for his advice, for his generous hospitality during my stays at the Niels Bohr Institute in Copenhagen and for supporting and encouraging me in many ways.

I also want to express my thank to Iris Abt for helping me with difficult decisions and for taking the time to accompany me on my way through the world of Science.

I owe many thanks to Géza Giedke. He is a remarkable and extremely knowledgeable scientist and I'm very grateful that he shares his time and expertise so generously. I also want to express my gratitude to another very special person, conformal Anne, who shared her ideas, knowledge and sometimes also a room with me.

During the last years, I had the opportunity to work with various people to whom I'm very thankful for their contributions. I am particularly happy that I had the possibility to work with Diego Porras to whom I express my enthusiastic thanks for many intense, lively and stimulating discussions. I also thank successful Klemens, my co-conspirator on quantum interfaces with whom it is always a joy to work.

It was a great pleasure to work with Hanna Krauter. I am very grateful to her for the fantastic collaboration on the generation of entanglement by dissipation. I am also thankful to the team working on the Cesium experiment, Kasper Jensen, Thomas Fernholz and Jonas Meyer Petersen and to the whole QUANTOP crew. My three-month stay at the Niels Bohr Institute was not only a very good opportunity to learn many new things, but also a awesome and inspiring time for which I want to thank in particular Jürgen Appel, Jonathan Bohr Brask, Rodolphe Le Targat, Franziska Kaminski, Jörg Helge Müller, Nir Kampel and Eran Kot. I'm also very thankful to Anders Sørensen for his input and advise during my time in Copenhagen.

I am also very happy that I had the possibility to spend several very interesting research visits in Vienna and Aarhus for which I thank Markus Aspelmeyer and Klaus Mølmer very much.

Many people contributed to a great working environment at the MPQ. There are

various people with whom I had the pleasure to discuss or share an office with. Among the many people to name here, I would like to thank Dominic Kohler for working with me on atomic ensembles and Norbert Schuch, Alastair Kay, Matteo Rizzi, Birger Horstmann, Christina Kraus, Mari Carmen Banuls and Michael Lubasch for a good time. Moreover, I thank Thomas Schulte-Herbrüggen, the coordinator of the PhD-programme QCCC for his commitment and efforts in organizing the QCCC seminars and workshops.

I am very grateful to my ballet teacher Frau Rosteck for her patience and understanding during the many weeks when there was no time to dance and for giving me the unique opportunity to learn the solo seal syllabus in individual lessons when there was time for ballet. Her advice and encouragement was of great help in both parts of my life.

Many thanks are devoted to Gise Gerlach for her psychological support, her good ideas and for bringing so much inspiration to my world. I am also very grateful to "Zauberfee" Sabrina Mandel who shines like the sun at day and sparkles like a star at night.

I owe many thanks to smart Kalle for his magic Zebraness. Last but not least, I would like to thank my favorite sister Annemarie for the hours we spent together and my parents for their incredible unlimited support and everything else :)

I gratefully acknowledge support from the ENB project QCCC, the EU project COMPAS, the Nanosystems Initiative Munich (NIM) and the Max Planck Society.

Bibliography

[1] P. W. Shor. *Algorithms for quantum computation: discrete logarithms and factoring.* In *Proceedings,* 35^{th} *Annual Symposium on Foundations of Computer Science*, pp. 124 – 134. IEEE Press, Los Alamitos (1994).

[2] P. W. Shor. *Polynomial–time algorithms for prime factorization and discrete logarithms on a quantum computer*, SIAM J. Comp. **26**, 1484 (1997).

[3] M. A. Nielsen and I. Chuang. *Quantum Computation and Quantum Information.* Cambridge University Press, Cambridge (2000).

[4] C. H. Bennett and G. Brassard. In *Proceedings of IEEE International Conference on Computers, Systems and Signal Processing, Bangalore, India*, pp. 175–179. IEEE, New York (1984).

[5] N. Gisin, G. Ribordy, W. Tittel, and H. Zbinden. *Quantum cryptography*, Rev. Mod. Phys. **74**, 145 (2002).

[6] N. Gisin and R. Thew. *Quantum communication*, Nature Photon. **1**, 165 (2007).

[7] R. P. Feynman. *Simulating physics with computers*, Int. J. Theor. Phys. **21**, 467 (1982).

[8] S. Lloyd. *Universal quantum simulators*, Science **273**, 1073 (1996).

[9] K. L. Brown, W. J. Munro, and V. M. Kendon. *Using Quantum Computers for Quantum Simulation*, Entropy 2010 **12**, 2268 (2010).

[10] W. Wootters and W. Zurek. *A single quantum cannot be cloned*, Nature **299**, 802 (1982).

[11] H. Mabuchi and A. C. Doherty. *Cavity Quantum Electrodynamics: Coherence in Context*, Science **298**, 1372 (2002).

[12] K. Hammerer, A. S. Sørensen, and E. S. Polzik. *Quantum interface between light and atomic ensembles*, Rev. Mod. Phys. **82**, 1041 (2010).

[13] N. Sangouard, C. Simon, H. de Riedmatten, and N. Gisin. *Quantum repeaters based on atomic ensembles and linear optics*, Rev. Mod. Phys. **83**, 33 (2011).

[14] B. Julsgaard, J. Sherson, J. I. Cirac, J. Fiurášek, and E. S. Polzik. *Experimental demonstration of quantum memory for light*, Nature **432**, 482 (2004).

[15] J. F. Sherson, *et al.*. *Quantum teleportation between light and matter*, Nature **443**, 557 (2006).

[16] B. Julsgaard, A. Kozhekin, and E. S. Polzik. *Experimental long–lived entanglement of two macroscopic objects*, Nature **413**, 400 (2001).

[17] W. Wasilewski, *et al.*. *Quantum Noise Limited and Entanglement–Assisted Magnetometry*, Phys. Rev. Lett. **104**, 133601 (2010).

[18] K. Jensen, *et al.*. *Quantum memory for entangled continuous–variable states*, Nature Physics **7**, 13 (2010).

[19] D. Jaksch and P. Zoller. *The cold atom Hubbard toolbox*, Ann. of Phys. **315**, 52 (2005).

[20] M. Lewenstein, *et al.*. *Ultracold atomic gases in optical lattices: mimicking condensed matter physics and beyond*, Adv. Phys. **56**, 243 (2007).

[21] I. Bloch, J. Dalibard, and W. Zwerger. *Many–body physics with ultracold gases*, Rev. Mod. Phys. **80**, 885 (2008).

[22] U. Schnorrberger, *et al.*. *Electromagnetically Induced Transparency and Light Storage in an Atomic Mott Insulator*, Phys. Rev. Lett. **103**, 033003 (2009).

[23] D. Jaksch, C. Bruder, J. I. Cirac, C. W. Gardiner, and P. Zoller. *Cold Bosonic Atoms in Optical Lattices*, Phys. Rev. Lett. **81**, 3108 (1998).

[24] M. Greiner, O. Mandel, T. Esslinger, T. W. Hänsch, and I. Bloch. *Quantum phase transition from a superfluid to a Mott insulator in a gas of ultracold atoms*, Nature **415**, 39 (2002).

[25] J. F. Poyatos, J. I. Cirac, and P. Zoller. *Quantum Reservoir Engineering with Laser Cooled Trapped Ions*, Phys. Rev. Lett. **77**, 4728 (1996).

[26] M. B. Plenio, S. F. Huelga, A. Beige, and P. L. Knight. *Cavity–loss–induced generation of entangled atoms*, Phys. Rev. A **59**, 2468 (1999).

[27] A. Beige, D. Braun, and P. L. Knight. *Driving atoms into decoherence–free states*, New J. Phys. **2**, 22 (2000).

[28] A. Beige, *et al.*. *Entangling atoms and ions in dissipative environments*, J. Mod. Opt. **47**, 2583 (2000).

[29] A. Beige, D. Braun, B. Tregenna, and P. L. Knight. *Quantum Computing Using Dissipation to Remain in a Decoherence–Free Subspace*, Phys. Rev. Lett. **85**, 1762 (2000).

[30] C. J. Myatt, *et al.*. *Decoherence of quantum superpositions through coupling to engineered reservoirs*, Nature **403**, 269 (2000).

[31] M. B. Plenio and S. F. Huelga. *Entangled Light from White Noise*, Phys. Rev. Lett. **88**, 197901 (2002).

[32] X. X. Yi, C. S. Yu, L. Zhou, and H. S. Song. *Noise–assisted preparation of entangled atoms*, Phys. Rev. A **68**, 052304 (2003).

[33] B. Kraus and J. I. Cirac. *Discrete Entanglement Distribution with Squeezed Light*, Phys. Rev. Lett. **92**, 013602 (2004).

[34] B. Baumgartner, H. Narnhofer, and W. Thirring. *Analysis of quantum semigroups with GKS – Lindblad generators: I. Simple generators*, J. Phys. A **41**, 065201 (2007).

[35] S. Mancini and J. Wang. *Towards feedback control of entanglement*, Eur. Phys. J. D **32**, 257 (2004).

[36] R. Doll, M. Wubs, P. Hänggi, and S. Kohler. *Incomplete pure dephasing of N–qubit entangled W states*, Phys. Rev. B **76**, 045317 (2007).

[37] B. Kraus, *et al.*. *Preparation of entangled states by quantum Markov processes*, Phys. Rev. A **78**, 042307 (2008).

[38] M. P. A. Branderhorst, *et al.*. *Coherent Control of Decoherence*, Science **320**, 638 (2008).

[39] N. Syassen, *et al.*. *Strong Dissipation Inhibits Losses and Induces Correlations in Cold Molecular Gases*, Science **320**, 1329 (2008).

[40] S. Diehl, *et al.*. *Quantum states and phases in driven open quantum systems with cold atoms*, Nature Physics **4**, 878 (2008).

[41] R. Doll, P. Hänggi, S. Kohler, and M. Wubs. *Fast initial qubit dephasing and the influence of substrate dimensions on error correction rates*, Eur. Phys. J. B **68**, 523 (2009).

[42] F. Verstraete, M. M. Wolf, and J. I. Cirac. *Quantum computation and quantum–state engineering driven by dissipation*, Nature Physics **5**, 633 (2009).

[43] M. Hor-Meyll, *et al.*. *Environment–induced entanglement with a single photon*, Phys. Rev. A **80**, 042327 (2009).

[44] G. Vacanti and A. Beige. *Cooling atoms into entangled state*, New J. Phys. **11**, 083008 (2009).

[45] A. Isar. *Entanglement generation and evolution in open quantum systems*, Open Sys. Inf. Dynamics **16**, 205 (2009).

[46] M. Ludwig, K. Hammerer, and F. Marquardt. *Entanglement of mechanical oscillators coupled to a nonequilibrium environment*, Phys. Rev. A **82**, 012333 (2010).

[47] D. G. Angelakis, S. Mancini, and S. Bose. *Steady–state entanglement between hybrid light–matter qubits*, Europhys. Lett. **85**, 20007 (2009).

[48] D. G. Angelakis, L. Dai, and L.-C. Kwek. *Coherent control of long–distance steady state entanglement in lossy resonator arrays*, Europhys. Lett. **91**, 10003 (2010).

[49] H. Weimer, M. Müller, I. Lesanovsky, P. Zoller, and H. P. Büchler. *A Rydberg quantum simulator*, Nature Phys. **6**, 382 (2010).

[50] F. Benatti, R. Floreanini, and U. Marzolino. *Entangling two unequal atoms through a common bath*, Phys. Rev. A **81**, 012105 (2010).

[51] K. Temme, M. M. Wolf, and F. Verstraete. *Stochastic exclusion processes versus coherent transport* (2009). ArXiv:0912.0858.

[52] S. Pielawa, L. Davidovich, D. Vitali, and G. Morigi. *Engineering atomic quantum reservoirs for photons*, Phys. Rev. A **81**, 043802 (2010).

[53] G. Goldstein, *et al.*. *Environment Assisted Precision Measurement*, Phys. Rev. Lett. **106**, 140502 (2011).

[54] X. Wang and S. G. Schirmer. *Generating maximal entanglement between non-interacting atoms by collective decay and symmetry breaking* (2010). ArXiv:1005.2114.

[55] E. del Valle. *Steady state entanglement of two coupled qubits*, JOSA B **28**, 228 (2011).

[56] M. Kiffner and M. J. Hartmann. *Master equation approach for interacting slow– and stationary–light polaritons*, Phys. Rev. A **82**, 033813 (2010).

[57] M. Kiffner and M. J. Hartmann. *Dissipation–induced Tonks–Girardeau gas of polaritons*, Phys. Rev. A **81**, 021806 (2010).

[58] J. T. Barreiro, *et al.*. *Experimental multiparticle entanglement dynamics induced by decoherence*, Nature Physics **6**, 943 (2010).

[59] J. T. Barreiro, *et al.*. *An open–system quantum simulator with trapped ions*, Nature **470**, 486 (2011).

[60] D. P. DiVincenzo. *The Physical Implementation of Quantum Computation*, Fortschr. Phys. **48**, 771 (2000).

[61] H. Häffner, *et al.*. *Robust entanglement*, Appl. Phys. B **81**, 151 (2005).

[62] C. Langer, *et al.*. *Long–Lived Qubit Memory Using Atomic Ions*, Phys. Rev. Lett. **95**, 060502 (2005).

[63] K. Hammerer, E. S. Polzik, and J. I. Cirac. *Teleportation and spin squeezing utilizing multimode entanglement of light with atoms*, Phys. Rev. A **72**, 052313 (2005).

[64] K. Eckert, L. Zawitkowski, A. Sanpera, M. Lewenstein, and E. S. Polzik. *Quantum Polarization Spectroscopy of Ultracold Spinor Gases*, Phys. Rev. Lett. **98**, 100404 (2007).

[65] K. Eckert, *et al.*. *Quantum non–demolition detection of strongly correlated systems*, Nature Physics **4**, 50 (2007).

[66] H. J. Kimble. *The quantum internet*, Nature **453**, 1023 (2008).

[67] L.-M. Duan, M. D. Lukin, J. I. Cirac, and P. Zoller. *Long–distance quantum communication with atomic ensembles and linear optics*, Nature **414**, 413 (2001).

[68] D. Jaksch, H.-J. Briegel, J. I. Cirac, C. W. Gardiner, and P. Zoller. *Entanglement of Atoms via Cold Controlled Collisions*, Phys. Rev. Lett. **82**, 1975 (1999).

[69] O. Mandel, *et al.*. *Controlled collisions for multi–particle entanglement of optically trapped atoms*, Nature **425**, 937 (2003).

[70] M. D. Lukin and A. Imamoğlu. *Nonlinear Optics and Quantum Entanglement of Ultraslow Single Photons*, Phys. Rev. Lett. **84**, 1419 (2000).

[71] A. André, M. Bajcsy, A. S. Zibrov, and M. D. Lukin. *Nonlinear Optics with Stationary Pulses of Light*, Phys. Rev. Lett. **94**, 063902 (2005).

[72] A. Faraon, *et al.*. *Coherent generation of non–classical light on a chip via photon–induced tunnelling and blockade*, Nature Phys. **4**, 859 (2008).

[73] B. Weber, *et al.*. *Photon–Photon Entanglement with a Single Trapped Atom*, Phys. Rev. Lett. **102**, 030501 (2009).

[74] T. Aoki, *et al.*. *Efficient Routing of Single Photons by One Atom and a Microtoroidal Cavity*, Phys. Rev. Lett. **102**, 083601 (2009).

[75] M. Hafezi, D. Chang, V. Gritsev, E. Demler, and M. Lukin. *Quantum transport of strongly interacting photons in a one–dimensional nonlinear waveguide* (2009). ArXiv:0911.4766.

[76] A. V. Gorshkov, J. Otterbach, E. Demler, M. Fleischhauer, and M. D. Lukin. *Photonic Phase Gate via an Exchange of Fermionic Spin Waves in a Spin Chain*, Phys. Rev. Lett. **105**, 060502 (2010).

[77] E. Knill, R. Laflamme, and G. J. Milburn. *A scheme for efficient quantum computation with linear optics*, Nature **409**, 46 (2001).

[78] A. E. Kozhekin, K. Mølmer, and E. Polzik. *Quantum memory for light*, Phys. Rev. A **62**, 33809 (2000).

[79] K.-J. Boller, A. Imamolu, and S. E. Harris. *Observation of electromagnetically induced transparency*, Phys. Rev. Lett. **66**, 2593 (1991).

[80] M. Fleischhauer, A. Imamoglu, and J. P. Marangos. *Electromagnetically induced transparency: Optics in coherent media*, Rev. Mod. Phys. **77**, 633 (2005).

[81] B. Kraus, *et al.*. *Quantum memory for nonstationary light fields based on controlled reversible inhomogeneous broadening*, Phys. Rev. A **73**, 020302 (2006).

[82] S. A. Moiseev and S. Kröll. *Complete Reconstruction of the Quantum State of a Single–Photon Wave Packet Absorbed by a Doppler–Broadened Transition*, Phys. Rev. Lett. **87**, 173601 (2001).

[83] L.-M. Duan, J. I. Cirac, P. Zoller, and E. S. Polzik. *Quantum Communication between Atomic Ensembles Using Coherent Light*, Phys. Rev. Lett. **85**, 5643 (2000).

[84] K. Hammerer. *Quantum information processing with atomic ensembles and light*. Ph.D. thesis, Max-Planck Institute for Quantumoptics (2006).

[85] L.-M. Duan, J. Cirac, and P. Zoller. *Three–dimensional theory for interaction between atomic ensembles and free–space light*, Phys. Rev. A **66**, 23818 (2002).

[86] M. G. Raymer, I. A. Walmsley, J. Mostowski, and B. Sobolewska. *Quantum theory of spatial and temporal coherence properties of stimulated Raman scattering*, Phys. Rev. A **32**, 332 (1985).

[87] A. Silberfarb and I. Deutsch. *Continuous measurement with traveling–wave probes*, Phys. Rev. A **68**, 13817 (2003).

[88] L. Madsen and K. Mølmer. *Spin squeezing and precision probing with light and samples of atoms in the Gaussian description*, Phys. Rev. A **70**, 52324 (2004).

[89] T. Holstein and H. Primakoff. *Field Dependence of the Intrinsic Domain Magnetization of a Ferromagnet*, Phys. Rev. **58**, 1098 (1940).

[90] C. Kittel. *Quantum Theory of Solids*. Wiley, New York (1987).

[91] B. Kraus, K. Hammerer, G. Giedke, and J. I. Cirac. *Entanglement generation and Hamiltonian simulation in continuous–variable systems*, Phys. Rev. A **67**, 42314 (2003).

[92] D. V. Kupriyanov, O. S. Mishina, I. M. Sokolov, B. Julsgaard, and E. S. Polzik. *Multimode entanglement of light and atomic ensembles via off–resonant coherent forward scattering*, Phys. Rev. A **71**, 032348 (2005).

[93] O. Mishina, D. Kupriyanov, and E. S. Polzik. In *Proceedings of the NATO Advanced Research Workshop, Crete 2005: Quantum Communication and Security*, vol. 199, p. 346. ISO Press, Amsterdam (2006).

[94] O. S. Mishina, D. V. Kupriyanov, J. H. Müller, and E. S. Polzik. *Spectral theory of quantum memory and entanglement via Raman scattering of light by an atomic ensemble*, Phys. Rev. A **75**, 042326 (2007).

[95] W. Wasilewski, *et al.*. *Single mode quadrature entangled light from room temperature atomic vapor*, Opt. Express **16**, 14444 (2010).

[96] B. Julsgaard. *Entanglement and Quantum Interactions with Macroscopic Gas Samples*. Ph.D. thesis, University of Aarhus (2003).

[97] K. Hammerer, E. S. Polzik, and J. I. Cirac. *High–fidelity teleportation between light and atoms*, Phys. Rev. A **74**, 064301 (2006).

[98] J. Fiurášek, J. Sherson, T. Opatrný, and E. S. Polzik. *Single–passage readout of atomic quantum memory*, Phys. Rev. A **73**, 022331 (2006).

[99] C. A. Muschik, K. Hammerer, E. S. Polzik, and J. I. Cirac. *Efficient quantum memory and entanglement between light and an atomic ensemble using magnetic fields*, Phys. Rev. A **73**, 062329 (2006).

[100] J. F. Sherson and K. Mølmer. *Polarization Squeezing by Optical Faraday Rotation*, Phys. Rev. Lett. **97**, 143602 (2006).

[101] T. Lahaye, C. Menotti, L. Santos, M. Lewenstein, and T. Pfau. *The physics of dipolar bosonic quantum gase*, Rep. Prog. Phys. **72**, 126401 (2009).

[102] J. Sebby-Strabley, M. Anderlini, P. S. Jessen, and J. V. Porto. *Lattice of double wells for manipulating pairs of cold atoms*, Phys. Rev. A **73**, 033605 (2006).

[103] M. Anderlini, *et al.*. *Controlled exchange interaction between pairs of neutral atoms in an optical lattice*, Nature **448**, 452 (2007).

[104] S. Fölling, *et al.*. *Direct observation of second–order atom tunnelling*, Nature **448**, 1029 (2007).

[105] J. Sebby-Strabley, *et al.*. *Preparing and Probing Atomic Number States with an Atom Interferometer*, Phys. Rev. Lett. **98**, 200405 (2007).

[106] S. Trotzky, *et al.*. *Time–Resolved Observation and Control of Superexchange Interactions with Ultracold Atoms in Optical Lattices*, Science **319**, 295 (2008).

[107] W. S. Bakr, *et al.*. *Probing the Superfluid-to-Mott Insulator Transition at the Single–Atom Level*, Science **329**, 547 (2010).

[108] J. F. Sherson, *et al.*. *Single–atom–resolved fluorescence imaging of an atomic Mott insulator*, Nature **467**(6872) (2010).

[109] C. Weitenberg, *et al.*. *Single–spin addressing in an atomic Mott insulator*, Nature **471**, 319 (2011).

[110] H. J. Metcalf and P. van der Straten. *Laser Cooling and Trapping*. Springer, Berlin (1999).

[111] S. Haroche and J. M. Raimond. *Exploring the Quantum: Atoms, Cavities, and Photons*. Oxford University Press, New York (2006).

[112] H. J. Kimble. *Strong interactions of single atoms and photons in cavity QED*, Phys. Scr. **T76**, 127 (1998).

[113] A. Boca, *et al.*. *Observation of the Vacuum Rabi Spectrum for One Trapped Atom*, Phys. Rev. Lett. **93**, 233603 (2004).

[114] Y. Colombe, *et al.*. *Strong atom-field coupling for Bose-Einstein condensates in an optical cavity on a chip*, Nature **450**, 272 (2007).

[115] K. M. Birnbaum, *et al.*. *Photon blockade in an optical cavity with one trapped atom*, Nature **436**, 87 (2005).

[116] S. Gleyzes, *et al.*. *Quantum jumps of light recording the birth and death of a photon in a cavity*, Nature **446**, 297 (2007).

[117] C. Guerlin, *et al.*. *Progressive field–state collapse and quantum non–demolition photon counting*, Nature **448**, 889 (2007).

[118] M. Hijlkema, *et al.*. *A single–photon server with just one atom*, Nature Phys. **3**, 253 (2007).

[119] A. Kubanek, *et al.*. *Two–Photon Gateway in One–Atom Cavity Quantum Electrodynamics*, Phys. Rev. Lett. **101**, 203602 (2008).

[120] M. Mücke, *et al.*. *Electromagnetically induced transparency with single atoms in a cavity*, Nature **465**, 755758 (2010).

[121] L.-M. Duan and H. J. Kimble. *Scalable Photonic Quantum Computation through Cavity–Assisted Interactions*, Phys. Rev. Lett. **92**, 127902 (2004).

[122] M. Fox. *Quantum Optics*. Oxford University Press, New York (2006).

[123] E. T. Jaynes and F. W. Cummings. *Comparison of quantum and semiclassical radiation theories with application to the beam maser*. In *Proc. IEEE*, vol. 51, pp. 89–109. IEEE Press (1963).

[124] B. Wang and L.-M. Duan. *Engineering superpositions of coherent states in coherent optical pulses through cavity–assisted interaction*, Phys. Rev. A **72**, 022320 (2005).

[125] J. Kerckhoff, L. Bouten, A. Silberfarb, and H. Mabuchi. *Physical model of continuous two–qubit parity measurement in a cavity–QED network*, Phys. Rev. A **79**, 024305 (2009).

[126] H. Mabuchi. *Cavity–QED models of switches for attojoule–scale nanophotonic logic*, Phys. Rev. A **80**, 045802 (2009).

[127] A. Nielsen. *Private communication* (2011).

[128] R. Gehr, *et al.*. *Cavity–Based Single Atom Preparation and High–Fidelity Hyperfine State Readout*, Phys. Rev. Lett. **104**, 203602 (2010).

[129] J. Bochmann, *et al.*. *Lossless State Detection of Single Neutral Atoms*, Phys. Rev. Lett. **104**, 203601 (2010).

[130] R. J. Schoelkopf and S. M. Girvin. *Wiring up quantum systems*, Nature **451**, 664 (2008).

[131] S. Bose. *Plancks Gesetz und Lichtquantenhypothese*, A. Phys. **26**, 178 (1924).

[132] A. Einstein. *Quantentheorie des einatomigen idealen Gases: Zweite Abhandlung*, Sitzungsber. Kgl. Preuss. Akad. Wiss. (1925).

[133] M. H. Anderson, J. R. Ensher, M. R. Matthews, C. E. Wieman, and E. A. Cornell. *Observation of Bose–Einstein Condensation in a Dilute Atomic Vapor*, Science **269**, 198 (1995).

[134] K. B. Davis, *et al.*. *Bose-Einstein Condensation in a Gas of Sodium Atoms*, Phys. Rev. Lett. **75**, 3969 (1995).

[135] C. C. Bradley, C. A. Sackett, J. J. Tollett, and R. G. Hulet. *Evidence of Bose–Einstein Condensation in an Atomic Gas with Attractive Interactions*, Phys. Rev. Lett. **75**, 1687 (1995).

[136] R. H. Dicke. *Coherence in Spontaneous Radiation Processes*, Phys. Rev. **93**, 99 (1954).

[137] M. Gross and S. Haroche. *Superradiance: An essay on the theory of collective spontaneous emission*, Phys. Rep. **93**, 301 (1982).

[138] S. Inouye, *et al.*. *Superradiant Rayleigh Scattering from a Bose-Einstein Condensate*, Science **285**, 571 (1999).

[139] D. Schneble, *et al.*. *The Onset of Matter–Wave Amplification in a Superradiant Bose–Einstein Condensate*, Science **300**, 475 (2003).

[140] A. Hilliard, *et al.*. *Rayleigh superradiance and dynamic Bragg gratings in an end–pumped Bose–Einstein condensate*, Phys. Rev. A **78**, 051403 (2008).

[141] D. Schneble, *et al.*. *Raman amplification of matter waves*, Phys. Rev. A **69**, 041601 (2004).

[142] Y. Yoshikawa, T. Sugiura, Y. Torii, and T. Kuga. *Observation of superradiant Raman scattering in a Bose–Einstein condensate*, Phys. Rev. A **69**, 041603 (2004).

[143] C. Olaussen. *A Rubidium Bose–Einstein Condensate. Toward the BEC–Light Interface*. Ph.D. thesis, Niels Bohr Institute Copenhagen (2007).

[144] M. M. Cola and N. Piovella. *Theory of collective Raman scattering from a Bose–Einstein condensate*, Phys. Rev. A **70**, 045601 (2004).

[145] H. Uys and P. Meystre. *Superradiant Raman scattering in an ultracold Bose gas at finite temperature*, Phys. Rev. A **77**, 063614 (2008).

[146] S. Inouye, *et al.*. *Phase–coherent amplification of atomic matter waves*, Nature **402**, 641 (1999).

[147] M. Kozuma, *et al.*. *Phase–Coherent Amplification of Matter Waves*, Science **286**, 2309 (1999).

[148] T. Wang and S. F. Yelin. *Theory for Raman superradiance in atomic gases*, Phys. Rev. A **72**, 043804 (2005).

[149] R. Bloomer, M. Pysher, and O. Pfister. *Nonlocal restoration of two–mode squeezing in the presence of strong optical loss*, New J. Phys. **13**, 063014 (2011).

[150] J. Cho, S. Bose, and M. S. Kim. *Optical Pumping into Many–Body Entanglement*, Phys. Rev. Lett. **106**, 020504 (2011).

[151] M. J. Kastoryano, F. Reiter, and A. S. Sørensen. *Dissipative Preparation of Entanglement in Optical Cavities*, Phys. Rev. Lett. **106**, 090502 (2011).

[152] F. Pastawski, L. Clemente, and J. I. Cirac. *Quantum memories based on engineered dissipation*, Phys. Rev. A **83**, 012304 (2011).

[153] J. Kerckhoff, H. I. Nurdin, D. S. Pavlichin, and H. Mabuchi. *Designing Quantum Memories with Embedded Control: Photonic Circuits for Autonomous Quantum Error Correction*, Phys. Rev. Lett. **105**, 040502 (2010).

[154] J. P. Paz and W. H. Zurek. *Continuous error correction*. In *Proc. R. Soc. A*, vol. 454, p. 355 (1998).

[155] H.-J. Briegel, W. Dür, J. I. Cirac, and P. Zoller. *Quantum Repeaters: The Role of Imperfect Local Operations in Quantum Communication*, Phys. Rev. Lett. **81**, 5932 (1998).

[156] P. Zoller, *et al.*. *Quantum information processing and communication*, Eur. Phys. J. D **36**, 203 (2005).

[157] T. Chanelière, *et al.*. *Storage and retrieval of single photons transmitted between remote quantum memories*, Nature **438**, 833 (2005).

[158] C. W. Chou, *et al.*. *Measurement–induced entanglement for excitation stored in remote atomic ensembles*, Nature **438**, 828 (2005).

[159] M. Eisaman, *et al.*. *Electromagnetically induced transparency with tunable single–photon pulses*, Nature **438**, 837 (2005).

[160] Z.-S. Yuan, *et al.*. *Experimental demonstration of a BDCZ quantum repeater node*, Nature **454**, 1098 (2008).

[161] K. S. Choi, H. Deng, J. Laurat, and H. J. Kimble. *Mapping photonic entanglement into and out of a quantum memory*, Nature **452**, 67 (2008).

[162] Y.-A. Chen, *et al.*. *Memory–built–in quantum teleportation with photonic and atomic qubits*, Nature Physics **4**, 103 (2008).

[163] A. S. Parkins, E. Solano, and J. I. Cirac. *Unconditional Two–Mode Squeezing of Separated Atomic Ensembles*, Phys. Rev. Lett. **96**, 053602 (2006).

[164] M. G. Raymer, A. C. Funk, B. C. Sanders, and H. de Guise. *Separability criterion for separate quantum systems*, Phys. Rev. A **67**, 052104 (2003).

[165] C. Cohen-Tannoudji, J. Dupont-Roc, and G. Grynberg. *Atom–Photon Interactions*. Wiley, New York (1998).

[166] R. H. Lehmberg. *Radiation from an N–Atom System. I. General Formalism*, Phys. Rev. A **2**, 883 (1970).

[167] D. Porras and J. I. Cirac. *Quantum engineering of photon states with entangled atomic ensembles* (2007). ArXiv:0704.0641.

[168] D. Porras and J. I. Cirac. *Collective generation of quantum states of light by entangled atoms*, Phys. Rev. A **78**, 053816 (2008).

[169] J. Appel, *et al.*. *Mesoscopic atomic entanglement for precision measurements beyond the standard quantum limit*, Proc. Natl. Acac. Sci. U.S.A. **106**, 10960 (2009).

[170] M. H. Schleier-Smith, I. D. Leroux, and V. Vuletić. *States of an Ensemble of Two–Level Atoms with Reduced Quantum Uncertainty*, Phys. Rev. Lett. **104**, 073604 (2010).

[171] M. Koschorreck, M. Napolitano, B. Dubost, and M. W. Mitchell. *Quantum Nondemolition Measurement of Large–Spin Ensembles by Dynamical Decoupling*, Phys. Rev. Lett. **105**, 093602 (2010).

[172] G. Giedke and J. Ignacio Cirac. *Characterization of Gaussian operations and distillation of Gaussian states*, Phys. Rev. A **66**, 032316 (2002).

[173] T. J. Kippenberg and K. Vahala. *Cavity Optomechanics: Back–Action at the Mesoscale*, Science **321**, 1172 (2008).

[174] F. Marquart and S. M. Girvin. *Optomechanics*, Physics **2**, 40 (2009).

[175] M. Aspelmeyer, S. Gröblacher, K. Hammerer, and N. Kiesel. *Quantum optomechanics – throwing a glance*, JOSA B **27**, A189 (2010).

[176] I. Wilson-Rae, N. Nooshi, W. Zwerger, and T. J. Kippenberg. *Theory of Ground State Cooling of a Mechanical Oscillator Using Dynamical Backaction*, Phys. Rev. Lett. **99**, 093901 (2007).

[177] F. Marquardt, J. P. Chen, A. A. Clerk, and S. M. Girvin. *Quantum Theory of Cavity–Assisted Sideband Cooling of Mechanical Motion*, Phys. Rev. Lett. **99**, 093902 (2007).

[178] C. Genes, D. Vitali, P. Tombesi, S. Gigan, and M. Aspelmeyer. *Ground–state cooling of a micromechanical oscillator: Comparing cold damping and cavity–assisted cooling schemes*, Phys. Rev. A **77**, 033804 (2008).

[179] C. H. Bennett, *et al.*. *Purification of Noisy Entanglement and Faithful Teleportation via Noisy Channels*, Phys. Rev. Lett. **76**, 722 (1996).

[180] W. Dür, H.-J. Briegel, J. I. Cirac, and P. Zoller. *Quantum repeaters based on entanglement purification*, Phys. Rev. A **59**, 169 (1999).

[181] R. F. Werner. *Quantum states with Einstein–Podolsky–Rosen correlations admitting a hidden–variable model*, Phys. Rev. A **40**, 4277 (1989).

[182] M. Horodecki and P. Horodecki. *Reduction criterion of separability and limits for a class of distillation protocols*, Phys. Rev. A **59**, 4206 (1999).

[183] C. H. Benett, D. P. DiVincenzo, J. A. Smolin, and W. K. Wootters. *Mixed–state entanglement and quantum error correction*, Phys. Rev. A **54**, 3824 (1996).

[184] S. J. van Enk, H. J. Kimble, J. I. Cirac, and P. Zoller. *Quantum communication with dark photons*, Phys. Rev. A **59**, 2659 (1999).

[185] M. Riebe, *et al.*. *Deterministic quantum teleportation with atoms*, Nature **429**, 724 (2004).

[186] M. Barrett, *et al.*. *Deterministic quantum teleportation of atomic qubits*, Nature **429**, 737 (2004).

[187] M. Riebe, *et al.*. *Quantum teleportation with atoms: quantum process tomography*, New J. Phys. **9**, 211 (2007).

[188] S. Olmschenk, *et al.*. *Quantum Teleportation Between Distant Matter Qubits*, Science **323**, 486 (2009).

[189] C. Bennett, *et al.*. *Teleporting an unknown quantum state via dual classical and Einstein–Podolsky–Rosen channels*, Phys. Rev. Lett. **70**, 1895 (1993).

[190] D. Gottesman and I. L. Chuang. *Demonstrating the viability of universal quantum computation using teleportation and single-qubit operations*, Nature **402**, 390 (1999).

[191] D. Bouwmeester, *et al.*. *Experimental quantum teleportation*, Nature **390**, 575 (1997).

[192] D. Fattal, E. Diamanti, K. Inoue, and Y. Yamamoto. *Quantum Teleportation with a Quantum Dot Single Photon Source*, Phys. Rev. Lett. **92**, 037904 (2004).

[193] H. de Riedmatten, *et al.*. *Long Distance Quantum Teleportation in a Quantum Relay Configuration*, Phys. Rev. Lett. **92**, 047904 (2004).

[194] I. Marcikic, H. de Riedmatten, W. Tittel, H. Zbinden, and N. Gisin. *Long–distance teleportation of qubits at telecommunication wavelengths*, Nature **421**, 509 (2003).

[195] Y.-H. Kim, S. Kulik, and Y. Shih. *Quantum Teleportation of a Polarization State with a Complete Bell State Measurement*, Phys. Rev. Lett. **86**, 1370 (2001).

[196] D. Boschi, S. Branca, F. D. Martini, L. Hardy, and S. Popescu. *Experimental Realization of Teleporting an Unknown Pure Quantum State via Dual Classical and Einstein–Podolsky–Rosen Channels*, Phys. Rev. Lett. **80**, 1121 (1998).

[197] R. Ursin, *et al.*. *Quantum teleportation across the Danube*, Nature **430**, 849 (2004).

[198] J.-W. Pan, M. Daniell, S. Gasparoni, G. Weihs, and A. Zeilinger. *Experimental Demonstration of Four–Photon Entanglement and High–Fidelity Teleportation*, Phys. Rev. Lett. **86**, 4435 (2001).

[199] A. Furusawa, *et al.*. *Unconditional quantum teleportation*, Science **282**, 706 (1998).

[200] T. C. Zhang, K. W. Goh, C. W. Chou, P. Lodahl, and H. J. Kimble. *Quantum teleportation of light beams*, Phys. Rev. A **67**, 033802 (2003).

[201] W. P. Bowen, *et al.*. *Experimental investigation of continuous–variable quantum teleportation*, Phys. Rev. A **67**, 032302 (2003).

[202] H. Yonezawa, T. Aoki, and A. Furusawa. *Demonstration of a quantum teleportation network for continuous variables*, Nature **431**, 430 (2004).

[203] N. Takei, H. Yonezawa, T. Aoki, and A. Furusawa. *High–Fidelity Teleportation beyond the No–Cloning Limit and Entanglement Swapping for Continuous Variables*, Phys. Rev. Lett. **94**, 220502 (2005).

[204] X.-M. Jin, *et al.*. *Experimental free–space quantum teleportation*, Nature Photonics **4**, 376 (2010).

[205] Z. Zhao, *et al.*. *Experimental demonstration of five–photon entanglement and open–destination teleportation*, Nature **430**, 54 (2004).

[206] Q. Zhang, *et al.*. *Experimental quantum teleportation of a two–qubit composite system*, Nature Physics **2**, 678 (2006).

[207] C. Schmid, *et al.*. *Quantum teleportation and entanglement swapping with linear optics logic gates*, New J. Phys. **11**, 033008 (2009).

[208] A. Kuzmich and E. S. Polzik. *Atomic Quantum State Teleportation and Swapping*, Phys. Rev. Lett. **85**, 5639 (2000).

[209] A. Dantan, N. Treps, A. Bramati, and M. Pinard. *Teleportation of an Atomic Ensemble Quantum State*, Phys. Rev. Lett. **94**, 050502 (2005).

[210] J. Sherson. *Quantum memory and teleportation using macroscopic gas samples*. Ph.D. thesis, Niels Bohr Institute Copenhagen (2006).

[211] L. Vaidman. *Teleportation of quantum states*, Phys. Rev. A **49**, 1473 (1994).

[212] P. van Loock and S. L. Braunstein. *Unconditional teleportation of continuous–variable entanglement*, Phys. Rev. A **61**, 010302 (1999).

[213] S. L. Braunstein and P. van Loock. *Quantum information with continuous variables*, Rev. Mod. Phys. **77**, 513 (2005).

[214] S. L. Braunstein, H. J. Kimble, and C. A. Fuchs. *Criteria for continuous–variable quantum teleportation*, J. Mod. Opt. **47**, 267 (2000).

[215] K. Hammerer, M. M. Wolf, E. S. Polzik, and J. I. Cirac. *Quantum Benchmark for Storage and Transmission of Coherent States*, Phys. Rev. Lett. **94**, 150503 (2005).

[216] P. Medley, D. M. Weld, H. Miyake, D. E. Pritchard, and W. Ketterle. *Spin Gradient Demagnetization Cooling of Ultracold Atoms*, Phys. Rev. Lett. **106**, 195301 (2011).

[217] D. M. Weld and W. Ketterle. *Towards quantum magnetism with ultracold atoms*, J. Phys.: Conf. Ser. **264**, 012017 (2001).

[218] J. Simon, *et al.*. *Quantum simulation of antiferromagnetic spin chains in an optical lattice*, Nature **472**, 307 (2011).

[219] A. V. Gorshkov, *et al.*. *Two–orbital SU(N) magnetism with ultracold alkaline–earth atoms*, Nature Phys. **6**, 289 (2010).

[220] M. Hermele, V. Gurarie, and A. M. Rey. *Mott Insulators of Ultracold Fermionic Alkaline Earth Atoms: Underconstrained Magnetism and Chiral Spin Liquid*, Phys. Rev. Lett. **103**, 135301 (2009).

[221] A. J. Daley, M. M. Boyd, J. Ye, and P. Zoller. *Quantum Computing with Alkaline–Earth–Metal Atoms*, Phys. Rev. Lett. **101**, 170504 (2008).

[222] S. Sachdev. *Quantum magnetism and criticality*, Nature Phys. **4**, 173 (2008).

[223] M. Rigol, V. Dunjko, and M. Olshanii. *Thermalization and its mechanism for generic isolated quantum systems*, Nature **452**, 854 (2008).

[224] M. A. Cazalilla and M. Rigol. *Focus on Dynamics and Thermalization in Isolated Quantum Many–Body Systems*, New J. Phys. **12**, 055006 (2010).

[225] G. Birkl, M. Gatzke, I. H. Deutsch, S. L. Rolston, and W. D. Phillips. *Bragg Scattering from Atoms in Optical Lattices*, Phys. Rev. Lett. **75**, 2823 (1995).

[226] M. Weidemüller, A. Hemmerich, A. Görlitz, T. Esslinger, and T. W. Hänsch. *Bragg Diffraction in an Atomic Lattice Bound by Light*, Phys. Rev. Lett. **75**, 4583 (1995).

[227] J. Stenger, *et al.*. *Bragg Spectroscopy of a Bose–Einstein Condensate*, Phys. Rev. Lett. **82**, 4569 (1999).

[228] D. M. Stamper-Kurn, *et al.*. *Excitation of Phonons in a Bose–Einstein Condensate by Light Scattering*, Phys. Rev. Lett. **83**, 2876 (1999).

[229] P. T. Ernst, *et al.*. *Probing superfluids in optical lattices by momentum–resolved Bragg spectroscopy*, Nature Physics **6**, 56 (2009).

[230] P. M. Chaikin and T. C. Lubensky. *Principles of condensed matter physics*. Cambridge University Press, Cambridge (1995).

[231] I. de Vega, J. I. Cirac, and D. Porras. *Detection of spin correlations in optical lattices by light scattering*, Phys. Rev. A **77**, 051804 (2008).

[232] I. B. Mekhov and H. Ritsch. *Quantum Nondemolition Measurements and State Preparation in Quantum Gases by Light Detection*, Phys. Rev. Lett. **102**, 020403 (2009).

[233] T. Roscilde, *et al.*. *Quantum polarization spectroscopy of correlations in attractive fermionic gases*, New J. Phys. **11**, 055041 (2009).

[234] G. De Chiara, O. Romero-Isart, and A. Sanpera. *Probing magnetic order in ultracold lattice gases*, Phys. Rev. A **83**, 021604 (2011).

[235] V. B. Braginsky and F. Y. Khalili. *Quantum measurement*. Cambridge University Press, Cambridge (1992).

[236] A. I. Lvovsky, B. C. Sanders, and W. Tittel. *Optical quantum memory*, Nature Photon. **3**, 706 (2009).

[237] L. Van Hove. *Correlations in Space and Time and Born Approximation Scattering in Systems of Interacting Particles*, Phys. Rev. **95**, 249 (1954).

[238] P. Barmettler, *et al.*. *Quantum many–body dynamics of coupled double–well superlattices*, Phys. Rev. A **78**, 012330 (2008).

[239] D. Rossini, A. Silva, G. Mussardo, and G. E. Santoro. *Effective Thermal Dynamics Following a Quantum Quench in a Spin Chain*, Phys. Rev. Lett. **102**, 127204 (2009).

[240] D. Rossini, S. Suzuki, G. Mussardo, G. E. Santoro, and A. Silva. *Long time dynamics following a quench in an integrable quantum spin chain: Local versus nonlocal operators and effective thermal behavior*, Phys. Rev. B **82**, 144302 (2010).

[241] J. Sherson, B. Julsgaard, and E. Polzik. *Deterministic atom–light quantum interface*, Adv. At. Mol. Phys. **54** (2006).

[242] H.-J. Briegel, T. Calarco, D. Jaksch, J. I. Cirac, and P. Zoller. *Quantum computing with neutral atoms*, J. Mod. Opt. **47**, 415 (2000).

[243] G. K. Brennen, C. M. Caves, P. S. Jessen, and I. H. Deutsch. *Quantum Logic Gates in Optical Lattices*, Phys. Rev. Lett. **82**, 1060 (1999).

[244] A. Barenco, *et al.*. *Elementary gates for quantum computation*, Phys. Rev. A **52**, 3457 (1995).

[245] U. Dorner, T. Calarco, P. Zoller, A. Browaeys, and P. Grangier. *Quantum logic via optimal control in holographic dipole traps*, J. Opt. B **7**, 341 (2005).

[246] C. K. Hong, Z. Y. Ou, and L. Mandel. *Measurement of subpicosecond time intervals between two photons by interference*, Phys. Rev. Lett. **59**, 2044 (1987).

[247] R. Okamoto, *et al.*. *An Entanglement Filter*, Science **323**, 483 (2009).

[248] B. P. A. Einstein and N. Rosen. *Can Quantum–Mechanical Description of Physical Reality Be Considered Complete?*, Phys. Rev. **47**, 777 (1935).

[249] S. L. Braunstein and H. J. Kimble. *Teleportation of Continuous Quantum Variables*, Phys. Rev. Lett. **80**, 869 (1998).

[250] X. Jia, *et al.*. *Experimental Demonstration of Unconditional Entanglement Swapping for Continuous Variables*, Phys. Rev. Lett. **93**, 250503 (2004).

[251] M. Żukowski, A. Zeilinger, M. A. Horne, and A. K. Ekert. *"Event–ready–detectors" Bell experiment via entanglement swapping*, Phys. Rev. Lett. **71**, 4287 (1993).

[252] E. G. Cavalcanti, C. J. Foster, M. D. Reid, and P. D. Drummond. *Bell Inequalities for Continuous–Variable Correlations*, Phys. Rev. Lett. **99**, 210405 (2007).

[253] J. S. Bell. *On the Einstein–Podolsky–Rosen paradox*, Physics **1**, 195 (1964).

[254] J.-W. Pan, S. Gasparoni, R. Ursin, G. Weihs, and A. Zeilinger. *Experimental entanglement purification of arbitrary unknown states*, Nature **423**, 417 (2003).

[255] Z. Zhao, T. Yang, Y.-A. Chen, A.-N. Zhang, and J.-W. Pan. *Experimental Realization of Entanglement Concentration and a Quantum Repeater*, Phys. Rev. Lett. **90**, 207901 (2003).

[256] B. Hage, *et al.*. *Preparation of distilled and purified continuous–variable entangled states*, Nature Physics **4**, 915 (2008).

[257] R. Dong, *et al.*. *Experimental entanglement distillation of mesoscopic quantum states*, Nature Physics **4**, 919 (2008).

[258] G. Giedke and J. Cirac. *Characterization of Gaussian operations and distillation of Gaussian states*, Phys. Rev. A **66**, 32316 (2002).

[259] J. Eisert, S. Scheel, and M. Plenio. *Distilling Gaussian States with Gaussian Operations is Impossible*, Phys. Rev. Lett. **89**, 137903 (2002).

[260] J. Fiurášek. *Gaussian Transformations and Distillation of Entangled Gaussian States*, Phys. Rev. Lett. **89**, 137904 (2002).

[261] J. Eisert, D. Browne, S. Scheel, and M. Plenio. *Distillation of continuous–variable entanglement with optical means*, Ann. Phys. (N.Y.) **311**, 431 (2004).

[262] D. Menzies and N. Korolkova. *Weak values and continuous–variable entanglement concentration*, Phys. Rev. A **76**, 062310 (2007).

[263] A. Ourjoumtsev, A. Dantan, R. Tualle-Brouri, and P. Grangier. *Increasing Entanglement between Gaussian States by Coherent Photon Subtraction*, Phys. Rev. Lett. **98**, 030502 (2007).

[264] T. Opatrný, G. Kurizki, and D.-G. Welsch. *Improvement on teleportation of continuous variables by photon subtraction via conditional measurement*, Phys. Rev. A **61**, 032302 (2000).

[265] L.-M. Duan, G. Giedke, J. I. Cirac, and P. Zoller. *Entanglement Purification of Gaussian Continuous Variable Quantum States*, Phys. Rev. Lett. **84**, 4002 (2000).

[266] J. Fiurášek, L. Mišta, and R. Filip. *Entanglement concentration of continuous–variable quantum states*, Phys. Rev. A **67**, 022304 (2003).

[267] H. Takahashi, *et al.*. *Entanglement distillation from Gaussian input states*, Nat. Photonics **4**, 178 (2010).

[268] P. Kok, *et al.*. *Linear optical quantum computing with photonic qubits*, Rev. Mod. Phys. **79**, 135 (2007).

[269] J. L. O'Brien. *Optical Quantum Computing*, Science **318**, 1567 (2007).

[270] C. Śliwa and K. Banaszek. *Conditional preparation of maximal polarization entanglement*, Phys. Rev. A **67**, 030101 (2003).

[271] T. B. Pittman, *et al.*. *Heralded two–photon entanglement from probabilistic quantum logic operations on multiple parametric down–conversion sources*, IEEE J. Sel. Top. Quant. Elec. **9**, 1478 (2003).

[272] P. van Loock and N. Lütkenhaus. *Simple criteria for the implementation of projective measurements with linear optics*, Phys. Rev. A **69**, 012302 (2004).

[273] W.-Y. Hwang. *Quantum Key Distribution with High Loss: Toward Global Secure Communication*, Phys. Rev. Lett. **91**, 057901 (2003).

[274] J. Calsamiglia, S. M. Barnett, and N. Lütkenhaus. *Conditional beam–splitting attack on quantum key distribution*, Phys. Rev. A **65**, 012312 (2001).

[275] K. Edamatsu, R. Shimizu, and T. Itoh. *Measurement of the Photonic de Broglie Wavelength of Entangled Photon Pairs Generated by Spontaneous Parametric Down–Conversion*, Phys. Rev. Lett. **89**, 213601 (2002).

[276] A. J. Shields. *Semiconductor quantum light sources*, Nat. Photonics **1**, 215 (2007).

[277] D. Achilles, C. Silberhorn, and I. A. Walmsley. *Direct, Loss–Tolerant Characterization of Nonclassical Photon Statistics*, Phys. Rev. Lett. **97**, 043602 (2006).

[278] B. E. Kardynał, Z. L. Yuan, and A. J. Shields. *An avalanche–photodiode–based photon–number–resolving detector*, Nat. Photonics **2**, 425 (2008).

[279] D. Achilles, *et al.*. *Photon–number–resolving detection using time–multiplexing*, J. Mod. Opt. **51**, 1499 (2004).

[280] K. Banaszek and I. A. Walmsley. *Photon counting with a loop detector*, Optics Lett. **28**, 52 (2003).

[281] J. Kim, S. Takeuchi, S. Yamamoto, and H. H. Hogue. *Multiphoton detection using visible light photon counter*, Appl. Phys. Lett. **74**, 902 (1999).

[282] B. Cabrera, *et al.*. *Detection of single infrared, optical, and ultraviolet photons using superconducting transition edge sensors*, Appl. Phys. Lett. **73**, 735 (1998).

[283] S. Somani, S. Kasapi, K. Wilsher, W. L. amd R. Sobolewski, and G. N. Gol'stman. *New photon detector for device analysis: Superconducting single–photon detector based on a hot electron effect*, Vac. Sci. Technol. B **19**, 2766 (2001).

[284] P. Eraerds, M. Legré, J. Zhang, H. Zbinden, and N. Gisin. *Photon Counting OTDR: Advantages and Limitations*, J. Lightwave Technol. **28**, 952 (2010).

[285] A. J. Miller, S. W. Nam, J. M. Martinis, and A. V. Sergienko. *Demonstration of a low–noise near–infrared photon counter with multiphoton discrimination*, Appl. Phys. Lett. **83**, 791 (2003).

[286] M. Fujiwara and M. Sasaki. *Multiphoton discrimination at telecom wavelength with charge integration photon detector*, Appl. Phys. Lett. **86**, 111119 (2005).

[287] B. E. Kardynał, *et al.*. *Photon number resolving detector based on a quantum dot field effect transistor*, Appl. Phys. Lett. **90**, 181114 (2007).

[288] E. J. Gansen, *et al.*. *Photon–number–discriminating detection using a quantum–dot, optically gated, field–effect transistor*, Nat. Photonics **1**, 585 (2007).

[289] S. Gleyzes, *et al.*. *Quantum jumps of light recording the birth and death of a photon in a cavity*, Nature **446**, 297 (2007).

[290] C. Guerlin, *et al.*. *Progressive field–state collapse and quantum non–demolition photon counting*, Nature **448**, 889 (2007).

[291] D. I. Schuster, *et al.*. *Resolving photon number states in a superconducting circuit*, Nature **445**, 515 (2007).

[292] N. Imoto, H. A. Haus, and Y. Yamamoto. *Quantum nondemolition measurement of the photon number via the optical Kerr effect*, Phys. Rev. A **32**, 2287 (1985).

[293] M. J. Holland, D. F. Walls, and P. Zoller. *Quantum nondemolition measurements of photon number by atomic beam deflection*, Phys. Rev. Lett. **67**, 1716 (1991).

[294] K. Jacobs, P. Tombesi, M. J. Collett, and D. F. Walls. *Quantum–nondemolition measurement of photon number using radiation pressure*, Phys. Rev. A **49**, 1961 (1994).

[295] W. J. Munro, K. Nemoto, R. G. Beausoleil, and T. P. Spiller. *High–efficiency quantum–nondemolition single–photon–number–resolving detector*, Phys. Rev. A **71**, 033819 (2005).

[296] J. Larson and M. Abdel-Aty. *Cavity QED nondemolition measurement scheme using quantized atomic motion*, Phys. Rev. A **80**, 053609 (2009).

[297] T. Bastin, J. von Zanthier, and E. Solano. *Measure of phonon–number moments and motional quadratures through infinitesimal–time probing of trapped ions*, J. Phys. B: At. Mol. Opt. Phys. **39**, 685 (2006).

[298] A. N. Boto, *et al.*. *Quantum Interferometric Optical Lithography: Exploiting Entanglement to Beat the Diffraction Limit*, Phys. Rev. Lett. **85**, 2733 (2000).

[299] C. Simon and D. Bouwmeester. *Theory of an Entanglement Laser*, Phys. Rev. Lett. **91**, 053601 (2003).

[300] B. M. Terhal. *Detecting quantum entanglement*, Theor. Comp. Sci. **287**, 313 (2002).

[301] J. I. DeVicente. *Separability criteria based on the Bloch representation of density matrices*, Quantum Inf. Comput. **7**, 624 (2007).

[302] P. Rungta, *et al.*. *Directions in Quantum Optics*, pp. 149–164. Springer, Berlin (2001).

[303] G. Adesso and F. Illuminati. *Entanglement in continuous–variable systems: recent advances and current perspective*, J. Phys. A: Math. Theor. **40**, 7821 (2007).

[304] J. I. C. Lu. M. Duan, G. Giedke and P. Zoller. *Inseparability Criterion for Continuous Variable Systems*, Phys. Rev. Lett **84**, 2722 (2000).

[305] R. Simon. *Peres–Horodecki Separability Criterion for Continuous Variable Systems*, Phys. Rev. Lett **84**, 2726 (2000).

[306] M. D. Reid. *Demonstration of the Einstein–Podolsky–Rosen paradox using nondegenerate parametric amplification*, Phys. Rev. A **40**, 913 (1989).

[307] S. Mancini, V. Giovannetti, D. Vitali, and P. Tombesi. *Entangling Macroscopic Oscillators Exploiting Radiation Pressure*, Phys. Rev. Lett. **88**, 120401 (2002).

[308] V. Giovannetti, S. Mancini, D. Vitali, and P. Tombesi. *Characterizing the entanglement of bipartite quantum systems*, Phys. Rev. A **67**, 022320 (2003).

[309] P. van Loock and A. Furusawa. *Detecting genuine multipartite continuous–variable entanglement*, Phys. Rev. A **67**, 052315 (2003).

[310] Z. Y. Ou, S. F. Pereira, H. J. Kimble, and K. C. Peng. *Realization of the Einstein–Podolsky–Rosen paradox for continuous variables*, Phys. Rev. Lett. **68**, 3663 (1992).

[311] C. Schori, J. L. Sørensen, and E. S. Polzik. *Narrow–band frequency tunable light source of continuous quadrature entanglement*, Phys. Rev. A **66**, 033802 (2002).

[312] M. G. Moore and P. Meystre. *Theory of Superradiant Scattering of Laser Light from Bose–Einstein Condensates*, Phys. Rev. Lett. **83**, 5202 (1999).

[313] M. G. Moore and P. Meystre. *Generating Entangled Atom–Photon Pairs from Bose–Einstein Condensates*, Phys. Rev. Lett. **85**, 5026 (2000).

[314] V. Yukalov. *Entanglement production under collective radiation*, Laser Phys. **14**, 1403 (2004).

[315] M. M. Cola, M. G. A. Paris, and N. Piovella. *Robust generation of entanglement in Bose–Einstein condensates by collective atomic recoil*, Phys. Rev. A **70**, 043809 (2004).

[316] T. Brandes. *Coherent and collective quantum optical effects in mesoscopic systems*, Phys. Rep. **408**, 315 (2005).

[317] N. Piovella, M. Cola, and R. Bonifacio. *Quantum fluctuations and entanglement in the collective atomic recoil laser using a Bose–Einstein condensate*, Phys. Rev. A **67**, 013817 (2003).

[318] L.-M. Duan, A. Sørensen, J. Cirac, and P. Zoller. *Squeezing and Entanglement of Atomic Beams*, Phys. Rev. Lett. **85**, 3991 (2000).

[319] H. Pu and P. Meystre. *Creating Macroscopic Atomic Einstein–Podolsky–Rosen States from Bose–Einstein Condensates*, Phys. Rev. Lett. **85**, 3987 (2000).

[320] R. Bonifacio, N. Piovella, G. R. M. Robb, and A. Schiavi. *Quantum regime of free electron lasers starting from noise*, Phys. Rev. ST Accel. Beams **9**, 090701 (2006).

[321] S. Janssen, D. Schwahn, and T. Springer. *Mean–field Ising crossover and the critical exponents γ, ν, and η for a polymer blend: d–PB/PS studied by small–angle neutron scattering*, Phys. Rev. Lett. **68**, 3180 (1992).

[322] K. V. Kheruntsyan, M. K. Olsen, and P. D. Drummond. *Einstein–Podolsky–Rosen Correlations via Dissociation of a Molecular Bose–Einstein Condensate*, Phys. Rev. Lett. **95**, 150405 (2005).

[323] C. M. Savage, P. E. Schwenn, and K. V. Kheruntsyan. *First–principles quantum simulations of dissociation of molecular condensates: Atom correlations in momentum space*, Phys. Rev. A **74**, 033620 (2006).

[324] P. Deuar and P. D. Drummond. *Correlations in a BEC Collision: First–Principles Quantum Dynamics with 150 000 Atoms*, Phys. Rev. Lett. **98**, 120402 (2007).

[325] J. M. Vogels, K. Xu, and W. Ketterle. *Generation of Macroscopic Pair–Correlated Atomic Beams by Four–Wave Mixing in Bose–Einstein Condensates*, Phys. Rev. Lett. **89**, 020401 (2002).

[326] A. Perrin, *et al.*. *Observation of Atom Pairs in Spontaneous Four–Wave Mixing of Two Colliding Bose–Einstein Condensates*, Phys. Rev. Lett. **99**, 150405 (2007).

[327] K. M. Hilligsøe and K. Mølmer. *Phase–matched four wave mixing and quantum beam splitting of matter waves in a periodic potential*, Phys. Rev. A **71**, 041602 (2005).

[328] G. K. Campbell, *et al.*. *Parametric Amplification of Scattered Atom Pairs*, Phys. Rev. Lett. **96**, 020406 (2006).

[329] H. F. Hofmann and S. Takeuchi. *Violation of local uncertainty relations as a signature of entanglement*, Phys. Rev. A **68**, 032103 (2003).

[330] O. Gühne. *Characterizing Entanglement via Uncertainty Relations*, Phys. Rev. Lett. **92**, 117903 (2004).

[331] D. E. Browne, J. Eisert, S. Scheel, and M. B. Plenio. *Driving non–Gaussian to Gaussian states with linear optics*, Phys. Rev. A **67**, 062320 (2003).

[332] S. J. Freedman and J. F. Clauser. *Experimental Test of Local Hidden–Variable Theories*, Phys. Rev. Lett. **28**, 938 (1972).

[333] E. S. Fry and R. C. Thompson. *Experimental Test of Local Hidden–Variable Theories*, Phys. Rev. Lett. **37**, 465 (1976).

[334] A. Aspect, P. Grangier, and G. Roger. *Experimental Tests of Realistic Local Theories via Bell's Theorem*, Phys. Rev. Lett. **47**, 460 (1981).

[335] A. Aspect, P. Grangier, and G. Roger. *Experimental Realization of Einstein–Podolsky–Rosen–Bohm Gedankenexperiment: A New Violation of Bell's Inequalities*, Phys. Rev. Lett. **49**, 91 (1982).

[336] A. Aspect, J. Dalibard, and G. Roger. *Experimental Test of Bell's Inequalities Using Time–Varying Analyzers*, Phys. Rev. Lett. **49**, 1804 (1982).

[337] W. Tittel, *et al.*. *Experimental demonstration of quantum correlations over more than 10 km*, Phys. Rev. A **57**, 3229 (1998).

[338] J.-W. Pan, D. Bouwmeester, M. Daniell, H. Weinfurter, and A. Zeilinger. *Experimental test of quantum nonlocality in three–photon Greenberger-Horne-Zeilinger entanglement*, Nature **403**, 515 (2000).

[339] D. Salart, A. Baas, J. A. W. van Houwelingen, N. Gisin, and H. Zbinden. *Spacelike Separation in a Bell Test Assuming Gravitationally Induced Collapses*, Phys. Rev. Lett. **100**, 220404 (2008).

[340] M. Ansmann, *et al.*. *Violation of Bell's inequality in Josephson phase qubits*, Nature **461**, 504 (2009).

[341] J. F. Clauser, M. A. Horne, A. Shimony, and R. A. Holt. *Proposed Experiment to Test Local Hidden–Variable Theories*, Phys. Rev. Lett. **23**, 880 (1969).

[342] R. Landauer. *Information is physical.* In *Proc. Workshop on Physics and Computation PhysComp. '92*, pp. 1–4. IEEE Comp. Sci.Press, Los Alamitos (1993).

[343] R. Landauer. *The Physical Nature of Information*, Phys. Lett. A **217**, 188 (1996).

[344] R. Landauer. *Quantum theory, the Church–Turing Principle and the universal quantum computer*, Proc. R. Soc. Lond. A **400**, 97 (1985).

[345] D. Deutsch and R. Jozsa. *Rapid solution of problems by quantum computation*, Proc. R. Soc. Lond. A **439**, 553 (1992).

[346] R. Cleve, A. Ekert, C. Macchiavello, and M. Mosca. *Quantum algorithms revisited*, Proc. R. Soc. Lond. A **454**, 339 (1998).

[347] A. Kitaev. *Quantum measurements and the Abelian stabilizer problem* (1995). Quant-ph/9511026.

[348] D. Simon. *On the power of quantum computation.* In *Proceedings,* 35^{th} *Annual Symposium on Foundations of Computer Science*, pp. 116–123. IEEE Press, Los Alamitos (1994).

[349] R. L. Rivest, A. Shamir, and L. M. Adleman. *A method for obtaining digital signatures and public–key cryptosystems*, Comm. ACM **21**, 120 (1978).

[350] C. Lomont. *The Hidden Subgroup Problem – Review and Open Problems* (2004). Quant-ph/0411037.

[351] L. Grover. *A fast quantum mechanical algorithm for database search.* In *Proc.* 28^{th} *Annual ACM Symposium on the Theory of Computation*, pp. 212–219. ACM Press, New York (1996).

[352] L. K. Grover. *Quantum mechanics helps in searching for a needle in a haystack*, Phys. Rev. Lett. **79**, 325 (1997).

[353] G. Brassard, P. Hoyer, and A. Tapp. *Quantum Counting.* In *25th International Colloquium on Automata, Languages and Programming (ICALP'98)*, vol. 1443, pp. 820–831. Springer-Verlag, Berlin (1998).

[354] A. W. Harrow, A. Hassidim, and S. Lloyd. *Quantum Algorithm for Linear Systems of Equations*, Phys. Rev. Lett. **103**, 150502 (2009).

[355] K. Temme, T. J. Osborne, K. G. Vollbrecht, D. Poulin, and F. Verstraete. *Quantum Metropolis sampling*, Nature **471**, 87 (2011).

[356] A. Ambainis. *Quantum walks and their algorithmic applications*, International Journal of Quantum Information **1**, 507 (2003).

[357] D. Berry, G. Ahokas, R. Cleve, and B. C. Sanders. *Efficient quantum algorithms for simulating sparse Hamiltonians*, Comm. Math. Phys. **270**, 359 (2007).

[358] E. Farhi, J. Goldstone, and S. Gutmann. *A quantum algorithm for the Hamiltonian NAND tree*, Theory of Computing **4**, 169 (2008).

[359] A. M. Childs, R. Cleve, S. P. Jordan, and D. Yeung. *Discrete–query quantum algorithm for NAND trees*, Theory of Computing **5**, 119 (2009).

[360] A. Ambainis, A. M. Childs, B. W. Reichardt, R. Špalek, and S. Zheng. *Every AND–OR formula of size N can be evaluated in time* $N^{1/2+o(1)}$ *on a quantum computer.* In *Proceedings of the* 48^{th} *IEEE Symposium on the Foundations of Computer Science*, pp. 363–372. IEEE Press, Los Alamitos (2007).

[361] A. Ambaini. *A nearly optimal discrete query quantum algorithm for evaluating NAND formulas* (2007). ArXiv:0704.3628.

[362] A. M. Childs, *et al.*. *Exponential algorithmic speedup by quantum walk.* In *Proc.* 35^{th} *ACM Symposium on Theory of Computing (STOC 2003)*, pp. 59–68 (2003).

[363] L. M. K. Vandersypen, *et al.*. *Experimental realization of Shor's quantum factoring algorithm using nuclear magnetic resonance*, Nature **414**, 883 (2001).

[364] L. M. K. Vandersypen, *et al.*. *Experimental Realization of an Order–Finding Algorithm with an NMR Quantum Computer*, Phys. Rev. Lett. **85**, 5452 (2000).

[365] S. Gulde, *et al.*. *Implementation of the Deutsch–Jozsa algorithm on an ion–trap quantum computer*, Nature **421**, 48 (2003).

[366] L. DiCarlo, *et al.*. *Demonstration of two–qubit algorithms with a superconducting quantum processor*, Nature **460**, 240 (2009).

[367] J. A. Jones, M. Mosca, and R. H. Hansen. *Implementation of a quantum search algorithm on a quantum computer*, Nature **393**, 344 (1998).

[368] I. L. Chuang, N. Gershenfeld, and M. Kubinec. *Experimental Implementation of Fast Quantum Searching*, Phys. Rev. Lett. **80**, 3408 (1998).

[369] P. G. Kwiat, J. R. Mitchell, P. D. D. Schwindt, and A. G. White. *Implementation of Grover's quantum search algorithm: an optical approach*, J. Mod. Opt. **47**, 257 (2000).

[370] K.-A. Brickman, *et al.*. *Implementation of Grover's quantum search algorithm in a scalable system*, Phys. Rev. A **72**, 050306 (2005).

[371] L. M. K. Vandersypen, *et al.*. *Implementation of a three–quantum–bit search algorithm*, Appl. Phys. Lett. **76**, 646 (1999).

[372] G. L. Long and L. Xiao. *Experimental realization of a fetching algorithm in a 7 qubit NMR quantum computer*, J. Chem.Phys. **119**, 8473 (2003).

[373] C. H. Bennett and S. J. Wiesner. *Communication via one– and two–particle operators on Einstein–Podolsky–Rosen states*, Phys. Rev. Lett. **69**, 2881 (1992).

[374] R. Cleve, D. Gottesman, and H.-K. Lo. *How to Share a Quantum Secret*, Phys. Rev. Lett. **83**, 648 (1999).

[375] M. Hillery, V. Bužek, and A. Berthiaume. *Quantum secret sharing*, Phys. Rev. A **59**, 1829 (1999).

[376] D. Gottesman and I. Chuang. *Quantum Digital Signatures* (2001). ArXiv:quant-ph/0105032.

[377] H. Buhrman, R. Cleve, J. Watrous, and R. de Wolf. *Quantum Fingerprinting*, Phys. Rev. Lett. **87**, 167902 (2001).

[378] D. Gottesman. *Uncloneable Encryption*, Quantum Information and Computation **3**, 581 (2003).

[379] K. Chen and H.-K. Lo. *Conference key agreement and quantum sharing of classical secrets with noisy GHZ states*. In *International Symposium on Information Theory (ISIT) 2005*, pp. 1607 – 1611. IEEE Press, Los Alamitos (2005).

[380] S. Wiesner. *Conjugate coding*, Sigact News **15**, 78 (1983).

[381] H.-K. Lo and Y. Zhao. *Quantum Cryptography*, Encyclopedia of Complexity and Systems Science **8**, 7265 (2009).

[382] G. Vernam. *Cipher printing telegraph systems for secret wire and radio telegraphic communications*, J. Am. Inst. Electr. Eng. **45**, 109 (1926).

[383] M. N. Wegman and J. L. Carter. *Universal classes of hash functions*, Journal of Computer and System Sciences **18**, 143 (1979).

[384] M. N. Wegman and J. L. Carter. *New hash functions and their use in authentication and set equality*, Journal of Computer and System Sciences **22**, 265 (1981).

[385] A. K. Ekert. *Quantum cryptography based on Bell's theorem*, Phys. Rev. Lett. **67**, 661 (1991).

[386] A. K. Ekert, J. G. Rarity, P. R. Tapster, and G. Massimo Palma. *Practical quantum cryptography based on two–photon interferometry*, Phys. Rev. Lett. **69**, 1293 (1992).

[387] V. Coffman, J. Kundu, and W. K. Wootters. *Distributed entanglement*, Phys. Rev. A **61**, 052306 (2000).

[388] B. Toner. *Monogamy of nonlocal quantum correlations*, Proc. R. Soc. A **465** (2009).

[389] R. Renner. *Security of Quantum Key Distribution*, Int. J. Quant. Inf. **6**, 1 (2008).

[390] C. H. Bennett. *Quantum cryptography using any two nonorthogonal states*, Phys. Rev. Lett. **68**, 3121 (1992).

[391] D. Bruß. *Optimal Eavesdropping in Quantum Cryptography with Six States*, Phys. Rev. Lett. **81**, 3018 (1998).

[392] C. H. Bennett, G. Brassard, S. Breidbart, and S. Wiesner. *Eavesdrop–Detecting Quantum Communications Channel*, IBM Technical Disclosure Bulletin **26**, 4363 (1984).

[393] W.-Y. Hwang. *Quantum Key Distribution with High Loss: Toward Global Secure Communication*, Phys. Rev. Lett. **91**, 057901 (2003).

[394] F. Grosshans, *et al.*. *Quantum key distribution using gaussian–modulated coherent states*, Nature **421**, 238 (2003).

[395] C. H. Bennett, F. Bessette, G. Brassard, L. Salvail, and J. Smolin. *Experimental Quantum Cryptography*, J. of Cryptography **5**, 3 (1992).

[396] P. D. Townsend, J. G. Rarity, and P. R. Tapster. *Single photon interference in 10–km–long optical fibre interferometer*, Electron. Lett **29**, 634 (1993).

[397] A. Müller, H. Zbinden, and N. Gisin. *Underwater quantum coding*, Nature **378**, 449 (1995).

[398] D. Stucki, N. Gisin, O. Guinnard, G. Robordy, and H. Zbinden. *Quantum key distribution over 67 km with a plug&play system*, New J. of Physics **4**, 41 (2002).

[399] J.-W. Pan, D. Bouwmeester, H. Weinfurter, and A. Zeilinger. *Experimental Entanglement Swapping: Entangling Photons That Never Interacted*, Phys. Rev. Lett. **80**, 3891 (1998).

[400] C. H. Bennett, H. J. Bernstein, S. Popescu, and B. Schumacher. *Concentrating partial entanglement by local operations*, Phys. Rev. A **53**, 2046 (1996).

[401] T. Schmitt-Manderbach, *et al.*. *Experimental Demonstration of Free–Space Decoy–State Quantum Key Distribution over 144 km*, Phys. Rev. Lett. **98**, 010504 (2007).

[402] R. Ursin, *et al.*. *Entanglement–based quantum communication over 144 km*, Nature Phys. **3**, 481 (2007).

[403] S. Perseguers, M. Lewenstein, A. Acín, and J. I. Cirac. *Quantum random networks*, Nature Phys. **6**, 539 (2010).

[404] B. Horstmann, B. Reznik, S. Fagnocchi, and J. I. Cirac. *Hawking Radiation from an Acoustic Black Hole on an Ion Ring*, Phys. Rev. Lett. **104**, 250403 (2010).

[405] C. Barcelo, S. Liberati, and M. Visser. *Analogue Gravity*, Living Rev. Rel. **8**, 12 (2005).

[406] T. G. Philbin, *et al.*. *Fiber–Optical Analog of the Event Horizon*, Science **319**, 1367 (2008).

[407] R. Balbinot, A. Fabbri, S. Fagnocchi, A. Recati, and I. Carusotto. *Nonlocal density correlations as a signature of Hawking radiation from acoustic black holes*, Phys. Rev. A **78**, 021603 (2008).

[408] O. Lahav, *et al.*. *Realization of a Sonic Black Hole Analog in a Bose–Einstein Condensate*, Phys. Rev. Lett. **105**, 240401 (2010).

[409] K. L. Brown, W. J. Munro, and V. M. Kendon. *Using Quantum Computers for Quantum Simulation*, **12**, 2268 (2010).

[410] H. F. Trotter. *On the product of semi–groups of operators*, Proc. Am. Math. Phys. **10**, 545 (1959).

[411] M. Suzuki. *Improved Trotter–like formula*, Phys. Lett. A **180**, 232 (1993).

[412] I. Buluta and F. Nori. *Quantum simulators*, Science **326**, 108 (2009).

[413] D. J. Wineland. *Quantum information processing and quantum control with trapped atomic ions*, Physica Scripta **T137**, 014007 (2009).

[414] T. Schätz, A. Friedenauer, H. Schmitz, L. Petersen, and S. Kahra. *Towards (scalable) quantum simulations in ion traps*, J. Mod. Optic. **54**, 2317 (2007).

[415] X.-L. Deng, D. Porras, and J. I. Cirac. *Effective spin quantum phases in systems of trapped ions*, Phys. Rev. A **72**, 063407 (2005).

[416] D. Porras and J. I. Cirac. *Effective Quantum Spin Systems with Trapped Ions*, Phys. Rev. Lett. **92**, 207901 (2004).

[417] D. Porras and J. I. Cirac. *Bose–Einstein Condensation and Strong–Correlation Behavior of Phonons in Ion Traps*, Phys. Rev. Lett. **93**, 263602 (2004).

[418] A. Friedenauer, H. Schmitz, J. Z. Glueckert, D. Porras, and T. Schätz. *Simulating a quantum magnet with trapped ions*, Nature Phys. **4**, 757 (2008).

[419] R. Islam, *et al.*. *Onset of a quantum phase transition with a trapped ion quantum simulator*, Nat. Commun. **2**, 377 (2011).

[420] R. Gerritsma, *et al.*. *Quantum Simulation of the Klein Paradox with Trapped Ions*, Phys. Rev. Lett. **106**, 060503 (2011).

[421] R. Gerritsma, *et al.*. *Quantum Simulation of the Dirac equation*, Nature **463**, 68 (2010).

[422] E. E. Edwards, *et al.*. *Quantum simulation and phase diagram of the transverse–field Ising model with three atomic spins*, Phys. Rev. B **82**, 060412 (2010).

[423] T. Kinoshita, T. Wenger, and D. Weiss. *Observation of a one–dimensional Tonks–Girardeau gas*, Science **305**, 1125 (2004).

[424] J. A. Jones. *NMR quantum computation: A critical evaluation*, Fortschr. Phys. **48**, 909 (2000).

[425] C. H. Tseng, *et al.*. *Quantum simulation of a three–body–interaction Hamiltonian on an NMR quantum computer*, Phys. Rev. A **61**, 012302 (1999).

[426] K. R. Brown, R. J. Clark, and I. L. Chuang. *Limitations of Quantum Simulation Examined by Simulating a Pairing Hamiltonian Using Nuclear Magnetic Resonance*, Phys. Rev. Lett. **97**, 050504 (2006).

[427] C. Negrevergne, R. Somma, G. Ortiz, E. Knill, and R. Laflamme. *Liquid–state NMR simulations of quantum many–body problems*, Phys. Rev. A **71**, 032344 (2005).

[428] B. P. Lanyon, *et al.*. *Towards Quantum Chemistry on a Quantum Computer*, Nature Chem. **2**, 106 (2009).

[429] X. Ma, B. Dakic, W. Naylor, A. Zeilinger, and P. Walther. *Quantum simulation of the wavefunction to probe frustrated Heisenberg spin systems*, Nature Phys. **7**, 399405 (2011).

[430] J. Cho, D. G. Angelakis, and S. Bose. *Simulation of high–spin Heisenberg models in coupled cavities*, Phys. Rev. A **78**, 062338 (2008).

[431] A. Micheli, G. K. Brennen, and P. Zoller. *A toolbox for lattice–spin models with polar molecules*, Nature Phys. **2**, 341 (2006).

[432] R. Hanson, L. P. Kouwenhoven, J. R. Petta, S. Tarucha, and L. M. K. Vandersypen. *Spins in few–electron quantum dots*, Rev. Mod. Phys. **79**, 1217 (2007).

[433] J. Wrachtrup and F. Jelezko. *Processing quantum information in diamond*, J. Phys.: Condens. Matter **18**, 807 (2006).

[434] G. Ortiz, J. E. Gubernatis, E. Knill, and R. Laflamme. *Quantum algorithms for fermionic simulations*, Phys. Rev. A **64**, 022319 (2001).

[435] A. Aspuru-Guzik, A. D. Dutoi, P. J. Love, and M. Head-Gordon. *Simulated Quantum Computation of Molecular Energies*, Science **309**, 1704.

[436] B. M. Boghosian and W. Taylor. *Quantum lattice–gas model for the many–particle Schrödinger equation in d dimensions*, Phys. Rev. E **57**, 54 (1998).

[437] R. Schützhold and S. Mostame. *Quantum simulator for the O(3) nonlinear sigma model*, JETP Letters **82**, 248 (2005).

[438] T. Byrnes and Y. Yamamoto. *Simulating lattice gauge theories on a quantum computer*, Phys. Rev. A **73**, 022328 (2006).

[439] S. Tewari, V. W. Scarola, T. Senthil, and S. Das Sarma. *Emergence of Artificial Photons in an Optical Lattice*, Phys. Rev. Lett. **97**, 200401 (2006).

[440] E. Haller, *et al.*. *Pinning quantum phase transition for a Luttinger liquid of strongly interacting bosons*, Nature **466**, 597 (2010).

[441] A. Bermudez, *et al.*. *Wilson Fermions and Axion Electrodynamics in Optical Lattices*, Phys. Rev. Lett. **105**, 190404 (2010).

[442] H. P. Büchler, G. Blatter, and W. Zwerger. *Commensurate–Incommensurate Transition of Cold Atoms in an Optical Lattice*, Phys. Rev. Lett. **90**, 130401 (2003).

[443] J. I. Cirac, P. Maraner, and J. K. Pachos. *Cold Atom Simulation of Interacting Relativistic Quantum Field Theories*, Phys. Rev. Lett. **105**, 190403 (2010).

[444] D. N. Matsukevich, *et al.*. *Entanglement of Remote Atomic Qubits*, Phys. Rev. Lett. **96**, 030405 (2006).

[445] B. Julsgaard, J. Sherson, J. L. Sørensen, and E. S. Polzik. *Characterizing the spin state of an atomic ensemble using the magneto–optical resonance method*, J. Opt. B: Quantum Semiclass. Opt. **6**, 5 (2004).

[446] L.-M. Duan, J. I. Cirac, P. Zoller, and E. S. Polzik. *Quantum Communication between Atomic Ensembles Using Coherent Light*, Phys. Rev. Lett. **85**, 5643 (2000).

[447] M. Fleischhauer and M. Lukin. *Dark–State Polaritons in Electromagnetically Induced Transparency*, Phys. Rev. Lett. **84**, 5094 (2000).

[448] M. D. Lukin. *Colloquium: Trapping and manipulating photon states in atomic ensembles*, Rev. Mod. Phys. **75**, 457 (2003).

[449] A. V. Gorshkov, A. André, M. D. Lukin, and A. S. Sørensen. *Photon storage in Λ –type optically dense atomic media. I. Cavity model*, Phys. Rev. A **76**, 033804 (2007).

[450] J. B. Brask, *et al.*. *Fast entanglement distribution with atomic ensembles and fluorescent detection*, Phys. Rev. A **81**, 020303 (2010).

[451] C. A. Muschik, E. S. Polzik, and J. I. Cirac. *Dissipatively driven entanglement of two macroscopic atomic ensembles* (2010). ArXiv:1007.2209.

[452] H. Krauter, *et al.*. *Entanglement generated by dissipation* (2010). ArXiv:1006.4344.

[453] M. Horodecki, P. W. Shor, and M. B. Ruskai. *Entanglement Breaking Channels*, Rev. Math. Phys. **15**, 629 (2003).

[454] J. Dehaene, M. Van den Nest, B. De Moor, and F. Verstraete. *Local permutations of products of Bell states and entanglement distillation*, Phys. Rev. A **67**, 022310 (2003).